



University of HUDDERSFIELD

University of Huddersfield Repository

Colley, Gareth

Design, Operation and Diagnostics of a Vertical Axis Wind Turbine

Original Citation

Colley, Gareth (2012) Design, Operation and Diagnostics of a Vertical Axis Wind Turbine. Doctoral thesis, University of Huddersfield.

This version is available at <http://eprints.hud.ac.uk/id/eprint/17547/>

The University Repository is a digital collection of the research output of the University, available on Open Access. Copyright and Moral Rights for the items on this site are retained by the individual author and/or other copyright owners. Users may access full items free of charge; copies of full text items generally can be reproduced, displayed or performed and given to third parties in any format or medium for personal research or study, educational or not-for-profit purposes without prior permission or charge, provided:

- The authors, title and full bibliographic details is credited in any copy;
- A hyperlink and/or URL is included for the original metadata page; and
- The content is not changed in any way.

For more information, including our policy and submission procedure, please contact the Repository Team at: E.mailbox@hud.ac.uk.

<http://eprints.hud.ac.uk/>

DESIGN, OPERATION AND DIAGNOSTICS OF A
VERTICAL AXIS WIND TURBINE

A THESIS SUBMITTED FOR THE DEGREE OF

DOCTOR OF PHILOSOPHY

BY

GARETH COLLEY (BSc)

Supervisor: Prof. R.Mishra

Co-Supervisor: Prof. H.V.Rao

Industrial Collaborator: Mr Ray Woolhead, Insight Renewables

School of Computing & Engineering

University of Huddersfield, UK

2012

'Design, Operation and Diagnostics of a Vertical Axis Wind Turbine'
By Gareth Colley, Department of Engineering & Technology, University of Huddersfield, UK

ABSTRACT

The need for sustainable energy sources becomes greater each year due to the continued depletion of fossil fuels and the resulting energy crisis. Solutions to this problem are potentially in the form of wind turbines which have been receiving increased support at a micro level. At present a number of wind turbines are being developed that are of cross-flow vertical axis operation which have shown significant increases in performance compared to existing technologies. From an extensive literature review a number of key issues have been highlighted which are concerned with design, operation and diagnostics of this new wind power technology which have been used to formulate the scope of this research.

A design procedure for a cross-flow machine that features both a multi-blade rotor and fixed outer stator guide vanes has been derived in which both rotor and stator blade profiles have been generated for a low wind speed urban application. Using these blade profiles a prototype wind turbine has been fabricated and used for full scale development testing.

In the presented work both experimental and numerical investigations have been carried out to determine the operational characteristics of this new technology. The experimental data obtained under controlled laboratory conditions has been used to validate a Computational Fluid Dynamic (CFD) model which has been used throughout. A flow field analysis of the machine has highlighted large asymmetries in both pressure and velocity about the central axis of the machine in both stationary and rotating frames of reference. This has identified primary inefficiencies within the design which limit the torque generating capability of the rotor due to blockage effects and downstream blade interactions. This asymmetry has been quantified in the form asymmetry ratio and used to determine downstream rotor effects and the optimum location of multiple wind turbines which is seen to be $x/D > 10$ in order to minimize performance reductions.

The torque and power generation capabilities of the machine have been characterised at both 'design' and 'off-design' conditions in which individual blade torque contributions have been quantified. This has highlighted specific energy transfer zones within the turbine namely at a few key blades on the windward side of the rotor. It has also shown counter-rotating torques generated on the leeward side of the machine at specific blade positions during the cycle. Overall performance has been quantified in which a maximum $C_T = 1.7$ and $C_p = 0.24$ has been observed which has some similarities to the Savonius rotor. Geometric effects on torque and power response have been quantified in which a strong dependence on stator blade number is noticed. Further, maximum performance output of the machine is generated at the baseline design condition. Using torque response data a multiple regression model has been developed in which a design equation for cross-flow rotor torque has been derived which can be used during the conceptual design phase.

Finally, the effectiveness of a two-dimensional transient CFD model to predict cross-flow wind turbine rotor blade loss has been evaluated against full scale experimental data. It has shown that from analysis in the frequency domain specific blade faults can be recognised which agrees well with experimental data obtained. The use of this model for wind turbine performance emulation has been described.

"To know is to know that you know nothing.

That is the meaning of true knowledge"

Socrates (BC 469 - BC 399)

DECLARATION

- i. The author of this thesis (including any appendices and/or schedules to this thesis) owns any copyright in it (the “Copyright”) and s/he has given The University of Huddersfield the right to use such Copyright for any administrative, promotional, educational and/or teaching purposes.
- ii. Copies of this thesis, either in full or in extracts, may be made only in accordance with the regulations of the University Library. Details of these regulations may be obtained from the Librarian. This page must form part of any such copies made.
- iii. The ownership of any patents, designs, trademarks and any and all other intellectual property rights except for the Copyright (the “Intellectual Property Rights”) and any reproductions of copyright works, for example graphs and tables (“Reproductions”), which may be described in this thesis, may not be owned by the author and may be owned by third parties. Such Intellectual Property Rights and Reproductions cannot and must not be made available for use without the prior written permission of the owner(s) of the relevant Intellectual Property Rights and/or Reproductions.

ACKNOWLEDGEMENTS

Firstly my parents who have provided support and encouragement throughout and made it possible to undertake such a project. Secondly to my partner Sara who listened patiently to my problems and helped to maintain a positive approach to the challenges faced. The industrial collaborator Mr Ray Woolhead of Insight Renewables who provided financing for the project and who's vision allowed for the development of this technology. Primary supervisor and friend Prof. Rakesh Mishra who had faith in my ability to deliver the project. I am forever grateful for his support and encouragements and for the opportunity of working with him. My secondary supervisor Prof. Vasu Rao for his guidance during the early stages of the project and support provided throughout.

A special thanks to Dr Violetta Holmes and Mr Ibad Kureshi of the University of Huddersfield's High Performance Computing (HPC) centre for the use of their systems and overwhelming support throughout. Prof. Andrew Ball for the use of Diagnostic Engineering Research Group (DERG) equipment during experiments. I would like to personally give thanks to Dr Feng Gu for his technical assistance in instrumentation and signal processing which is greatly appreciated. The fantastic technical support staff at the University of Huddersfield in particular Dennis Town, Richard Bailey, Richard Midlam, Phil Holdsworth, Chris Stubbs, Steve Goldstein, Peter Norman, Keith Mallinson, Dave Andrews and Anwar Hussain. I would like to personally thank each of them for their continued support, innovation and expertise during this project.

Thanks to close friends from the University in no particular order, Dr David Bryant, Dr Faisal Al-Tobanni, Taimoor Asim and Kyoo-seon Park for their support and technical input throughout this project. Special thanks to Dr Edward Palmer, Oliver Gilkes, Dr Belachew Tesfa and Dr Vihar Malviya for their personality, enthusiasm, sense of humour and encouragements throughout.

Finally the authors who have been referenced in this thesis where permission could not be requested. It is assumed that figures published from their work will be greeted in good spirit through our combined efforts to improve renewable energy technologies.

LIST OF PUBLICATIONS

Colley, G., Mishra, R., Rao, V. and Woolhead, R. (2009) 'Effect of External Structures on Vertical Axis Wind Turbine Flow Field' *Proceedings of the National Conference on Fluid Mechanics & Fluid Power, December 17-19,2009,College of Engineering,Pune .2*

Colley, G., Mishra, R., Rao, V. and Woolhead, R. (2010) 'Effect of rotor blade position on Vertical Axis Wind Turbine performance' *Proceedings of the International Conference on Renewable Energies and Power Quality (ICREPQ'10) Granada (Spain), 23th to 25th March, 2010 .4*

Colley, G., Mishra, R., Rao, H. and Woolhead, R. (2009) 'Performance evaluation of three cross flow vertical axis wind turbine configurations.' *In: Proceedings of Computing and Engineering Annual Researchers' Conference 2009: CEARC'09. Huddersfield: University of Huddersfield. pp. 130-136. ISBN 9781862180857*

Colley, G. and Mishra, R. (2011) 'Computational flow field analysis of a Vertical Axis Wind Turbine'. *In: International Conference on Renewable Energies and Power Quality (ICREPQ'11), 13-15 April 2011, Las Palmas de Gran Canaria, Spain 6*

Colley, G. and Mishra, R. (2011) 'Performance characteristics of a Vertical Axis Wind Turbine (VAWT) under transient conditions'. *In: Proceedings of the 24th International Congress on Condition Monitoring and Diagnostics Engineering Management. Stavanger, Norway: COMADEM. . ISBN 0954130723 8*

TABLE OF CONTENTS

ABSTRACT.....	II
DECLARATION	IV
ACKNOWLEDGEMENTS	V
LIST OF PUBLICATIONS	VI
TABLE OF CONTENTS	VII
LIST OF FIGURES	X
LIST OF TABLES	XIV
NOMENCLATURE.....	XV
CHAPTER 1 INTRODUCTION	2
1.1 WIND ENERGY: A GLOBAL PERSPECTIVE	3
1.2 URBAN WIND POWER	4
1.3 WIND POWER TECHNOLOGIES	6
1.4 WIND TURBINE DIAGNOSTICS	8
1.5 MOTIVATION	11
1.6 ORGANIZATION OF THESIS	13
CHAPTER 2 LITERATURE REVIEW.....	16
2.1 INTRODUCTION	17
2.2 DARRIEUS WIND TURBINES	17
2.3 SAVONIUS WIND TURBINES	19
2.4 CROSS-FLOW WIND TURBINES.....	22
2.5 WIND TURBINE DIAGNOSTICS	27
2.6 SCOPE OF RESEARCH.....	28
2.7 SPECIFIC RESEARCH AIMS AND OBJECTIVES.....	31
CHAPTER 3 DESIGN & TEST SETUP.....	33
3.1 WIND TURBINE DESIGN AND MANUFACTURE	34
3.1.1 Rotor Blade Derivation.....	37
3.1.2 Stator Blade Derivation.....	39
3.1.3 Rotor/Stator Blade Profile Computation	41
3.2 PROTOTYPE MANUFACTURE.....	43
3.3 EXPERIMENTAL TEST SETUP	45
3.3.1 Transmission System.....	46
3.3.2 Power Generation.....	47

3.3.3	<i>Wind Tunnel System Overview</i>	48
3.3.4	<i>Instrumentation and Specifications</i>	50
3.4	NUMERICAL MODELLING APPROACH	52
3.4.1	<i>Computational Hardware</i>	52
3.4.2	<i>Computer Aided Design (CAD) Model</i>	53
3.4.3	<i>Grid Resolution and Discretization Scheme</i>	56
3.4.4	<i>Wind Turbine Boundary Conditions</i>	58
3.4.5	<i>Numerical Formulation and Flow Physics Modelling</i>	60
3.4.6	<i>Wind Turbine Rotation</i>	61
3.4.7	<i>Verification</i>	62
CHAPTER 4	PRESSURE AND VELOCITY FIELD ANALYSIS	63
4.1	NUMERICAL VALIDATION	64
4.2	NUMERICAL PRESSURE FIELD ANALYSIS	69
4.2.1	<i>Variation of Pressure Field in Vertical Direction</i>	69
4.2.2	<i>Variation of Pressure Field with Blade Position</i>	71
4.2.3	<i>Variation of Pressure Field in Angular Direction</i>	75
4.2.4	<i>Summary</i>	80
4.3	NUMERICAL VELOCITY FIELD ANALYSIS.....	82
4.3.1	<i>Variation of Velocity Field in Vertical Direction</i>	82
4.3.2	<i>Variation of Velocity Field with Blade Position</i>	85
4.3.3	<i>Variation of Velocity Field in Angular Direction</i>	87
4.3.4	<i>Summary</i>	92
CHAPTER 5	FLOW DISTRIBUTION AND ASYMMETRY ANALYSIS	93
5.1	MASS FLOW DISTRIBUTION.....	94
5.1.1	<i>Effect of λ and V_∞ on stator passage mass efflux</i>	94
5.1.2	<i>Effect of λ and V_∞ on rotor passage mass efflux</i>	97
5.1.3	<i>Summary</i>	100
5.2	ASYMMETRY RATIO.....	101
5.2.1	<i>Pressure Field Asymmetry Ratio</i>	102
5.2.1	<i>Velocity Field Asymmetry Ratio</i>	103
5.2.2	<i>Summary</i>	105
CHAPTER 6	PERFORMANCE CHARACTERISATION	107
6.1	EXPERIMENTAL PERFORMANCE CHARACTERISTICS	108
6.1.1	<i>Steady State Analysis</i>	108
6.1.2	<i>Summary</i>	114
6.2	NUMERICAL VALIDATION	115
6.3	NUMERICAL TORQUE CHARACTERISTICS	117
6.3.1	<i>Summary</i>	123
6.4	NUMERICAL POWER CHARACTERISTICS	124

6.4.1	<i>Summary</i>	125
6.5	NUMERICAL TOPOGRAPHICAL EFFECTS.....	126
6.5.1	<i>Building Geometry</i>	126
6.5.2	<i>Torque Characteristics</i>	129
6.5.3	<i>Power Characteristics</i>	134
6.5.4	<i>Summary</i>	137
CHAPTER 7	OPTIMIZATION & ROTOR DIAGNOSTICS	139
7.1	PARAMETRIC OPTIMIZATION.....	140
7.1.1	<i>Dimensional Analysis</i>	140
7.1.2	<i>Geometric Configurations</i>	146
7.1.3	<i>Torque Characteristics</i>	147
7.1.4	<i>Power Characteristics</i>	150
7.1.5	<i>Regression Analysis</i>	153
7.1.6	<i>Summary</i>	156
7.2	ROTOR DIAGNOSTICS.....	158
7.2.1	<i>Numerical Rotor Diagnostics</i>	158
7.2.2	<i>Experimental Rotor Diagnostics</i>	164
7.3	SUMMARY.....	168
CHAPTER 8	CONCLUSIONS AND FUTURE WORK	170
8.1	RESEARCH PROBLEM SYNOPSIS.....	171
8.2	RESEARCH AIMS AND MAJOR ACHIEVEMENTS.....	171
8.3	THESIS CONCLUSIONS.....	174
8.4	THESIS CONTRIBUTIONS.....	178
8.5	RECOMMENDATIONS FOR FUTURE WORK.....	180
REFERENCES	182

LIST OF FIGURES

FIGURE 1-1 GWEC/EWEA GLOBAL CUMULATIVE INSTALLED GENERATION CAPACITY (MW), 1990-2007 [7]	4
FIGURE 1-2 HORIZONTAL AXIS WIND TURBINE (HAWT) [24]	6
FIGURE 1-3 SAVONIUS VERTICAL AXIS WIND TURBINE (VAWT) [25]	6
FIGURE 1-4 DARRIEUS VERTICAL AXIS WIND TURBINE (VAWT) [26]	6
FIGURE 1-5 FAILURE NUMBER DISTRIBUTION [%] FOR SWEDISH WIND POWER PLANTS [44]	10
FIGURE 1-6 FAILURES AND SEVERITY (RPN/CPN) FROM 3MW DIRECT DRIVE WIND TURBINE [45].....	10
FIGURE 2-1 DARRIEUS C_p CURVES USING NACA 0012 BLADES AS REPORTED BY BLACKWELL ET AL [48]	18
FIGURE 2-2 SAVONIUS ROTOR TORQUE OUTPUT (C_Q) PLOTTED WITH ANGULAR BLADE POSITION (θ) FOR TWO BLADED ROTOR WITH $h/D = 1.5$ AND $s/D = 0$ AS REPORTED BY BLACKWELL ET AL [53]	20
FIGURE 2-3 CROSS-FLOW TURBINE GEOMETRY REPORTED BY KLEMM ET AL [60]	23
FIGURE 2-4 JET-WHEEL-TURBO WIND TURBINE AS PROPOSED BY LEE AND PARK ET AL [61], [62].....	24
FIGURE 2-5 CROSS-FLOW WIND TURBINE USING SYMMETRICAL CASING AS PROPOSED BY SHIGEMITSU & FUKOTOMI ET AL [64]	25
FIGURE 2-6 ZEPHYR® WIND TURBINE AS REPORTED BY POPE ET AL [67], [68]	26
FIGURE 3-1 PLAN VIEW OF WIND TURBINE STATOR/ROTOR BLADE CONFIGURATION	34
FIGURE 3-2 WIND TURBINE ROTOR BLADE VELOCITY TRIANGLE DEFINITION.....	35
FIGURE 3-3 WIND TURBINE ROTOR BLADE DEFINITION	38
FIGURE 3-4 WIND TURBINE STATOR BLADE DEFINITION	39
FIGURE 3-5 ROTOR BLADE PROFILE GEOMETRY	42
FIGURE 3-6 STATOR BLADE PROFILE GEOMETRY	43
FIGURE 3-7 TOP PROJECTION OF STATOR/ROTOR BLADE ARRANGEMENT.....	44
FIGURE 3-8 SIDE ELEVATION OF WIND TURBINE ASSEMBLY	44
FIGURE 3-9 WIND TURBINE TEST STRUCTURE.....	44
FIGURE 3-10 WIND TURBINE CONTROL SYSTEM	44
FIGURE 3-11 WIND TURBINE SYSTEM OVERVIEW	45
FIGURE 3-12 WIND TURBINE TRANSMISSION SETUP WITH GEAR ENGAGEMENT RAILS	46
FIGURE 3-13 WIND TURBINE POWER GENERATION SYSTEM	47
FIGURE 3-14 WIND TUNNEL SIDE ELEVATION OF WORKING SECTIONS	48
FIGURE 3-15 XZ VIEW OF WIND TURBINE RELATIVE TO TEST CHAMBER EXIT PLANE.....	49
FIGURE 3-16 XY VIEW OF WIND TURBINE RELATIVE TO TEST CHAMBER EXIT PLANE	49
FIGURE 3-17 THREE-DIMENSIONAL WIND TURBINE ROTOR/STATOR GEOMETRY	54
FIGURE 3-18 CFD FLOW DOMAIN IN XY PLANE	54
FIGURE 3-19 CFD FLOW DOMAIN IN XY PLANE	55
FIGURE 3-20 CFD FLOW DOMAIN ZONE BREAKDOWN	56
FIGURE 3-21 CROSS SECTIONAL VIEW OF THREE-DIMENSIONAL CFD MODEL GRID IN XY PLANE	57
FIGURE 3-22 WIND TURBINE STATOR/ROTOR BLADE PASSAGE BOUNDARY DEFINITION	59
FIGURE 3-23 TURBINE ZONE BOUNDARY CONDITIONS FOR NUMERICAL VALIDATION.....	60

FIGURE 4-1 MEASURED VELOCITY FIELD (M/S) AT WIND TUNNEL EXIT PLANE	64
FIGURE 4-2 CFD INTERPOLATED VELOCITY FIELD (M/S) AT VELOCITY INLET BOUNDARY	65
FIGURE 4-3 WIND TURBINE ZONE DEFINITION	66
FIGURE 4-4 CROSS EXAMINATION OF EXPERIMENTAL AND CFD PRESSURE FIELD ($P_{\text{COEFFICIENT}}$)	67
FIGURE 4-5 CROSS EXAMINATION OF EXPERIMENTAL AND CFD VELOCITY FIELD (V/V_{AVG})	68
FIGURE 4-6 STREAM WISE PLOT OF $P_{\text{COEFFICIENT}}$ AT $\Lambda=0$ FOR $V_{\infty}=4\text{M/S}$ IN ZX PLANE	70
FIGURE 4-7 STREAM WISE PLOT OF $P_{\text{COEFFICIENT}}$ AT $\Lambda=0.4$ FOR $V_{\infty}=4\text{M/S}$ IN ZX PLANE	70
FIGURE 4-8 NORMAL TO STREAM WISE PLOT OF $P_{\text{COEFFICIENT}}$ AT $\Lambda=0$ FOR $V_{\infty}=4\text{M/S}$ IN ZY PLANE	70
FIGURE 4-9 NORMAL TO STREAM WISE PLOT OF $P_{\text{COEFFICIENT}}$ AT $\Lambda=0.4$ FOR $V_{\infty}=4\text{M/S}$ IN ZY PLANE	70
FIGURE 4-10 ROTOR BLADE POSITION ANGULAR DEFINITION	72
FIGURE 4-11 PLOT OF $P_{\text{COEFFICIENT}}$ AT ROTOR BLADE POSITION OF 0° FOR $\Lambda=0.4$ AND $V_{\infty}=4\text{M/S}$ AT MID-PLANE	72
FIGURE 4-12 PLOT OF $P_{\text{COEFFICIENT}}$ AT ROTOR BLADE POSITION OF 10° FOR $\Lambda=0.4$ AND $V_{\infty}=4\text{M/S}$ AT MID-PLANE	73
FIGURE 4-13 PLOT OF $P_{\text{COEFFICIENT}}$ AT ROTOR BLADE POSITION OF 20° FOR $\Lambda=0.4$ AND $V_{\infty}=4\text{M/S}$ AT MID-PLANE	73
FIGURE 4-14 PRESSURE COEFFICIENT PLOTTED WITH Θ AT $R = 1\text{M}$ FOR $\Lambda = 0$ AND 0.4	76
FIGURE 4-15 PRESSURE COEFFICIENT PLOTTED WITH Θ AT $R = 0.8\text{M}$ FOR $\Lambda = 0$ AND 0.4	76
FIGURE 4-16 PRESSURE COEFFICIENT PLOTTED WITH Θ AT $R = 0.6\text{M}$ FOR $\Lambda = 0$ AND 0.4	76
FIGURE 4-17 PRESSURE COEFFICIENT PLOTTED WITH Θ AT $R = 0.4\text{M}$ FOR $\Lambda = 0$ AND 0.4	77
FIGURE 4-18 PRESSURE COEFFICIENT PLOTTED WITH Θ AT $R = 0.2\text{M}$ FOR $\Lambda = 0$ AND 0.4	77
FIGURE 4-19 STREAM WISE PLOT OF V/V_{AVG} AT $\Lambda=0$ FOR $V_{\infty}=4\text{M/S}$ IN ZX PLANE	83
FIGURE 4-20 STREAM WISE PLOT OF V/V_{AVG} AT $\Lambda=0.4$ FOR $V_{\infty}=4\text{M/S}$ IN ZX PLANE	83
FIGURE 4-21 NORMAL TO STREAM WISE PLOT OF V/V_{AVG} AT $\Lambda=0$ FOR $V_{\infty}=4\text{M/S}$ IN ZY PLANE	83
FIGURE 4-22 NORMAL TO STREAM WISE PLOT OF V/V_{AVG} AT $\Lambda=0.4$ FOR $V_{\infty}=4\text{M/S}$ IN ZY PLANE	83
FIGURE 4-23 VELOCITY VECTOR FIELD AT TURBINE MID-PLANE FOR $\Lambda=0$	84
FIGURE 4-24 VELOCITY VECTOR FIELD AT TURBINE MID-PLANE FOR $\Lambda=0.4$	84
FIGURE 4-25 PLOT OF V/V_{AVG} AT ROTOR BLADE POSITION OF 0° FOR $\Lambda=0.4$ AND $V_{\infty}=4\text{M/S}$ AT MID-PLANE	85
FIGURE 4-26 PLOT OF V/V_{AVG} AT ROTOR BLADE POSITION OF 10° FOR $\Lambda=0.4$ AND $V_{\infty}=4\text{M/S}$ AT MID-PLANE	86
FIGURE 4-27 PLOT OF V/V_{AVG} AT ROTOR BLADE POSITION OF 20° FOR $\Lambda=0.4$ AND $V_{\infty}=4\text{M/S}$ AT MID-PLANE	86
FIGURE 4-28 V/V_{AVG} PLOTTED WITH Θ AT $R = 1\text{M}$ FOR $\Lambda = 0$ AND 0.4	88
FIGURE 4-29 V/V_{AVG} PLOTTED WITH Θ AT $R = 0.8\text{M}$ FOR $\Lambda = 0$ AND 0.4	88
FIGURE 4-30 V/V_{AVG} PLOTTED WITH Θ AT $R = 0.6\text{M}$ FOR $\Lambda = 0$ AND 0.4	88
FIGURE 4-31 V/V_{AVG} PLOTTED WITH Θ AT $R = 0.4\text{M}$ FOR $\Lambda = 0$ AND 0.4	89
FIGURE 4-32 V/V_{AVG} PLOTTED WITH Θ AT $R = 0.2\text{M}$ FOR $\Lambda = 0$ AND 0.4	89
FIGURE 5-1 MASS FLOW RATE (KG/S) PLOTTED WITH STATOR BLADE PASSAGE NUMBER AT $V_{\infty} = 4\text{M/S}$ FOR $\Lambda = 0 - 0.5$	95
FIGURE 5-2 MASS FLOW RATE (KG/S) PLOTTED WITH STATOR BLADE PASSAGE NUMBER AT $V_{\infty} = 6\text{M/S}$ FOR $\Lambda = 0 - 0.5$	96
FIGURE 5-3 MASS FLOW RATE (KG/S) PLOTTED WITH STATOR BLADE PASSAGE NUMBER AT $V_{\infty} = 8\text{M/S}$ FOR $\Lambda = 0 - 0.5$	97
FIGURE 5-4 MASS FLOW (KG/S) PLOTTED WITH ROTOR BLADE PASSAGE NUMBER AT $V_{\infty} = 4\text{M/S}$ FOR $\Lambda = 0 - 0.4$	98
FIGURE 5-5 MASS FLOW (KG/S) PLOTTED WITH ROTOR BLADE PASSAGE NUMBER AT $V_{\infty} = 6\text{M/S}$ FOR $\Lambda = 0 - 0.4$	99
FIGURE 5-6 MASS FLOW (KG/S) PLOTTED WITH ROTOR BLADE PASSAGE NUMBER AT $V_{\infty} = 8\text{M/S}$ FOR $\Lambda = 0 - 0.4$	99
FIGURE 5-7 NORMAL TO STREAM-WISE STATOR PASSAGE PRESSURE ASYMMETRY RATIO AT V_{∞} OF 4M/S	102
FIGURE 5-8 NORMAL TO STREAM-WISE STATOR PASSAGE VELOCITY ASYMMETRY RATIO AT V_{∞} OF 4M/S	103
FIGURE 5-9 VELOCITY ASYMMETRY RATIO VS. x/D AT $\Lambda=0.4$ FOR $V_{\infty}=4\text{M/S}$	105
FIGURE 6-1 WIND TURBINE TORQUE OUTPUT (C_T) FOR $\Lambda = 0.12, 0.18$ AND 0.25 AT V_{∞} OF 13M/S VERSUS TIME.	109

FIGURE 6-2 CLOSE-UP WIND TURBINE TORQUE OUTPUT (C_T) FOR $\lambda = 0.12, 0.18$ AND 0.25 AT V_∞ OF 13M/S VERSUS TIME.....	110
FIGURE 6-3 TIME AVERAGED WIND TURBINE TORQUE OUTPUT (C_T) AT $V_\infty = 11\text{M/S}$ OVER FULL RANGE OF λ	111
FIGURE 6-4 TIME AVERAGED WIND TURBINE POWER OUTPUT (C_P) AT $V_\infty=11\text{M/S}$ OVER FULL RANGE OF λ	113
FIGURE 6-5 WIND TURBINE TORQUE OUTPUT (C_T) PLOTTED WITH λ FOR EXPERIMENTAL AND CFD DATA	116
FIGURE 6-6 WIND TURBINE POWER OUTPUT (C_P) PLOTTED WITH λ FOR EXPERIMENTAL AND CFD DATA	116
FIGURE 6-7 T/T_{MAX} COMPUTED FOR $V_\infty = 4\text{M/S}$ AND $\lambda = 0$ FOR $\theta = 0,5,10,15,20$ AND 25°	118
FIGURE 6-8 T/T_{MAX} COMPUTED FOR $V_\infty = 4\text{M/S}$ AND $\lambda = 0.2$ FOR $\theta = 0,5,10,15,20$ AND 25°	119
FIGURE 6-9 T/T_{MAX} COMPUTED FOR $V_\infty = 4\text{M/S}$ AND $\lambda = 0.4$ FOR $\theta = 0,5,10,15,20$ AND 25°	119
FIGURE 6-10 ROTOR BLADE TORQUE OUTPUT PLOTTED OVER $\lambda = 0 - 0.5$ AT $V_\infty=4\text{M/S}$	120
FIGURE 6-11 WIND TURBINE ROTOR TORQUE OUTPUT (C_T) PLOTTED AGAINST ROTOR BLADE TIP SPEED RATIO (λ) AT $V_\infty=4\text{M/S}$ FOR ROTOR BLADE POSITIONS (θ) OF $0, 5, 10, 15, 20$ AND 25°	121
FIGURE 6-12 WIND TURBINE ROTOR TORQUE OUTPUT (C_T) PLOTTED AGAINST ROTOR BLADE TIP SPEED RATIO (λ) FOR $V_\infty = 4,$ $6, 8, 10$ AND 12M/S	122
FIGURE 6-13 WIND TURBINE ROTOR POWER OUTPUT (C_P) PLOTTED AGAINST ROTOR BLADE TIP SPEED RATIO (λ) FOR $V_\infty = 4 -$ 12M/S	124
FIGURE 6-14 PLAN ELEVATION (XY) OF BUILDING FOOTPRINT IN MM	127
FIGURE 6-15 SIDE ELEVATION (ZX) OF BUILDING IN MM	127
FIGURE 6-16 TOPOGRAPHY CFD MODEL DOMAIN SHOWING FLAT-ROOF BUILDING, WIND TURBINE AND GROUND.....	128
FIGURE 6-17 UPSTREAM ROTOR TORQUE OUTPUT (C_T) PLOTTED WITH λ FOR A RANGE OF H/D	130
FIGURE 6-18 UPSTREAM ROTOR TORQUE OUTPUT (C_T) PLOTTED WITH H/D FOR A RANGE OF λ	130
FIGURE 6-19 UPSTREAM VELOCITY FIELD IN ZX PLANE FOR H/D OF 1 AT $\lambda = 0.3$ AND $V_\infty = 4\text{M/S}$	131
FIGURE 6-20 DOWNSTREAM ROTOR TORQUE OUTPUT (C_T) PLOTTED WITH λ FOR A RANGE OF H/D	132
FIGURE 6-21 DOWNSTREAM ROTOR TORQUE OUTPUT (C_T) PLOTTED WITH H/D FOR A RANGE OF λ	133
FIGURE 6-22 DOWNSTREAM VELOCITY FIELD IN ZX PLANE FOR H/D OF 1.5 AT $\lambda = 0.3$ AND $V_\infty = 4\text{M/S}$	134
FIGURE 6-23 UPSTREAM ROTOR POWER OUTPUT (C_P) PLOTTED WITH λ FOR A RANGE OF H/D	135
FIGURE 6-24 UPSTREAM ROTOR POWER OUTPUT (C_P) PLOTTED WITH H/D FOR A RANGE OF λ	135
FIGURE 6-25 DOWNSTREAM ROTOR POWER OUTPUT (C_P) PLOTTED WITH λ FOR A RANGE OF Γ	136
FIGURE 6-26 DOWNSTREAM ROTOR POWER OUTPUT (C_P) PLOTTED WITH H/D FOR A RANGE OF λ	136
FIGURE 7-1 STATOR BLADE GEOMETRY CORRESPONDING TO $\phi/\phi_{\text{MAX}} = 0.25$	146
FIGURE 7-2 STATOR BLADE GEOMETRY CORRESPONDING TO $\phi/\phi_{\text{MAX}} = 0.5$	146
FIGURE 7-3 STATOR BLADE GEOMETRY CORRESPONDING.....	146
FIGURE 7-4 ROTOR BLADE GEOMETRY CORRESPONDING TO $\text{RBR/R} = 0.86$	147
FIGURE 7-5 ROTOR BLADE GEOMETRY CORRESPONDING TO $\text{RBR/R} = 1$	147
FIGURE 7-6 ROTOR BLADE GEOMETRY CORRESPONDING TO $\text{RBR/R} = 1.14$	147
FIGURE 7-7 WIND TURBINE TORQUE OUTPUT (C_T) PLOTTED WITH π_2 AT $\pi_4 = 0.86$ FOR RANGE OF π_3	148
FIGURE 7-8 WIND TURBINE TORQUE OUTPUT (C_T) PLOTTED WITH π_2 AT $\pi_4 = 1$ FOR RANGE OF π_3	149
FIGURE 7-9 WIND TURBINE TORQUE OUTPUT (C_T) PLOTTED WITH π_2 AT $\pi_4 = 1.14$ FOR RANGE OF π_3	150
FIGURE 7-10 WIND TURBINE TORQUE OUTPUT (C_P) PLOTTED WITH π_2 AT $\pi_4 = 0.86$ FOR RANGE OF π_3	151
FIGURE 7-11 WIND TURBINE TORQUE OUTPUT (C_P) PLOTTED WITH π_2 AT $\pi_4 = 1$ FOR RANGE OF π_3	152
FIGURE 7-12 WIND TURBINE TORQUE OUTPUT (C_T) PLOTTED WITH π_2 AT $\pi_4 = 1.14$ FOR RANGE OF π_3	152
FIGURE 7-13 WIND TURBINE TORQUE OUTPUT (C_T) PREDICTED AND CFD	154
FIGURE 7-14 WIND TURBINE TORQUE OUTPUT (C_T) PREDICTED % VARIATION RELATIVE TO CFD	155

FIGURE 7-15 WIND TURBINE HEALTHY GEOMETRY FEATURING 12 ROTOR BLADES.....	159
FIGURE 7-16 WIND TURBINE FAULTY GEOMETRY FEATURING 11 ROTOR BLADES	159
FIGURE 7-17 PREDICTED DYNAMIC TORQUE OUTPUT FOR HEALTHY AND FAULTY ROTOR CONDITIONS FOR $\lambda=0.34$ OVER ONE REVOLUTION.....	160
FIGURE 7-18 PREDICTED WIND TURBINE FFT TORQUE OUTPUT (0-100Hz) FOR HEALTHY AND FAULTY OPERATING CONDITIONS AT $\lambda=0.34$	161
FIGURE 7-19 CLOSE-UP PREDICTED WIND TURBINE FFT TORQUE OUTPUT (0-50Hz) FOR HEALTHY AND FAULTY OPERATING CONDITIONS AT $\lambda=0.34$	162
FIGURE 7-20 WIND TURBINE PREDICTED TIME-AVERAGED C_T PLOTTED WITH λ FOR HEALTHY AND FAULTY CONDITIONS AT $\lambda=0.34$	163
FIGURE 7-21 WIND TURBINE PREDICTED TIME-AVERAGED C_p PLOTTED WITH λ FOR HEALTHY AND FAULTY CONDITIONS AT $\lambda=0.34$	163
FIGURE 7-22 EXPERIMENTAL DYNAMIC TORQUE OUTPUT FOR HEALTHY AND FAULTY ROTOR CONDITIONS FOR $\lambda=0.34$ OVER ONE REVOLUTION.....	164
FIGURE 7-23 WIND TURBINE FFT TORQUE OUTPUT (0-100Hz) FOR HEALTHY AND FAULTY OPERATING CONDITIONS AT $\lambda=0.34$	166
FIGURE 7-24 WIND TURBINE FFT TORQUE OUTPUT (0-10Hz) FOR HEALTHY AND FAULTY OPERATING CONDITIONS AT $\lambda=0.34$	166
FIGURE 7-25 WIND TURBINE TIME-AVERAGED C_T PLOTTED WITH λ FOR HEALTHY AND FAULTY CONDITIONS	167
FIGURE 7-26 WIND TURBINE TIME-AVERAGED C_p PLOTTED WITH λ FOR HEALTHY AND FAULTY CONDITIONS	167

LIST OF TABLES

TABLE 1 WIND TURBINE BLADE DESIGN PARAMETERS.....	42
TABLE 2 WIND TUNNEL WORKING SECTION DESCRIPTION.....	48
TABLE 3 WIND TUNNEL AXIAL FAN SPECIFICATION	50
TABLE 4 COBRA PROBE SPECIFICATIONS	50
TABLE 5 WIND BLUE POWER GENERATOR SPECIFICATION.....	51
TABLE 6 TORQUE/SPEED TRANSDUCER SPECIFICATION	51
TABLE 7 SINOCERA DATA ACQUISITION SPECIFICATION	52
TABLE 8 THREE-DIMENSIONAL GRID INDEPENDENCE AS USED FOR MRF COMPUTATION	57
TABLE 9 TWO-DIMENSIONAL GRID INDEPENDENCE AS USED FOR SM COMPUTATION.....	58
TABLE 10 STATOR BLADE PASSAGE CENTRE PRESSURE VARIATION.....	75
TABLE 11 STATOR BLADE PASSAGE CENTRE VELOCITY VARIATION.....	87
TABLE 12 ROTOR MEAN TORQUE, RMS AND CREST FACTORS.....	110
TABLE 13 DEPENDENT AND INDEPENDENT WIND TURBINE VARIABLES	141
TABLE 14 RANGE OF PI TERM VALUES	144
TABLE 15 SIMULATION RUN ORDER AND PI CONFIGURATIONS	145
TABLE 16 WIND TURBINE TORQUE OUTPUT REGRESSION COEFFICIENTS	155
TABLE 17 DESIGN VARIABLE DESCRIPTIONS	156
TABLE 18 ROTOR TORQUE RMS FOR FAULTY AND HEALTHY OPERATING CONDITIONS.....	160
TABLE 19 CFD ROTOR DRIVING FREQUENCIES	160
TABLE 20 ROTOR TORQUE RMS FOR FAULTY AND HEALTHY OPERATING CONDITIONS.....	165
TABLE 21 EXPERIMENTAL ROTOR DRIVING FREQUENCIES.....	165

NOMENCLATURE

A	Wind turbine inlet area [m ²]
C _P	Wind turbine power coefficient
C _T	Wind turbine torque coefficient
d	Wind turbine X axis wind tunnel offset [m]
d ₁	Wind turbine Z axis wind tunnel offset [m]
D	Diameter of turbine [m]
h	Wind turbine roof installation height [m]
H	Height of wind turbine [m]
L	Length [m]
P	Wind turbine power output [W]
p _∞	Free-Stream Static Pressure [Pa]
p	Local Pressure [Pa]
r	Wind turbine radial position [m]
R	Rotor radius [m]
r ₁	Radius of outlet tip of rotor blade [m]
r ₂	Radius of inlet tip of rotor blade [m]
r ₃	Radius of inlet tip of fixed /guide blade [m]
r _{br}	Blade arc radius for rotor blade [m]
s _{br}	Blade arc radius for stator guide blades [m]
T	Torque [Nm]
T _{TOTAL}	Wind turbine rotor torque output [Nm]
v	Velocity of blade [m/s]
V	Velocity of jet [m/s]
V _{AVG}	Area-weighted average velocity [m/s]
V _F	Component of flow velocity at right angle to direction of motion of blade [m/s]
V _∞	Free-stream velocity [m/s]
V _R	Relative velocity of jet with respect to blade [m/s]
V _W	Component of absolute velocity in direction of motion of blade [m/s]
X _D	Domain stream-wise length [m]
Y _D	Domain normal to stream-wise length [m]

Y_{D1}	Domain turbine offset in Y axis [m]
Z_D	Domain height [m]
Z_{D1}	Domain height offset in Z axis [m]

Greek Symbols

ρ	Air Density [kg/m^3]
μ	Dynamic Air Viscosity [Pa.S]
α	Guide blade angle [$^\circ$]
β	Rotor blade tip angle between tangent to the blade and direction of whirl [$^\circ$]
θ	Wind turbine angular position [$^\circ$]
λ	Rotor blade tip speed ratio
ω	Rotor angular velocity [rad/s]
Ψ_N	Normal Asymmetry Ratio

CHAPTER 1

INTRODUCTION

Scope

This chapter provides a general review of the wind energy sector from a global perspective and describes how recent climatic developments have created further emphasis on renewable energy technologies. Within this review a number of key areas are described including installed generation capacity, wind energy directives and areas of future growth. Attention is given to the urban environment in which the scope for wind energy development is evaluated.

The second part of this chapter provides an overview of current wind power technologies and their associated benefits. From this review a number of key questions are raised which correspond to recent trends observed in the micro wind energy community and in particular the suitability of current technologies to operate effectively within this environment. The latter part of this chapter discusses the need for wind turbine diagnostics and how current state of the art techniques can be implemented onto wind turbine systems to determine specific fault conditions. From this review, limitations in current technologies are described with a view to proposing recommendations for future developments in this area.

From these reviews a general research problem has been formulated which is used to define the scope of this research. The specific research aims and objectives are provided in Chapter 2 as per areas highlighted in the literature review.

1.1 Wind Energy: A Global Perspective

The need for sustainable energy sources becomes greater each year due to the continued depletion of fossil fuels and the resulting energy crisis. For the past decade there has been a call for immediate and concrete solutions to the climatic challenges the world is currently facing with a view to providing long term energy security. Solutions to this problem are in the form of renewable energy technologies on both micro and macro scales. Globally over the past few years, considerable efforts have been made to develop renewable technologies for a diverse range of applications. The primary drives for this development are the depletion of fossil fuel reserves of which 98% of power generation sources are dependent on. Further pressure is provided from environmental councils which are concerned with the reduction of greenhouse gas emissions which are potentially responsible for the global warming phenomena [1]. It is evident that based on such drives there is a need for a clean sustainable energy resource which can provide long term energy and environmental security. An answer to this need is potentially in the form of wind turbines, which are being promoted heavily within the renewable energy sector. Wind power is the first renewable power generation technology (excluding large hydro projects) to become a genuine mainstream alternative for increasing the generation capacity across the globe. Over the past few decades installed generation capacity of wind energy sources has increased significantly due to directives proposed by renewable energy councils and global states.

Since the last major European wind energy review the sector has seen a rise of 22,000 MW in European installed generation capacity between 2004 and 2007. This rise has contributed to an increase in global annual growth rates with 60% of installed capacity now present in Europe. This has placed Europe firmly as a global leader in wind energy conversion as depicted in Figure 1-1 [2], [3]. Currently it is estimated that worldwide wind energy installed generation capacity is in the order of 94 GW, which is 2.1% of the overall power generation capacity [3–5]. With the wind energy sector growing rapidly each year it is predicted that by 2050 the global wind energy installed capacity will be in excess of 4000 GW producing approximately 10,000 TWh of electricity. This increased capacity has the potential to reduce as much as 5,000 million tonnes of global CO₂ emissions per year [6], [7] which makes a significant contribution to the conservation of the environment.

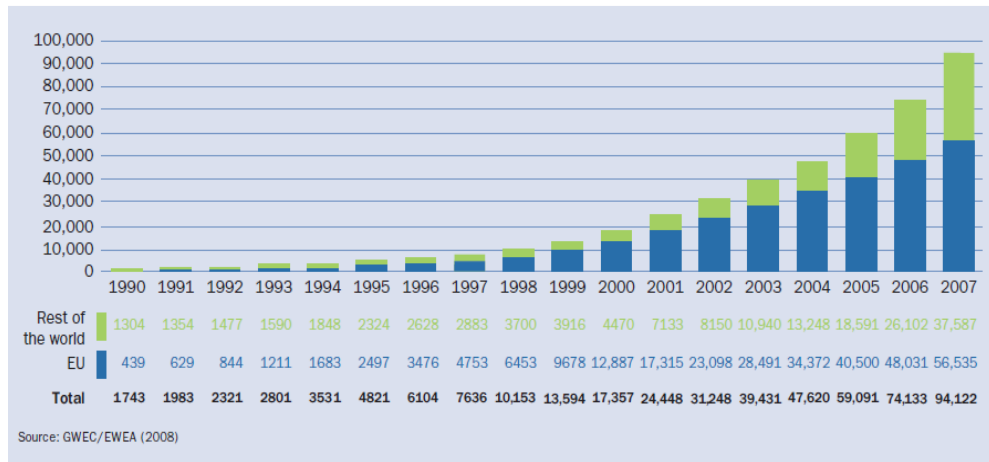


Figure 1-1 GWEC/EWEA Global Cumulative Installed Generation Capacity (MW), 1990-2007 [7]

In 2009 a motion was passed in the European Union (EU) in the form of the new 20:20 directive which focuses on addressing key energy concerns for the future. The aim is to have at least 20% (currently 8.5%) of all energy demands supplied from renewable sources by the year 2020. This directive has varying effects on each of the EU member states depending on their current level of installed capacity. The UK for example currently generates around 1.5% of its electricity demands from renewable sources. In the new directive the UK is required to increase its capacity by 15% before the year 2020 [8], [9] which is a very demanding target and requires the growth of many areas within the renewable energy sector. Wind energy is one of the main areas targeted for growth due to the relatively low installed capacity currently present. To increase this capacity the number of installed wind turbines must be increased and although future large scale projects are planned, many nearby residents have raised questions over the impact on the landscape of the UK which must be addressed [10–12]. The concerns associated to such projects have led to alternative wind power generation sites being investigated which are described in the following section.

1.2 Urban Wind Power

The urban landscape has been identified as a new area for wind energy development in the UK due to strict rural planning guidelines and limited areas to develop. Given the problems associated with large scale wind turbine projects and in particular gaining planning permission, many wind site developers have suggested the use of the urban environment for future wind turbine developments.

Additionally, the large costs involved with large scale projects and problems encountered during the planning stage have resulted in micro wind technology receiving increased support [13–15].

There is a growing body of opinion that policy should be developed to promote the widespread adoption of highly distributed, micro-scale wind turbines that can operate effectively in the urban environment. Micro wind turbines are generally defined as those that can be used within residential roof-spaces without the application for planning consent. This form of distributed generation is widely seen as a beneficial development in terms of both energy security and decarbonisation for urban energy supplies. At present the UK Government is seeking to promote micro generation technologies through the adoption of current building regulations and by setting a target for zero carbon new build housing by 2016 [16]. At present as part of the UK's Low Carbon Building Programme (LCBP), grants are available for home owners wishing to purchase and install micro-wind turbines for domestic applications [17]. A maximum of 30% of the total eligible costs is available which makes micro-wind energy a much more affordable technology for the domestic market. Previously the majority of micro wind turbines installed in this environment were used as promotional tools to increase the appeal of the technology further. Initial horizontal axis machines suffered from poor performance which was partly due to inefficiencies present in the machine along with poor installation locations on the building roof space. One of the primary concerns from the consumer is the low power generation within the urban environment due to inconsistent wind conditions and generally low speeds. This lack of confidence in micro wind energy is fuelled by recent machines marketed within the UK that are little understood and do not generate useable power resulting in some of the more recent attempts being withdrawn due to consumer complaints [18].

Although urban wind characteristics are well documented [13], [19–21], wind turbine performance when installed on typical urban rooftop geometry is little understood. This has resulted in mechanical system failures due to unexpected flow conditions experienced during operation and has been the major factor which resulted in the UK's leading micro wind energy supplier 'Proven Energy' entering into receivership [22]. Further, the current breed of turbines aimed at this market are often a scaled down version of a full scale machine with the assumption that similar performance characteristics will be present. In the case of micro-horizontal axis machines it has been observed at numerous sites that they struggle to operate in this highly turbulent environment [23]. Although this characteristic has considerable effect on horizontal axis performance, constant variations in wind direction result in further problems due to poor response times of passive yawing systems. The use of vertical axis machines to potentially exploit this wind resource is currently

being investigated. It is well established that this type of wind power technology has significant advantages over the horizontal format when operating under such conditions; these are described in the following.

1.3 Wind Power Technologies

At present a number of wind power technologies exist with some considerably more advanced than others. Such technologies fall into two main categories depending on their rotational axis relative to the ground. The first type of wind turbine is the Horizontal Axis Wind Turbine (HAWT) which during normal operation has its axis of rotation parallel to the ground. These wind turbines are now considered industry standard particularly for large wind farms located both on and off shore. An example of a typical horizontal axis machine is provided in Figure 1-2 where a domestic three-bladed rotor and nacelle are depicted:



Figure 1-2 Horizontal Axis Wind Turbine (HAWT) [24]

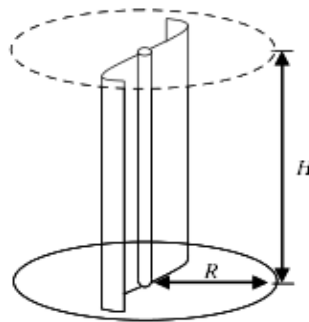


Figure 1-3 Savonius Vertical Axis Wind Turbine (VAWT) [25]

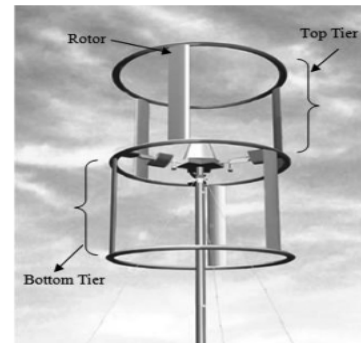


Figure 1-4 Darrieus Vertical Axis Wind Turbine (VAWT) [26]

Current HAWTs have encountered a number of problems since their birth such as their effectiveness to generate power in winds that constantly change direction [23]. On large scale projects many systems are fitted with yawing mechanisms such that the machine can be directed into the wind upon a change in direction. Although this control mechanism is well proven its response times during varied wind conditions are relatively high. Further, due to large component inertias a considerable amount of power is used in directing the rotor into the primary wind direction and hence results in further inefficiencies. Similar systems are employed in the micro

wind field in which small scale HAWTs are fitted with a basic yawing device which consists of a sail like paddle. Using the energy contained in the prevailing wind this paddle is yawed such that it sits in line with the dominant stream wise flow component resulting in the rotor being subjected to the full force of the wind. It is seen that the most recent generation of micro HAWTs have proven to be widely inefficient due to this system [18], [27]. Additionally, it is observed that when using this passive paddle system further problems are experienced during highly turbulent conditions which result in large power fluctuations giving rise to structural and electrical instabilities. Reducing this variation in power can therefore help prolong machine life and reduce the need for regular maintenance [28]. Such problems have led to the development of the Vertical Axis Wind Turbine (VAWT) as a potential successor to the horizontal axis turbine [23], [29].

A VAWT uses similar principals as a traditional horizontal axis turbine to extract energy from the wind using both a combination of aerodynamic lift and drag but has its axis of rotation normal to the ground. Vertical axis technologies have the advantage of being uni-directional in design and hence can accept and respond to changes in local wind direction [23], [30–32]. This has resulted in many micro VAWTs outperforming equivalent horizontal axis technologies in environments where wind direction is constantly changing. Further, vertical axis technologies have major differences in structural dynamics, control systems and maintenance which make these machines less complex and cheaper to install [29]. Although clear advantages of using this technology are documented they have not been investigated in sufficient detail and hence existing designs suffer from lower efficiencies when compared to more mainstream horizontal axis machines. Figure 1-3 provides an example of a typical Savonius type VAWT which utilises the principle of aerodynamic drag as its primary torque generating mechanism.

At this point it is important to observe two subtle differences between the Darrieus and Savonius vertical axis rotors. The Darrieus turbine as depicted in Figure 1-4 operates using some degree of aerodynamic drag but primarily relies on aerodynamic lift for torque generation [30], [31]. The opposite applies to the Savonius rotor in that its reaction type operation utilizes the principal of aerodynamic drag and the exchange of momentum from the air to the rotor surface [30], [32]. This report will focus on the Savonius rotor due to its suitability for low speed environments and the similarities with the wind turbine described in this thesis.

The basic configuration of the Savonius drag rotor has two semi circular blades with a central gap defined as overlap [32], [33]. Previous studies were mostly conducted on the optimization of design parameters such as blade number, blade shape and overlap distances. Experimental studies carried out by Sheldahl et al [34], Sivasegaram [35], Clayton [36] and Fujisawa et al [37] all report varying

power coefficients (C_p) for Savonius rotors ranging from 0.14 to 0.33 within a Tip Speed Ratio (λ) range of 0.8 to 1.0. Given the high solidity of this type of rotor significant torque output was observed during static and rotational modes of operation making start-ability consistent at low wind speeds. Due to this high solidity/low speed design the acoustic emission from this machine during normal operation is considerably less than the traditional HAWT described previously. With current UK planning legislation in mind this type of machine lends it's self to installation in the built urban environment where noise restrictions are of primary concern [38].

One problem that was present in some machines was the large variation in rotor torque output due to the fixed two blade design. Upon detailed investigations into the flow fields across the machine it was found that blade interaction effects were present on the non-torque generating blade. It was identified that unfavourable pressure gradients were the primary cause which resulted in a counter-rotating torque which significantly reduced the efficiency of the rotor. These blade interaction effects have become one of the major limitations of this type of turbine given torque generation is only provided by one bucket each rotor cycle. Such limitations provide strong justification for exploring alternative reaction type devices which maintain similar high levels of starting torque and provide a more consistent power delivery.

1.4 Wind Turbine Diagnostics

Renewable energy sources such as wind energy are available without any limitations. Harnessing this energy using wind power technologies allows for the potential extraction of millions of MW worldwide. In order to extract this energy effectively, the reliability of such technologies is critical if pay back periods and power generation requirements are to be met.

Wind power technologies have experienced rapid technological advancement over the past 20 years in aerodynamics, structural dynamics and power electronics. The integration of each of these technologies to enhance energy extraction is paramount in the success of wind turbine design and performance. It is reported that the annual power output from wind turbines can be increased by the establishment of more wind monitoring stations, improved maintenance procedures and condition monitoring [39]. The benefits of diagnostic systems that allow for characterisation of wind turbine health are documented in [40], [41] in which tools that allow for identification of component wear and failure can be used to minimize wind turbine downtime. Research has therefore been focussed on developing new Condition Monitoring Systems (CMS) and Fault Detection Systems (FDS) for

use on wind turbines to maintain system reliability. CMS with integrated fault detection algorithms allow for early warnings of mechanical and electrical defects to prevent major component failures along with reducing side effects on other components. The need for such a system is clear and has been shown by the 'Scientific Measurements and Evaluation Program' in which field tests showed that 25% of a total number of 5500 repair actions were caused by loose components, wear and failure. Providing this early detection of component fault can be achieved, repair actions can be planned thus eliminating the need for reactive type maintenance. Using this strategy, machine downtime can be minimized considerably which is seen to have huge cost implications particularly on off-shore applications [42].

CMS are now widely used for analysis of component condition and can be used for predictive fault detection and preventive maintenance. Such practices are documented in the recent EN 13306:2010 Maintenance Terminology standard which can be used to determine remaining useful life [43]. The nature of wind turbine faults is seen to vary considerably between different machines which are due to the differences in design and system complexity. When considering the fundamental components that make up a wind turbine system, namely rotor assembly, transmission and electronics it is clear that such components are common to any wind power technology. Hence regardless of the design and scale of the machine each is prone to component failures corresponding to the above sub-systems. Figure 1-5 depicts the percentage of failure number distribution on Swedish wind turbines as reported in [44]. It highlights the large failure rate of blades/pitch components which is in the order of 13.4% between 2000 and 2004. Further studies described in [45] are concerned with types of wind turbine failure along with overall severity from a cost perspective. In this study Kahrobaee et al report a total Cost Priority Number (CPN) of \$25.5k over the period of the study which highlights the significant costs of wind turbine faults and gives further justification for developing improved maintenance strategies.

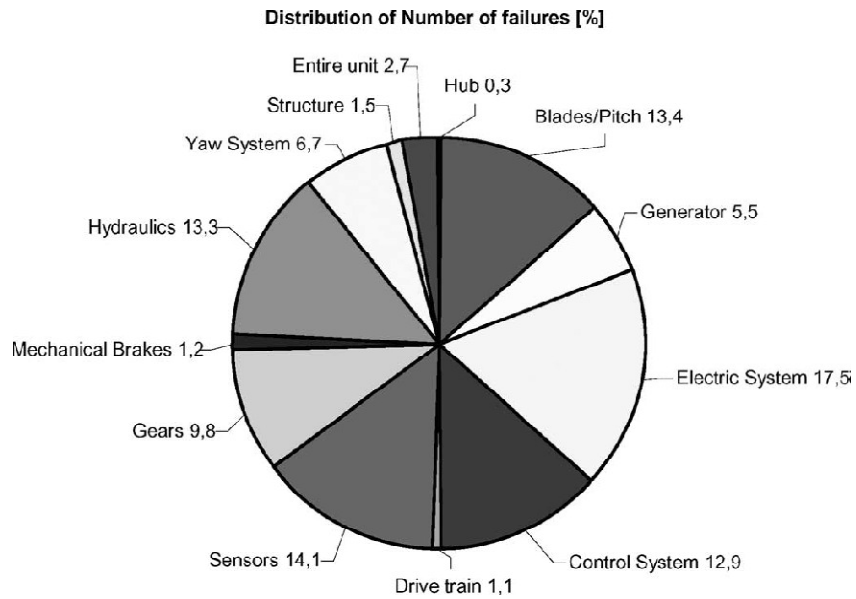


Figure 1-5 Failure number distribution [%] for Swedish wind power plants [44]

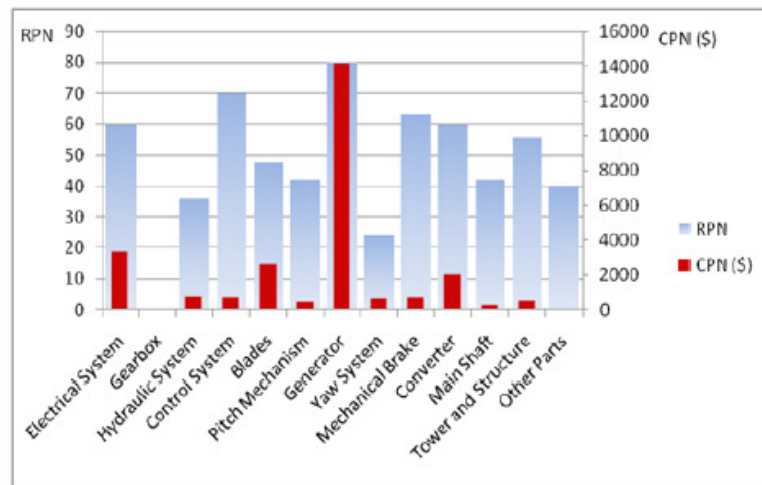


Figure 1-6 Failures and severity (RPN/CPN) from 3MW direct drive wind turbine [45]

It is however well accepted that at present particularly for large scale machines that drive-train problems are most common [46] given the lack of understanding of the flow conditions at the installation site and standard gearbox design practice not being sufficient for turbulent wind spectra. Such problems as documented from leading gear manufacturers have resulted in a requirement for more sophisticated condition monitoring systems that allow for prediction of specific types of failure. At present the use of simulation based condition monitoring is at an early stage and hence requires considerable development particularly when considering aerodynamic,

structural and mechanical aspects which are required for accurate prediction of wind turbine operational signatures. In addition and in relation to the machine described in this thesis, the use of multi-blade technology for micro scale cross-flow machines significantly increases the probability of rotor faults and hence any future developments in simulation based condition monitoring should have the ability to predict micro variations in wind turbine outputs. This general research problem is addressed in the following chapter where a detailed review of literature in this area is conducted and a more application based review is provided.

1.5 Motivation

Based on the global demand to reduce carbon emissions and generate clean forms of power it was found necessary to review existing wind power technologies and evaluate their effectiveness to operate within more diverse installation locations. It is clear that in order to meet targets set for renewable energy growth the current level of installed generation capacity should be increased and hence the use of the urban environment as a potential installation location is evaluated.

From the general review carried out in this chapter a number of key areas have been identified for further investigation in this thesis. These key areas are concerned with the design, operation and diagnostics of micro wind turbines and in particular new reaction type machines aimed at the urban environment [13–15], [19–21], [23], [38], [47]. Although this environment has potential, one of the major concerns is the low wind speeds, highly turbulent flow conditions and variations in flow direction. The development of any new micro technology must therefore address these issues in terms of design, operational behaviour and size envelope to facilitate roof structure integration.

Based on limitations in current technologies a requirement for a bespoke wind turbine designed specifically for this environment was identified. This requirement was initiated from the industrial collaborator Insight Renewables who provided a technical design brief and space envelope to work from. Based on this requirement a prototype machine has been designed using a model for one-dimensional flow across the turbine blades. The wind turbine takes influences from current reaction type wind turbines that feature multi stator and rotor blade arrays and is of vertical axis format. This therefore provides uni-directionality and hence is well suited to turbulent flow conditions and variations in flow direction. Further motivation for using this design stems from the reported increases in power output and the high torque characteristics when using stator guide vane blades

which make start-ability more reliable. Additionally, the use of multi blade rotors minimizes power output fluctuations which are particularly common in more conventional Savonius rotors.

In order to understand the operational characteristics of this new form of wind turbine a number of studies are required. One of the fundamental analyses to be carried out is concerned with the flow field generated across the machine at both design and off-design operating conditions. From such studies the flow regimes generated within both stationary and rotating frames of reference can be established and the primary torque generating mechanisms of the rotor identified. Detailed analysis focussed on transient related effects is also required in order to understand the dynamic wind turbine performance and in particular the effect of using multi-blade rotors on torque generation.

Further motivation stems from the need to understand cross-flow wind turbine performance in order to benchmark the design against existing technologies. At present there is a requirement for performance based analysis under both uniform flow conditions which are typically used during testing and also more representative conditions when installed on a rooftop. The effects of specific installation locations on performance requires considerable investigation such that more realistic pay-back periods can be calculated at a given wind site. From a general review of literature a considerable amount of research has been communicated on the wind characteristics in the urban environment. In many of these works authors make reference to wind power generation and comment on the suitability of different types of ground topography. One of the major limitations of such works along with primary reasons behind poor urban wind turbine performance is lack of knowledge on micro urban wind turbine performance. Hence this thesis aims to investigate the combined effects of urban wind patterns on the performance of a rooftop mounted turbine. Using a Computational Fluid Dynamic (CFD) model wind turbine performance will be studied when installed on the top of a typical flat roof commercial building in which the effect of installation position and height are considered.

A final problem identified from the general review is the requirement for wind turbine diagnostic tools that allow for fault detection and condition monitoring. Given that new wind technologies feature increased numbers of blades the probability of blade faults increases considerably. Hence, a study is required to understand the effects associated to blade loss on the resultant torque generating capabilities of the machine. This thesis investigates a novel area of research aimed at simulation based fault detection whereby machine signatures can be predicted and used for a range of applications.

1.6 Organization of Thesis

The basic outline of the thesis is described in the following:

Chapter One

Provides an overview of wind energy from a global and local perspective along with urban wind power considerations, current wind power technologies and wind turbine diagnostics. From this overview the motivation for carrying out this research is described which identifies key areas to be reviewed in Chapter Two.

Chapter Two

In this chapter a review of existing literature is provided which is concerned with vertical axis wind power technologies namely Darrieus, Savonius and Cross-Flow machines. Within each of these sections the major works are reviewed and in the case of the new cross-flow technology the major limitations described. Additionally, literature associated to wind turbine diagnostics is also presented where current state of the art techniques are discussed and scope for future developments evaluated. Details of the scope of research are provided in the form of specific research aims and objectives at the end of this chapter.

Chapter Three

This chapter documents the design procedure for a new cross-flow wind turbine aimed at overcoming technical challenges associated to installation in the urban environment. Details of a derived design methodology for stator and rotor blade profile computation are provided using a one-dimensional approach. Using computed blade geometry details of a full scale prototype are given including primary design features and specifications. Additionally, technical details of the experimental test setup used in this thesis are provided including the prototype machine, transmission, power generation and instrumentation. Further, the design of a Computational Fluid Dynamic (CFD) model is described including grid resolution, boundary conditions and numerical formulation. All experiments and numerical simulations presented in this thesis are conducted using these approaches unless otherwise stated.

Chapter Four

This chapter provides both qualitative and quantitative analyses of the flow fields generated across the wind turbine for both static and rotational operating modes. These flow fields are predicted

'Design, Operation and Diagnostics of a Vertical Axis Wind Turbine'
By Gareth Colley, Department of Engineering & Technology, University of Huddersfield, UK

using a three-dimensional CFD model and validated against full scale experimental data. From such analyses the flow field features associated to the energy transfer process at unique rotor operating states are described. The variation of primary flow parameters namely pressure and velocity are computed as a function of vertical, angular and radial wind turbine positions again at specific rotor operating conditions. From this study key operational characteristics of the cross-flow machine are highlighted which provides a basis for future work in this area.

Chapter Five

Chapter Five contains data associated with the mass flow distribution around the wind turbine as a function of both wind speed and tip speed ratio. Data is computed at specific zones corresponding to blade passage inlet and outlets to characterise the energy transfer process. Additionally, the flow field data obtained previously is used to compute a new performance related parameter named asymmetry ratio which provides unique wind turbine information associated to asymmetric energy transfer and stream wise capture. This ratio is then applied to determine downstream effects of multi-blade wind turbines and optimum location of a secondary machine.

Chapter Six

This chapter investigates the performance characteristics of the wind turbine using both experimental and numerical techniques at static and rotational operating conditions. The torque generation capabilities of the machine are examined at steady-state conditions along with calculation of the machines power coefficient. Using data obtained from CFD, the micro variations in rotor blade torque are correlated with the key energy transfer zones computed during flow field analysis. The effect of flow and rotor tip speed ratio on both the micro and macro performance data is presented in which rotor interaction effects associated to this fixed blade design are discussed. Finally, the effect of local topography on wind turbine performance is investigated numerically in which wind turbine installation location on rooftop structures is evaluated in terms of torque and power generation capability.

Chapter Seven

This chapter presents an optimization study aimed at investigating torque response at unique geometric and fluid flow conditions. Using a Buckingham Pi technique a number of non-dimensional parameters are defined and using a Design of Experiments (DOE) approach and evaluated in terms of resultant effect on wind turbine torque output. Using a multiple regression analysis the relationship between the non-dimensional parameters is determined such that unique coefficients are generated. Using these coefficients a functional relationship is defined in the form of a design equation that allows for torque prediction for a range of geometric and fluid conditions which is a novelty of this work.

The final section in this chapter documents a novel approach to wind turbine fault detection using a CFD prediction model. Data is obtained during both healthy and faulty states of rotor operation such that key machine signatures related to rotor blade loss can be identified. Similar analysis is carried out using experimental data such that numerically predicted data can be verified. Finally, the application of CFD to predict machine faults is evaluated and a scope for future work provided.

Chapter Eight

This chapter provides concluding remarks on the areas covered in this thesis. Within these conclusions, limitations of the work and recommendations for future work are provided such that the present research can be extended further in the future.

CHAPTER 2

LITERATURE REVIEW

Scope

The following chapter provides a detailed review of the available literature in the field of wind engineering with emphasis given to the vertical axis technologies namely Darrieus, Savonius and cross-flow. The main areas addressed in this chapter are associated to wind turbine design, operation and diagnostics which form the basis of this thesis. Within each of these areas specific limitations have been identified which have been used to define the scope of the research. From this scope the specific aims and objectives of this thesis are provided such that efforts are made to provide novel contributions in each of the areas investigated.

2.1 Introduction

In recent years the majority of wind turbine research has been focussed on the development of existing technologies using both experimental and numerical techniques. From the late 1970's a considerable amount of research has been communicated which documents the design and development of the Vertical Axis Wind Turbine (VAWT). From a general review of literature it is noticed that each technology produces a wide range of operating characteristics depending on both the geometric configuration and fluid flow condition. This chapter aims to provide a clear and concise review of the major works conducted in this area with reference made to Darrieus, Savonius and cross-flow wind turbines. Additionally, the need for simulation based diagnostics as described in Chapter 1 is also considered in which a review of relevant literature in this area is documented. Throughout this chapter emphasis will be given to reaction type wind turbines given the similarities to the machine presented in this thesis.

2.2 Darrieus Wind Turbines

For consistency a brief review of works related to the Darrieus rotor and its performance characteristics are provided in the following. Initial works conducted by Sandia National Laboratories from the late 1970's provided baseline performance data for the Darrieus rotor along with additional data related to optimized rotor configurations. Darrieus rotor performance was initially reported by Blackwell et al [48] in which wind tunnel investigations of a NACA 0012 bladed machine were conducted. Here the effects of rotor solidity and free-stream velocity on the resultant torque and power outputs of the rotor were studied. Figure 2-1 depicts the rotor C_p curves as a function of rotor solidity at a fixed free-stream velocity. From this figure a C_p of 0.3 – 0.325 is observed depending on the solidity ratio studied. One of the most important aspects noticed from this figure is the range of λ the Darrieus machine operates in. At this particular free-stream velocity the range of λ is seen to be 1 to 7.5 which is significantly higher than that observed for the Savonius machines (as described later).

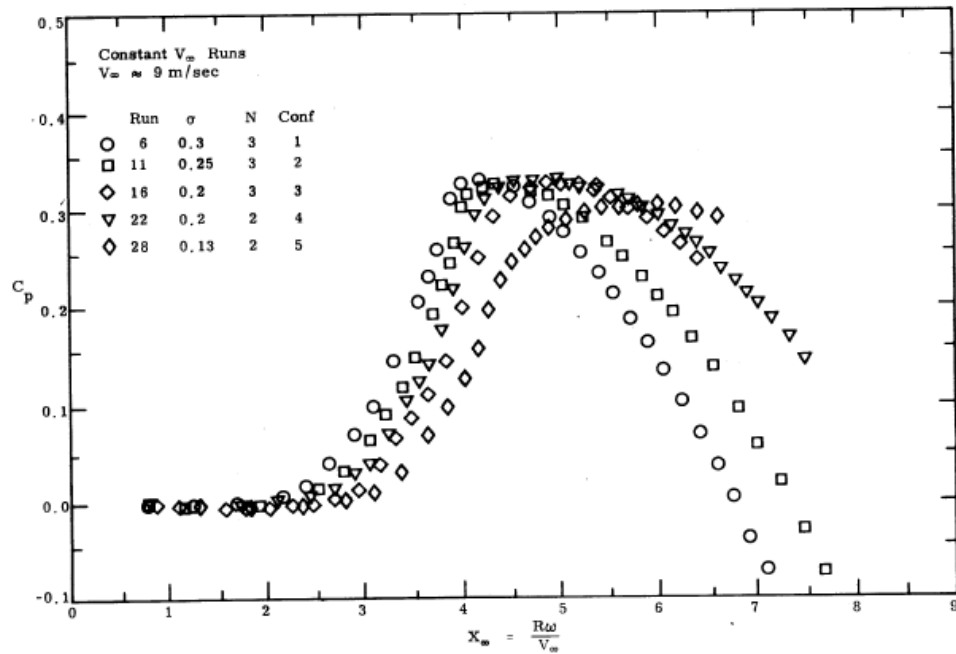


Figure 2-1 Darrieus C_p curves using NACA 0012 blades as reported by Blackwell et al [48]

Additional studies into Darrieus wind turbine performance are reported by Sheldahl et al [49] again from Sandia National Laboratories. Here, a 5m diameter Darrieus rotor is studied under free-air conditions in which reported C_p curves are lower than anticipated. In this study the wind turbine is operated at a fixed rotational speed using an induction motor/generator on the output shaft of the machine. From wind tunnel tests the maximum C_p obtained was 0.273 which was lower than numerically predicted output. Authors conclude that this reduction in expected performance is due to the straight bladed sections towards the central hub which results in aerodynamic inefficiencies. Later studies conducted by Worstell [50] on a 17m diameter three bladed machine reported C_p values range from 0.33 - 0.36 depending on local wind conditions. The high speed nature of the Darrieus rotor is again exhibited in which a λ range of 2.5 - 9 is observed. Here authors report that both two and three blade configurations show similar peak C_p . It is however noted that varying Darrieus blade number results in modification to the C_p curve in which peak power shift towards lower values of λ for the three bladed rotor.

Although the Darrieus machine has shown to provide significant levels of power, one problem that is present throughout is its poor start ability characteristics in low wind speeds. Such behaviour has resulted in a need for cranking motors and self-start devices attached to the main transmission shaft to accelerate the rotor up to synchronous speed. This characteristic is particularly unfavourable in

urban landscapes where wind speeds are typically much lower [17], [38]. Due to this characteristic, studies have been conducted where the Darrieus rotor is used in combination with the S-rotor such that both high starting torque and high efficiency are obtained. In [51] Galvalda et al reports significant performance gains when using both rotors for combined operation. Here a power coefficient of 0.35 is reported at an overlap ratio of 1/6. Similar studies aimed at power augmentation are presented in [52] where Gupta et al reports a C_p of 0.51 for combined rotor with no overlap. Although the use of combined rotors has proven to be successful in a small number of cases, increased cost and height are deemed to be a significant drawback.

2.3 Savonius Wind Turbines

Savonius wind turbines use the principal of aerodynamic drag and the exchange of momentum from the air to the surface of the blade as the primary torque generating mechanism [32]. Studies have been carried out since the late 1970's to understand the nature of its performance with a view to improving power generation capabilities. The major works documented around this time were communicated by Blackwell [53], Sheldahl [34], Clayton [36], Sivasegaram [35] and Modi [33] in which a range of studies were conducted into Savonius performance.

In 1977 Blackwell et al [53] conducted a thorough investigation into Savonius wind turbine performance which at the time was being investigated alongside the Darrieus rotor. Blackwell studied a total of fifteen rotor configurations using a low speed wind tunnel in which major wind turbine design parameters such as number of buckets, height, diameter and rotor overlap were varied. To ensure performance was investigated at a number of design points the effect of varying free-stream velocity was also considered. Here authors report large variations in rotor torque output particularly for a two bladed rotor when compared to the three bladed designs. Further, starting torque of the machine is increased when using three-blades compared to two although reductions in dynamic performance are reported for the three-blade rotor. The following figure depicts this variation in rotor torque output for a two-bladed rotor. The torque curve obtained from the dynamic rotor highlights the significant variation in torque as a function of relative blade position. Additionally it also highlights the primary inefficiency with this type of machine which is the counter-rotating torque generated between $\theta = 25^\circ$ and 60° . This 'dead-band' is a result of blade interaction effects with the blade travelling upwind. Results obtained from this study show good agreement with additional works reported by Sheldahl [34] and Sivasegaram [35] and from combined data a range of power coefficients (C_p) for this machine were obtained. This range was

'Design, Operation and Diagnostics of a Vertical Axis Wind Turbine'
By Gareth Colley, Department of Engineering & Technology, University of Huddersfield, UK

within a specific operating band relative to the rotor tip speed ratio (λ) in which maximum C_p was generated between 0.7 and 1. From the above works a range of C_p values of 0.15 – 0.25 were communicated.

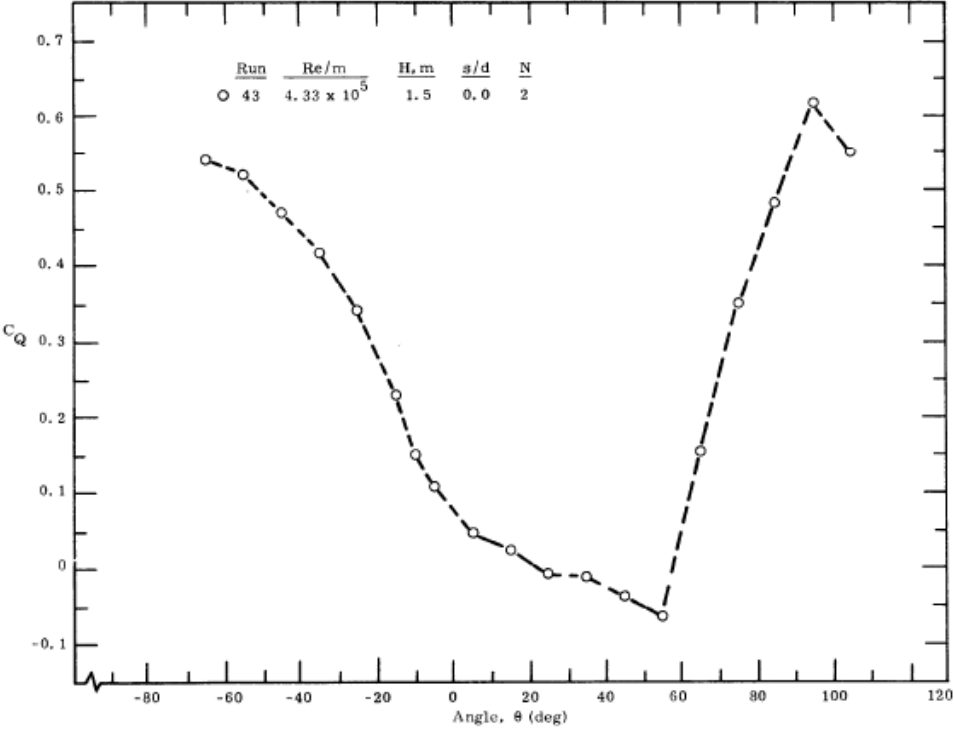


Figure 2-2 Savonius rotor torque output (C_Q) plotted with angular blade position (θ) for two bladed rotor with $h/D = 1.5$ and $s/d = 0$ as reported by Blackwell et al [53]

V.J Modi et al [33] carried out investigations into Savonius rotor performance characteristics using a semi-empirical approach in which baseline performance characteristics were obtained for both static and rotational rotor conditions. The effect of blade geometry, wind tunnel blockages and frictional losses are all evaluated with a view to monitoring performance output. It is reported that baseline Savonius power coefficients lie reliably within a range of 0.12 - 0.15 which is considerably lower than those observed in [53]. From the optimization studies conducted in this work Modi has inferred that the rotor generates a peak power coefficient of around 0.32 at a λ of 0.79 with a possible error of +/- 10%. Such an increase over standard Savonius rotors is due to the optimization of blade gap size, blade overlap, blade arc angle and aspect ratio which have all been configured to maximise power output. In [54], experimental investigations were carried out to determine the optimum overlap configuration for a Savonius rotor for maximum power generation.

Here a three bucket design at 20% overlap generated a power coefficient of 0.37 which is considerably higher than others reported in literature.

One of the major advances in wind turbine aerodynamic analysis was the ability to evaluate the flow field characteristics within the machine. In the late 1980's Fujisawa et al 1987 [55] conducted a series of experiments using hot wire anemometers to obtain flow field data across a Savonius rotor. Using such data the authors hoped to determine a relation between the experimental flow field pattern and the torque generating mechanism of the S-rotor [32]. In this study a square outlet wind tunnel measuring 0.9m x 0.9m and a blower type fan was used to provide the mass of air. The turbine was fixed downstream of the wind tunnel exit plane at a distance of 0.7m and tested under uniform flow conditions. Here the authors study the flow field for both static and rotational dynamic rotor conditions to determine the variations in flow through the machine. In the static test the angle of the rotor blade relative to the stream-wise flow direction is varied from $\theta=0^\circ$ – $\theta=135^\circ$ in steps of 45° to understand the effect of blade position on flow. The characteristics of the machine vary considerably depending on this angle of attack and result in significant changes to both the upstream and downstream flow field. Furthermore, it is reported that due to changes in pressure stagnation around the machine a counter rotating torque may act against the direction of rotation.

Further advances in flow field measurement techniques allowed Massons et al [56] to study the Savonius flow field using a paper image processing technique in a towing water tank. The flow field distribution around the machine in terms of velocity vectors highlights the nature of the flow for a given angle. Over a small time change this transient flow gives rise to the formation of two small vortices downstream of the rotor showing a closed wake characteristic. Although this work provided an interesting insight into the flow behaviour, the primary performance related flow data that corresponds to peak performance condition was little understood.

Later studies carried out by Fujisawa et al [57] investigate the torque mechanism of the Savonius rotor by means of measuring the pressure distributions on the blades using flow visualization techniques. In this study special attention has been given to the effect of overlap ratio on the mechanism of torque and power production which has been identified as a critical performance related parameter. The flow fields generated over the static rotor are shown to give rise to a counter rotating torque which supports previous work communicated. The torque data obtained here used the pressure field data from both the convex and concave side of the rotor blade and allowed local torque variation to be computed as a function blade angle relative to the flow. Further analysis in terms of the flow patterns generated over the machine show that for a static rotor the torque

performance can be improved by the presence of blade overlap due to the increased pressure on the concave blade side.

More recent studies into Savonius wind turbine performance are aimed at improving the performance output using flow conditioning devices. One of the initial works carried out in this area was by Sivasegaram [58] in which a two vane power augmentation system was installed on a typical Savonius rotor. Authors report considerable gains in power output (up to 80%) although practical operation of the machine is not well defined. Additional studies carried out by Altan et al [59] investigate similar measures to increase the power generation capabilities of a Savonius rotor. Here the authors install a curtain arrangement upstream of the rotor with a view to directing the main flow at a single blade thus removing downstream blade interaction effects. Authors report increases in power output of 38% which is a considerable improvement from the standard rotor. As the curtain arrangement is placed at a fixed location the machines uni-directionality will be lost and hence one of the major benefits of this technology removed.

2.4 Cross-Flow Wind Turbines

The major references used throughout this thesis are contained in the following section and are associated to cross-flow wind turbine design and operation. Cross-flow wind turbines are a new breed of vertical axis machines which are currently being developed generally with high solidity ratios as a result of a multi-blade design. Additionally, flow conditioning devices to modify the incoming free-stream flow are also being used in parallel with the multi-blade rotor due to the increases in performance as reported previously. The current opinion is that by utilising both high torque output which is a result of the multi-blade configuration along with the use of stator guide vanes the inefficiencies present in existing reaction machines can be minimised and power generation capability enhanced.

Klemm et al [60] present a cross flow fan and evaluate its effectiveness to be used as a wind turbine. This particular machine features a 36 blade arrangement of 0.3m in height and 0.098m in outer blade diameter.

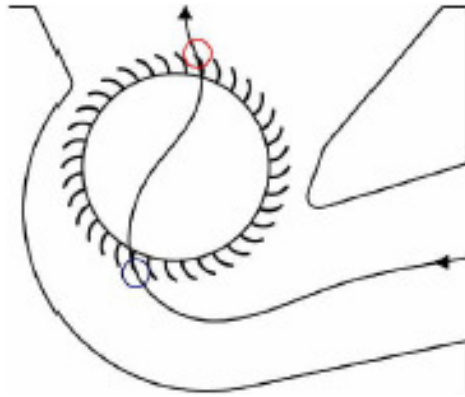


Figure 2-3 Cross-flow turbine geometry reported by Klemm et al [60]

The authors conduct a series of tests using both experimental and numerical techniques in the form of Particle Image Velocimetry (PIV) and Computational Fluid Dynamics (CFD). This machine takes influences from previous literature [58], [59] in which a flow conditioning device is used on one side of the machine. It is noted that this particular device has significant limitations when considering practical operation given that the uni-directionality of the machine is lost. Authors report a large variation in volumetric flow rate between experimental and numerical tests although contours of absolute velocity computed over the machine show some similarities in the rotating frame of reference. One of the major observations are the un-favourable flow distributions in the left of centre within the rotor assembly where a large vortex is generated resulting in a reduction in energy transfer to the blade channels. To improve volumetric flow rate into the rotor an optimization scheme is undertaken by modifying the outer casing profile and analysing the resultant effects on the velocity field inside the machine. Although the authors report gains in performance this is not well quantified with the majority of analysis conducted qualitatively. Additional limitations of this work are the lack of performance related data given its application as a wind turbine with no reference given to expected torque or power generation.

In [61] and [62] authors present work on a new type of cross flow turbine labelled jet-wheel-turbo wind turbine. This type of machine features a multi-blade design along with both upstream and side guide vanes/collectors. Initial observations of the design show similar limitations to that reported by Klemm et al in which the collectors would limit the machines ability to accept wind from any direction which in reality is common place. Additionally, the orientation that the wind turbine is depicted has the axis of rotation horizontal to the ground yet the machine is defined as being vertical axis. This incurs a further problem in that the machine would have no means to pivot if

mounted in this orientation and hence significant losses in output would be seen. The authors conduct a series of experiments using a low speed wind tunnel and prototype model turbine with diameter of 500mm and height of 220mm.

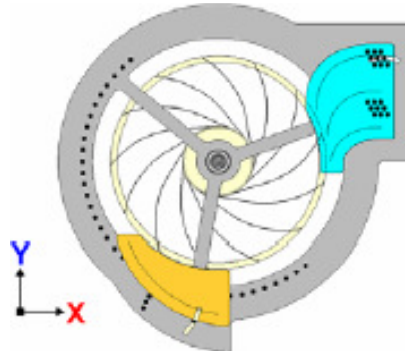


Figure 2-4 Jet-Wheel-Turbo Wind Turbine as proposed by Lee and Park et al [61], [62]

The performance data presented the machine is seen to operate within a range of λ between 0 – 1.1 which is to be expected given its high solidity. This also shows agreement with operating ranges observed for the Savonius machine as previously described. The number of blades was set to 13 and blade inlet angle of 40° given by numerical simulation although no details of this design approach are provided. Authors report maximum power coefficients of 0.593 at $\lambda = 0.666$ using both the upstream and side guide vanes. This value corresponds exactly to the Betz limit of $16/27$ or 0.593 and is obtained at 7m/s. It is however noticed that when evaluating power output at lower wind speeds (3m/s) maximum C_p is in the order of 0.425. Depending on the application of this machine and in particular its use in the urban environment a 7m/s free-stream velocity may not be common [38], [63]. In this study no test setup information is provided and hence it is unknown as to how power data has been obtained. Additionally, authors do not comment on what power data is presented in terms of peak dynamic and time-averaged results.

In 2009 Shigemitsu and Fukotomi et al [64] investigated performance improvements on a cross-flow wind turbine featuring a symmetrical casing. Here both experimental and numerical investigations have been undertaken using a 150mm diameter turbine with a total of 24 blades equally spaced about the central axis. For experimental analysis a 500mm x 500mm cross sectional wind tunnel is used with a free-stream flow speed measured at the exit plane of 20m/s. The use of this wind speed is justified as to minimize the measurement error on the performance of the turbine however this is not described.

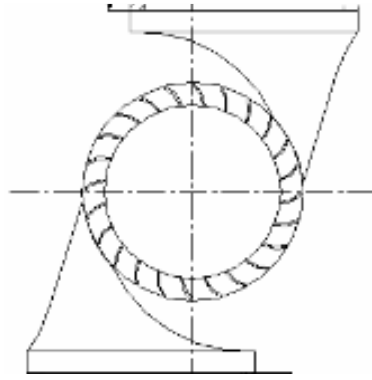


Figure 2-5 Cross-flow wind turbine using symmetrical casing as proposed by Shigemitsu & Fukotomi et al [64]

Here authors present both performance data gained from experiments and streamlines predicted using CFD code *Fluent 6.1*®. It is noticed from experiments that the operating range of this machine lies between a $\lambda = 0$ and 1 which shows agreement with machines presented by Lee et al. Further, rotor torque output is seen to be maximum when λ tends to be zero, above which it reduces showing some linear characteristics. Streamlines are computed using CFD and presented at rotational rotor conditions which correspond to the peak power condition. This qualitative analysis has not been verified or validated against experimental data and hence the accuracy of the predicted flow fields is not clear. Further limitations of the flow field analysis are associated to the transient related effects which have been neglected. Here authors report streamlines for three casing inclination angles at a fixed rotor blade position. Hence true micro dynamic related behaviour is unknown and the relation with the global experimental performance data is not described. Authors do however report experimental fully transient C_p of 0.1 using a bare rotor. With the addition of casing geometry this has been increased to a maximum of 0.17 which further highlights the effectiveness of flow conditioning devices [59], [65]. Although considerable increases in performance are noted this machines application as a wind turbine is limited given lack of unidirectionality in the stator design and hence would have difficulties operating in winds that vary in direction.

In [66] Takao et al present studies on a straight bladed VAWT with directed guide vane. This machine has a similar configuration to that described in [61], [62] where an outer collector is used to direct the air flow into the rotor assembly. This study investigates its effectiveness when used on a Darrieus type rotor using three NACA 4518 straight blades. Authors report C_p values of 0.2 which is considerably lower than the gains reported by Park and Lee et al [61], [62].

Recent investigations into cross-flow technology are provided by Pope et al [67], [68] in which a *Zephyr*[®] type wind turbine is studied. This wind turbine features a 5 bladed rotor which is surrounded by 9 stator guide vanes which allow for true uni-directional operation.

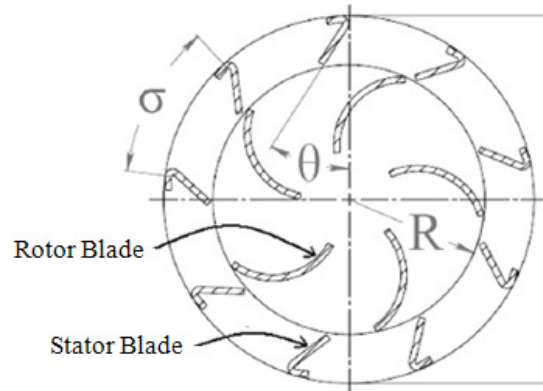


Figure 2-6 *Zephyr*[®] Wind Turbine as reported by Pope et al [67], [68]

Here both experimental and numerical studies are conducted to evaluate wind turbine performance. Dynamic operating range corresponds to $\lambda = 0 - 0.7$ which is slightly lower than machines described previously. This characteristic is likely to be a result of the increased stator guide vane solidity ratio which will introduce losses due to reductions in the velocity head before the flow enters the rotor assembly. The numerical models described in this work are twofold; Firstly a three-dimensional Multi-Reference Frame (MRF) and secondly a two-dimensional Sliding Mesh (SM). In the three-dimensional work a scaled down version of the wind turbine geometry is presented which appears to be un-validated against experimental data. Authors conduct a comparative study using this method in which a single equation turbulence model has been employed. Justification of the use of the model and verification of the CFD results is not clear. Further limitations of this work include the steady state analysis performed using the three-dimensional model. Here a singular blade position is taken and used to compute power output for a range of conditions. The usefulness of this data is not well defined and given practical operation of the machine is likely to be considerably different from the true dynamic power curves. The C_p values obtained at this blade position are in the order of 0.095 for the machine with stator tabs and 0.12 without tabs. Such performance data is considerably lower than that reported by Park and Lee et al [61], [62] for similar machines. However no references are made to the dynamic performance and hence transient and three-dimensional effects have not been considered.

2.5 Wind Turbine Diagnostics

Due to recent developments in the field of wind energy and in particular the expansion of installed capacity around the world, the need for reliable and intelligent diagnostic tools is of greater importance. As the rated capacity of wind turbines increases so does the overall system cost along with the need to have online diagnostic capabilities. The following section describes briefly some of the tools available not only in the field of wind engineering but also from the field of rotating machinery given the similarities between the two. It assumes the reader is familiar with traditional well established measurements techniques such as vibration, acoustic and current signal analysis and focuses on application issues and scope for future development in this field.

Condition monitoring and fault detection techniques have been used to predict and determine machine faults in a diverse range of industries and are particularly common for rotating machinery. Hameed et al [40], [41] provides a general review of existing techniques used to determine wind turbine system and component faults. The authors discuss the limitations of such technologies and make general remarks regarding future advancements in this area. The major techniques described are associated to vibration, acoustic, current signal analysis and oil spectrum analysis which have been widely used in industry for the last 60 years. It is shown that by carrying out spectral analysis on vibration, acoustic and current signals [69–74], [75] the nature of machine faults can be characterized and used for predictive maintenance strategies and on-line fault detection

One of the most common techniques used in this industry is the study of noise and vibration in which from operational machine signatures and the driving frequencies of the drive-train specific faults can be determined [76]. Due to complexities in rotating machinery drive-trains namely large number of components and hence potential fault locations vibration analysis can be an extremely expensive method of diagnostics. Assuming instrumentation is located at critical positions within the drive-train another issue is the large amount of data generated and the need for high speed data acquisition. The use of motor current signal analysis has also been used extensively to determine the nature of faults in induction generators[70], [73]. Although this technique has been used successfully to determine specific faults inherent to the generator/motor its application on wind turbine systems to determine both upstream and downstream drive-train faults has not been explored.

Recent advancements in computational modelling namely CFD have allowed for complex simulation of fluid flow systems and in particular wind turbines [60–62], [64], [66–68]. Although the use of CFD is relatively new its applications are developing with recent advancements made in the area of diagnostics and control [77–79]. Given improvements in computational hardware its use as a simulation based condition monitoring tool is becoming more realistic. This therefore has the potential to reduce diagnostic costs from minimizing the amount of instrumentation required when obtaining machine signatures.

One of the major areas in the field of wind engineering relates to the control system used to regulate power delivery to the grid. Its primary function is to regulate wind turbine rotor speed depending on local flow conditions close to the rotor. This is achieved through varying the pitch of the blades, yaw of the nacelle structure and regulating the load at the gearbox. Through varying these elements of the system rotor synchronous speed can be maintained to allow for optimum power generation. Over the past few years more emphasis has been put on wind turbine control systems to improve the efficiency of power generation and also provide safety measures during high wind speeds. At present the use of such control systems on small scale machines is being explored particularly for peak power tracking. In [80] the authors simulate wind turbine characteristics in order to develop a control system to respond to changes in power reference, load disturbance and power effect. This emulation of wind turbine signatures is becoming more popular particularly during the development stages of control system design as described in [81]. The purpose of this emulation is to accurately generate torque and speed signatures from the turbine shaft for a range of load conditions such that power responses of the machine can be computed and power tracking capability developed. The use of CFD to emulate real-time wind turbine performance data is a potential application which will be explored in this thesis.

2.6 Scope of Research

At present cross-flow Vertical Axis Wind Turbines (VAWTs) are in the initial stages of development. The key design and operational characteristics of these machines is not well understood and hence primary areas have been identified from the literature review for investigation. These areas are used to define the general scope of this research along with specific aims and objectives which are described in the following section. In general the scope of this thesis is concerned with the design, operation and diagnostics of a cross-flow VAWT which is

investigated alongside industrial collaborator Insight Renewables. The first major area considered relates to the design and manufacture of a prototype machine aimed at urban applications in which wind speeds are relatively low ($<10\text{m/s}$) and rotor self start-up is a primary concern. The scope of the design phase of the project involves computation of blade profiles to suit the required application and provide a preliminary prototype design which can be used for development testing. The structural design work is carried out using a sub-contractor who is responsible for fabrication and assembly of the machine. In this design phase blade geometry is calculated for both the wind turbine rotor and for a set of guide vanes which are used to increase the energy capture of the machine. Matched blade profiles are computed using a set of derived ideal design equations which can be used to generate both stator and rotor blade profiles. Using this methodology wind turbine geometry is computed for an urban low wind speed application. The scope of the design stage is extended to allow for the development and manufacture of a test installation such that the wind turbine can be studied in a controlled environment which supports the experimental studies documented in this thesis.

The second main area of this research is aimed at the investigation and evaluation of the wind turbines operation at micro and macro levels. Micro level analysis is concerned with the flow field characteristics across the machine at both steady state and transient modes of operation. The wind turbine operational behaviour is characterized at both 'design' and 'off-design' conditions such that the conceptual design is examined over a diverse range of expected operational conditions. In general this investigation considers the development of both pressure and velocity fields within the stationary and rotating frames of reference namely stator and rotor blade passages. Further, the unique distribution of flow around the machine is evaluated and where possible its relation with torque generating mechanisms within the rotor described.

Macro level analysis is aimed at understanding the machines performance characteristics by the quantification of both the torque and power outputs of the rotor. These performance signatures are evaluated again for both steady and transient conditions along with stationary and rotational modes of operation. From reviewed literature the torque generation capabilities of the cross-flow wind turbine are not well documented particularly when considering individual blade contributions as a function of angular position. Understanding such characteristics is critical if the unique behaviour of this format is to be determined and design inefficiencies are to be highlighted. The performance study is extended to consider effects related to topography which at present have not been determined. Here the effect of rooftop installation of this micro cross-flow VAWT on torque and power outputs is evaluated for a range of installation heights and at multiple rooftop positions. This

novel analysis gives an insight into the effectiveness of such wind power technologies to operate in an urban location which is of primary concern to the consumer. This particular area of research is at present largely unknown and has resulted in major machine failures as described previously.

The third facet of this research is the determination of the parametric inter-relation of variables related to fluid, flow and geometry and their associated effects on torque output. In the present study a dimensional analysis is conducted that identifies critical performance related variables such that a set of non-dimensional parameters can be established. Over a range of operating conditions the effect varying these parameters on performance is investigated and a regression model developed to determine the functional relationship of each. From this analysis performance can be predicted for a unique geometric, fluid and flow condition which can be used during conceptual design stages for cross-flow wind turbines. At present the effects of varying these parameters on performance are widely unknown and hence is a novelty of this particular work.

The final area investigated in this thesis is focussed on the development of a CFD based fault detection model which can be used to predict specific rotor faults. Although wind turbine condition monitoring is well documented in the form of vibration and acoustic techniques much of this research is focussed on non-rotor faults. Given the recent emphasis on multi-blade rotor designs the probability of failure is significantly increased. The present work investigates the use of CFD to determine the nature of rotor blade faults during transient operation of the machine. Using full scale experiments the accuracy of the CFD model to predict fault characteristics is evaluated.

2.7 Specific Research Aims and Objectives

The major aim of this thesis is to evaluate the performance characteristics of a novel cross-flow wind turbine which utilizes an outer stator guide vane to enhance energy capture. The individual project objectives are defined as follows:

Objective 1: Design & manufacture of a small scale cross-flow multi blade VAWT

- Derivation of design methodology for computation of rotor and stator blade profiles at flow condition similar to that experienced in the urban environment.
- Manufacture of full-scale prototype machine for development testing and benchmarking.

Objective 2: Evaluation of wind turbine flow field characteristics

- Analysis of wind turbine flow fields at 'design' and 'off design' conditions to highlight effect of multi blade geometry.
- Evaluation of wind turbine flow field variation during transition from static to rotational modes of operation.
- Transient analysis of flow field development at a range of rotor blade positions.
- Investigation into wind turbine mass flow distribution and associated effects related to non-uniform torque generation.
- Investigation into flow field asymmetry and energy capture of the wind turbine.

Objective 3: Analysis of wind turbine torque and power generation capabilities

- Analysis of torque and power spectra in the time domain using full scale wind turbine.
- Numerical prediction of torque and power characteristics as a function of blade position, tip speed ratio and wind speed.
- Evaluation of topographical effects on wind turbine performance output when installed on flat roof geometry for a range of installation positions.

Objective 4: Parametric optimization of wind turbine performance

- Derivation of critical performance related machine parameters.
- Computation of torque and power responses at each parametric configuration using a Design of Experiments (DOE) strategy.

- Analysis of factorial responses and development of functional relationship to allow for prediction of torque for range of fluid, flow and geometric conditions.

Objective 5: Development of CFD based fault prediction model

- Development of CFD based fault prediction model capable of predicting dynamic torque output along with variations between healthy and faulty modes of operation.
- Conduct empirical study into effects of rotor blade loss and correlate effectiveness of CFD model to determine micro variations in torque spectra.

CHAPTER 3

DESIGN & TEST SETUP

Scope

This chapter documents the design and manufacture of a novel cross-flow wind turbine system for use in the urban environment where wind speeds are typically low and have frequent changes in direction. The machine presented employs a high solidity ratio to generate large torque output at low wind and rotor speeds to facilitate reliable start-up from rest. Further design features include a multi blade stator array which surrounds the rotor assembly with a view to increasing energy capture and improving energy transfer as described in literature. The machine is of vertical axis format which provides further advantages of uni-directionality and allows for power generation independent of wind direction which is one of the primary flow characteristics within the urban environment.

Within this chapter a design methodology is provided in the form of a set of derived Euler equations which are used for blade profile computation at a specific design point. Using the computed blade profile geometry a full scale prototype machine is manufactured and used for development testing and benchmarking. Details of this test setup are provided in the following along with the numerical formulation of a Computational Fluid Dynamic (CFD) model.

3.1 Wind Turbine Design and Manufacture

The wind turbine presented in this study is of multi-blade design and cross-flow operation. It features an outer array of guide vanes (stators) along with an inner set of rotating blades (rotor). The outer stator blades will be used to condition the incoming flow before entry into the rotor passages. The proposed system is aimed at making performance consistent over a wide range of operating conditions to maximise the energy capture process.

In the following section an overview of the wind turbine design specification and a step by step design methodology is provided. The VAWT geometry consists of two distinct zones as depicted in the following figure.

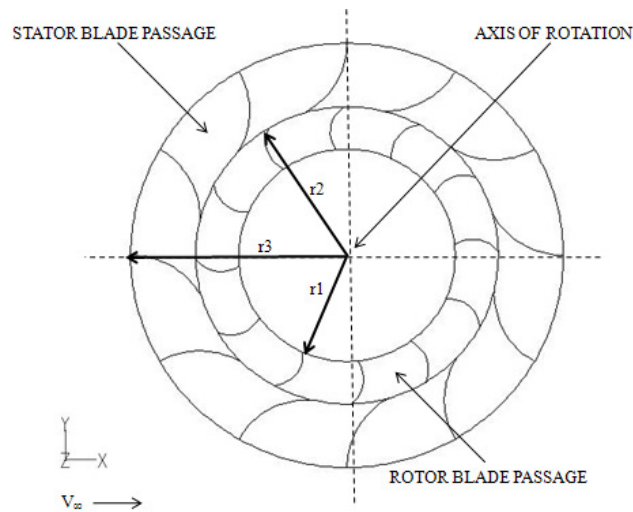


Figure 3-1 Plan view of wind turbine stator/rotor blade configuration

As shown in Figure 3-1 both stator and rotor blade sets feature twelve equally spaced blades about the central axis of the machine. The design envelope used for this machine is selected by the industrial collaborator such that the machine can be easily integrated into urban roof spaces. The outer diameter of the machine is governed by the outer blade tip radius of the stator blade. This stator blade radius is defined by 'r3' and corresponds to 1.0m. Further, rotor blade outer and inner tip radii 'r2' and 'r1' are fixed at 0.7m and 0.5m respectively. The wind turbine height has been set at 1.0m in the Z axis as shown in Figure 3-1. Given height restrictions as described by Peacock [17] wind turbine height should be minimised wherever possible when considering urban installation sites. In this design a total number of 12 rotor blades have been employed and have been selected

on the basis of a high starting torque and to facilitate consistent energy transfer which has been identified as a problem with machines that feature lower number of blades.

In the following, the design methodology used for both rotor and stator blade profile computation is described. The design equations presented are one-dimensional and correspond to an ideal flow theory [82]. The inlet and outlet velocity triangles derived for a typical radial cross-flow rotor blade are provided in the following figure with the assumption of using a fixed outer guide blade (stator). Using this nomenclature a set of design equations are derived to allow for computation of primary blade geometric features namely rotor blade inlet (β_i) and outlet angles (β_o) along with rotor blade radius (rbr).

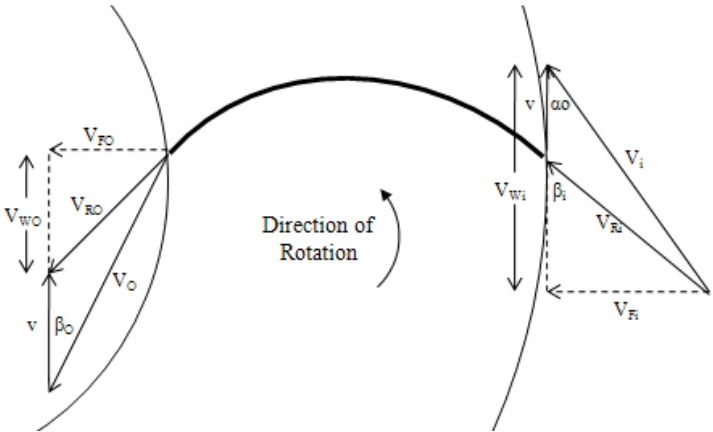


Figure 3-2 Wind turbine rotor blade velocity triangle definition

In the above figure the direction of rotor blade rotation is taken in the anti-clockwise direction with the main flow direction from right to left or radially inward. The first stage of the rotor blade design is to derive a relation for rotor blade inlet angle (β_i) with respect to the flow, whirl and blade tip velocities. This rotor blade inlet angle is subtended between the tangent of the blade and the direction of motion. This angle can be represented by the following expression (3-1).

$$\tan\beta_i = \frac{V_{Fi}}{V_{wi} - v} \tag{3-1}$$

This equation can be expressed in alternative form where sine and cosine functions are used on the parameter V_i as per equation (3-2).

$$\tan\beta_i = \frac{V_i \sin\alpha_o}{V_i \cos\alpha_o - v}$$

(3-2)

Here v is defined as the blade tip velocity and allows for calculation of rotor angular velocity. Using this relation the rotor blade Tip Speed Ratio (λ) can be computed which is the ratio of blade angular velocity relative to the free-stream velocity or wind speed given by:

$$\lambda = \frac{\omega r}{V_i}$$

(3-3)

Modification of equation (3-2) using this relationship of V_i and λ gives the following:

$$\tan\beta_i = \frac{V_i \sin\alpha_o}{V_i \cos\alpha_o - V_i \lambda}$$

(3-4)

This equation can be simplified for a given operating condition where rotor blade inlet angle can be computed for a design stator outlet angle and expected tip speed ratio as per equation (3-5).

$$\tan\beta_i = \frac{\sin\alpha_o}{\cos\alpha_o - \lambda}$$

(3-5)

Using the principal of conservation of mass the following expression can be given for the volumetric flow rate through the blade passage from inlet to outlet:

$$V_{Fi} \times (2 \times r_2) \times h = V_{Fo} \times (2 \times r_1) \times h$$

(3-6)

Simplifying equation (3-6) by removing constants yields:

$$\frac{V_{Fi}}{V_{Fo}} = \frac{r_1}{r_2}$$

(3-7)

The following expression gives V_{Fi} in the form of $V_{Ri} \sin\beta_i$ along with a frictional constant 'K'. Here this constant allows for frictional losses over the surface of the blade and an initial value of 0.99 has been used for conceptual design of the rotor blade.

$$V_{Ri} \sin\beta_i / KV_{Ro} \sin\beta_o \quad (3-8)$$

Simplification gives:

$$\sin\beta_o = \left(\frac{1}{k}\right) \left(\frac{r2}{r1}\right) \sin\beta_i \quad (3-9)$$

In the above, relations for both rotor blade inlet and outlet angles have been derived which can be used during the design phase. These relations assume the inner and outer extremes of the rotor blade tip radii are known along with the stator blade outlet angle which has been assumed on the basis of existing cross-flow turbines. The remaining rotor blade design parameter corresponds to the blade radius. A relation for this parameter is defined in the following section to complete the rotor blade profile design procedure.

3.1.1 Rotor Blade Derivation

This section describes the derivation of the primary rotor blade design equation which allows for computation of the full rotor blade profile. This assumes both inlet and outlet blade angles have been computed using previous equations provided and allows for calculation of the blade profile radius. Here two triangles namely OAC and OCB are constructed from key blade features and are used to formulate the design equation. In order to obtain this relation two triangles are constructed about the blade profile as shown below. Using previously described nomenclature key elements of each triangle can be related to critical rotor blade design parameters:

Triangle OAC: AC = rbr, OA = r1 and Angle OAC = $180 - \beta_o$

Triangle OBC: BC = rbr, OB = r2 and Angle OBC = β_i

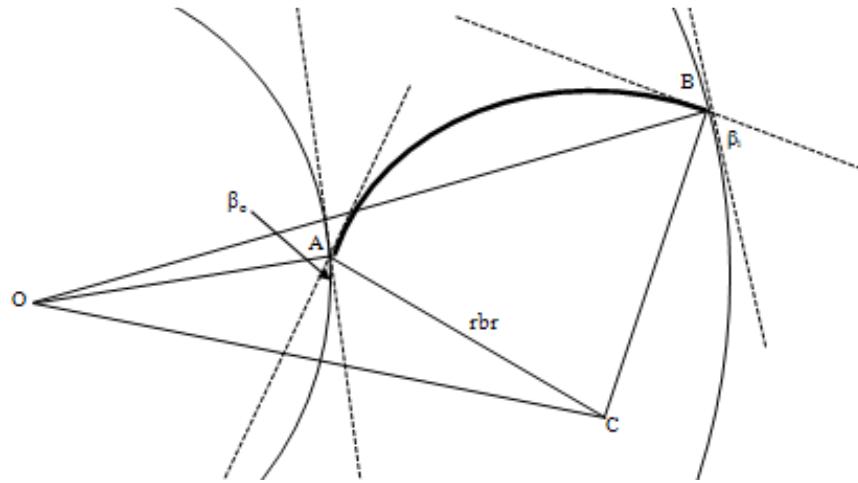


Figure 3-3 Wind turbine rotor blade definition

Using the cosine relation to compute side OC gives the following two expressions from triangles OAC and OBC.

$$OC^2 = OA^2 + AC^2 - 2OA AC \cos (180 - \beta_o) \quad (3-10)$$

$$OC^2 = OB^2 + BC^2 - 2OB BC \cos \beta_i \quad (3-11)$$

Solving (3-10) and (3-11) simultaneously gives an expression to compute r_{br} using both inlet and outlet angles along with r_1 and r_2 :

$$r_{br} = r_1^2 - \frac{r_2^2}{(2(r_1 \cos \beta_i + r_2 \cos \beta_o))} \quad (3-12)$$

Or,

$$r_{br} = 0.5 * \frac{r_1^2 - r_2^2}{r_1 \cos(\beta_i) + r_2 \cos(\beta_o)} \quad (3-13)$$

3.1.2 Stator Blade Derivation

The key feature of this cross-flow wind turbine is the use of a fixed stator guide vane to condition the flow into the rotating rotor blade passages and enhance power generation capabilities. As already described the stator blade outlet angle has been used to compute the rotor blade inlet angle such that energy losses are minimized assuming a no-shock inlet condition. The following section describes the design procedure for the stator blade profile when used in conjunction with the rotor blade described previously. The stator blade used in this design is of fixed radius and has its inlet blade tip tangentially constrained such that it is parallel to the main flow direction. Again two triangles are constructed about the blade profile in order to derive a relation between the key blade design parameters. Here the rotor blade inlet tip (r_2) is of a modified form (r_{2c}) and allows for a small clearance to be maintained between the two blades given variations in manufacturing tolerances and the nature of the fabricated prototype design. This stator blade outlet radius (r_{2c}) is taken as 0.71m from the central axis of the rotor assembly as depicted in the following figure.

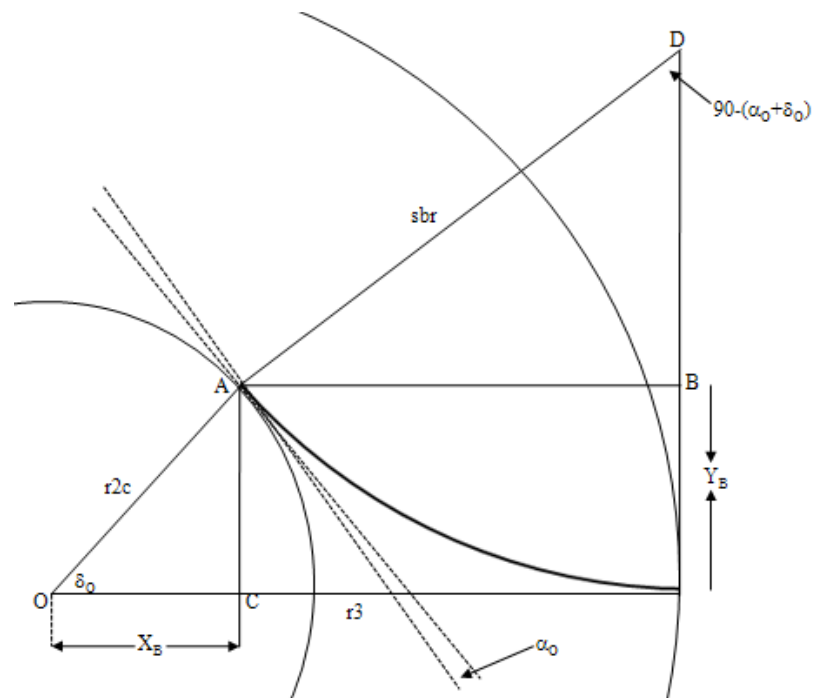


Figure 3-4 Wind turbine stator blade definition

Triangle OAC: $OC = X_B$, $OA = r_{2c}$ and Angle $AOC = \delta_0$

Triangle DAB: $DA = sbr$ and Angle $ADB = 90 - (\alpha_0 + \delta_0)$

'Design, Operation and Diagnostics of a Vertical Axis Wind Turbine'
By Gareth Colley, Department of Engineering & Technology, University of Huddersfield, UK

When considering X_B which relates the x coordinate of position A and Y_B which defines the y coordinate relative to origin O the following relation can be derived using the stator blade outlet angle given by:

$$\tan \delta_o = \frac{Y_B}{X_B} \quad (3-14)$$

Also relations for Y_B and X_B can be derived using stator blade radius (sbr), stator blade inlet radius (r3), stator blade outlet angle (α_o) and the angle subtended between tangent of blade inlet tip and point A:

$$Y_B = sbr(1 - \sin(\alpha_o + \delta_o)) \quad (3-15)$$

$$X_B = r3 - sbr \cos(\alpha_o + \delta_o) \quad (3-16)$$

Or in alternative form:

$$Y_B = r2c \sin(\delta_o) \quad (3-17)$$

$$X_B = r2c \cos(\delta_o) \quad (3-18)$$

Solving the above two equations yields: the following expressions for r2c:

$$r2c \sin \delta_o = (sbr)(1 - \sin(\alpha_o + \delta_o)) \quad (3-19)$$

$$r2c \cos \delta_o = r3 - sbr \cos(\alpha_o + \delta_o) \quad (3-20)$$

Also,

$$sbr = r3 - r2c \cos\delta_o / \cos(\alpha_o + \delta_o) \quad (3-21)$$

Combining equations (3-19) and (3-21) provides a relation that allows for calculation of δ_o which governs the location of point A and hence the stator blade outlet tip. Hence, for a given $r2c$, $r3$ and α_o , δ_o could be computed from the following equation:

$$r2c \sin\delta_o = \left(r3 - \frac{r2c \cos\delta_o}{\cos(\alpha_o + \delta_o)} (1 - \sin(\alpha_o + \delta_o)) \right) \quad (3-22)$$

In alternative form:

$$\sin\delta_o = \left(\frac{r3}{r2c} - 1 \right) (1 - \sin(\alpha_o + \delta_o)) / \cos(\alpha_o + \delta_o) \quad (3-23)$$

Once δ_o has been computed the stator blade radius (sbr) can be calculated from (3-21) and hence the stator profile is fully defined for use with a rotating rotor blade. Using the design equations derived for the rotor and stator blade profiles the wind turbine presented in this thesis has been designed. Its design parameters are documented in the following section which have been used for design and manufacture of a prototype machine.

3.1.3 Rotor/Stator Blade Profile Computation

Using the design procedure documented in this thesis it is possible to design for specific conditions experienced at the installation site. The application for this machine is the urban environment where wind speeds are constantly changing and generally features relatively low wind speeds when compared to free-air conditions. Hence the design wind speed used for this machine is selected on the basis of data obtained from a local rooftop mounted weather station which generated an annual average wind speed of approximately 4m/s. This value has been used as a conservative starting point and both 'design' and 'off-design' wind speeds are investigated in this thesis for completeness. Further, in order to calculate rotor blade inlet angle the corresponding stator guide vane outlet angle (α_o) and rotor blade tip speed ratio (λ) is required. These values have been specified on the basis of

existing machines and in the case of λ is a realistic mid-range speed as observed for high solidity cross-flow wind turbines.

A summary of these input design parameters is provided in the following table which allows for computation of the rotor blade geometry.

Input Parameters	Initial Value
r1	0.5 m
r2	0.7 m
r2c	0.71m
r3	1 m
V	4 m/s
λ	0.5
α_0	20°
k	0.99

Table 1 Wind turbine blade design parameters

The computed rotor blade geometry shown in two-dimensional form is provided in the following figure. Here rotor inlet and outlet angles have been calculated as 38.2° and 61.2° respectively along with a rotor blade radius of 0.145m.

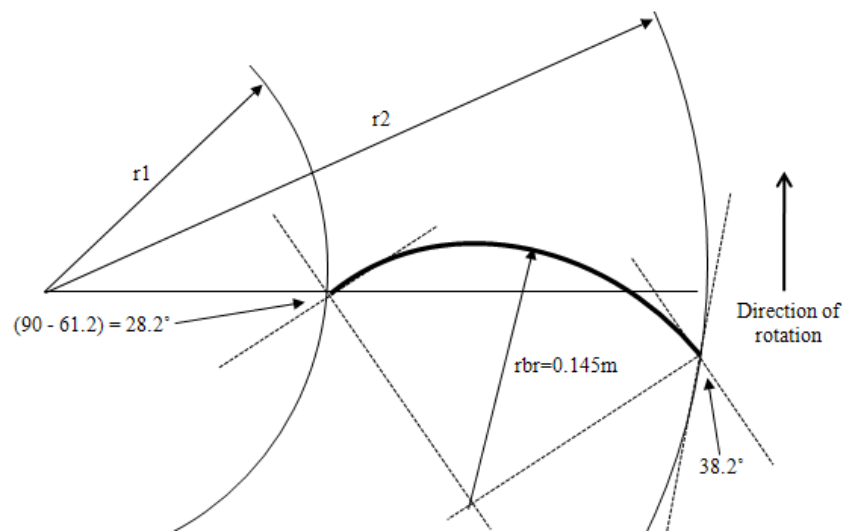


Figure 3-5 Rotor blade profile geometry

In addition to the rotor blade geometry the following stator blade profile is computed using the above design equations. This features stator blade outlet angle and blade radius given a parallel flow entry to the stator inlet tip. Using the assumed stator blade outlet angle (α_0) of 20° a stator blade radius of 0.372m is computed along with δ_0 of 12° .

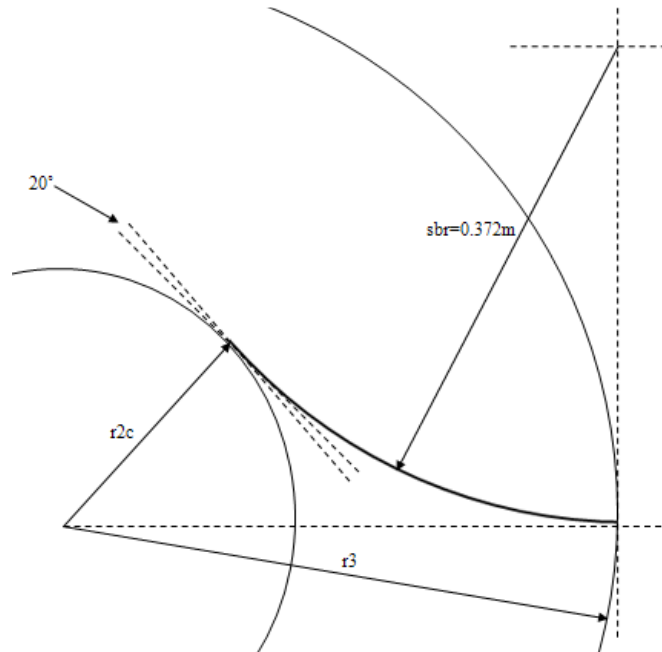


Figure 3-6 Stator blade profile geometry

3.2 Prototype Manufacture

Using the computed blade geometry a full scale prototype machine has been fabricated for development testing. The wind turbine uses the same rotor/stator configuration and has a design envelope with outer diameter of 2.0m and 1.0m in height. Within this space the machine features two distinct zones namely the stator and rotor rings. Each of these rings contains 12 blades fabricated from 1mm thick sheet aluminium cold rolled to create a fixed radius profile which corresponds to that computed using the design equations. The blades are installed such that a 30° angular spacing is maintained and hence blades are equally spaced relative to the central axis of rotation which is concentric to the transmission shaft. The material used is aluminium due to its lightweight and relatively stiff characteristics once formed. Both stator and rotor blades are located between two support rings both above and below the blade end sections. In order to fix the blade in

place a tab is created on the bottom of each blade which mates to a slot in each of the rings, hence during operation the blades are held in shear. Both stator and rotor assemblies are located by two cradle like structures on the upper and lower sides of the machine. At the centre of each cradle is a bearing housing which is welded to each of the support arms which connects to the blade support rings. The vertical and radial position of the rotor is maintained using two taper roller bearings which provides a fixed tip clearance of 10mm between the rotor and stator assemblies. For reference the stator and rotor support rings are laser cut to ensure high accuracy and reduce material distortions. The following images show the full scale wind turbine prototype:

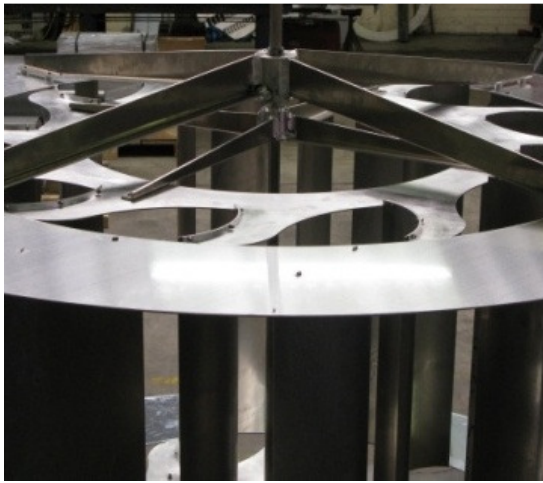


Figure 3-7 Top projection of stator/rotor blade arrangement



Figure 3-8 Side elevation of wind turbine assembly



Figure 3-9 Wind turbine test structure



Figure 3-10 Wind turbine control system

3.3 Experimental Test Setup

The following section provides details of the experimental test setup and system configuration used for development testing of the wind turbine. The wind turbine test rig consists of a low speed wind tunnel with a 0.6m x 0.6m square test chamber and a full-scale prototype wind turbine as per the baseline geometry presented previously. This arrangement has the wind turbine positioned downstream of the wind tunnel test chamber exit and hence is studied under jet flow conditions. The turbine has been instrumented such that operational and performance related data can be obtained via a data acquisition card. An overview of the wind turbine system used is provided in Figure 3-11.

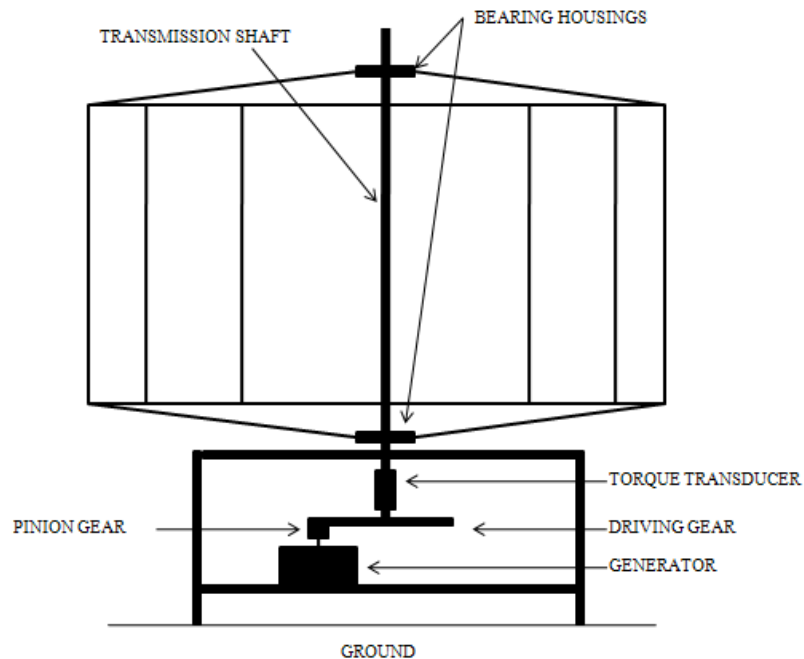


Figure 3-11 Wind turbine system overview

The wind turbine is mounted on a square box section profile frame. The square frame is fabricated from 40mm x 40mm x 4mm box section steel and fillet welded together such that it is structurally rigid. The machine is mounted to the top surface of the frame and is held in place using eight equally spaced M10 x 60mm cap head bolts. To allow for easy access and adjustment of the machines position relative to the wind tunnel exit, the frame work uses castor wheels such that the machine can be aligned in any orientation. During operation the frame work is lifted off the ground

using adjustment screws which are located on mounting platforms such that the machine is stable at high wind and rotational speeds.

3.3.1 Transmission System

The turbine consists of two zones namely the stator blade ring and the inner rotor ring each containing twelve blades. Both blade zones are held in place using four angled support sections which minimize flexing during operation. The rotor assembly is located on a central transmission shaft which in turn is located with two bearing housings at the top and bottom as shown on the above figure. To keep the transmission shaft fixed, two holes are placed in both the upper and lower bearing carriers. Using four M10 grub screws both the rotor and transmission are held at a fixed position with zero slip. To transfer power from the shaft to the generator a simple gearing arrangement is used to increase generator shaft speed by a ratio of 8.3:1 relative to the input shaft. The gearing arrangement used in this setup consists of a pair of matched, lightened and balanced spur gears which are synchronised with a total tooth to tooth backlash of 150 μ m as shown in the following figure.

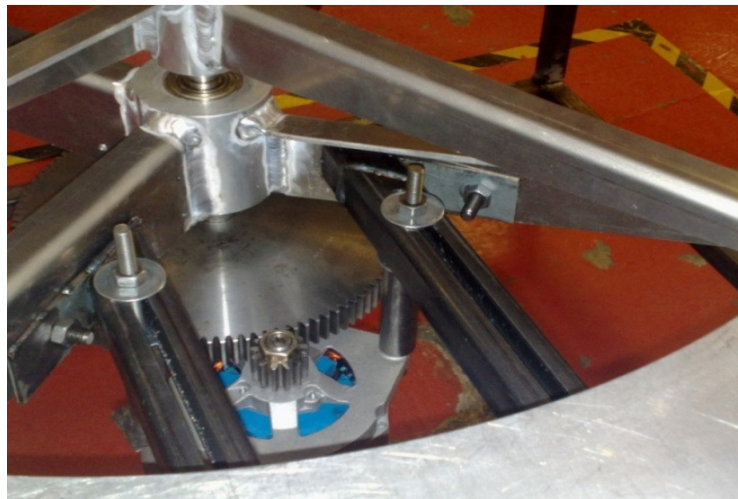


Figure 3-12 Wind turbine transmission setup with gear engagement rails

3.3.2 Power Generation

The power generation system used at the output of the turbine transmission shaft is described in the following section. This generation system contains the generator, power analyzer, rectifier, resistive load and data acquisition system. Using this system it is possible to generate AC current, control wind turbine rotor speed and sample real-time instantaneous three phase current and voltage data. This system is depicted by Figure 3-13.

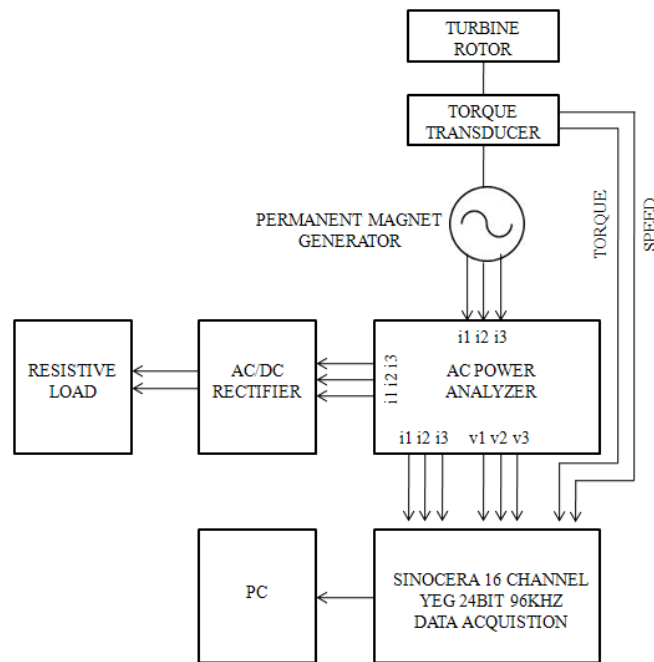


Figure 3-13 Wind turbine power generation system

As per the above figure the three phase current output is connected to an AC power analyzer which contains a series of current and voltage transducers and an individual power supply. As shown in the figure the primary three phase current enters the analyzer where it is fed into an AC/DC rectifier such that a DC signal is produced. This rectifier is required given the type of resistive load bank that is used to control wind turbine rotor speed. On the opposite side of the analyzer six terminals are present each with a linear 0-10v output. These terminals allow for acquisition of instantaneous current and voltage which in this case is connected to a high speed data acquisition system. Two further signals taken from the torque transducer unit namely torque and speed are fed into the data acquisition which are sampled with the electrical data. The output of this DAQ is then connected to a PC for post processing.

3.3.3 Wind Tunnel System Overview

The primary apparatus used for experimental studies is a low speed wind tunnel, which features a 0.6m x 0.6 test chamber and 0.8m diameter axial fan. Figure 3-14 depicts the working sections of the wind tunnel from a side elevation.

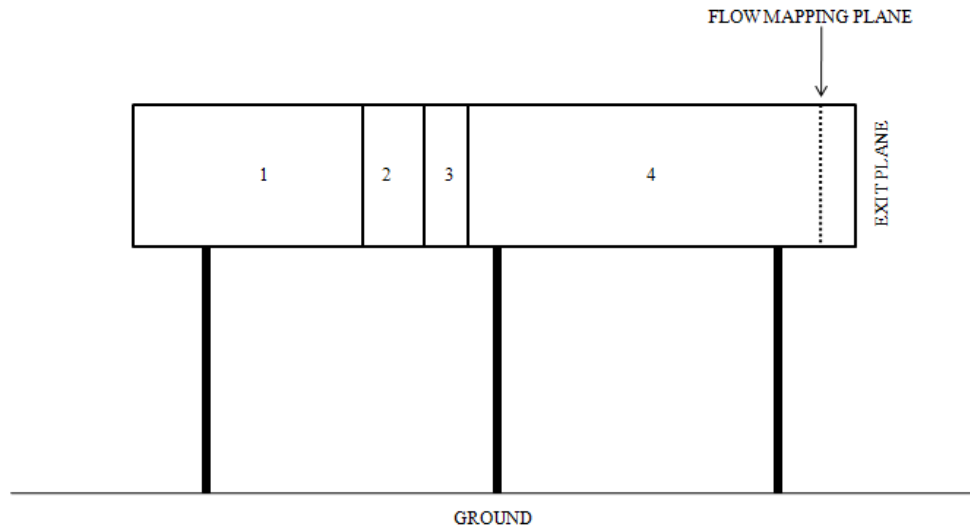


Figure 3-14 Wind Tunnel side elevation of working sections

Working Section	Description
1	Woods Varofoil single stage axial fan
2	Post fan guide vanes
3	Honeycomb flow straightener
4	Perspex 0.6m x 0.6 square working section

Table 2 Wind tunnel working section description

Due to the nature of the tests carried out in this thesis, the wind turbine is located downstream of the wind tunnel test chamber exit. The location of the turbine relative to the test section exit is fixed dimensionally in the X, Y and Z-axis. The orientation of the machine is depicted in the following figures. The first figure shows the turbine position in the XZ view plane. Here the turbine is constrained in the X and Z axis using distances 'd' and 'd1'. The offset distance 'd' from the exit plane of the test section is fixed at 0.5m for the following experiments. This distance allows

sufficient clearance between the machine and test chamber and facilitates the use of a three-axis traverse accurate to 100 μm for flow mapping in this region. The secondary location parameter is 'd1' and acts in the Z axis, this dimension is 0.193m.

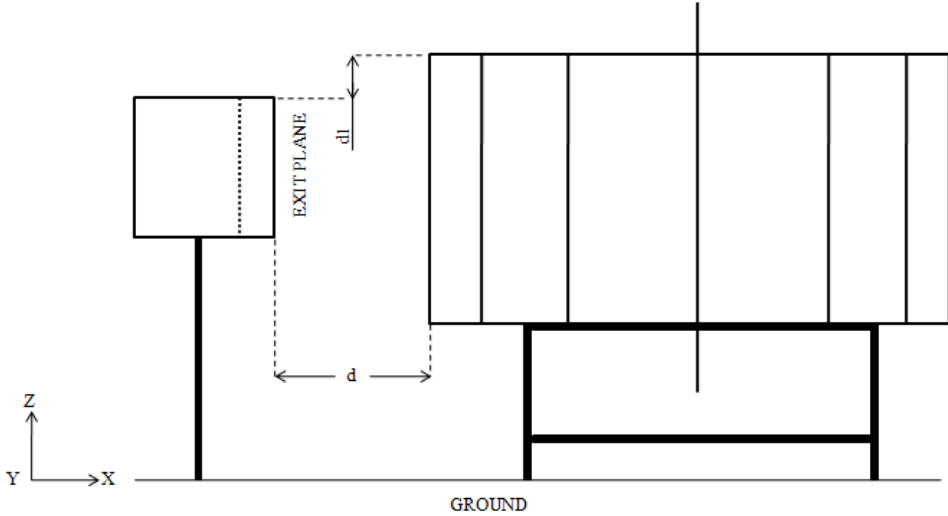


Figure 3-15 XZ view of wind turbine relative to test chamber exit plane

The second figure shows the turbine from a plan view orientation in the XY plane. This view provides information of how the machine is constrained in an angular direction. Here the turbine geometry is aligned to the test chamber wall using a parallel constraint between the outer chamber wall and a line that is fixed tangentially to the outer stator tip. This line is taken from the central axis of the turbine geometry and extended radially where it meets the stator tip face as shown in Figure 3-16.

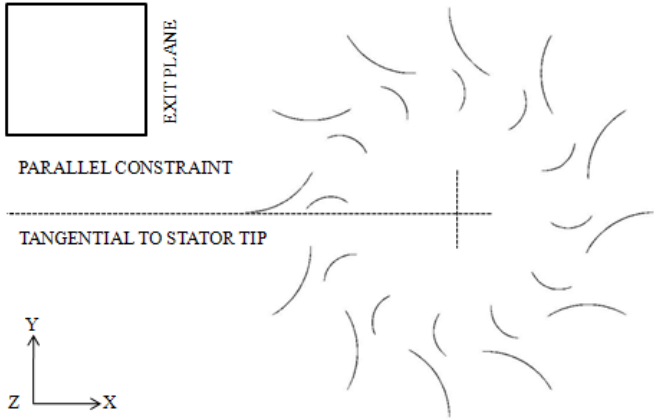


Figure 3-16 XY view of wind turbine relative to test chamber exit plane

'Design, Operation and Diagnostics of a Vertical Axis Wind Turbine'
 By Gareth Colley, Department of Engineering & Technology, University of Huddersfield, UK

3.3.4 Instrumentation and Specifications

The instrumentation used to obtain experimental data is documented in the following section in which individual specifications are provided. The major instruments used are associated to flow and rotor torque/speed measurement. The fan used to provide mass flow air through the wind tunnel is of axial type operation using a pneumatic regulator to control the pitch of the blades. The specification of the unit is provided below for reference:

Manufacturer	Woods Air Flow
Model Type	71KG/40A/F Class / 380/420V
Air Pressure	1.76 kg/cm ²
Speed Range	0-2950 rpm
Control Type	Varofoil Pneumatic

Table 3 Wind Tunnel Axial Fan Specification

To obtain flow field data at the exit of the wind tunnel along with the angular distribution about the wind turbine a cobra head pressure probe has been used connected to a high speed data acquisition.

Manufacturer	Turbulent Flow Instruments
Model	Cobra 1.5mm Head
Number of Velocity Components	3
Conical Head Range	+/- 45°
Frequency	1.25KHz

Table 4 Cobra Probe Specifications

The generator used is of permanent magnet type and is connected to the wind turbine transmission shaft. The generator specification is provided in the following table:

Manufacturer	Wind Blue Power
Model Type	DC-540
Number Of Poles	7
Output	15A at 2000rpm using 12v Battery

Table 5 Wind Blue Power Generator Specification

To characterize the performance of the turbine both torque and speed data is taken from the transducer unit mounted between the generator and the bottom bearing arrangement of the rotor as per Figure 3-11. The specification of the torque transducer is provided below:

Torque Rating	100Nm
Speed Rating	30,000 rpm
Torque Scale Equation	Torque (Nm) = 20*V
Speed Scale Equation	Speed (rpm) = V+1.577/1.388
Overload Capacity	1.3 x rated torque, 2 x rated torque
Break Capacity	>5 rated torque
Alternating Torque	1 x rated torque
Protection Class	IP40
Speed Transducer	60 Pulses
Linearity Deviation	<0.1% of full scale
Hysteresis	<0.1% of full scale
Device Class Acc. According to DIN 51 309	Typ 0.2% (Depends on measured value) >20% rated torque
Limit Frequency	1 KHz
Output	+/- 5V at rated torque
Load Resistance	>10KΩ
Nominal Temperature Range	+10°C - +60°C
Temperature Influence on Zero	0.05% / 10K
Torque control signal	100% +/- 0.2%
Power Supply	16 – 30V DC
Current Consumption	110 mA

Table 6 Torque/Speed Transducer specification

Analogue data is obtained using a Sinocera AD convertor of the following specifications and is used as per the arrangement described in Figure 3-13.

Manufacturer	Sinocera
Model	YEG
Resolution	24Bit
Number of Channels	16
Sampling Frequency	96Khz
Accuracy	+/- 0.4%

Table 7 Sinocera Data Acquisition Specification

3.4 Numerical Modelling Approach

The predicted flow field and wind turbine performance data presented in this thesis have been obtained from numerical simulation using a commercial Computational Fluid Dynamics (CFD) code *Fluent 6.3*® [83]. This section provides a detailed description of the modelling approach used in which CAD model design, grid generation, boundary conditions, numerical formulation and wind turbine rotation are all described in full. In this work CFD discretization is performed using *Gambit 2.4.6*® [84] pre-processor.

3.4.1 Computational Hardware

Numerical simulations have been carried out on both single (stand-alone) and parallel (multiple) workstations. Generally single workstations have been employed during model generation and meshing processes where system memory was sufficient. For this process a quad core *Intel i7*® platform was used with a clock speed of 3.0 GHz along with 6GB of PC1833Mhz DDR3 physical memory. The simulations were performed using a high performance compute cluster on the University of Huddersfield's Queensgate Grid. On this grid the Eridani cluster was used to perform parallel batch simulations where six processing cores per simulation were used depending on the discretized size of the CFD flow domain. A rough approximation of core usage was one or two cores per one million mesh elements determined from experimentation. The advantages of using

grouped workstations in the form of cluster computers has been observed during the present work in which significant speed ups have been reported. Additionally, constraints associated with single workstations such as multi-core usage and memory allocation problems are considerably reduced during parallel computation. The time required to complete typical simulations as presented in Chapters 4-7 varied between 8-10 hours when using Eridani. As a comparison the same simulations when employed on a single workstation varied between 32-36 hours depending on local hardware loads.

3.4.2 Computer Aided Design (CAD) Model

The design of the numerical model and associated zones is described in the following section. The model used for CFD analysis consists of full scale three-dimensional geometry such that some of the limitations identified in literature can be overcome. The dimensions of the wind turbine are consistent to those described previously in this chapter; the following figure depicts this three-dimensional geometry within the *Gambit*® modelling space in a wireframe representation. The wind turbine shown here consists of twenty-five discrete volumes that correspond to each of the stator/rotor blade passages along with a central core. To create these volumes face geometry is shared within the machine to allow volume stitching. This methodology of generating a three-dimensional structure significantly improves the meshing phase given that each volume mesh can be individually written back to hard disc and thus reducing memory demands. This also provides a means of individually monitoring mesh quality in each zone and in particular the region of interface where both stationary and rotating reference frame merge. The wind turbine geometry spacing relative to the outer boundaries of the flow domain is based around the experimental laboratory test area which has shown to provide free-air operation and also allows for a direct comparison with empirical data. This flow domain and the wind turbine geometry is depicted in Figure 3-18 where a cross sectional view is provided in the XY plane.

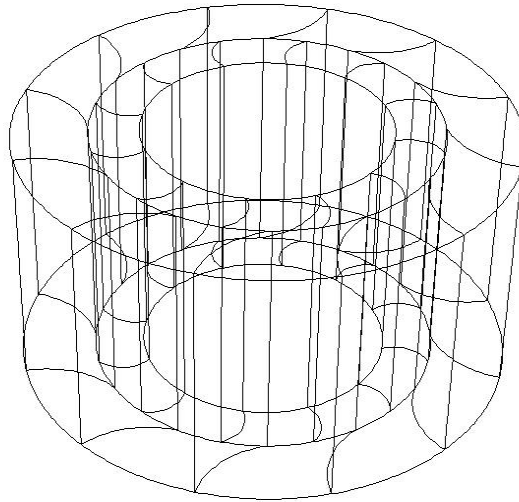


Figure 3-17 Three-dimensional wind turbine rotor/stator geometry

In the following figure, the location of the wind turbine in the Y axis relative to the domain side faces is central and hence distance 'Y1' is constant at either side. The location of the machine in the ZX plane is shown in Figure 3-19.

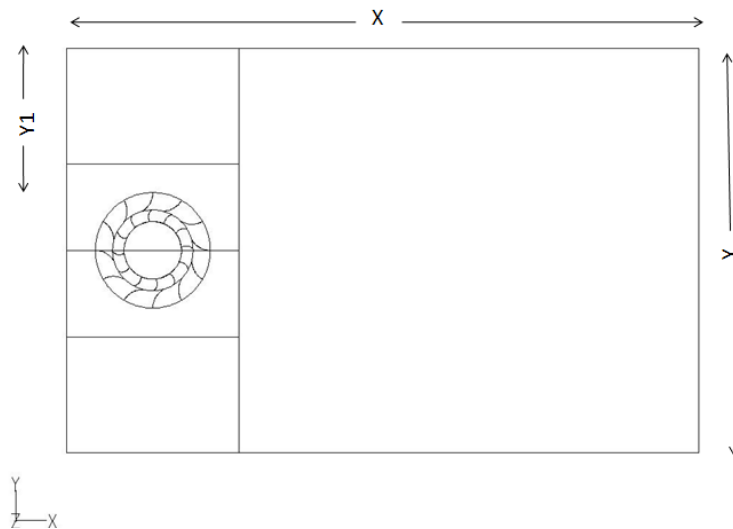


Figure 3-18 CFD Flow domain in XY plane

Where: $X = 11\text{m}$, $Y = 7\text{m}$, $Y1 = 2.5\text{m}$

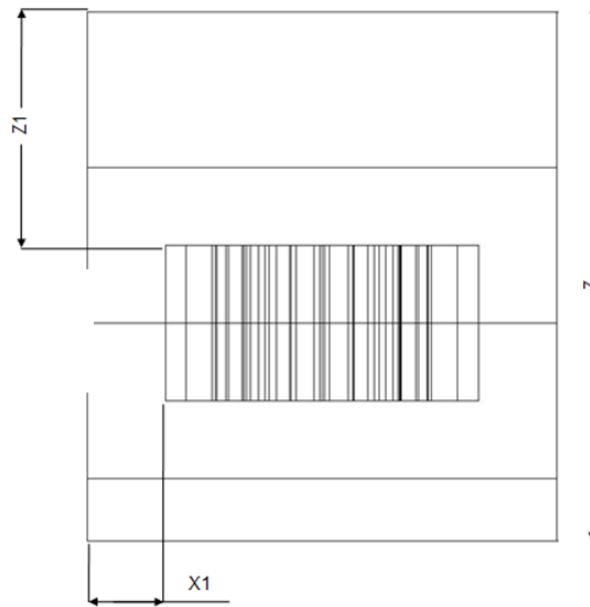


Figure 3-19 CFD Flow domain in XY plane

Where: $Z = 3.4\text{m}$, $Z1 = 1.5\text{m}$, $X1 = 0.5\text{m}$

In the above figure, the wind turbine is located at 0.5m from the velocity inlet boundary as defined using $X1$. This distance has been held constant throughout all studies such that comparisons can be made with experimental data and to minimize reductions in velocity magnitude at the inlet of the rotor. The flow domain used in this study is broken down into a number of discrete volumes which correspond to different zones within the domain. These zones are present to facilitate mesh control in and around the turbine geometry with the aim of improving mesh cell quality.

Figure 3-20 shows four regions within the flow domain which are labelled inlet chamber, turbine zone, mesh gradient zone and outer flow domain. Surrounding the wind turbine geometry are small geometric volumes which are used to control mesh cell growth and quality. This particular region is defined as 'Mesh Gradient Zone' and features four discrete volumes that are connected to both the wind turbine geometry and the outer flow domain. The distance between the outer radius of the turbine and the outer faces associated to these zones is 0.5m in the X and Y axis. These regions are split into smaller discrete volumes where their associated lower topological entities are used to govern mesh nodal spacing in and around the turbine blades. Due to the high concentration of mesh elements within this region such volumes also reduce computational demands by distributing the mesh over a larger number of volumes. As stated, this process significantly reduces the memory demands during the meshing process by allowing the mesh to be written before meshing the next

zone. Beyond these zones two further control volumes are present which make up the remaining fluid domain in the Y direction. These regions are simple singular rectangular volumes which carry the outer flow domain mesh scheme. The size of these volumes is again governed by the dimensions of the laboratory test area. The final volume that makes up the flow domain is the outer flow domain. This is again a simple one piece rectangular volume that spans the remaining void in the X direction.

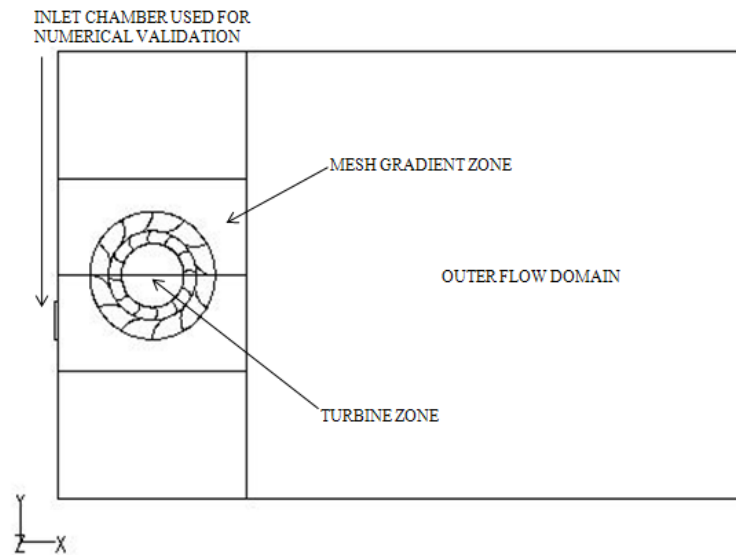


Figure 3-20 CFD flow domain zone breakdown

3.4.3 Grid Resolution and Discretization Scheme

Computational grid resolution is a significant factor in the accuracy and computational time of each simulation. The grid resolution used for both Multi Reference Frame (MRF) and Sliding Mesh (SM) computations is different in that MRF grid is three-dimensional and SM grid is two-dimensional. However, both model flow domains are of comparable size when viewed from a two-dimensional plan view and hence the structure and segregation of the mesh is consistent between the two. In each case a hybrid mesh is used to facilitate accurate body mapping of the complex wind turbine geometry whilst providing a structured hexagonal/quadratic mesh in the outer flow domain. To allow for hybrid mesh creation the boundaries at which triangular and quadratic cells meet a uniform mesh nodal spacing is used such that mesh quality can be maintained and positive faces/volumes are forced to generate. An overview of the discretized flow domain is depicted in the following figure where a plan view is presented.

'Design, Operation and Diagnostics of a Vertical Axis Wind Turbine'
 By Gareth Colley, Department of Engineering & Technology, University of Huddersfield, UK

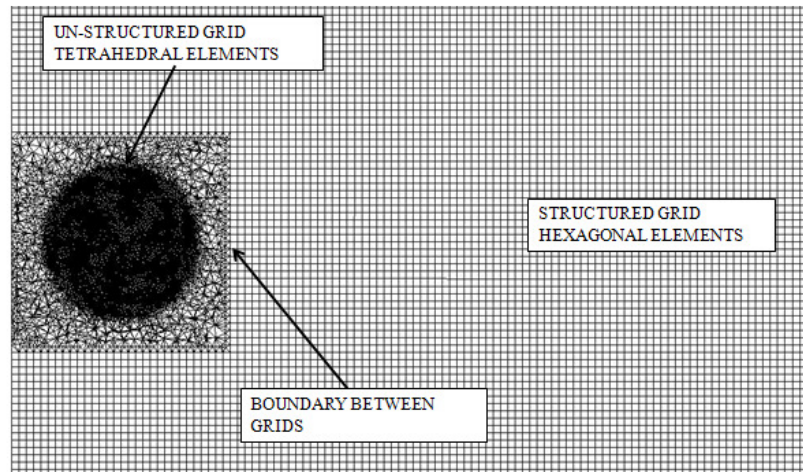


Figure 3-21 Cross sectional view of three-dimensional CFD model grid in XY plane

To ensure mesh independence three grids were studied for both MRF and SM models at identical solver and flow conditions. The following table provides details of the number of control faces/volumes used, wind turbine and outer flow domain edge nodal spacing size (m) and rotor torque response (Nm). From this table the torque output of the rotor shows a small variation between grids with maximum variation of 1.03% and hence does not justify the additional computation resources required for the larger grids. For MRF simulations a grid of 3200000 volumes is used due to increased mesh control around areas of complex geometry and increased solution stability over more extreme operating conditions.

Wind Turbine Nodal Spacing (m)	Outer Flow Domain Nodal Spacing (m)	Number of control volumes	Rotor Torque Response (Nm)
0.025	0.125	1800000	22.51
0.02	0.1	3200000	22.39
0.015	0.075	7500000	22.29

Table 8 Three-dimensional grid independence as used for MRF computation

The grid employed for two-dimensional computation is also examined for solution independence in which three grids are again studied. Here due to the reduction in computational requirement the spacing is reduced by 50% for each grid. As per previous analysis the solution is seen to show

minor variations between grids in which maximum variation of 2.6% is observed. Given the increased computational expense for higher number of cells the grid with 34000 elements is selected for SM computations. The torque output depicted below is independent of time-step size and is the mean rotor torque output.

Wind Turbine Nodal Spacing (m)	Outer Flow Domain Nodal Spacing (m)	Number of control elements	Rotor Torque Response (Nm)
0.02	0.1	34000	16.48
0.01	0.05	140000	16.8
0.005	0.025	440000	16.92

Table 9 Two-dimensional grid independence as used for SM computation

3.4.4 Wind Turbine Boundary Conditions

The wind turbine geometry used in CFD analysis is of identical geometric shape to that presented previously. It does however feature one simplification to increase mesh control and cell quality. This simplification is in the form of zero thickness blades compared to the prototype which uses 1mm thick aluminium. Such simplifications have been used by other authors in which zero thickness blades are employed in a Rushton turbine [9]. This simplification allows for a much higher quality mesh in the blade passage regions by eliminating such a short edge across the blade face. This simplification allows for a significant reduction in mesh cells and without it the scope of computational studies would be limited. To validate this effect a preliminary study has been carried out on a two-dimensional model. The results obtained from this simulation indicate a 2% variation between geometries with thickness and without. Given this small variation this simplification is used throughout.

In order to replicate the physical condition, a number of boundary conditions [83] are employed on the geometries within the flow domain. The stator and rotor fluid rings contain twelve blades each with an associated wall boundary condition as shown in Figure 3-22. The fluid volumes between them are referred to as blade passages and are generated from a pair of blades. Each turbine blade has two associated geometrical faces which are meshed on both sides. The primary face is defined

as blade whereas the secondary surface is defined as blade-shadow. This allows for data analysis on both sides of the blade given the zero thickness simplification. Each of these faces has been modelled as a non-porous surface using the 'wall' boundary condition within *Fluent*®. The upper and lower faces within each of the blade passages are defined as a wall boundary to replicate the annular support rings that are used on the prototype machine. The remaining two faces denoted as inlet and outlets on the figure are used as the inlet and outlet to each blade passage cavity. These faces have an interior boundary condition associated with them to allow the fluid to enter and exit without any wall interaction effects.

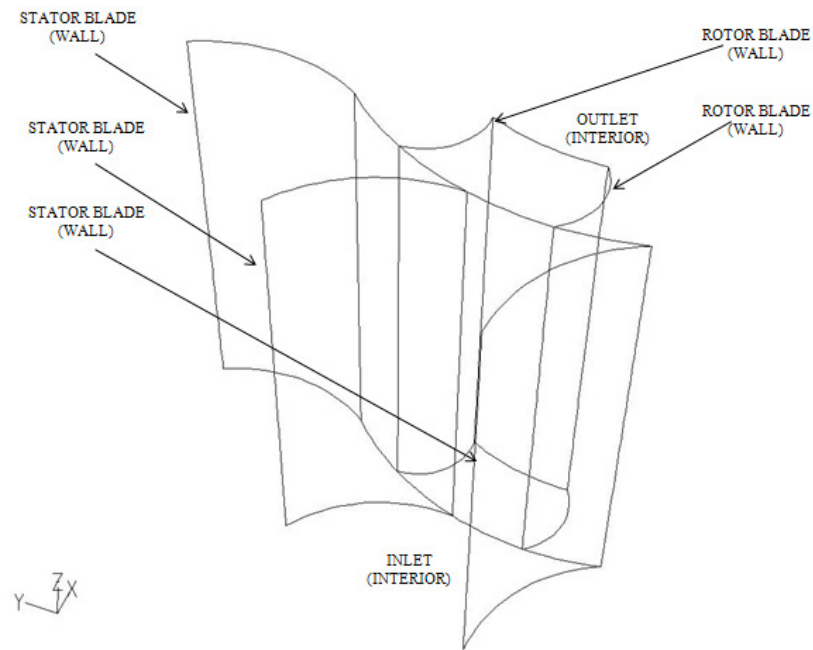


Figure 3-22 Wind turbine stator/rotor blade passage boundary definition

An overview of the wind turbine boundary conditions is provided in Figure 3-23 where the velocity inlet is depicted as used for validation. In this figure the velocity inlet represents the wind tunnel exit and is aligned as per the experimental test setup described previously. Under normal flow conditions the velocity inlet spans the complete length of the control box depicted in the figure and hence allows for free-air conditions.

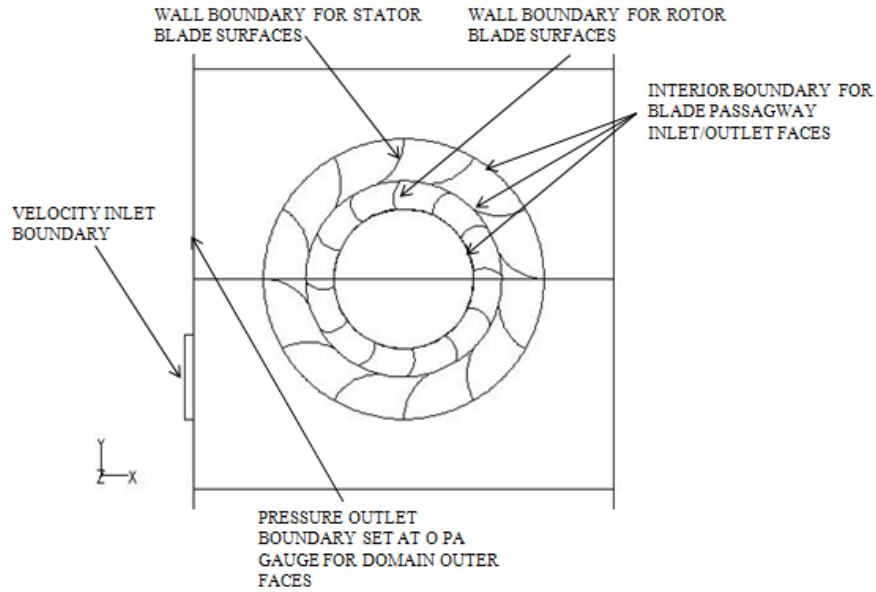


Figure 3-23 Turbine zone boundary conditions for numerical validation

3.4.5 Numerical Formulation and Flow Physics Modelling

The governing equations used in the present study are of an incompressible form of the Navier-Stokes equations. A time averaged turbulence solution has been used in which Reynolds Averaged Navier Stokes (RANS) equations have been used to compute turbulence stresses within the flow domain [83], [85], [86]. Given the approximations of the time average turbulent stresses a number of models have been developed which can be used for specific fluid flow conditions [83], [87]. Here for MRF and SM simulations the k-ε model is used [67], [83], [88], [89] to resolve the turbulent flow field across the machine which has proven to be stable for the conditions of interrogation and the rotational flows generated. The governing equations used to compute rotational flow are described in the following.

The mass conservation equation given by:

$$\frac{\partial \rho}{\partial t} + \nabla \cdot \rho \vec{v}_r = 0$$

(3-24)

The momentum equation given by:

$$\frac{\partial}{\partial t} (\rho \vec{v}_r) + \nabla \cdot (\rho \vec{v}_r \vec{v}_r) + \rho (2\vec{\omega} \times \vec{v}_r + \vec{\omega}_r \times \vec{\omega}_r \times \vec{r}) = -\nabla p + \nabla \bar{\tau} + \vec{F} \quad (3-25)$$

The conservation of momentum equation contains two additional acceleration terms to account for the Coriolis and Centripetal effects. Coriolis acceleration is given by $\left(2 \vec{\omega} \times \vec{v}_r\right)$ and centripetal by $\left(\vec{\omega}_r \times \vec{\omega}_r \times \vec{r}\right)$. Here, the viscous stress tensor $\bar{\tau}_r$ uses relative velocity derivatives \vec{v}_r .

3.4.6 Wind Turbine Rotation

Modelling of rotating machinery is complex due to the relative motion of the rotor/impeller and stationary vanes/baffles and results in cyclic variation of the solution domain. Two standard approaches are widely used which are MRF and SM where the flow domain is divided into an inner fluid zone containing the rotor and outer fluid zones containing both stator geometry and the outer flow domain. For the MRF approach steady-state calculations are performed with a rotating reference frame in the rotor fluid zone relative to a stationary reference frame housing the stator geometry. Hence, the effects of blade rotation are considered by virtue of the frame of reference which allows for explicit modelling of the rotor assembly geometry [83]. In the present study MRF simulations are performed to predict the steady-state flow field across the machine along with rotor performance for a three-dimensional model. This approach is also known as 'frozen-rotor' given that the blade geometry is static and the fluid volume rotates relative to it. Hence reaction forces generated on the blades are considered to be the force exerted on the fluid.

The SM model follows a similar principle in that both rotor and stator geometries are segregated using discrete fluid zones. The primary difference between the two approaches is that SM is fully transient and can be used to generate a rotating or sliding mesh. The mesh and hence the geometry mapped within can therefore rotate relative to the fixed stator vanes. This rotation of the rotor is governed by discrete intervals known as time steps. Although SM accounts for explicit transient behaviour accuracies are comparable for a range of operating conditions as described in [67], [68], [89]. In the present study SM computations are performed for a two-dimensional model due to

intensive computational requirements due to the fact a fully converged solution is required at each time step. For each model standard wall functions are applied as proposed in [90].

3.4.7 Verification

The verification process proposed by Roache [83] states that convergence error can be quantified by monitoring specific solution parameters and systematically varying the residual tolerance bands such that iterative error is minimized. Preliminary studies have been conducted in which the effect of convergence criteria on the torque output of the machine has been quantified. It is noticed that largest variation in torque is observed between $1e-1$ and $1e-3$ when set for each of the governing equations. Between $1e-3$ and $1e-4$ a significant variation is observed however residual magnitude is seen to stabilise approaching $1e-4$. Beyond this limit the effect of convergence criteria on torque output is seen to be negligible and does not justify additional computational expense. Additionally, throughout each simulation a real-time monitor is set on the torque output of the rotor such that convergence of moment coefficient can be determined both qualitatively and from data exported to an output file. From this study a convergence criteria of $1e-4$ has been used throughout this thesis unless otherwise stated.

CHAPTER 4

PRESSURE AND VELOCITY FIELD

ANALYSIS

Scope

The primary focus of this chapter is to investigate the flow field characteristics of the wind turbine using both experimental and numerical techniques. From this analysis some of the underlying questions highlighted in the literature review are addressed by providing a comprehensive analysis of the turbines operational characteristics. This chapter presents analyses carried out on the pressure and velocity fields during normal operation across the turbine and provides both qualitative and quantitative analyses of each. The experimental studies undertaken provide real-time flow field data under static rotor conditions at a unique rotor blade position. Using this data a full-scale three-dimensional CFD model is validated such that predicted flow fields can be used reliably. Numerically predicted flow fields are evaluated in both stationary and rotating frames of reference for a range of rotational speeds. In addition, transient related effects are considered for a range of rotor blade positions which provides novel dynamic flow field data for a cross-flow machine. Finally, the variations of both pressure and velocity as a function of vertical, angular and radial position are quantified over a cross-sectional plane such that the full flow field characteristics are known.

4.1 Numerical Validation

This section documents the validation strategy used to determine the accuracy of the CFD model to predict flow fields across the wind turbine. The model uses the MRF solving technique and is as per that described in Chapter 3 and is consistent throughout this thesis unless otherwise stated. The validation strategy follows that proposed by Oberkampff and Trucano [91] in which experimental data is used and cross examined against predicted CFD data for the same flow condition. CFD verification as described by Roache [92] is again in-line with described previously and is maintained throughout this thesis.

The first analysis presented in this chapter investigates the variation of pressure and velocity fields generated over the machine during static rotor conditions. Here, experimental data is obtained from full scale wind turbine tests and CFD data taken from the three-dimensional MRF model. Due to the complexities involved during dynamic flow field analysis a static validation is performed with the rotor fixed at a pre-defined point corresponding to the design condition described in Chapter 3. In order to replicate the flow conditions present during experiment the CFD model takes a modified form and features the wind tunnel outlet geometry which is used as an inlet to the flow domain as per Figure 3-20 . To ensure geometric similarity the location of the wind tunnel exit plane relative to the inlet of the wind turbine conforms to that described in Figure 3-15 and Figure 3-16. This validation is performed at a fixed wind tunnel operating velocity which generated a unique velocity profile at the exit of the wind tunnel test chamber. To re-create this profile in CFD a direct profile import method is used with data obtained using a four hole Cobra type pressure probe over the exit plane of the wind tunnel (Figure 3-14). The velocity field measured experimentally is depicted in the following figure in the ZY plane.

		Y - POSITION (m)					
		0.05	0.15	0.25	0.35	0.45	0.55
Z - POSITION (m)	0.05	9.23	9.97	9.45	10.41	11.54	9.93
	0.15	12.17	13.07	12.65	12.66	12.11	10.20
	0.25	11.57	11.90	11.15	11.08	11.45	11.03
	0.35	10.32	11.17	11.31	11.56	12.37	12.23
	0.45	10.21	12.12	12.94	12.77	12.78	11.88
	0.55	8.78	10.33	9.79	9.09	9.90	9.69

Figure 4-1 Measured velocity field (m/s) at wind tunnel exit plane

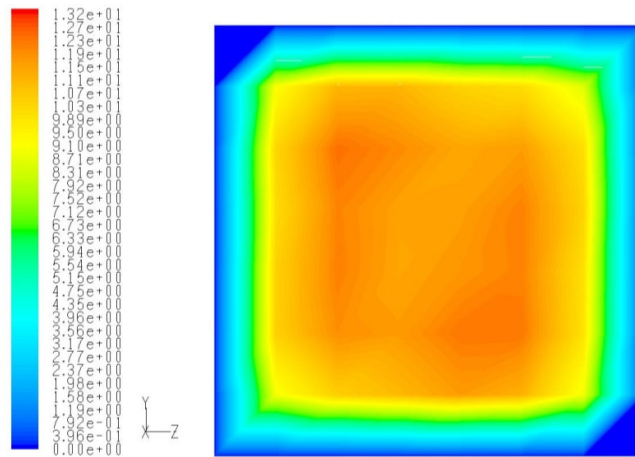


Figure 4-2 CFD interpolated velocity field (m/s) at velocity inlet boundary

In order to import this velocity field into the CFD solver, the surface is split into horizontal velocity profiles and a polynomial fitting technique is used to obtain an equation for each. Using these equations the velocity field is imported using a form of User Defined Function (UDF) which is interpolated over the velocity inlet boundary mesh in the solver.

Given the complexity in wind turbine geometry the following diagram is used to define critical zones within the turbine. In this figure four sides to the machine are defined namely windward, leeward, top and bottom which are used for analysis throughout. The relation of wind turbine geometry relative to the free-stream flow direction is provided in which V_∞ denotes the flow direction. The angular position of both stator and rotor blades is defined using the angular position or θ in which blade location is defined in degrees about the central axis of the turbine (also defined). Further, for clarity each blade is denoted a number such that it can be easily identifiable in the following analysis. Finally, a radial position indicator is provided in which the stator blade inlet tip corresponds to $R=1.0\text{m}$ and the central axis $R = 0\text{m}$.

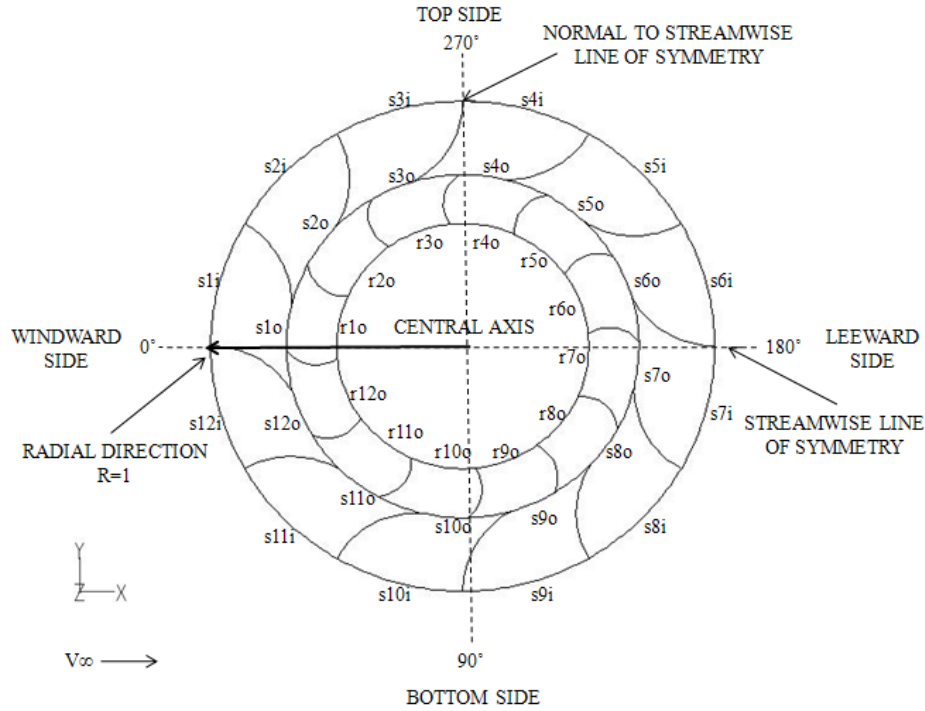


Figure 4-3 Wind turbine zone definition

The following data is obtained at the mid-plane of the wind turbine on the outer diameter which corresponds to a radial position of $R=1.025\text{m}$ as per Figure 4-3. This location is chosen due to problems associated to introducing the probe inside the stator and rotor blade passages and the resultant blockage effects. The data is taken over a range of angular positions which correspond to the area at which energy transfer occurs and is defined in Figure 4-3. This range has been limited to $270 - 360^\circ$ as per the above figure, outside this range velocity magnitude is seen to be below 1m/s at all positions studied and cannot be used reliably. This is due to the operating range of the cobra type pressure probe which is calibrated at a minimum flow speed of 1m/s .

For the purpose of this validation both experimental and CFD data is plotted in Figure 4-4 in which pressure coefficient is used to define the local pressure field. Here p_∞ is computed as an average over the velocity-inlet boundary which is the convention used throughout this thesis thus giving free-stream static pressure.

$$P_{COEFFICIENT} = \frac{p - p_\infty}{\frac{1}{2} \rho V_\infty^2}$$

(4-1)

It is noticed that a strong correlation between experimental and predicted pressures is present between 270° and 290° whereas between 290° and 335° a large variation in pressure is observed between data sets. Here, CFD pressure field is significantly lower than that observed during experiment. Although a large variation is present the overall characteristic of the profiles has some similarity although appears to be slightly out of phase indicative of some angular misalignment which could be from i) flexing of the turbine structure which is not accounted for in CFD ii) geometric inconsistencies on the fabricated structure and iii) probe angular misalignment relative to the wind turbine blades. Additionally, the ability of the three-dimensional model to accurately predict upstream and downstream pressure is limited by the degree of stator/rotor interaction from the MRF solving technique. Hence, such effects are likely to contribute significantly towards this variation in pressure given limited stator/rotor interactions at the boundary between stationary and rotating frames of reference.

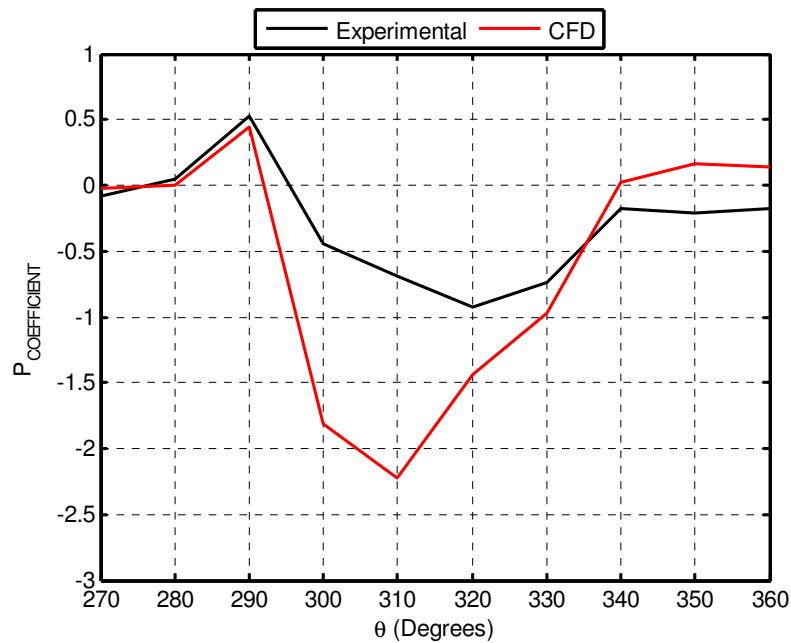


Figure 4-4 Cross examination of experimental and CFD pressure field ($P_{\text{COEFFICIENT}}$)

Figure 4-5 depicts the velocity profiles obtained over the same range. This velocity is presented in non-dimensional V/V_{AVG} where V_{AVG} is computed from the average velocity acting over the exit of the wind tunnel and velocity-inlet boundary respectively. Here a strong similarity in velocity magnitude is observed between experimental and predicted data. Both profiles indicate peak

velocity at 320° with magnitudes of 0.725 and 0.69 respectively which results in a 4.8% deviation. Between 270° and 310° the CFD model under-predicts the upstream velocity field although a strong similarity is present in terms of the velocity distribution and overall trend. Beyond the peak velocity at 320° a large reduction in magnitude is noticed which is consistent between both data sets. In this instance the experimental data shows some form of misalignment given that velocity reduces much sooner than that predicted with CFD. Such trends are again likely to be a result of variations in geometry, misalignment and limitations within the CFD model. It is however concluded that given the complexities in flow across this multi-blade machine the overall correlation between both data sets is relatively good particularly in the overall distribution of both the pressure and velocity fields for this rotor condition.

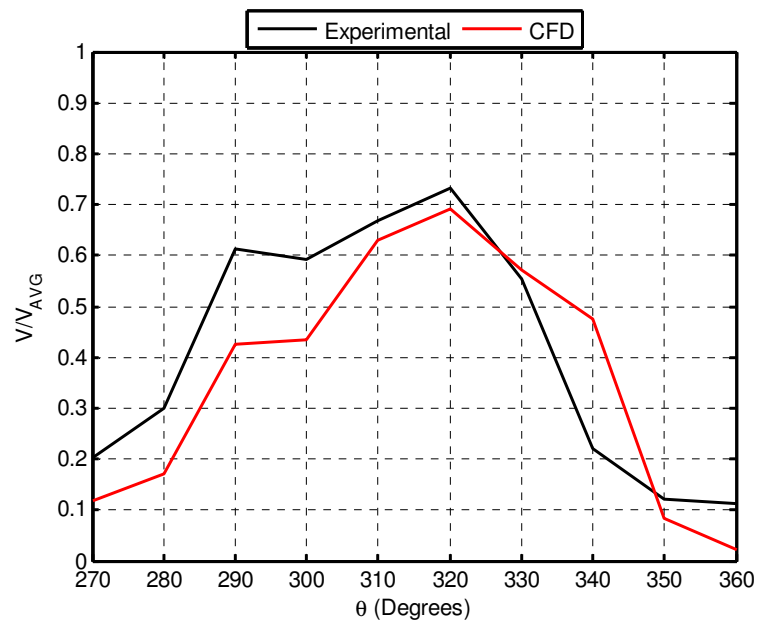


Figure 4-5 Cross examination of experimental and CFD velocity field (V/V_{AVG})

4.2 Numerical Pressure Field Analysis

This analysis investigates the pressure fields generated over the wind turbine using predicted data from the CFD model as described previously. Here both qualitative and quantitative approaches are taken to evaluate the nature of flow for stationary and rotating rotor conditions. This pressure field is investigated in vertical, angular and radial directions such that flow distribution and non-uniformities can be identified. This pressure data is obtained from the CFD model for two wind turbine operating states defined by rotor Tip Speed Ratio (λ) namely 0 and 0.4. This provides an insight into how the pressure field develops during a transition from static to rotational modes of rotor operation which is a novelty of this work. Additionally, effects related to rotor blade position provide transient data which highlights variations in flow for a complete blade cycle. In each of these analyses pressure is non-dimensional in the form of pressure coefficient given by (4-1). The wind speed (V_∞) is fixed at 4m/s throughout this study and has been specified based on velocity measurements in the local area and to determine operational characteristics at the design point. This velocity acts in the X axis as depicted in the following figures.

4.2.1 Variation of Pressure Field in Vertical Direction

The following analysis investigates the pressure field in the vertical direction through the wind turbine at cross sectional planes. This vertical direction is defined by the Z axis in Figure 3-21 and contours of pressure are evaluated in the respective ZX and ZY planes intersecting through the rotor central axis. This allows for a sectional view of the pressure generated within both the stator and rotor zones and hence provides critical information within stationary and rotating frames of reference. In addition, two operating states namely $\lambda=0$ and $\lambda=0.4$ are presented such that rotational induced effects of the rotor can be evaluated. The contours of pressure are provided below in which a global scale is used to allow for comparative analysis. The scales set on each of the figures are defined from the minimum and maximum pressures observed in the frame of reference, this governs the range of contour levels applied. In order to compute the flow field in the form of $P_{\text{COEFFICIENT}}$ a free-stream velocity (V_∞) of 4m/s is used and p_∞ is taken from the velocity-inlet boundary which corresponds to the free-stream flow condition. This pressure is computed as the area-weighted average on the velocity-inlet boundary which is the convention used throughout this thesis.

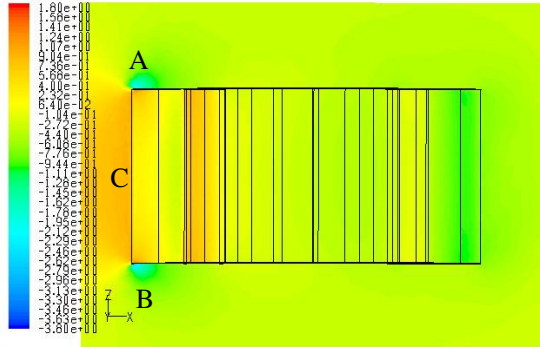


Figure 4-6 Stream wise plot of $P_{\text{COEFFICIENT}}$ at $\lambda=0$ for $V_{\infty}=4\text{m/s}$ in ZX plane

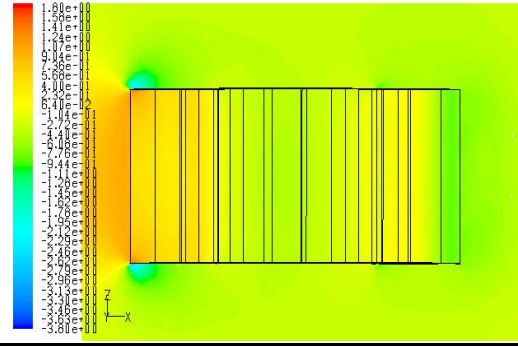


Figure 4-7 Stream wise plot of $P_{\text{COEFFICIENT}}$ at $\lambda=0.4$ for $V_{\infty}=4\text{m/s}$ in ZX plane



Figure 4-8 Normal to stream wise plot of $P_{\text{COEFFICIENT}}$ at $\lambda=0$ for $V_{\infty}=4\text{m/s}$ in ZY plane



Figure 4-9 Normal to stream wise plot of $P_{\text{COEFFICIENT}}$ at $\lambda=0.4$ for $V_{\infty}=4\text{m/s}$ in ZY plane

When considering the pressure field generated in the stream wise direction in the ZX plane a strong similarity between both rotor conditions is observed. The most notable trend is the strong symmetry of pressure about a plane taken mid wind turbine height in the XY plane. Here pressure shows a large degree of similarity which is consistent at both rotor conditions. One clear feature of this flow field is the local reduction of pressure over the leading edges of the stator assembly both positions A and B. This pressure drop is below atmospheric levels and is in the order of -2.41 at both positions. When compared to the rotating condition at $\lambda=0.4$ these pressures have reduced further to -2.68 which equates to a 10% reduction as a result of the rotating rotor assembly. Additional features of interest include the high pressure zone on the inlet side (C) of the machine which is expected given the large energy transfer in this region and the associated reductions in velocity as the flow interacts with the windward blade sets. At $\lambda=0$ and 0.4 these pressures are 1.02 and 0.93 indicative of a reduction in upstream pressure of 8.8%.

The pressure field generated in the ZY plane which acts normal to the stream wise direction highlights different trends when compared to the previous data. The local pressure reductions are now removed as expected given the increased distance from the stator tip positions A and B. The

effect of rotor speed on the pressure field in this region is negligible which requires further investigation. A large degree of symmetry is again noticed about the wind turbine mid-plane which is a consistent feature of this multi-blade design.

4.2.2 Variation of Pressure Field with Blade Position

The following analysis provides both qualitative and quantitative analysis of the pressure field generated in the XY plane at the mid-plane of the wind turbine. This allows for evaluation of the pressure field in the angular and radial directions which contributes towards the understanding of the energy transfer process within cross-flow wind turbines. This analysis considers effects associated to rotor blade position which provides novel information on the pressure characteristics related to transient operation. Here rotor blade position is defined relative to the adjacent stator blade. The rotor blade passing cycle is 30° given the twelve equi-spaced rotor blades employed in this design. Rotor blade position is varied from 0° to 20° incrementally at 10° intervals where the pressure field is computed at each. The rotor blade position of 30° is neglected given the same pressure field is generated as seen at 0° . The pressure contours shown in the following are obtained at the mid-plane of the turbine which corresponds to $Z = 0.5\text{m}$. Here the contour scale is consistent for each blade position to allow for identification of subtle variations in the flow field. In addition the vertex averaged pressure has been computed at a radius of 0.8m taken from the centre of the machine. Pressures are obtained at the mid position of each stator passage and are used to understand the effect of the downstream rotor and its associated position. This provides novel data about the flow field close to rotor blade passage entry which is a critical aspect of operation. The following figure defines the rotor cycle position relative to an adjacent fixed stator blade.

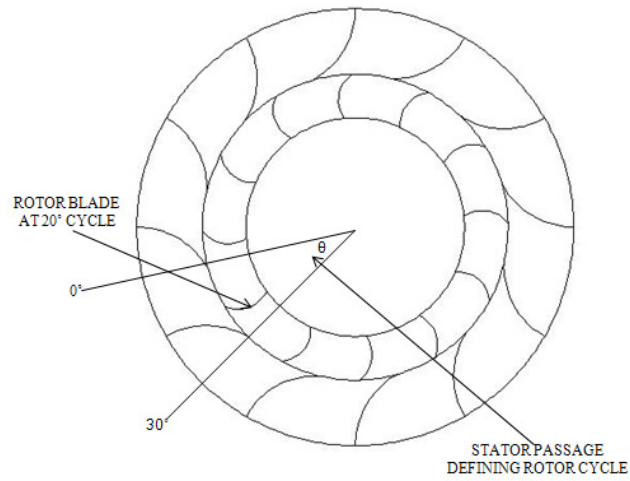


Figure 4-10 Rotor blade position angular definition

The figures presented below provide an overview of the local pressure field across the wind turbine under rotational conditions corresponding to $\lambda = 0.4$. This condition has been chosen such that true transient related phenomena can be observed when the rotor is in motion. Also based on operating data reported in [60–62], [64], [66–68] it is expected that this rotor tip speed ratio will be close to the peak power point hence being of further interest.

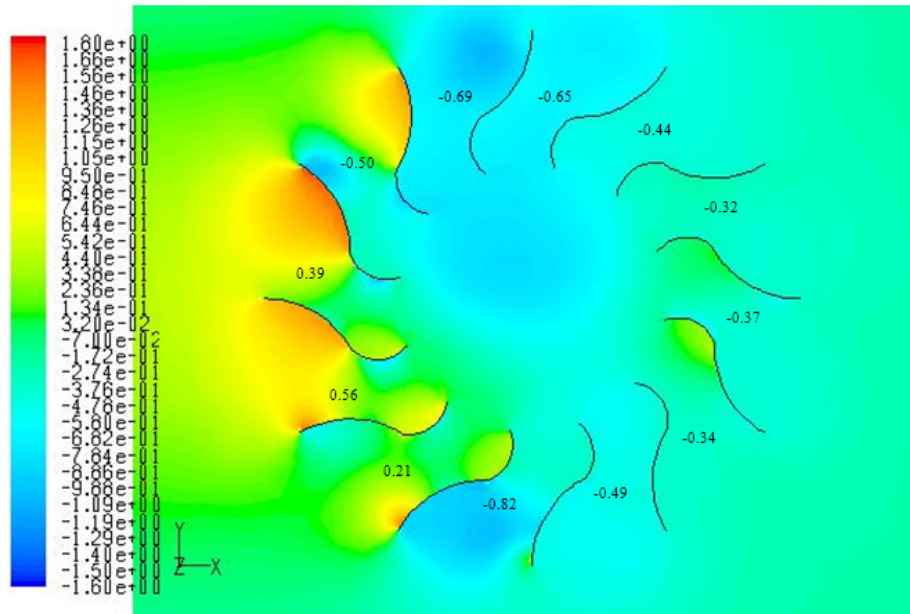


Figure 4-11 Plot of $P_{\text{COEFFICIENT}}$ at rotor blade position of 0° for $\lambda=0.4$ and $V_\infty=4\text{m/s}$ at mid-plane

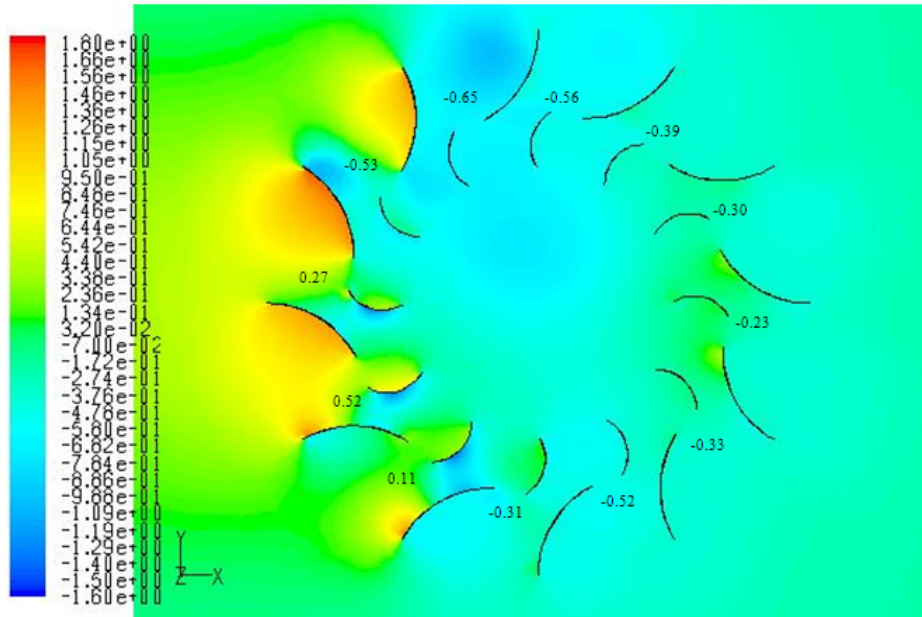


Figure 4-12 Plot of $P_{\text{COEFFICIENT}}$ at rotor blade position of 10° for $\lambda=0.4$ and $V_\infty=4\text{m/s}$ at mid-plane

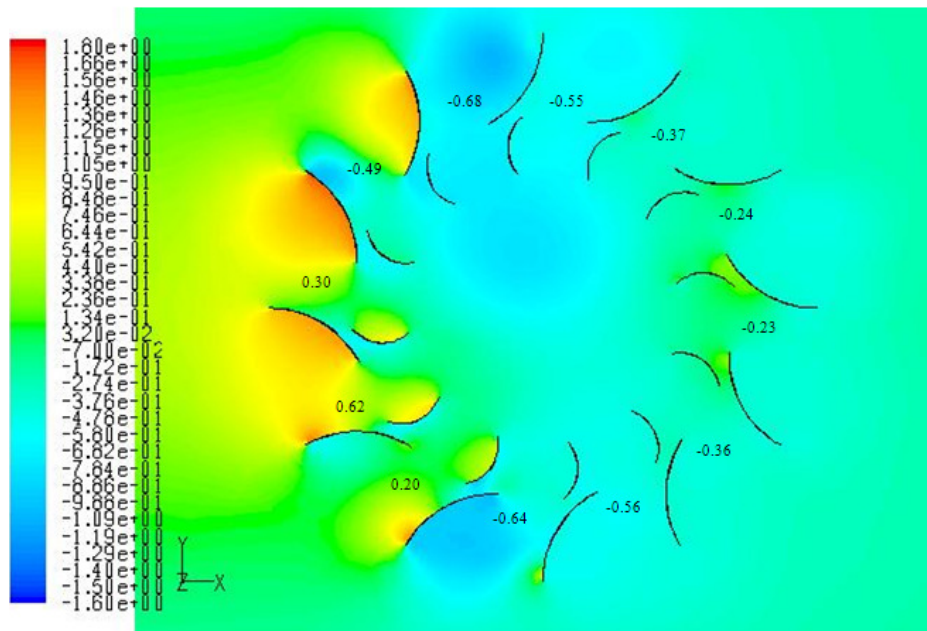


Figure 4-13 Plot of $P_{\text{COEFFICIENT}}$ at rotor blade position of 20° for $\lambda=0.4$ and $V_\infty=4\text{m/s}$ at mid-plane

The overall pressure distribution as a function of R and θ can be seen in the above pressure contours. In general, the pressure fields obtained show some similarities to those documented in [93] in which a highly asymmetric flow is generated over the turbine resulting in specific energy

transfer regions. It is noticed that a large variation in pressure is present and is largely dependent on both radial and angular positions within the machine. Given the stream wise flow direction is in the X axis a high pressure zone is generated upstream of the windward stator blade set and is considerably reduced in the wind turbine wake located downstream of the leeward stator blades. This trend highlights the effect of wind turbine energy capture and the associated pressure drop across the both stator and rotor passages. In terms of energy transfer within the machine this is heavily focussed on a few key blade passages on the windward side of the machine in which regions of relatively high pressure are observed at blade S2, S1, S12 and S11. Regions of pressure that are below atmospheric are present at opposing sides of the machine within S3, S4, S9 and S10 which is due to the high stator blade angles of attack relative to the main flow direction. This results in significant blockages to the adjacent stator passages which is a potential inefficiency of the cross-flow machine. This also provides justification for the insensitivity to rotor speed for the vertical pressure profile described in Figure 4-8 and Figure 4-9. The above trends appear to be relatively consistent over the range of rotor blade positions investigated although given the key energy transfer zones identified any small variations in pressure are expected to result in variations in blade torque as a function of blade position. Hence when considering blade position of 0° the centre pressures at $R=0.8\text{m}$ for S2, S1, S12 and S11 are -0.5, 0.39, 0.56 and 0.21 respectively. At a blade position of 10° these are -0.53, 0.27, 0.52 and 0.11. Such pressure magnitudes indicate a reduction of pressure within each of the blade passages which is likely to be a result of the local flow accelerations between the stator blade outlet tips and the rotor blade which is positioned more centrally to the stator passages. For the rotor blade position at 20° the corresponding stator passage pressures are now -0.49, 0.3, 0.62 and 0.20 which highlights an increase in pressure compared to the previous blade position for all passages considered. Given such variations in pressure the effect of the rotor blade assembly on the upstream pressure field is deemed to be significant and is predicted to result in large variations in blade torque in this particular region. A summary of these blade pressures is provided in the following table where the mean pressure is computed for the three blade positions and percentage variation given for specific blade positions relative to the mean.

Blade Passage	Mean Pressure	% Variation at 0°	% Variation at 10°	% Variation at 20°
S2	-0.51	1.32	-4.61	3.29
S1	0.32	21.9	-15.63	-6.25
S12	0.57	-1.18	-8.24	9.4
S11	0.17	21.2	-36.5	15.4

Table 10 Stator blade passage centre pressure variation

From the above, blade passage S2 is seen to be least sensitive to a change in rotor blade position when compared to S1, S12 and S11. Largest variations are present at passage S11 and hence torque output of the downstream rotor blade is expected to have similar sensitivity in torque output. Finally, it is noticed that on the leeward side of the machine at blade passages R6 and R7 a variation in pressure is present as a function of blade position. This is expected to be a result of interaction effects with the leeward rotor set and the stream wise flow. This is also a feature of existing Savonius machines and can result in significant reductions in performance due to counter-rotating torque generation which are quantified in Chapter 6.

4.2.3 Variation of Pressure Field in Angular Direction

From the previous analyses the wind turbine pressure field is seen to vary significantly in the angular direction (θ). Given this observation the following study is carried out to quantify this variation around the central axis of the machine at unique radial positions for both static and rotational rotor operation. This analysis has been performed at the design rotor blade position as described in Chapter 3 to provide operational characteristics at the design point. This pressure distribution is plotted in the form of pressure coefficient using the same reference values for free-stream flow and static pressure. The following plots show this angular pressure profile from 0° to 360° in the anti clockwise direction at which pressure is computed at 5° intervals. Given the strong uniformity of pressure in the vertical direction the following data is obtained at the wind turbine mid-plane. From the plots of pressure it can be seen that angular pressure changes as a function of radial position and hence for a more comprehensive study this angular variation is computed over a range of radii. This range of radius is taken from the origin of the machine which corresponds to the central axis of the rotor. This radial range is taken from 1m - 0m, which corresponds to the outer stator blade tip radius and origin of the machine. Angular pressure variation is computed at R= 1, 0.8, 0.6, 0.4, 0.2 and 0m, the following plots depict this angular pressure data over this range.

'Design, Operation and Diagnostics of a Vertical Axis Wind Turbine'
By Gareth Colley, Department of Engineering & Technology, University of Huddersfield, UK

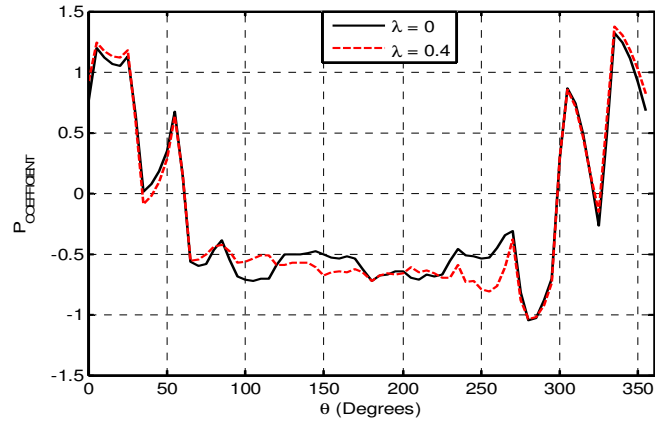


Figure 4-14 Pressure coefficient plotted with θ at $R = 1m$ for $\lambda = 0$ and 0.4

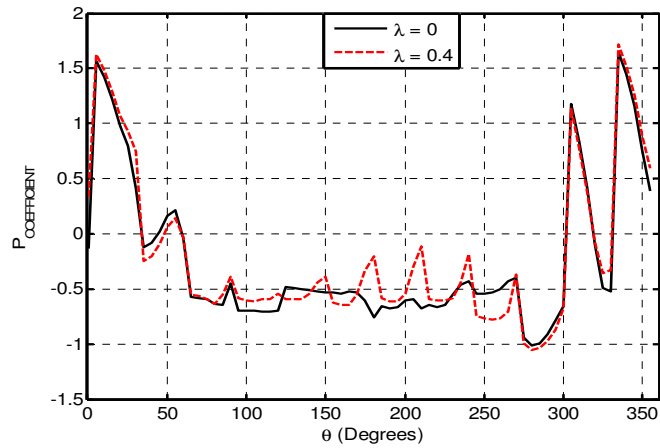


Figure 4-15 Pressure coefficient plotted with θ at $R = 0.8m$ for $\lambda = 0$ and 0.4

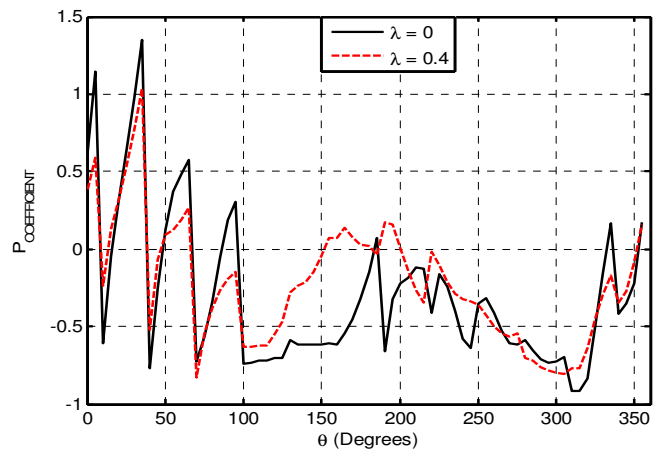


Figure 4-16 Pressure coefficient plotted with θ at $R = 0.6m$ for $\lambda = 0$ and 0.4

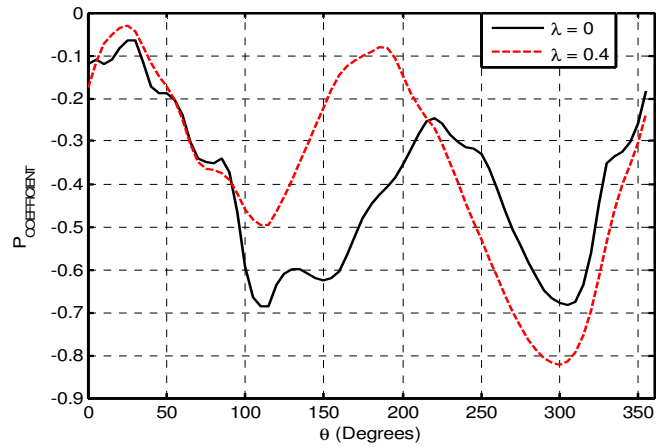


Figure 4-17 Pressure coefficient plotted with θ at $R = 0.4m$ for $\lambda = 0$ and 0.4

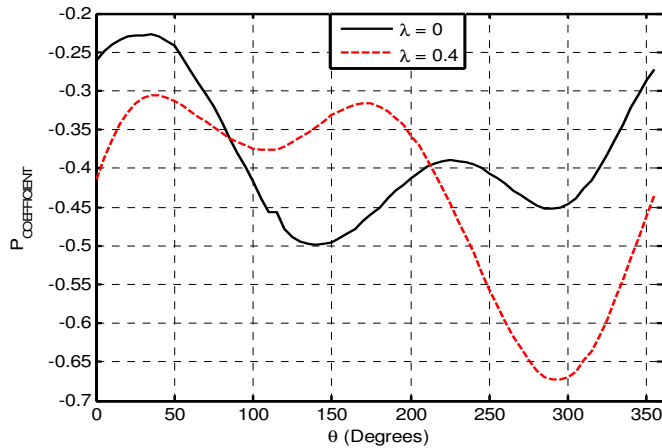


Figure 4-18 Pressure coefficient plotted with θ at $R = 0.2m$ for $\lambda = 0$ and 0.4

4.2.3.1 Angular pressure variation at R = 1m

The above plot of angular pressure distribution at $R=1m$ depicted by Figure 4-14 shows strong asymmetry about the central axis of the wind turbine. The magnitudes of pressure are seen to vary significantly depending on this angular position. Largest pressures are generated on the windward side of the turbine which is a result of large momentum exchange between the free-stream flow and the stator blades in this region. Peak pressures are located at specific angular positions within this distribution and are a result of flow interactions with the stator blade surfaces. Peak pressures are generated close to stator blades S2, S1 and S12 in which a peak pressure of 1.4 is generated at S2 and is relatively consistent regardless of the rotor being static or rotational. This insensitivity to

rotor speed is noticed across the majority of the windward side of the machine and is likely to be a result of increased proximity from the rotor inlets. On the leeward side of the machine between an angular position range of 90° - 270° a large reduction in pressure is observed which is well below atmospheric. This is a combined result of stator blade shielding effects along with the energy capture and resultant pressure drop across the rotor. The largest pressures observed within this distribution are generated at the windward side of the machine as highlighted in the plots of pressure contours in the previous study. Within this region the angular pressure distribution is seen to be much more sensitive to a change in λ which is expected given the flow is exiting the rotating rotor blade passages. Such trends are indicative of strong downstream rotor-stator interactions which are expected to be more pronounced at closer proximities to the rotor blade tips.

4.2.3.2 Angular pressure variation at R = 0.8m

The pressure field plotted in Figure 4-15 is computed at a radius of 0.8m close to the rotor blade inlet tips. As with the previous radial position, considerable pressure variation is seen in the angular direction. Maximum pressures are again noticed on the windward side of the turbine in which pressure is well above atmospheric. Here the magnitude of pressure exceeds 1.5 close to blades S1 and S12 which is due to the increased angle of attack relative to the free-stream flow direction and hence increased flow interaction at the blade surface. There is however a strong similarity between the distribution at R=1m in that the windward stator blades heavily influence the resultant pressure field. Again as observed previously the effect of λ on this pressure profile is only noticed on the leeward side of the machine and is well below atmospheric for $\lambda = 0$ and $\lambda = 0.4$. One interesting trend is the three pressure peaks at angular positions of 180° , 210° and 240° in the order of -0.2. These increases in pressure at $\lambda = 0.4$ are potentially induced from downstream energy transfer phenomena which requires further investigation. It is reported that the most notable variations in pressure are observed within the range of 100° - 300° at which the effect of rotor speed is most prominent as the flow exits the rotor assembly.

4.2.3.3 Angular pressure variation at R = 0.6m

The angular pressure variation shown in Figure 4-16 is plotted at $R = 0.6\text{m}$. At this radial position, pressure is obtained inside the rotor passage and hence for the first time gives an insight into the energy transfer process within the rotor. The magnitudes of pressure are slightly reduced when compared to those obtained in the stator ring and a more complex distribution is observed. Again highest pressures are present between 330° and 60° with a clear reduction in pressure on the leeward side of the machine due to energy losses in the fluid. At this radial position effects of blade geometry are again very clear with peak passage pressures generated at the blade surface. The most dominant characteristic of this profile is between 100° and 180° where a large variation in pressure is noticed between the two rotor operating states. Under rotational conditions a significant increase in pressure is generated at this radial position perhaps signifying un-desirable pressure characteristics within this region. The effect of such a distribution on the torque generation capabilities of the rotor requires further study and is provided in the performance analysis chapter.

4.2.3.4 Angular pressure variation at R = 0.4m

Figure 4-17 depicts the angular variation of pressure at a radius of 0.4m which resides within the central core of the wind turbine at a radial offset of 0.1m from the outlet tips. This distribution of pressure shows more stable characteristics which signifies the reduced effects of the rotor blades due to this decreased proximity. An interesting characteristic of this profile is that the pressures obtained are all negative and hence below atmospheric which provides some information on the pressure gradients present in the radial direction. The most notable observations from this plot are the variation in pressure between 100° and 225° shows considerable changes between rotor operating conditions. Here peak pressures are out of phase which indicates a strong change in flow direction through this zone dependent on rotor operating speed.

4.2.3.5 Angular pressure variation at R = 0.2m

Figure 4-18 shows the variation of angular pressure in the core region of the turbine at a radius of 0.2m . This region shows the smoothest pressure distribution re-enforcing statements about

'Design, Operation and Diagnostics of a Vertical Axis Wind Turbine'
By Gareth Colley, Department of Engineering & Technology, University of Huddersfield, UK

geometric interactions at close proximity. As per Figure 4-17 the pressure is negative at all positions investigated and governs the main direction of flow through the machine. Given the significant variation in pressure curves for $\lambda = 0$ and $\lambda = 0.4$ it is expected that the main jet flow of air through the machine will have different characteristics, these predictions are investigated in a study of the velocity fields generated over the wind turbine as provided in the following section.

4.2.4 Summary

The key conclusions from this pressure field study are summarised in the following:

- The wind turbine pressure field generated in the stream wise and normal to stream wise planes through the central axis of the turbine are seen to be highly symmetric about the mid-plane of the machine in the vertical direction. Such trends are consistent for both static and rotational rotor conditions.
- The pressure field generated at the mid-plane of the machine in the XY view indicates highly asymmetric pressures which are largely dependent on both angular and radial position within the turbine. Such trends are indicative of specific energy transfer zones within the turbine which have been highlighted to be passages S2, S1, S12 and S11 along with corresponding rotor passages of R2, R1, R12 and R11.
- The vertex averaged pressure computed mid stator passage at a radius of 0.8m is seen to vary significantly as a function of rotor blade position at these major energy transfer zones. Hence it is predicted that the torque contribution of these blades will be particularly sensitive to a change in blade position.
- Additional trends are noticed on the leeward side of the machine where variations in pressure are observed as a result of interactions between the leeward rotor blades R6 and R7 and the stream wise flow. Such effects are expected to result in primary inefficiencies given counter-rotating torques reported in literature for similar reaction machines.

- The use of multi-blade geometry significantly influences energy transfer regions within the rotor in which highest pressures are generated between 0° - 90° on the windward side of the machine. Further, effect of multi-blade geometry on the nature of the pressure profile is apparent when observing a reduction in pressure fluctuation in the core of the machine where geometric influences are reduced.
- The effect of rotor speed on pressure distribution about the machine varies depending on proximity to the rotor blade and in the core of the machine highlights a change in flow direction. Further, most notable effects are observed on the leeward side of the turbine indicative of strong downstream rotor interaction effects.

4.3 Numerical Velocity Field Analysis

The following section evaluates the velocity fields generated across the wind turbine during static and rotational modes of operation with a view to providing new information about this machine and to verify some of the predictions made during pressure field studies. The velocity field is studied in vertical, angular and radial directions and uses the same convention as described previously. This velocity field is presented in non-dimensional form of V/V_{AVG} where V_{AVG} is taken as the free-stream area weighted average at the velocity inlet boundary and is 4m/s throughout. The operating conditions correspond to those used in the previous pressure field analysis in that tip speed ratios of $\lambda=0$ and 0.4 are studied.

4.3.1 Variation of Velocity Field in Vertical Direction

The velocity field variation in the vertical direction or Z axis is presented in the following. The planes of interrogation correspond to cross sections in the ZY and ZX planes and intersect the central axis of the wind turbine. These planes are orientated in both stream wise and normal to stream wise directions and hence provide detailed flow field data within both stator and rotor blade passages. The velocity fields generated over the stream wise plane of interrogation show good agreement with pressure data in that a large degree of symmetry is observed about the mid-plane of the wind turbine. The influences of both stator and rotor blade geometry are noticed where velocity drops to zero at the wall boundaries. The reductions in local pressure at positions A and B are a result of flow accelerations of relatively large magnitude over the windward stator supports rings. In this region magnitudes of velocity for $\lambda=0$ are 1.37 at both positions which is 27% higher than the free-stream flow. At $\lambda=0.4$ the velocity field shows strong similarities in terms of the overall flow characteristics. Velocity magnitude at positions A and B is 1.4 which is an increase of 2.1% when compared to the static rotor. Such characteristics are further indications of a rotor induction effect upstream of the stator. The velocity field generated over a plane normal to the stream wise shows variations in flow structure although still maintains a highly symmetric flow. In both rotor conditions an extensive low velocity region is present at opposite extremes of the machine. This indicates that in these particular blade passages a low velocity exists which is potentially due to blockages as a result of the high solidity ratio employed. The effects of a rotating rotor are much more pronounced in the core of the machine where the region of low velocity extends into the

central core of the rotor. This is indicative of a change in flow direction which points towards rotational effects and variations as it exits the windward blade passages.

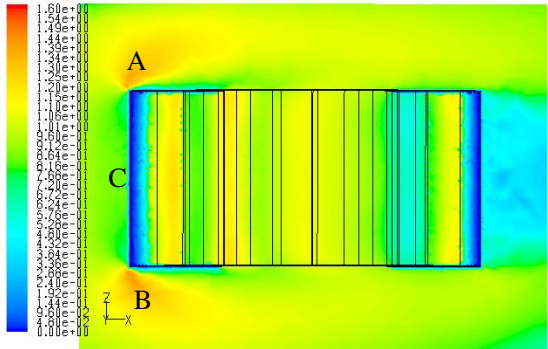


Figure 4-19 Stream wise plot of V/V_{AVG} at $\lambda=0$ for $V_{\infty}=4\text{m/s}$ in ZX plane

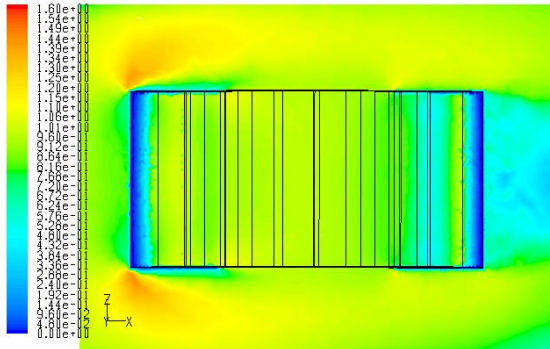


Figure 4-20 Stream wise plot of V/V_{AVG} at $\lambda=0.4$ for $V_{\infty}=4\text{m/s}$ in ZX plane

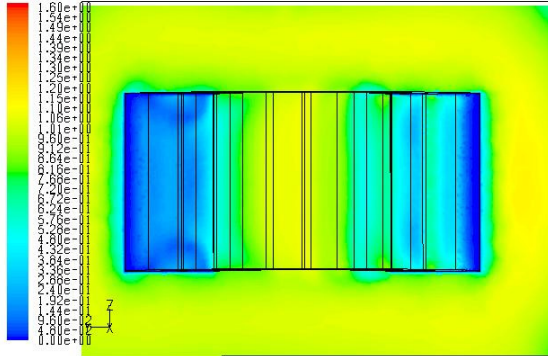


Figure 4-21 Normal to stream wise plot of V/V_{AVG} at $\lambda=0$ for $V_{\infty}=4\text{m/s}$ in ZY plane

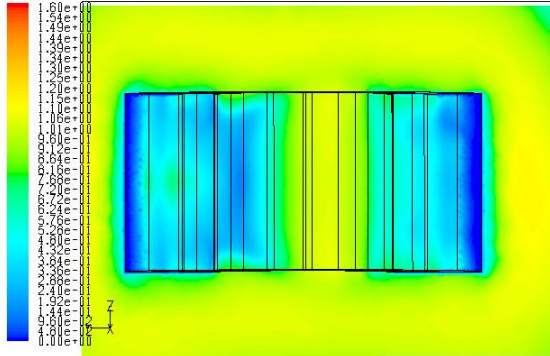


Figure 4-22 Normal to stream wise plot of V/V_{AVG} at $\lambda=0.4$ for $V_{\infty}=4\text{m/s}$ in ZY plane

To understand the nature of flow within the central core of the wind turbine in more detail a plot of velocity vectors is presented at the turbine mid-plane as shown below in the XY view. The magnitude of velocity governed by the length of the arrow along with its direction shows how the pressure field governs the direction of flow across the blades and through the core of the machine. The influence of the rotor under rotational conditions is apparent due to the change in flow structures within the core of the machine. In both static and rotational conditions a main jet of air can be seen as it enters the windward stator passages and passes through the rotor assembly. At an operating condition of $\lambda = 0.4$ the direction of this jet of air is seen to shift in the clockwise direction as per Figure 4-24 and further validates the conclusions drawn previously.

This directional shift results in the development of a low velocity region in the central core of the machine which has similar characteristics to those described in [60]. In both rotor operating conditions the cross-flow of air passing through the machine interacts with the leeward side rotor blades as it exits the assembly. Such interaction effects require further investigation given the

significant inefficiencies generated due to counter rotating torque as reported with the vertical axis fixed blade format [33], [35], [36], [53], [55], [57].

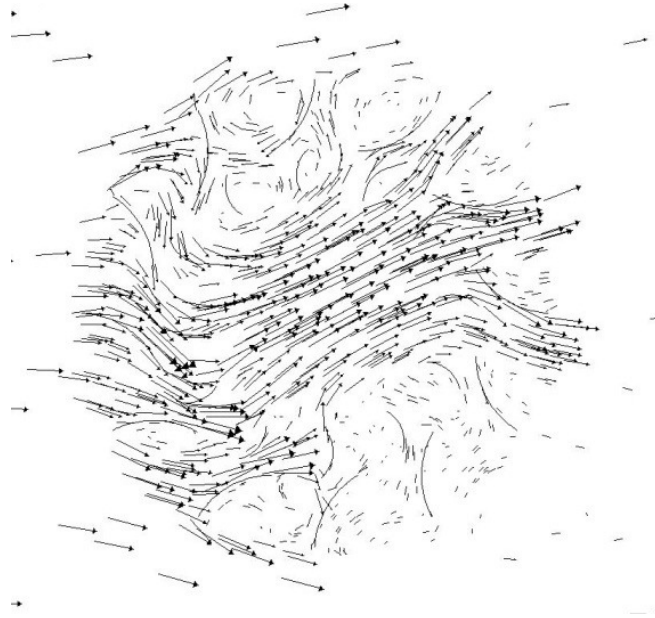


Figure 4-23 Velocity vector field at turbine mid-plane for $\lambda=0$

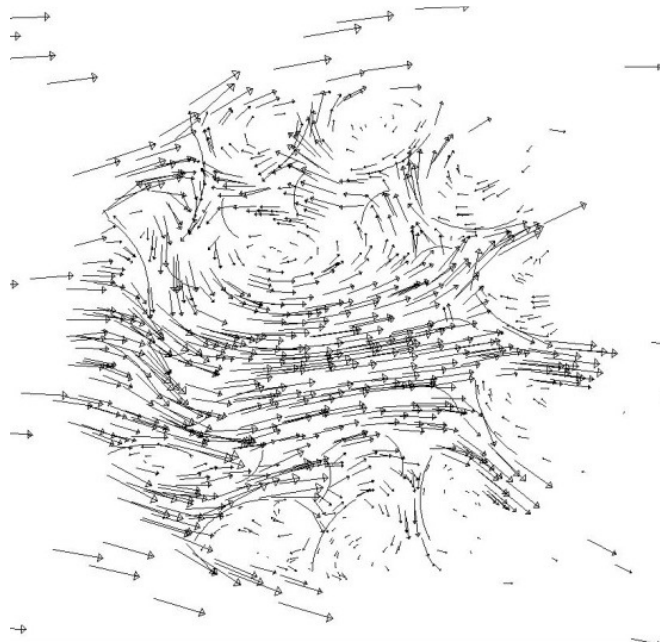


Figure 4-24 Velocity vector field at turbine mid-plane for $\lambda=0.4$

4.3.2 Variation of Velocity Field with Blade Position

This analysis considers effects associated to rotor blade position and follows the convention used for the pressure field analysis. Rotor blade positions are defined relative to the 30° cycle and rotated from 0° to 20° in steps of 10° at which the non-dimensional velocity field is computed at each. The velocity contours shown in the following are obtained at the mid-plane of the turbine which corresponds to $Z = 0.5\text{m}$. From the figures provided in the following the main characteristics of the transient velocity field can be seen.

The plots of velocity field over the wind turbine show interesting characteristics of the flow path through the machine and also provide good agreement with pressure field analysis carried out previously. As expected the velocity characteristics within the wind turbine are relatively complex given the large pressure gradients generated within areas of energy transfer. The flow restrictions as a result of blades with high angles of attack are noticed which agree with the passages described.

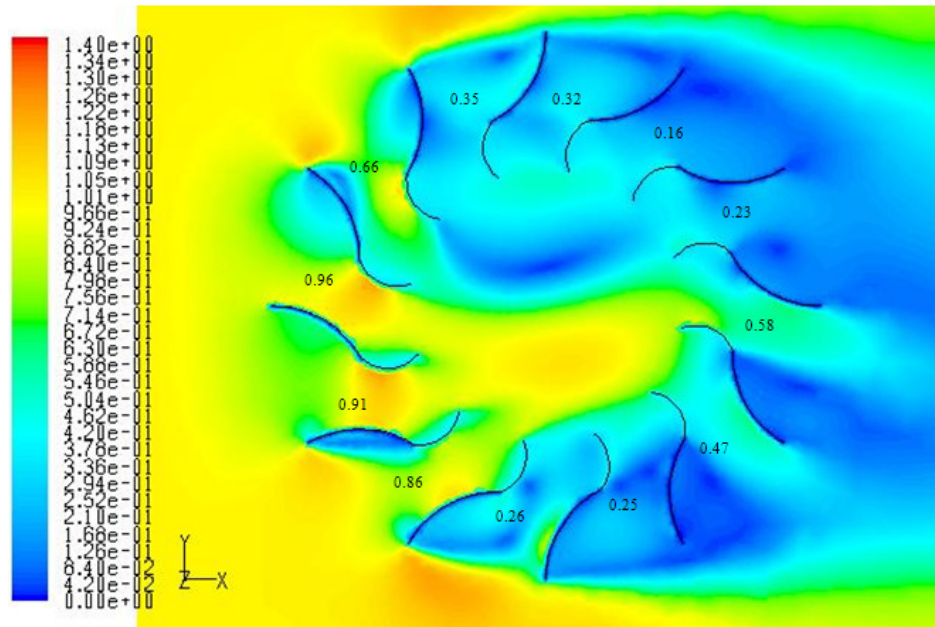


Figure 4-25 Plot of V/V_{AVG} at rotor blade position of 0° for $\lambda=0.4$ and $V_\infty=4\text{m/s}$ at mid-plane

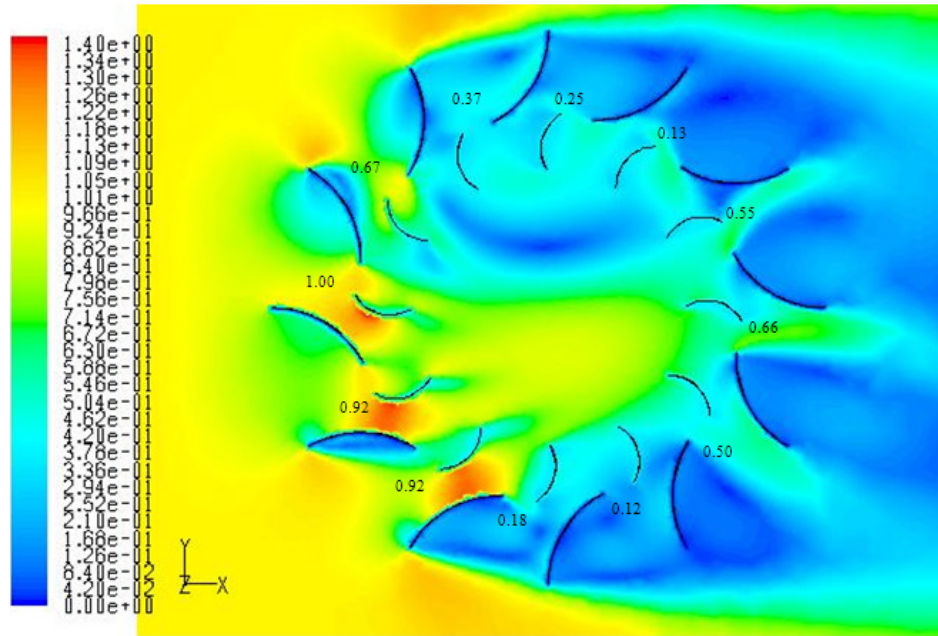


Figure 4-26 Plot of V/V_{AVG} at rotor blade position of 10° for $\lambda=0.4$ and $V_\infty=4\text{m/s}$ at mid-plane

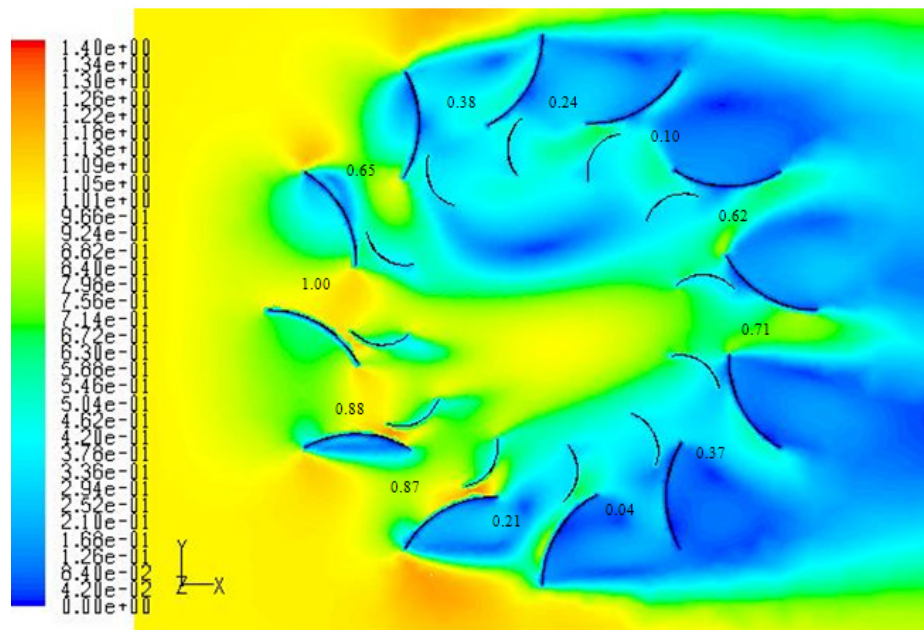


Figure 4-27 Plot of V/V_{AVG} at rotor blade position of 20° for $\lambda=0.4$ and $V_\infty=4\text{m/s}$ at mid-plane

The effect of rotor blade position highlights subtle changes to the flow field generated and based on previous conclusions results in significant changes at the zones where high energy transfer is present namely S1, S2, S12 and S11. The velocities at centre stator passage for a radius of 0.8 at blade position of 0° are 0.66, 0.96, 0.91 and 0.86 respectively. When the rotor blade rotates to 10°

the velocity magnitudes are 0.67, 1.00, 0.92 and 0.92. The relative insensitivity of blade passage S2 to a change in rotor position is again noticed. At a blade position of 20° velocity magnitudes of 0.65, 1.00, 0.88 and 0.87 are generated. To quantify such relative variations mean velocity is computed over the range of blade positions and percentage variations provided relative to the mean velocity.

Blade Passage	Mean Velocity	% Variation at 0°	% Variation at 10°	% Variation at 20°
S2	0.66	0	1.5	-1.5
S1	0.99	-2.7	1.35	1.35
S12	0.92	4.35	0	-4.35
S11	0.88	-2.64	4.15	-1.51

Table 11 Stator blade passage centre velocity variation

The variation in velocity magnitude at these critical locations is inconsistent with no clear trends present. Hence such changes in velocity as a function of blade position require further quantification from analysis of contribution of blade torque as provided in Chapter 6.

4.3.3 Variation of Velocity Field in Angular Direction

The variation of the local velocity field in the angular direction (θ) is an important performance related parameter given the strong asymmetry about the central axis of cross-flow machines [60], [62], [67]. Understanding this variation will support conclusions drawn on the primary energy transfer zones within this machine which to this point has not been investigated. The velocity computed in the following study is again presented in non-dimensional form and plotted with angular position about the machine as per the previous pressure field analysis. The velocity is computed at five different radii that correspond to $R = 1, 0.8, 0.6, 0.4$ and 0.2m respectively. The velocity is plotted at each of these radii for two different rotor conditions corresponding to $\lambda = 0$ and $\lambda = 0.4$. Such conditions are chosen with a view to identifying major differences between static and dynamic operating conditions which to date is not well documented. This velocity field is presented at the wind turbine mid-plane which corresponds to $Z = 0.5\text{m}$ given the large uniformity in vertical velocity described previously.

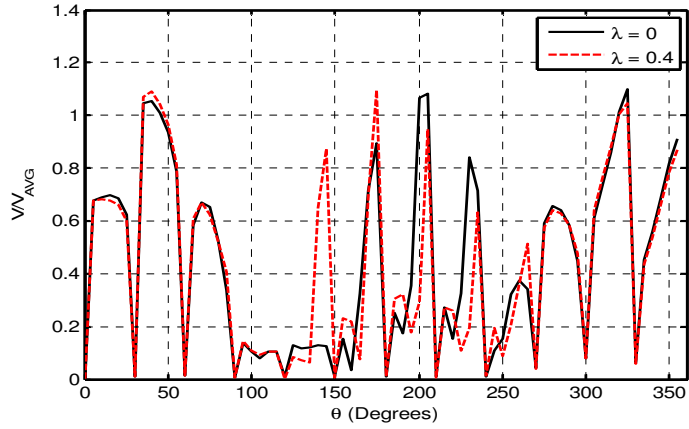


Figure 4-28 V/V_{AVG} plotted with θ at $R = 1\text{m}$ for $\lambda = 0$ and 0.4

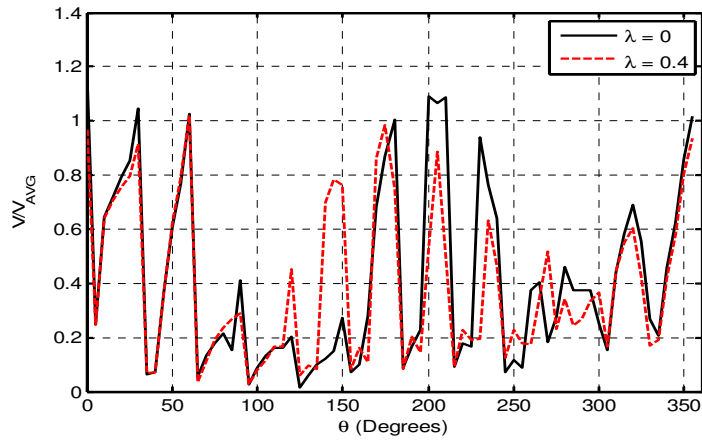


Figure 4-29 V/V_{AVG} plotted with θ at $R = 0.8\text{m}$ for $\lambda = 0$ and 0.4

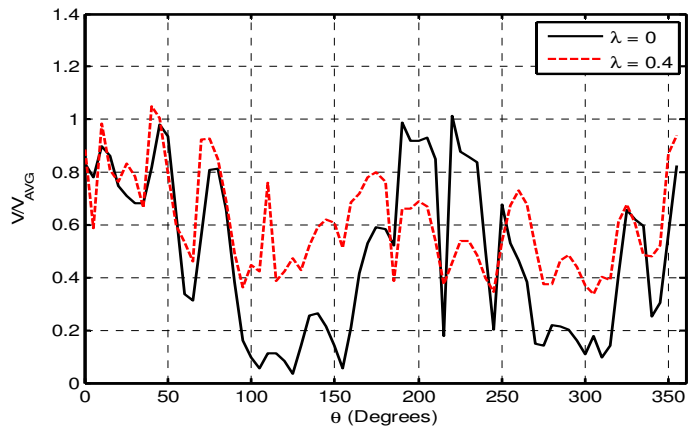


Figure 4-30 V/V_{AVG} plotted with θ at $R = 0.6\text{m}$ for $\lambda = 0$ and 0.4

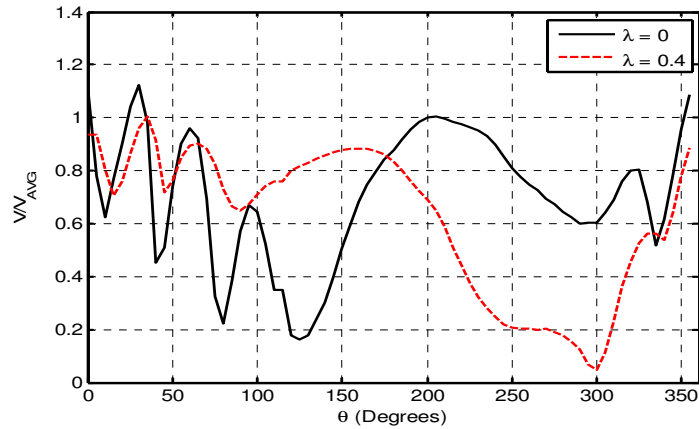


Figure 4-31 V/V_{AVG} plotted with θ at $R = 0.4m$ for $\lambda = 0$ and 0.4

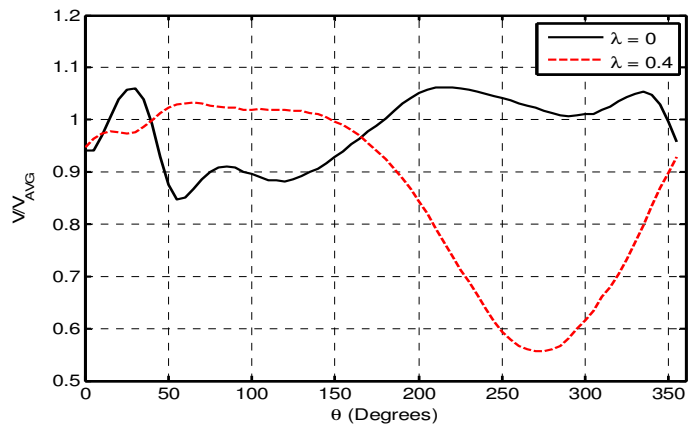


Figure 4-32 V/V_{AVG} plotted with θ at $R = 0.2m$ for $\lambda = 0$ and 0.4

4.3.3.1 Angular velocity variation at $R = 1m$

Figure 4-28 shows the variation of velocity as a function of angular position at a radius of $R = 1m$. This radius corresponds to the stator outer tip radius and hence is located on the outer diameter of the machine. Initial observations include the similarities in velocity for both rotor operating conditions with the exception of the region between 120° and 150° . The most notable observation is the significant variation in velocity magnitude over each 30° blade passage. It can be seen that every 30° the velocity drops to zero which is due to the presence of the blade tip and hence no-slip wall condition. One common trend is the peak velocity that occurs generally at the centre of each blade passage where effects of rotor geometry are reduced. Further observations include velocities

that exceed the free-stream flow speed, which indicates local flow accelerations through the diverging blade passageways. Peak flow velocities in such regions are in the order of 1.1 and are generated on both windward and leeward sides of the wind turbine. Such phenomena can be observed on the contours of pressure and velocity fields which provide foundation to this statement. A generic trend that can be observed from this plot is the relative low velocity regions present between angular positions of $90^\circ - 160^\circ$ and $240^\circ - 270^\circ$. This is due to the orientation of the blades relative to the free-stream flow which results in the associated blade passage being shielded from the main flow. This observation is further re-enforced by the plot of velocity magnitude contours, which highlights this phenomena in detail.

4.3.3.2 Angular velocity variation at $R = 0.8m$

The angular variation of velocity at a radius of $R = 0.8m$ depicted in Figure 4-29 shows similar trends. The magnitudes of velocity are of a similar order and the presence of blade geometry is evident where velocity tends towards zero. Individual blade passage characteristics are again identifiable in-between the surrounding blade geometry where velocities generally peak within the centre where wall effects are minimized. The region of low velocity is again present over the same range although slight variations in magnitude are observed when compared to the previous radial position. The effect of rotor speed has limited effect on the velocity magnitude overall although at 145° a significant increase in velocity is seen for $\lambda = 0.4$ which is highlighted in the plot of velocity vectors in which an increase in mass flow is noticed through this region.

4.3.3.3 Angular velocity variation at $R = 0.6m$

Velocity variations computed at a radius of $R = 0.6m$ presented in Figure 4-30 show considerable differences when compared to the previous radial positions. This profile is plotted inside the rotor blade passage regions and hence gives an insight to the characteristics of the flow as it enters and exits the rotor. One interesting observation is the large variation in velocity magnitude between both operational conditions. It is noticed that on the windward side of the machine at angular positions of $320^\circ - 90^\circ$ the velocity magnitude shows minimal variation between each operating condition which points to small upstream interaction effects. Interestingly between this angular

position range the variations in velocity magnitude are considerably lower for $\lambda = 0.4$ when compared to the static rotor. This results in much higher velocities over angular positions of $90^\circ - 160^\circ$ and $240^\circ - 270^\circ$

4.3.3.4 Angular velocity variation at R = 0.4m

At a radial position of $R = 0.4\text{m}$ within the core of the machine a much less complex velocity profile is observed for both rotor operating conditions as shown in Figure 4-31. The only similarities present in this profile are between angular positions of 330° and 100° , which correspond to the windward side of the machine. The region on the leeward side of the machine shows some interesting features in terms of the velocity gradients present. The overall velocity variation at both operating conditions shows a much smoother transition in which velocity rises and falls steadily. At $\lambda = 0$ this increase in velocity begins at 100° and peaks at 160° . Beyond this point a steady reduction in velocity magnitude is observed up to 300° . A similar trend is observed for $\lambda = 0.4$ at which velocity increases at 125° to a peak at 200° at which it reduces steadily to 300° . Beyond this point the velocity computed for both conditions increases significantly over a small distance.

4.3.3.5 Angular velocity variation at R = 0.2m

At a radial position of $R=0.2\text{m}$ in the centre of the machine the velocity profiles obtained show the smoothest curves when compared to previous analysis. This is to be expected given the trends highlighted during pressure field analysis and the large proximity from rotor blade geometries. From Figure 4-32 one notable observation is at $\lambda = 0$ where the velocity is consistently high around the machine. Here a minimum velocity of 0.85 is present at 55° . Beyond this point velocity increases above free-stream where small variations in magnitude are observed. Opposing trends are seen for dynamic rotor conditions in that velocity between $0^\circ - 150^\circ$ remains fairly constant with a magnitude close to free-stream. Beyond this angular position a considerable reduction in velocity magnitude is observed in which a minimum velocity of 0.57 is predicted at 275° . Between $275^\circ - 360^\circ$ velocity increases at a high rate where velocity magnitude recovers close to that observed for $\lambda = 0$.

4.3.4 Summary

A summary of the key conclusions from the velocity field analysis is provided in the following:

- The velocity field in the vertical direction within the wind turbine studied at stream wise and normal to stream wise planes of interrogation shows strong symmetry about the mid plane and agrees well with pressure data obtained.
- Effect of rotor blade position again highlights variation in velocity at critical energy transfer zones although are inconsistent. Additionally, rotor blade position is seen to influence local leeward rotor blade velocity field at R6 and R7 again as a result of interaction effects.
- Analysis of wind turbine velocity field at the mid-plane highlights significant asymmetry about the central axis of the machine which is a result of non-symmetrical multi-blade geometry. The effect of rotor speed on the local velocity field shows varying influence dependent on radial position within the machine. Most pronounced effects are observed over a radial range of 0.6m - 0m where rotor blade wall effects are most prominent.
- Further, the effect of rotor operating condition is seen to have considerable effect on the direction of the main flow through the machine. It is noticed that the direction of jet at $\lambda=0$ is clearly influenced by the orientation of the windward static rotor blades. This orientation re-directs the free-stream flow in an anti clockwise shift as it exits the stationary rotor assembly. At $\lambda=0.4$ main jet flow direction re-aligns with the dominant stream wise flow direction resulting in a shift in the main energy transfer zone as identified from the development of a central vortex.

CHAPTER 5

FLOW DISTRIBUTION AND ASYMMETRY ANALYSIS

Scope

As reported in Chapter 4, the flow fields generated across this cross-flow wind turbine are highly asymmetric about the central axis of the machine. This results in a unique flow distribution through the machine and is seen to vary depending on the rotational condition of the rotor assembly. Such distributions give rise to primary energy transfer regions within the machine which are expected to contribute significantly to overall performance. At present this characteristic is not well documented for this format of wind turbine and given the relation with energy transfer is a critical performance related parameter. The aim of this chapter is to investigate the flow distributions across the wind turbine using the full-scale MRF three-dimensional CFD model. Here, the mass flux distribution about the central axis of the machine has been computed for a range of operating points that correspond to the design condition and those that could be experienced at diverse installation locations. From this analysis the major flow paths through both stationary and rotating zones are quantified and their relation with blade torque generation described. Additionally, in order to quantify energy capture of this wind turbine a new performance based parameter is defined in the form of asymmetry ratio. This ratio relates both pressure and velocity field variation about a plane of symmetry normal to the stream wise direction such that energy capture of individual blade passages can be computed. In addition to this, the downstream effects of the wind turbine are evaluated with a view to determining optimum location of multiple wind turbine arrays.

5.1 Mass Flow Distribution

The following study is dedicated to evaluating the mass flow distribution across both stator and rotor blade passages within this cross-flow wind turbine. This study considers three-dimensional effects and uses the full scale MRF CFD model to predict the flow rates for various operating points. This parameter is computed at the inlet and outlet of each blade passage within the turbine and hence shows the balance of mass flow as a function of angular position and hence blade passage number. This study is presented in two sections; the first is concerned with the mass flow variation in the stator blades whereas the second section presents data computed within the rotor blade passages. Within each of these studies the effect of tip speed ratio and free-stream velocity is considered such that any significant variations can be identified which may result in a change in performance. The mass flow rate is presented in the form of efflux which corresponds to mass exiting the wind turbine radially outwards through the associated boundaries. This convention is used throughout and is taken directly from the CFD solver. Hence for negative efflux this indicates the flow direction being radially inward toward the central axis of the rotor. The zone definition used in this study conforms to that previously described in Figure 4-3 which allows for identification of specific blade passages within this multi-blade machine.

5.1.1 Effect of λ and V_∞ on stator passage mass efflux

The following figures depict the mass flow across the wind turbine stator blade passages over a range of λ such that rotational induced flow effects can be evaluated. For completeness this effect is considered over a range of flow speeds such that 'design' and 'off-design' variations can be identified.

In Figure 5-1, stator mass flow is presented for $V_\infty = 4\text{m/s}$ as per the design condition described in Chapter 3. The flow distribution about the central axis of the wind turbine is clear in which a large amount of symmetry is noticed between stator blade passage 6 and 7. This roughly conforms to the stream wise flow direction through the central axis of the rotor and is indicative of the main jet of air passing through the machine. Hence the stator passage flow rate is seen to be extremely sensitive to proximity to this centre line. Notable features include the low flow rates in passages 3, 4, 9 and 10 which is a result of the orientation of the windward stator blades relative to the stream-wise flow and the resulting shielding effects as reported in Chapter 4. It is therefore clear that such

blade passages are relatively ineffectual for increasing energy capture of the machine for this particular flow condition. This will therefore also limit the generation capabilities of the corresponding rotor blade which receives flow from the exit of the stator passage. Maximum flow rates are therefore observed at passages on the windward and leeward side of the machine which do not deviate far from the centre line. These stator passages are 1, 12, 6 and 7 and feature varied characteristics dependent on the rotor speed condition. It is noticed and confirms some of the predictions made in Chapter 4 that largest variations in flow are generated downstream of the rotor. This is most apparent in blade passage 6 where flow rate is seen to reduce with an increase in rotor speed and results in maximum and minimum flow rates of 1.22 and 0.6 respectively. This trend is however inconsistent as when considering passage 8 the inverse is noticed in that flow rate reduces with a reduction in tip-speed ratio which points towards local flow accelerations in this zone. The opposite is present on the windward side of the turbine where this effect is relatively small. Flow rates in windward passages 1, 2, 11 and 12 are largely unaffected by this change which is also highlighted in the contours of pressure and velocity in Chapter 4. Such weak interaction effects upstream of the rotor are a result of limitations of the MRF model along with the relatively large distance between the stator inlet and rotor tip and hence minimization of rotor induced effects

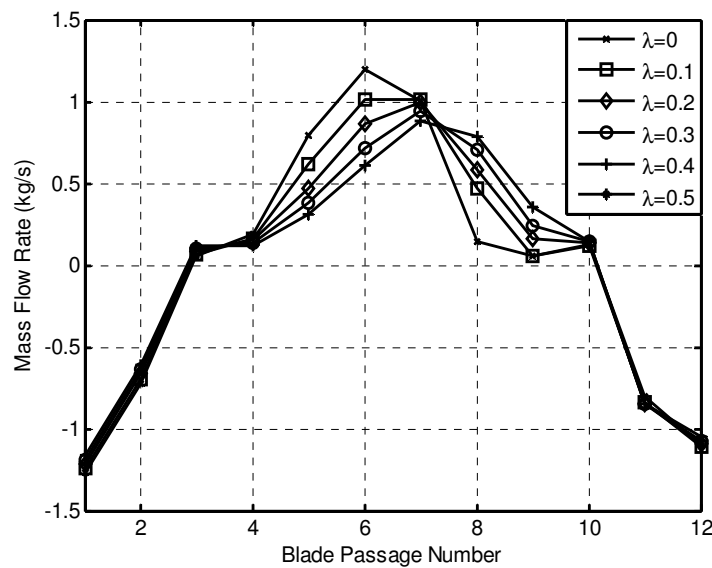


Figure 5-1 Mass flow rate (kg/s) plotted with stator blade passage number at $V_\infty = 4\text{m/s}$ for $\lambda = 0 - 0.5$

The flow distribution at a wind speed of 6m/s is presented in Figure 5-2 and hence operational behaviour away from the design condition is studied. The overall flow distribution is seen to be

almost identical to that observed previously in that a large degree of symmetry between blade passage 6 and 7 is generated. As expected the overall magnitudes of flow are increased at each location across the machine although the primary features of this distribution remain constant. Blade passages 5, 6 and 7 show increases in mass flow when λ is increased where as passages 8 and 9 again show the opposing trend. The maximum flow rate through the machine is again present at blade passage 6 for the static rotor. The magnitude of flow rate is in the order of 1.75 which is a 43% increase when compared to the previous free-stream velocity studied. Given the strong similarities in the flow distribution it is expected that the general torque and power curve characteristics will have strong similarities to that observed at 4m/s with the exception of increased overall magnitude.

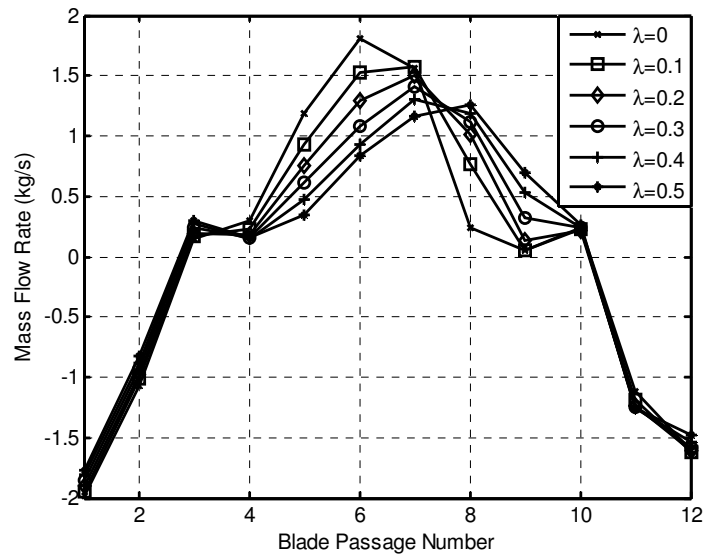


Figure 5-2 Mass flow rate (kg/s) plotted with stator blade passage number at $V_\infty = 6\text{m/s}$ for $\lambda = 0 - 0.5$

In Figure 5-3 mass flow rate is computed at $V_\infty = 8\text{m/s}$ again within the stator blade passages. Again at increased flow speed the flow distribution about the wind turbine shows strong resemblance to the previous two speeds. Rotor induced effects on the downstream side of the machine are also consistent in which passage 6 shows the same trend. One exception is at blade passage 8 where at $\lambda = 0.1$ a large increase in flow rate is observed which is likely to be result of local flow phenomena occurring in this region.

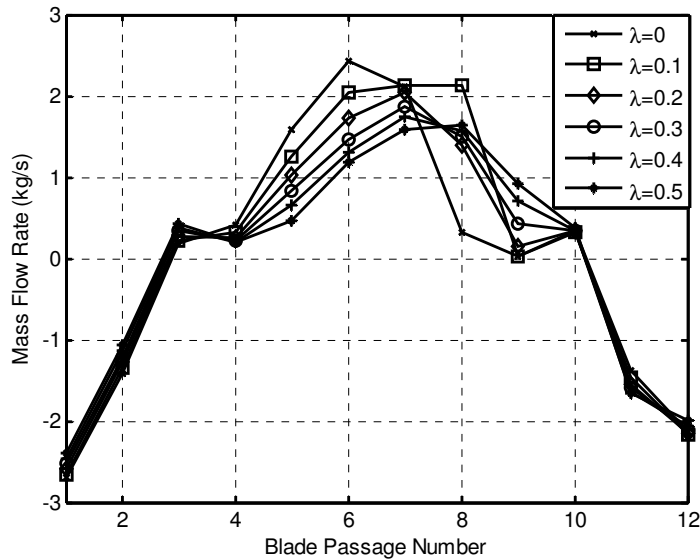


Figure 5-3 Mass flow rate (kg/s) plotted with stator blade passage number at $V_{\infty} = 8\text{m/s}$ for $\lambda = 0 - 0.5$

5.1.2 Effect of λ and V_{∞} on rotor passage mass efflux

In order to quantify the flow characteristics occurring within the rotating frame of reference the following analysis is carried out within the rotor blade passages. This analysis is carried out over the same range of flow conditions and again investigates the effect of rotor speed on the overall flow distribution across the machine. This flow distribution shows some similarity to those generated within the stator blade passage in which maximum flow is through the centre of the rotor with flow rate reducing significantly at passages 3 and 9. Such reductions are again due to the solidity ratio employed and more specifically the orientation of the upstream stator blades restricting flow to the rotor passage inlets. Hence it is expected the torque contribution of blades 3 and 9 is significantly reduced when compared to blades located on the windward side of the rotor. Rotor induced effects are again most prominent as the flow exits the rotor which is expected and at blade passages 5 and 6 increases with a reduction in rotor speed. This trend is identical to that observed in stator passages 5 and 6 although the magnitudes of flow show some variation. This variation is a result of both losses in the axial direction and the rotor blade inlet passage being offset to the exit of the stator and hence is not directly comparable. Peak flow rate is however of similar magnitude of 1.23 which is generated for a static rotor condition at passage 6.

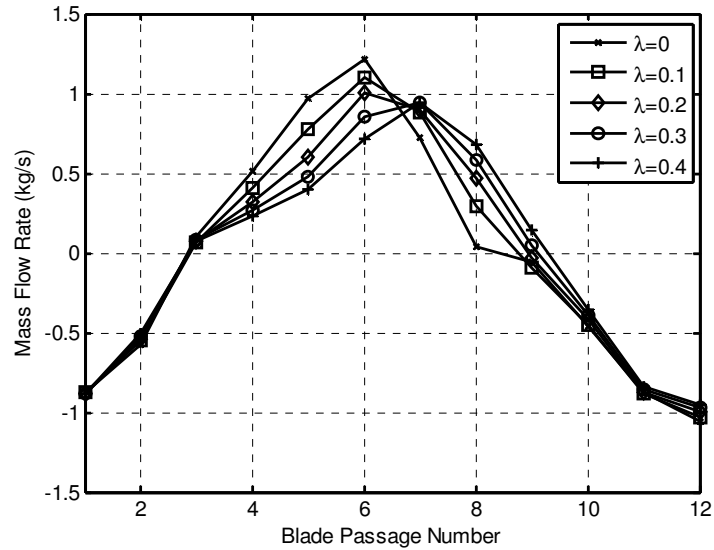


Figure 5-4 Mass flow (kg/s) plotted with rotor blade passage number at $V_\infty = 4\text{m/s}$ for $\lambda = 0 - 0.4$

Figure 5-5 and Figure 5-6 show the mass flow rate distribution at flow speeds of 6m/s and 8m/s respectively. As observed throughout the effect of free-stream velocity has little effect on the flow distribution around the wind turbine and hence at off-design conditions a large degree of similarity is noticed. Such trends are again indicative that performance characteristics are relatively consistent over this range which may result in this machine being able to operate at a range of installation sites. This statement is investigated further in the following chapter where the performance characteristics of the machine are quantified over a similar operational range. One of the most consistent trends present throughout this study is again the low flow rate regions within passages 3 and 9 which are expected to result in significant inefficiencies due to blockages. The effect of this high solidity ratio on torque generation capabilities of the cross-flow format is not well documented and hence is evaluated further in this thesis.

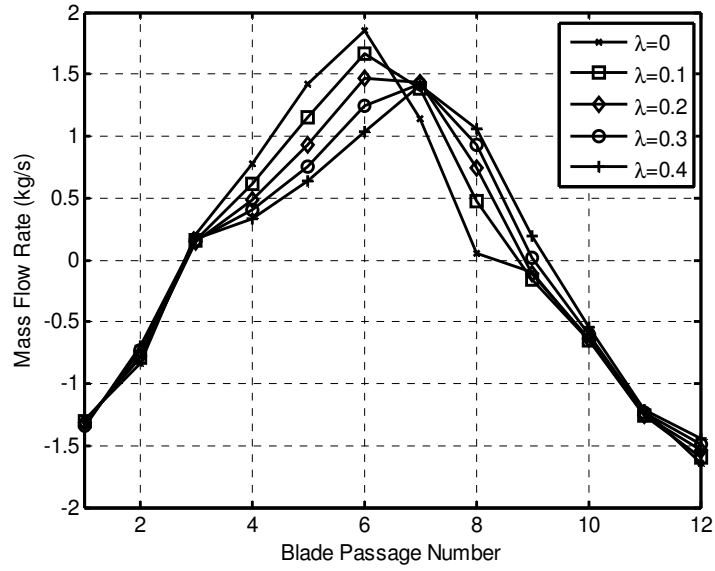


Figure 5-5 Mass flow (kg/s) plotted with rotor blade passage number at $V_{\infty} = 6\text{m/s}$ for $\lambda = 0 - 0.4$

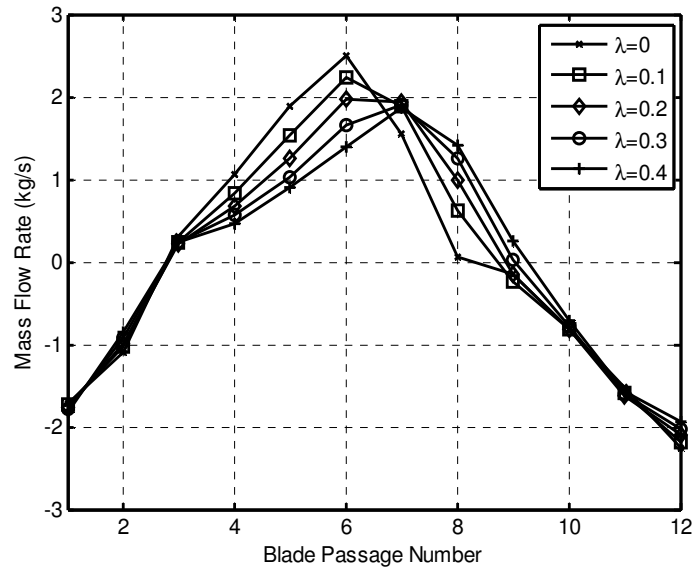


Figure 5-6 Mass flow (kg/s) plotted with rotor blade passage number at $V_{\infty} = 8\text{m/s}$ for $\lambda = 0 - 0.4$

5.1.3 Summary

A summary of the main findings from this analysis is provided in the following:

- The overall mass flow rate distribution shows a large degree of symmetry about the centre line of the wind turbine and is consistent for both stator and rotor passages at all conditions of λ and V_∞ .
- Maximum mass flow is observed through the centre of machine for both stator and rotor passages where minimum mass flow is present at blade passages close to normal to the stream wise flow direction namely 3, 4, 8 and 9. This characteristic is due to blade angle relative to the flow direction and the resulting blade shielding effects.
- Effect of λ is most prominent on the leeward side of the turbine due to interaction effects between free-stream flow and windward rotor blade set. The effects on performance are evaluated further in this thesis.
- For stator analysis increases in mass flow are observed with a decrease in λ at passages 5, 6 and 7. Conversely, opposing trends are noticed at passages 8 and 9 where increasing λ results in an increase in mass flow. Both trends are consistent for all flow conditions tested
- For rotor passage analysis similar trends are observed where at passages 4, 5 and 6 an increase in mass flow is observed during an increase in λ . Conversely, at passages 7, 8 and 9 mass efflux decreases with a reduction in λ . As per stator analysis trends are consistent at all flow conditions tested.

5.2 Asymmetry Ratio

The highly asymmetric flow fields reported in Chapter 4 are an important characteristic of the cross-flow wind turbine and a result of the high solidity ratio employed. This analysis aims to quantify the energy capture of the wind turbine at specific angular positions within the machine to determine inefficiencies inherent within the design. This energy capture is quantified in the form of a new performance related parameter namely asymmetry ratio which is defined in the following sections. This asymmetry also allows for quantification of wake induced effects and the application of using multiple wind turbine arrays. Using this parameter accurate downstream distance can be computed for optimum location of additional cross-flow machines.

The first analysis carried out relates to the wind turbine only and is performed in order to quantify energy capture within the machine. To determine this asymmetry, flow field data is computed at the stator passage inlet faces which are located at $R=1.0m$. On the leeward side of the machine these are the stator outlet faces given the cross-flow nature of the machine. This therefore provides the resultant energy capture of the complete wind turbine. This flow field data is taken in the form of an area weighted average over each of the associated blade passage faces for a flow speed of $4m/s$. The nature of asymmetry is studied about a principle axis which intersects the stream wise flow direction through the central axis of the machine. This principle axis is therefore normal to the stream wise direction and allows for computation of energy capture in the stream wise direction (Figure 4-3). This relation is given by:

$$\psi_N = \frac{\text{Windward Passage}}{\text{Leeward Passage}} \tag{5-1}$$

Using the above parameter rotational induced effects are evaluated which provides a direct relation between energy capture and rotor speed. Given the complexity of the flow fields reported for this type of machine, understanding this phenomena will overcome some of the limitations identified during the literature review and highlight inefficiencies within the design.

5.2.1 Pressure Field Asymmetry Ratio

The pressure field asymmetry ratio is presented in Figure 5-7 and depicts the variation in pressure about a line of symmetry normal to the stream wise direction. The resultant variations in pressure coefficient are noticed and are seen to vary depending on angular position/stator passage location. For a symmetric pressure field about this line of interrogation asymmetry is equal to 1. This is represented by a dashed red line for reference in the figure. For clarity the centre line of the wind turbine in the stream wise direction through the central axis is also shown as a vertical dashed red line.

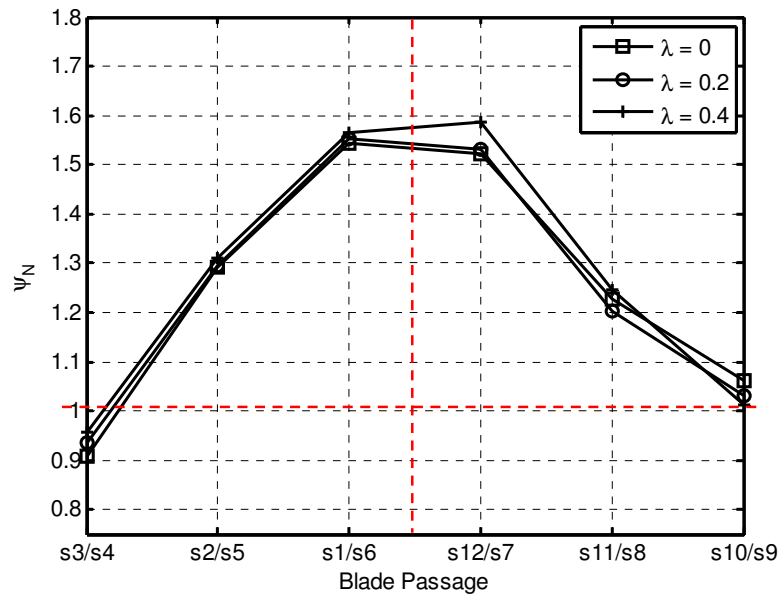


Figure 5-7 Normal to stream-wise stator passage pressure asymmetry ratio at V_∞ of 4m/s

Here, ψ_N is at its maximum across blade passages s1/s6 and s12/s7 which indicates a large reduction in pressure from the windward side of the machine to the leeward side of the machine. The maximum asymmetry ratio in this profile is generated at s12/s7 for $\lambda=0.4$ and is in the order 1.59. As identified in some of the previous analysis, the greater the distance from the wind turbine centre line a larger reduction in mass flow rate is noticed. This is also clearly identified from this plot of asymmetry ratio where at s3/s4 and s10/s9 asymmetry ratio is close to 1 hence limited pressure drop over these zones. Throughout the effect of rotor speed or λ on this distribution is limited with the exception of s12/s7. Therefore the downstream flow field of the wind turbine is

expected to be relatively consistent for a wide range of rotor speeds which agrees well with the pressure field data provided in Chapter 4.

5.2.1 Velocity Field Asymmetry Ratio

The following figure depicts the velocity asymmetry ratio normal to the stream wise flow direction and again signifies the energy capture of specific wind turbine passages as a function of λ . As per previous velocity field analysis the area-weighted average velocity is computed over the stator blade passage inlet face and is used to calculate asymmetry ratio about this plane.

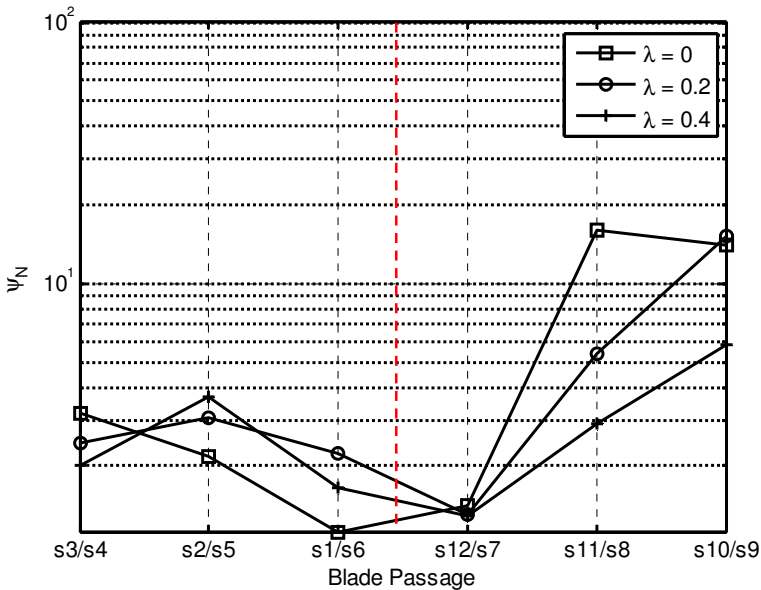


Figure 5-8 Normal to stream-wise stator passage velocity asymmetry ratio at V_∞ of 4m/s

In the above figure, velocity asymmetry ratio highlights the region within the wind turbine at which largest velocity drop occurs. It is seen that the magnitude of asymmetry is consistently above 1 at all stator locations which signifies a reduction in stream wise velocity across the wind turbine. The region in which maximum velocity variation is noticed corresponds to the bottom side of the machine (from plan view) between passages s11/s8 and s10.s9. The effect of rotor speed on this profile is more complex when compared to the pressure profile observed previously. A maximum asymmetry ratio of 15.9 is generated under static rotor conditions between s11/s8 which is indicative of highest energy capture in this direction across the machine. At this location the

magnitude of asymmetry reduces with an increase in rotor speed with values of 5.4 and 2.9 generated respectively. This location is seen to be the most sensitive to the rotor condition when compared to other zones within the machine. Further high magnitudes of asymmetry are generated between s_{10}/s_9 which indicates large velocity reductions and hence energy capture at the bottom side of the wind turbine.

Using this asymmetry ratio allows downstream effects to be quantified relative to the flow conditions experienced on the windward side of the machine. This relation can be extended such that wake induced effects can be quantified relative to a specific flow condition upstream of the wind turbine. This can therefore be used to identify downstream locations where favourable flow conditions exist with a view to installing multiple cross-flow wind turbines for similar power generation. At present these downstream effects are widely unknown and hence the following analysis provides novel information about the use of such high solidity turbines on the downstream velocity profile. To compute this velocity profile a reference velocity is required on the windward side of the turbine. Given the geometric induced effects of the upstream stator blades this reference velocity is taken away from the wind turbine at the velocity inlet boundary and hence is 4m/s. To calculate an asymmetry ratio across the wind turbine the downstream zone of interrogation is varied and incrementally increased away from the stator blade passage in steps of 1m. This downstream velocity is computed for $\lambda=0.4$ which is an expected operational condition for this machine. The downstream distance away from the stator passage is defined from the outer stator blade tip ($R=1m$) and is plotted in non-dimensional form of x/D where 'x' is downstream distance (m) and 'D' is outer wind turbine diameter (m) which is 2.0m. When considering the operation of multiple wind turbine arrays, in order to generate similar levels of performance the downstream machine should be located at a position where asymmetry is approaching 1.

Figure 5-9 depicts this velocity profile downstream of the wind turbine as a function of x/D . The magnitude of asymmetry ratio relative to the free-stream flow condition is relatively high close to the stator blade tip in which a value of 3.47 is observed. Such high asymmetry and hence low local velocity is expected given the near wall effects close to the blade structure. Beyond this position a significant reduction in asymmetry is noticed over a range of $x/D = 5$. At this downstream position a magnitude of 1.15 is noticed which equates to a reduction of 67%. This is indicative of considerable increases in local velocity as a result of the increased distance away from the machine and the recovery of both pressure and velocity. Hence when considering operating multiple cross-flow machines a significant reduction in performance would be expected in this region. Beyond $x/D = 5$ the magnitude of asymmetry continues to reduce indicative of a close similarity to the free-

stream flow velocity. At $x/D = 10$ a value of 1.06 is generated which when compared to Ψ_N max a reduction of 69% is noticed. At this location the local velocity is in the order of 3.79 m/s and hence a percentage change of only 5% from the free-stream condition. Between $x/D = 10$ and 20 further reductions in asymmetry are present at which a maximum deviation from the free-stream flow condition is in the order 1.75% which is within expected tolerances of numerical error within the simulation. Hence to conclude it is expected that appreciable reduction in wind turbine performance will be noticed when installing a second machine within $x/D = 0$ and 5. Where possible a distance of $x/D > 10$ should be maintained although the practicality of this may not be possible for stream wise installation.

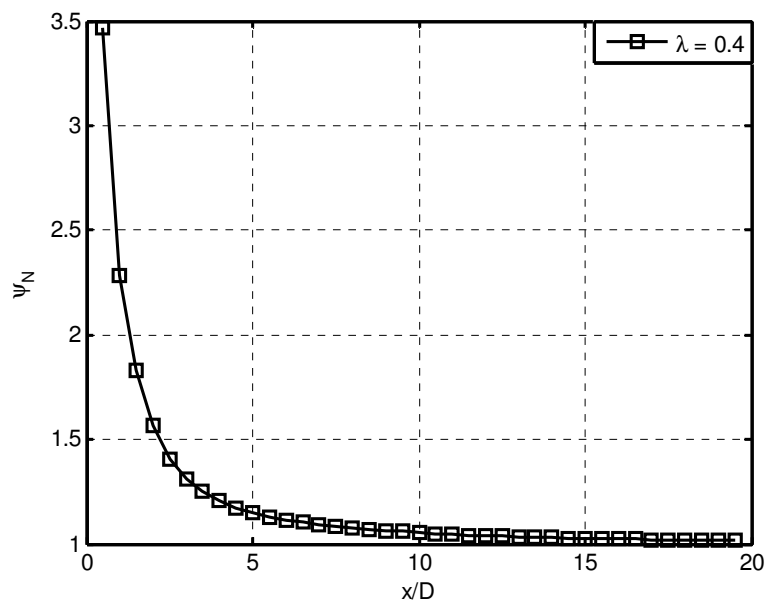


Figure 5-9 Velocity asymmetry ratio vs. x/D at $\lambda=0.4$ for $V_\infty=4\text{m/s}$

5.2.2 Summary

A summary of the key points from the analysis of wind turbine asymmetry are described below:

- It is seen that pressure asymmetry computed about a plane normal to stream wise is fairly symmetrical about the centre line of the wind turbine which confirms the central jet flow passing through the centre of the wind turbine.
- Further, maximum asymmetry is noticed at closest proximity to this centre line at locations s1/s6 and s12/s7 which indicates a large reduction in pressure from the

'Design, Operation and Diagnostics of a Vertical Axis Wind Turbine'
 By Gareth Colley, Department of Engineering & Technology, University of Huddersfield, UK

windward side of the machine to the leeward side of the machine. A maximum value of 1.59 is observed at s_{12}/s_7 for $\lambda=0.4$.

- The velocity asymmetry ratio is seen to be sensitive to a change in rotor speed and is of a more complex distribution compared to the pressure profile. Maximum velocity asymmetry is generated at s_{11}/s_8 for a static rotor and has a magnitude of 15.9 indicative of significant velocity reduction and energy capture at this location.
- Asymmetry ratio has been applied to the downstream velocity field to determine effect of this high solidity machine on the local velocity field. It has been reported that when plotting asymmetry as a function of downstream distance significant reductions in performance will be noticed when installing a secondary wind turbine between $x/D = 0$ and 5. Beyond $x/D = 10$ a maximum variation of 5% between the free-stream condition is observed and hence performance reductions are expected to be significantly less. For optimum location of a secondary machine $x/D > 10$ should be maintained in order to maximise power generation.

CHAPTER 6

PERFORMANCE

CHARACTERISATION

Scope

The flow field analysis carried out in previous chapters has provided a novel insight into machine operating behaviour at the micro level. From this analysis specific operating characteristics have been identified which are predicted to have considerable performance related effects. In this chapter such effects are quantified in the form of both torque and power outputs from the wind turbine. The scope of this chapter is defined by the areas identified during the literature review such that the data presented here provides novel information on cross-flow wind turbine performance. The performance characteristics of the prototype wind turbine are examined using experimental and numerical techniques. In general, the experimental analysis conducted provides new information on the steady state characteristics of the wind turbine. The scope of experimental work is limited to macro level torque and power analysis using the test setup described in Chapter 3. From this analysis the torque, speed and power spectra have been obtained from the wind turbine rotor and presented in dynamic and time-averaged forms.

Numerical analysis aims to overcome some of the limitations inherent during experiments and allows for more detailed analysis of wind turbine performance. In addition to the standard performance data this section investigates the effects of urban topography on wind turbine power output. From this analysis the suitability of a typical flat roof building is evaluated along with upstream and downstream interaction effects as a function of installation height

6.1 Experimental Performance Characteristics

In this section a series of experiments are conducted with a view to obtaining key performance related characteristics from the wind turbine at operating conditions similar to those experienced in the field. These experiments are configured such that they correspond to the experimental test setup defined in Chapter 3 which features the full scale wind turbine and low speed wind tunnel.

In each of the following experiments, torque, speed and power data is obtained from the wind turbine using the data acquisition setup as described in Figure 3-13. Here both torque and speed data is taken from the torque transducer unit and used to compute instantaneous power at the turbine transmission shaft. During experimental studies the effect of λ has again been investigated and is controlled using the load bank described in Figure 3-13. Wind speed is measured at the exit of the wind tunnel as per the test setup defined in Chapter 3 using a Cobra type pressure probe. The type of flow used in this study resembles a jet flow exiting the 0.6m x 0.6m square wind tunnel section. Using this flow the operating behaviour of the machine is characterised at three steady state speed.

6.1.1 Steady State Analysis

The following section is dedicated to evaluating wind turbine performance at steady state operating conditions where dynamic torque, speed and power data is presented. Steady state conditions are maintained using the load bank described previously such that generator current output is regulated and rotor speed remains constant. From this analysis the micro performance characteristics associated to using multi-blade geometry are described.

6.1.1.1 Wind Turbine Torque Output

The torque data presented in the following section is obtained from the torque transducer unit during normal operation. The data is sampled at 8 KHz using the Sinocera data acquisition system described in Chapter 3. The following analysis presents torque signatures at specific rotor operating points which are defined by rotor tip speed ratio (λ). In this study three values of λ are presented such that the effect of rotor speed on steady state torque fluctuations and nominal torque output can be quantified. The values of λ studied are $\lambda = 0.12$, 0.18 and 0.25 relative to the free-stream point velocity of 13m/s measured upstream of the turbine within the wind tunnel test section. The torque output of the machine is presented in non-dimensional form as per the following relation:

$$C_T = T / (0.5\rho A R V_\infty^2) \tag{6-1}$$

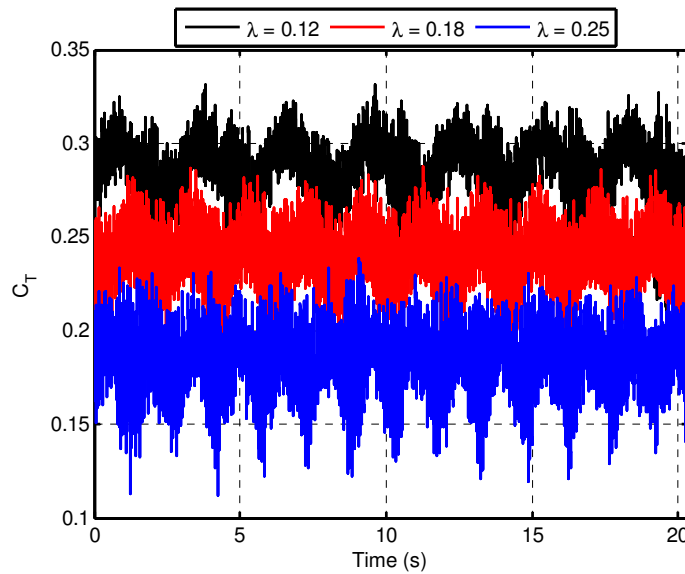


Figure 6-1 Wind turbine torque output (C_T) for $\lambda = 0.12$, 0.18 and 0.25 at V_∞ of 13m/s versus time.

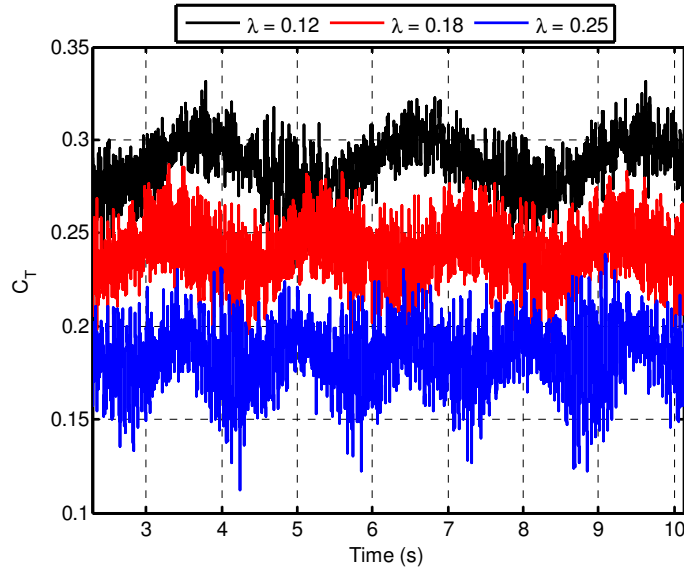


Figure 6-2 Close-up wind turbine torque output (C_T) for $\lambda = 0.12, 0.18$ and 0.25 at V_∞ of 13m/s versus time.

For each of the signals both RMS and crest factor have been computed as per the following two relations:

$$RMS = \sqrt{\text{mean}(C_T^2)}$$

(6-2)

$$\text{Crest Factor} = \text{Peak}(C_T) / \text{RMS}(C_T)$$

(6-3)

λ	RMS	Crest Factor
0.12	0.2854	1.1614
0.18	0.2405	1.2118
0.25	0.1850	1.3171

Table 12 Rotor mean torque, RMS and crest factors

Figure 6-1 and Figure 6-2 depict the wind turbine torque output in the time-domain over a time period of 20.3s and 10.15s respectively. Here a time period of 20.3s corresponds to six rotor revolutions at $\lambda = 0.12$ and highlights the nature of rotor steady state operation. From the above plots the torque characteristics of the wind turbine are seen to provide more consistent torque

output when compared to the Savonius type rotor. Such characteristics are a result of the high solidity multi-blade design which allows for more consistent torque generating capabilities. The most notable trend present in the above plots relates to the cyclic variation of torque output with time for all conditions of λ . This cyclic variation shows strong periodic features which are again indicative of the repeatability in performance output during each blade cycle. Further observations include the magnitudes of torque generated in which a peak RMS torque of 0.29 is observed $\lambda=0.12$. When rotor speed is increased a reduction in torque output is noticed with reductions of 17.2% and 35% at $\lambda=0.18$ and 0.25 respectively.

Using data obtained from a flow condition corresponding to 11m/s the following time-averaged torque output is presented. This flow speed is of slightly reduced magnitude compared to the previous data due to structural instabilities at high rotor speeds. Here time-averaging is done for a period of 60 seconds which is shown to provide time-independent data. The range of rotational speeds provided is extended such that the full operating curve is obtained for an example flow condition.

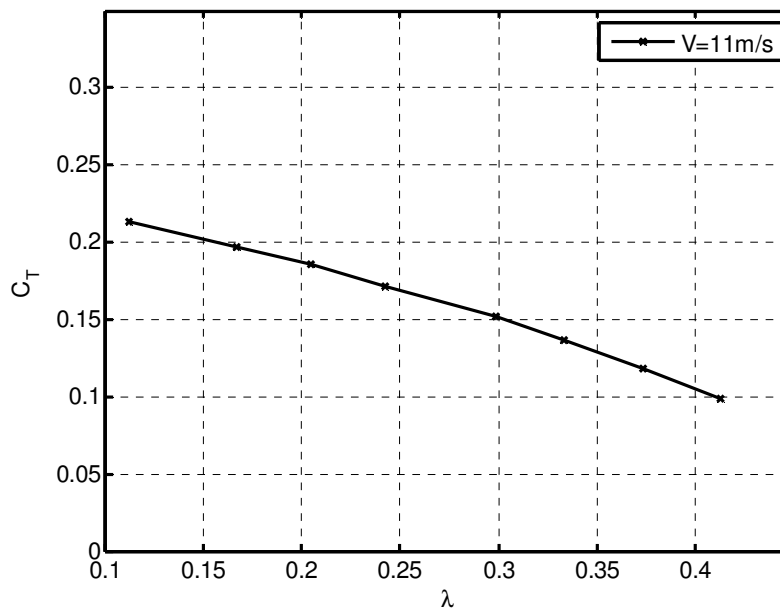


Figure 6-3 Time averaged wind turbine torque output (C_T) at $V_\infty = 11\text{m/s}$ over full range of λ

The most notable observation from the above figure is the low range of tip speed ratio the machine operates in which is to be expected given its high solidity ratio and figures reported previously in literature for similar machines [60], [61], [64], [66–68], [94]. Additionally, the jet flow condition

used in this study to provide preliminary performance data does not have sufficient energy to maximise wind turbine performance output given that the flow area is significantly less than the rotor inlet. It is therefore predicted that under a uniform full rotor inlet flow the wind turbine operating range will be considerably higher along with generating a higher level of torque output. Such characteristics are examined in the latter half of this chapter using CFD which overcomes some of the limitations experienced during experimental testing. One of the most apparent trends visible is the linearity of torque generation which is consistent over the full operating band of the machine. This torque output is seen to be highest at low values of λ which agrees well with previous dynamic analysis. Using the dynamic torque and speed signals the power output of the rotor is computed as described in the following analysis.

6.1.1.2 Time Averaged Power Output

The power generation capabilities of the wind turbine are presented in this section again for an example wind speed of 11m/s. Power output is computed over a the full operational range of the rotor as per the torque data given previously. Rotor power output is computed using dynamic speed and torque data from the transducer as per the following relation:

$$P = \omega T \tag{6-4}$$

Here power output is expressed in non-dimensional form and again plotted with λ .

$$C_p = P/(0.5\rho AV_\infty^3) \tag{6-5}$$

Figure 6-4 depicts the wind turbine rotor power output presented in a time averaged form. The nature of wind turbine power generation under jet flow conditions highlights some interesting trends. Due to the considerable variation between the wind tunnel exit cross-sectional area when compared to the wind turbine inlet area this power output is seen to be considerably lower than data presented on existing cross-flow machines. Although this power output is of reduced magnitude the characteristic of this power curve highlights some useful trends. The power curve generated for $V_\infty = 11\text{m/s}$ shows a steep increase in power output at low rotor speeds between $\lambda=0.12$ and 0.3

which is to be expected given the high starting torque characteristics described previously and the low inertia of the rotor assembly. It is noticed that maximum power output is generated close to 75% of the maximum rotor speed which in this case corresponds to $\lambda = 0.36$. At this rotor operating condition a maximum $C_p = 0.035$ is generated which is close to the design point specified in Chapter 3.

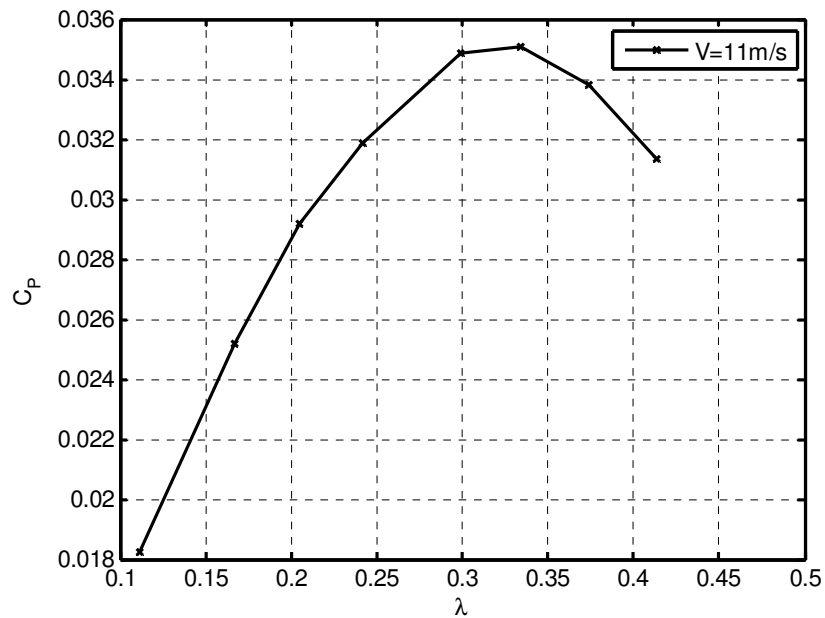


Figure 6-4 Time averaged wind turbine power output (C_p) at $V_\infty=11\text{m/s}$ over full range of λ

In order to evaluate wind turbine performance over an extended range the MRF CFD model is used to generate torque and power signatures of the wind turbine. This data is given in the following in which a numerical validation is performed using experimental torque and power data.

6.1.2 Summary

- The dynamic torque signal of the wind turbine has been measured for a range of rotor speeds. This torque output is seen to have strong periodic characteristics which are indicative of the multi-blade rotor and result in a more consistent torque delivery when compared to the Savonius rotor.
- The dynamic torque RMS is seen to reduce with an increase in tip speed ratio which is also consistent in the time-average torque data. Peak torque measured in the time-averaged data is in the order of $C_T = 0.22$ and generated at $\lambda = 0.11$. The torque magnitude measured at this speed is considered to be relatively high given the jet flow condition tested over a small proportion of the rotor.
- Using the instantaneous speed and torque spectra the wind turbine power output has also been computed and presented in a time averaged form. The power output of the machine is seen to peak at $\lambda = 0.36$ in which a $C_p = 0.035$ is generated.

6.2 Numerical Validation

The following section describes the validation strategy used to determine the accuracy of the MRF CFD model used extensively in this chapter. This macro level analysis is concerned with the correlation of both experimental and CFD performance characteristics using a similar approach to that proposed in [91]. Using the experimental setup described in Chapter 3, the full scale wind turbine performance is investigated over a range of λ for a fixed wind speed that corresponds to that described in Figure 4-1. As per previous analysis, data is obtained using the system configuration presented in Figure 3-13 where the torque transducer unit is used to measure instantaneous torque and speed output. From this instantaneous data the time-averaged torque and power outputs have been computed as per analysis presented previously.

The numerical data has been obtained using the full scale three-dimensional model under MRF rotational conditions. In order to validate CFD data with that obtained experimentally the flow profile present during experiment is imported into Fluent using a form of User Defined Function (UDF) as defined in Chapter 4. In order to correlate CFD steady-state data with time-averaged dynamic experimental data wind turbine performance has been studied at a number of blade positions using CFD. The following plot depicts time-averaged wind turbine performance over a range of λ in which both experimental and CFD data sets are presented. Here both torque and power outputs expressed in non-dimensional as per (6-1) and (6-5) again use facet-average velocity. In Figure 6-5 the torque output of the wind turbine is presented in which both experimental and CFD data is plotted. The torque curve generated using CFD shows good agreement with that measured experimentally in terms of profile. Torque magnitudes also show a strong correlation with CFD torque lying within +30% error for all values of λ indicative of strong correlation between both torque curves. In Figure 6-6, the wind turbine rotor power output is plotted with λ again using both experimental and CFD data sets. Similar observations are noticed in that CFD C_p lies within the +30% error band at all values of λ and is of similar shape. The magnitude of variation between both experimental and predicted data is within acceptable limits given that the CFD model does not allow for inertial effects and drive-train losses. Also due to the fabricated wind turbine structure some degree of flexing is present within each blade assembly which would result in reduced efficiency. Based on this analysis the MRF CFD model has been used for further performance prediction for a diverse range of operating points.

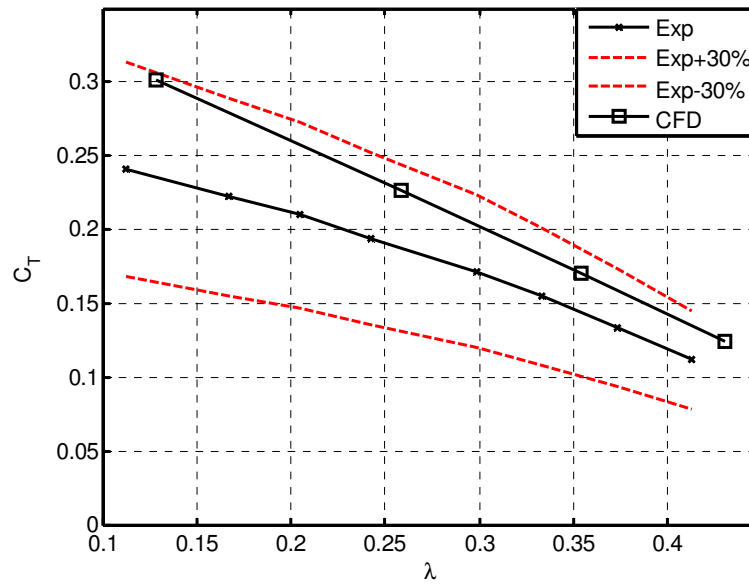


Figure 6-5 Wind turbine torque output (C_T) plotted with λ for experimental and CFD data

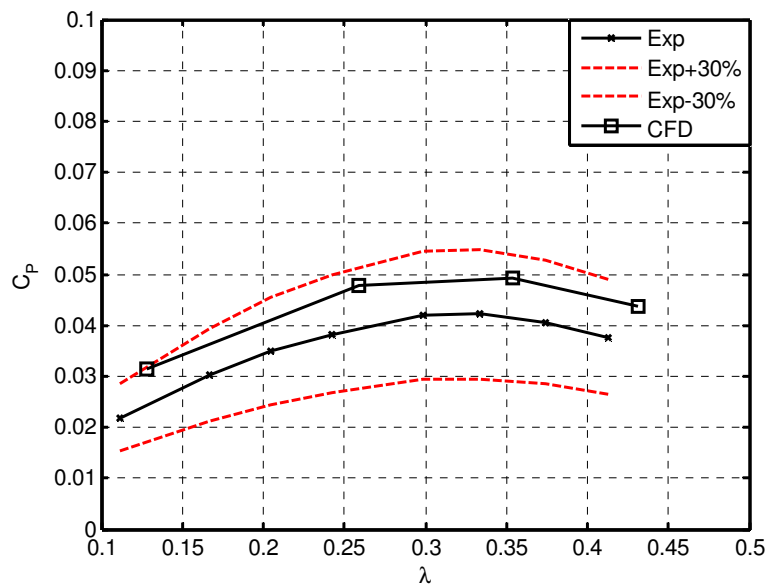


Figure 6-6 Wind turbine power output (C_p) plotted with λ for experimental and CFD data

6.3 Numerical Torque Characteristics

In the following section a computational approach has been used to determine primary performance related characteristics from the wind turbine. The work presented here provides novel information on the micro and macro level performance characteristics of this cross-flow wind turbine at specific operating points. From this analysis the effects of key findings described in Chapters 4 and 5 on wind turbine performance are described along with new performance related signatures. From this analysis a clear view of wind turbine performance is gained and evaluated as a potential solution to urban micro wind energy.

This section presents detailed torque data obtained from the MRF CFD model for a range of operating points and conditions. This study investigates both micro and macro level torque output generated by individual rotor blades and the complete rotor assembly. Additionally, the resultant effects of both λ and V_∞ are quantified such that wind turbine performance can be evaluated at both 'design' and 'off-design' conditions.

In the following figures cross-flow torque data is presented in which individual torque outputs generated from each blade are computed. This individual blade torque (T) is plotted in non-dimensional form T/T_{MAX} where T_{MAX} represents total rotor torque output. Here T_{MAX} is computed from the sum of individual blade torques contained within the rotor assembly and is considered to be shaft torque. For the purpose of this analysis, each rotor blade is defined as a unique blade number relative to its angular position around the wind turbine. The convention used here follows that described in Figure 4-3 and is consistent throughout. In this study a constant flow speed of $V_\infty = 4\text{m/s}$ is used in the X direction again as per Figure 4-3. The following plot shows the associated torque output from each rotor blade over a full range of rotor blade positions plotted as a function of λ . This therefore provides information on the dynamic wind turbine performance which has been identified as a limitation with existing studies. The blade position is again taken relative to the adjacent stator and follows the convention described in Chapter 4. The resolution of angular position is increased such that 5° intervals are used.

Figure 6-7 depicts the variation of wind turbine rotor blade torque at $\lambda=0$ when the rotor is static. The effect of the asymmetric flow fields described in Chapters 4 and 5 are prominent in which large variations in blade torque are observed. The regions in which large energy transfer has been identified also result in large torque contributions namely at rotor blades 1, 11 and 12. A peak torque output of 0.34 is generated by blade 12 at a cycle position of 15° . At these locations of

energy transfer the torque output of each of the blades is seen to be extremely sensitive to blade position. Such trends highlight the dynamic characteristics of the cross-flow format as shown in Figure 6-1. In addition to the large torque contribution of the windward blades a significant amount of torque is also generated on the leeward side of the rotor. The variations in both pressure and velocity fields in this location and the interaction effects already described result in blades 6 and 7 generating reasonable levels of torque. It is also noticed that at unique blade positions the torque output of blades 5, 8 and 9 becomes negative which results in a counter rotating torque similar to that reported in the Savonius rotor. Although this characteristic will result in inefficiencies the magnitude under static rotor conditions is minimal.

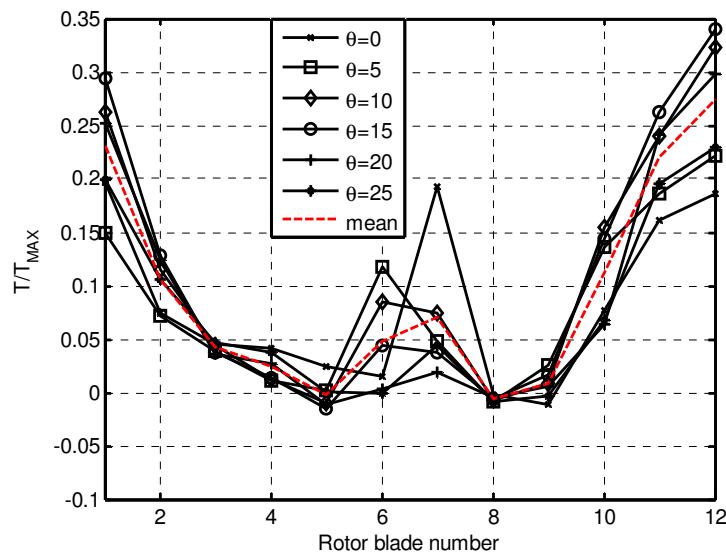


Figure 6-7 T/T_{MAX} computed for $V_{\infty} = 4\text{m/s}$ and $\lambda = 0$ for $\theta = 0, 5, 10, 15, 20$ and 25°

The torque contributions of each rotor blade as a function of angular position around the wind turbine have again been quantified under rotational conditions. A peak torque of 0.275 is generated again at blade 12 for an angular position of 15° , this results in a 19% reduction compared to the static rotor. The additional high torque generating blades are again present and correspond to blades 1 and 11 and are consistently high over the full blade passing cycle. Similar interaction effects are noticed at blades 6, 7 and 8 with a maximum negative torque output of -0.033 generated at blade 9. This equates to an increase of 67% in negative torque when compared to the peak negative torque blade from the previous rotor condition. Regions that feature low mass flow rate are again noticed and consistent with the previous condition. These blades correspond to 3, 4, 5 and 8 and are one of the primary inefficiencies identified from this torque analysis.

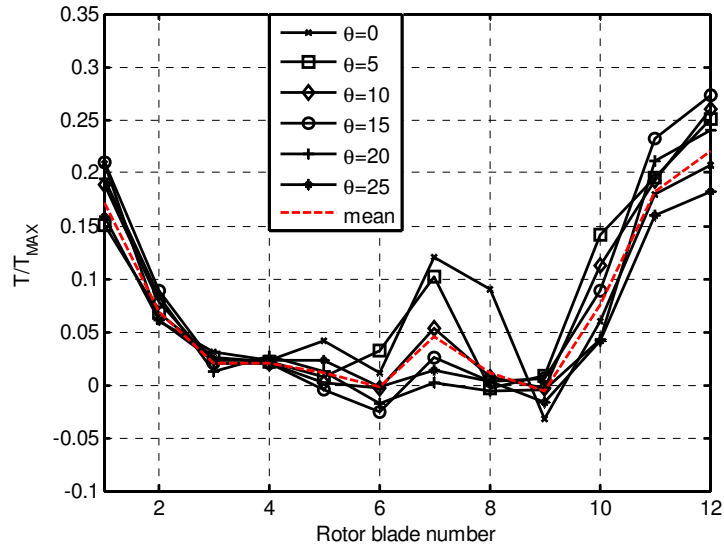


Figure 6-8 T/T_{MAX} computed for $V_{\infty} = 4\text{m/s}$ and $\lambda = 0.2$ for $\theta = 0, 5, 10, 15, 20$ and 25°

A large degree of similarity is again noticed at $\lambda=0.4$ which is to be expected given the consistency in mass flow distribution about the turbine over a diverse range of rotor speeds. This profile is seen to be more sensitive to rotor blade position particularly at blades 10, 11 and 12. At this rotor speed peak torque output is slightly increased at blade 12 which has a magnitude of 0.29 at 5° .

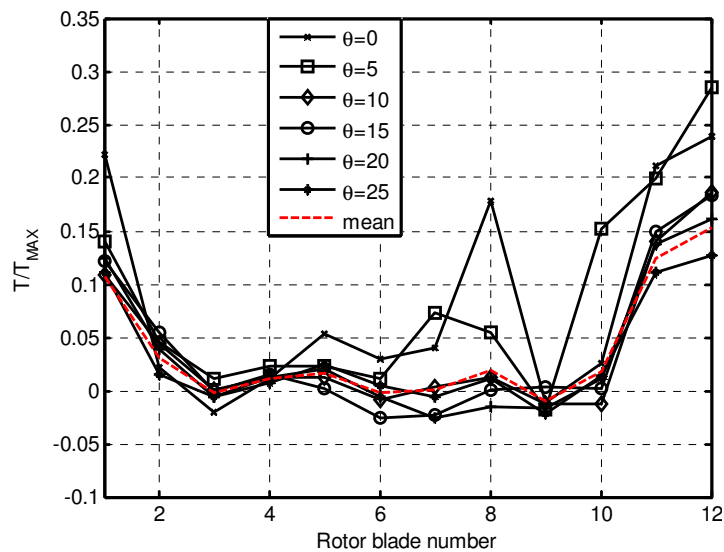


Figure 6-9 T/T_{MAX} computed for $V_{\infty} = 4\text{m/s}$ and $\lambda = 0.4$ for $\theta = 0, 5, 10, 15, 20$ and 25°

In order to evaluate the direct effect of λ on blade and rotor torque the following analysis is presented at the design rotor position as depicted in the blade profile generation section in Chapter 3. This position is close to mid-passage and shows clearly the effect of rotor speed on the torque contributions of each rotor blade at a flow speed of 4m/s.

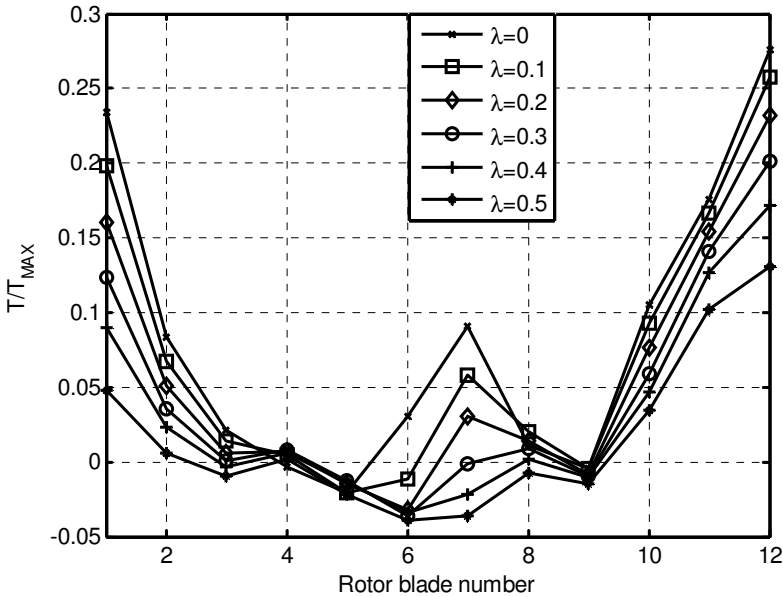


Figure 6-10 Rotor blade torque output plotted over $\lambda = 0 - 0.5$ at $V_{\infty}=4\text{m/s}$.

The clearest observation from this plot is a reduction in torque as rotor tip speed increases which agrees well with experimental data. This trend is consistent at all rotor blade positions with the exception of blades 4, 5 and 8. One of the most critical performance related characteristics of any fixed blade VAWT is the 'dead band' region which corresponds to the position at where blade torque is either zero or negative [34], [36], [48–50], [53], [58]. To varying degrees such trends have been highlighted in the previous torque profiles and are generally present on the leeward side of the rotor. In the above plot this dead band is noticed over rotor blades 3, 4, 5, 6, 7, 8 and 9 with varying magnitude. Negative torque is generated for rotor blade 5 at all rotational conditions and hence contributes considerably to dynamic inefficiency. Torque output computed for rotor blade 6 shows similar effects for dynamic conditions only and again generates opposing torque. Rotor blade 7 shows different characteristics at $\lambda = 0, 0.1$ and 0.2 where torque is positive. Justification for this variation in torque is still un-clear however a potential explanation for this sudden drop in torque is shown in Figure 4-16 where from $\lambda = 0$ to $\lambda = 0.4$ a sudden rise in pressure is observed at this

angular position close to the blade tip. In general the peak negative torque magnitude does not exceed -0.037 which when compared to peak torque in the direction of motion is relatively low. It is however clear that the overall torque output of the rotor for this cross-flow design relies primarily on the contributions of a few key blades and hence being relatively inefficient.

To summarise, this analysis has provided novel information about the energy conversion process within a cross-flow VAWT which has identified key energy transfer regions. It has also highlighted a large dead band on the leeward side of the turbine where flow interactions with the downstream rotor blades result in zero or negative torque generating blades. In addition it has also confirmed the inefficiencies inherent with this high solidity design at rotor blades where mass flow rate is minimal due to associated blade passage blockages. In order to understand macroscopic torque characteristics of the turbine, T_{MAX} is computed for each rotor blade position and is given in the form of C_T . Along with torque output from each blade position; a mean torque is presented and is computed from the torque output at each blade position.

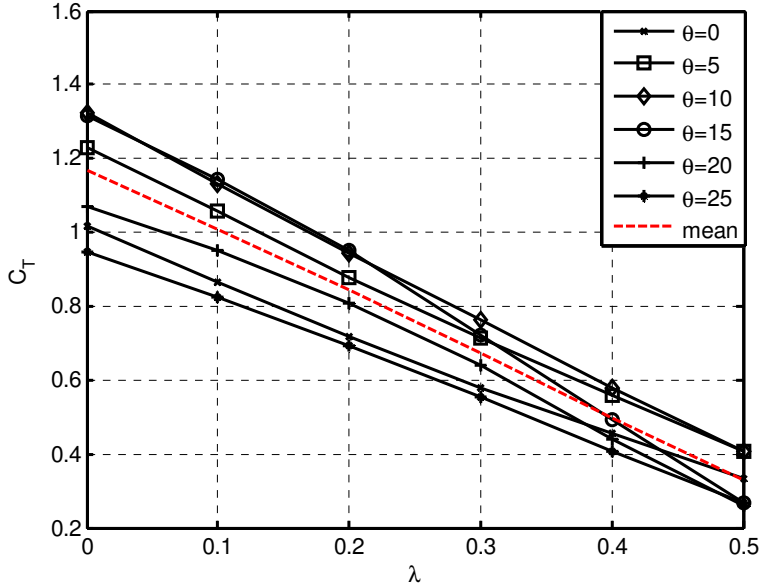


Figure 6-11 Wind turbine rotor torque output (C_T) plotted against rotor blade tip speed ratio (λ) at $V_\infty=4\text{m/s}$ for rotor blade positions (θ) of 0, 5, 10, 15, 20 and 25°.

The nature of rotor torque output is seen to decrease as a function of λ at all blade positions considered. The effect of using multi-blade geometry on the torque output of the machine is evident in which high levels of torque are observed. Here a mean torque of $C_T = 1.17$ is generated when the rotor is static. This is considerably higher than reported torque coefficients observed for the

'Design, Operation and Diagnostics of a Vertical Axis Wind Turbine'
 By Gareth Colley, Department of Engineering & Technology, University of Huddersfield, UK

Savonius rotor which are in the order of $C_T = 0.3$ [33], [34], [53], [95]. This also highlights the effect of using external guide vanes to enhance torque generation capabilities in which torque output exceeds theoretical maximum rotor torque output. This is due to the fact that the stator inlet area is significantly larger than the rotor and torque output is computed relative to the rotor inlet area. The effect of rotor blade position on the resultant rotor torque output is seen to be considerable although no consistent trends are noticed given the large variations observed in the torque profiles. Additionally, the linearity of torque generation is seen to vary at high values of λ and is most prominent for $\theta = 15^\circ$ and 20° . Mean torque output is considered to be average rotor torque output during normal operation given the data computed at multiple blade positions. This mean torque shows strong linearity over the full rotor speed range and is seen to decrease with λ .

To understand wind turbine torque generation at a range of flow conditions the effect of wind speed (V_∞) is presented in the following. Here, a range of V_∞ has been taken with the blade position held constant at the design condition described in Chapter 3. The range of wind speeds studied corresponds to 4m/s – 12m/s and allows for evaluation of 'design' and 'off-design' performance. As per previous analysis this C_T output is plotted over a full range of λ such that rotational effects can also be determined.

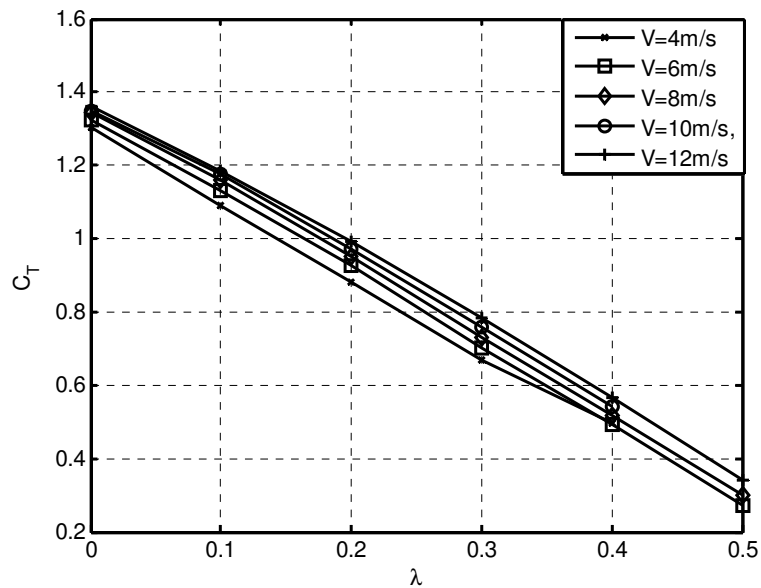


Figure 6-12 Wind turbine rotor torque output (C_T) plotted against rotor blade tip speed ratio (λ) for $V_\infty = 4, 6, 8, 10$ and 12m/s .

Torque output as a function of wind speed highlights maximum torque at a static rotor condition which agrees well with previous data and is consistent over the range of speeds tested. During dynamic operation ($\lambda = 0.1 - 0.5$) the torque output reduces with an increase in rotor speed and shows linear characteristics which agrees well with experimental data presented previously. The torque generation capabilities of the rotor are seen to be comparable over this flow range which gives insight to how the machine would perform outside of its design condition. Here torque output at the design blade position is in the order of $C_T = 1.35$.

6.3.1 Summary

The following points describe the key findings from this numerical study:

- Rotor blade torque output varies considerably depending on blade angular position. Highest torques are generated by blades 1, 2, 10, 11 and 12 which agrees with the key energy transfer zones reported from the flow field analysis described previously.
- Effect of λ on blade torque output is seen to be most prominent on the leeward side of the machine which is indicative of strong downstream interaction effects similar to those observed with the Savonius rotor.
- In addition the effects of θ and λ on blade torque have identified ‘dead-band’ characteristics on the leeward side of the wind turbine at which counter-rotating torque is generated opposing the direction of motion. Such trends are expected to be one of the primary inefficiencies of this format due to the fixed blades employed in the design all the magnitude of this opposing torque varies as a function of blade angular position.
- Plot of rotor torque output highlights high torque characteristics of the wind turbine ($C_T = 1.17$) and is generated when the rotor is static. This is considerably higher than reported torque coefficients observed for the Savonius rotor which are in the order of $C_T = 0.3$. At present limited information is available on existing cross-flow machines although such high torque output seen when using the present geometry is beneficial when considering low wind speed installation sites and the requirement for self start-up.

- In general the wind turbine torque output is seen to be linear over the rotor speed range studied. This linear output is however seen to vary considerably at high values of λ at blade positions $\theta = 15^\circ$ and 20° which is again indicative of geometric induced effects.
- Torque output is seen to be comparable over a range of wind speeds which allows for operation outside of its design condition and hence can be used outside of the urban environment where wind speeds are of increased magnitude.

6.4 Numerical Power Characteristics

In the following, wind turbine power characteristics are computed over a range of flow and rotor conditions similar to those used for torque investigation. This power output is computed from the total rotor torque output (T_{MAX}) and the instantaneous rotor speed which is determined from the rotor blade tip speed ratio (λ). The associated power curves for the turbine are presented in the following figure where a series of wind speeds are tested to benchmark the machine. This power output is presented using the power coefficient as per equation (6-5).

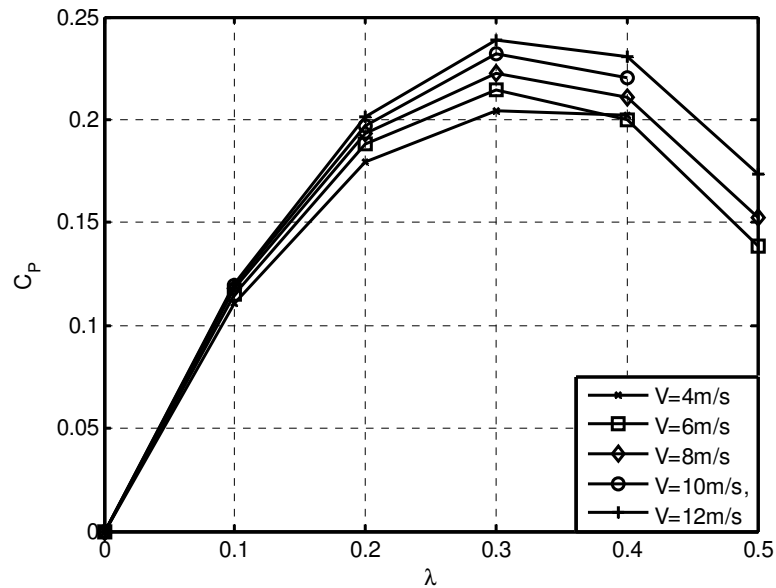


Figure 6-13 Wind turbine rotor power output (C_p) plotted against rotor blade tip speed ratio (λ) for $V_\infty = 4 - 12$ m/s.

Figure 6-13 depicts the machines power output at the rotor blade design condition over a range of operating conditions. The power characteristics of the machine show strong similarities to those obtained from experiments although the machine operates over an extended range of λ under uniform flow conditions as predicted. The peak power generation point is seen to vary depending on the wind speed tested in which power output increases with an increase in wind speed at all conditions with the exception of 6m/s at $\lambda = 0.4$. Peak power magnitude has strong similarities to the Savonius rotor as reported in [34], [36], [53] in which a C_p of 0.24 is observed at 12m/s. The overall nature of the power curves show some resemblance to those provided for similar cross-flow wind turbine as shown in [62], [64], [67], [93] although does not correlate with any other designs due to large inconsistencies in reported power coefficients. One of the most notable observations is the large variation in power output when compared to the data presented by Lee and Park et al [61], [62] in which C_p values exceed 0.5 using similar flow conditioning techniques. Based on such reports power generation potential for cross-flow machine has been exhibited although for this particular geometry additional work is required to enhance performance further. Providing primary inefficiencies within the machine can be minimized a more efficient energy transfer is expected particularly at higher rotational speeds. To achieve such conditions the interaction effects between the stream wise flow and leeward rotor blades should be minimized.

6.4.1 Summary

The main findings from the above are summarised below:

- The power output of this cross-flow wind turbine has been examined numerically in which the peak power output shows a large degree of similarity to the Savonius rotor. From this study a peak C_p of 0.24 is generated at $\lambda=0.3$ close to mid rotor speed range and the design point used for preliminary design. It is however significantly lower than machines reported in [61], [62]. A more comparable example is that reported in [67] in which the present machine generates double the power output of the Zephyr® wind turbine over a similar operational range.
- The power output generated at high rotor speeds is seen to drop off above $\lambda=0.3$ which is likely to be a result of the dead-band effects identified and the generally low speed

'Design, Operation and Diagnostics of a Vertical Axis Wind Turbine'
By Gareth Colley, Department of Engineering & Technology, University of Huddersfield, UK

nature of this design. Hence maximizing torque output at lower solidity ratios is expected to result in improved power delivery over this range along with enhancing electrical power generation by extending the tip speed ratio limit of the rotor.

6.5 Numerical Topographical Effects

Wind turbine torque and power characteristics have been well documented for existing technologies and from previous analysis for the machine described in this thesis. At present, the effects associated to installation in the urban environment have not been considered which is the aim of the following investigation. Here, a typical flat roof urban building has been modelled using CFD with the wind turbine installed above. For the purpose of this study the wind speed is held constant at 4m/s and the wind turbine tip speed ratio (λ) varied. The wind turbine installation location is taken at two positions denoted upstream and downstream relative to the rooftop geometry. At these positions the effect of wind turbine installation height is studied with a dimension defined relative to the rooftop and the underside of the turbine. The minimum height taken is 0.5m which allows for a practical installation space for transmission and power generation equipment. Maximum wind turbine height is defined on the basis of UK planning restrictions described in the following section.

6.5.1 Building Geometry

This section provides a detailed overview of the building geometry used in this study and defines the installation locations across the rooftop. This includes the building footprint, side elevation and wind turbine installation location/height. Given the large variation in urban buildings in the UK a typical structure is taken from surrounding areas which features a flat roof. Measurements taken from the building are used to create the CAD model used in CFD. The footprint of the building is shown in the following figure where dimensions are given in mm. A side elevation in the XZ plane is provided in Figure 6-15 where the height and wind turbine installation locations are defined. The height defined as 'h' is varied at 0.5m increments up to a maximum of 5m. This maximum height offset is set given the increases in structural requirements needed at high installation heights along

with UK planning restrictions as given in [38], [63]. Hence, more realistic installation heights are studied that will allow for simple integration into roof spaces.

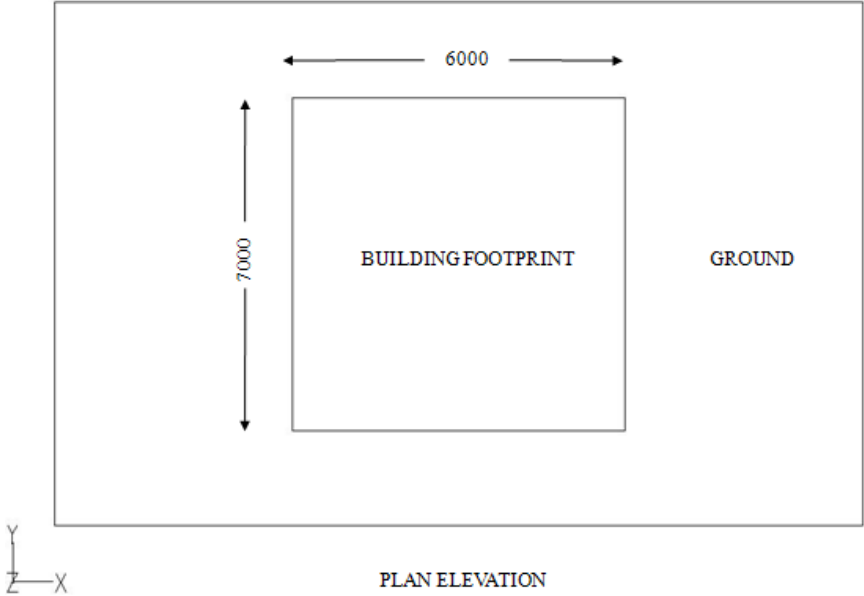


Figure 6-14 Plan elevation (XY) of building footprint in mm

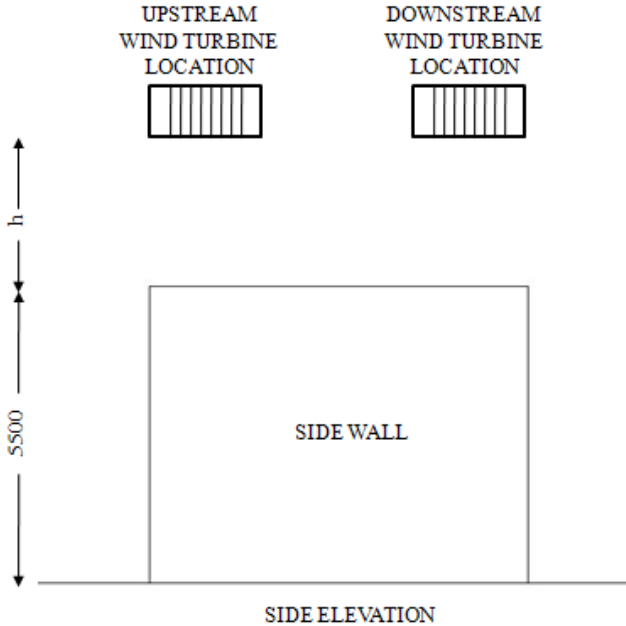


Figure 6-15 Side elevation (ZX) of building in mm

The CFD model used to simulate wind turbine topographical effects features a rectangular flow domain similar to that described in Chapter 3 and as used throughout this thesis. Given the nature of flow and the size of the building geometry both lateral and downstream boundaries have been extended to minimize boundary interaction effects on wind turbine operation. From preliminary simulations the effect of the building geometry is most dominant in the stream wise flow direction and hence this distance is increased further than the lateral boundary offsets. The distances of both lateral and stream wise boundaries have been determined from an independence study such that distances were continually increased until output data is independent of boundary position. The domain size is shown in Figure 6-16 in which building, wind turbine location and domain extents are all shown. Convergence is again determined as per the method described in Chapter 3 in which data is independent of convergence criteria beyond residual values of $1e-4$ for each of the governing equations. Additionally, monitors of wind turbine rotor torque set within the solver are used to further confirm convergence by reaching steady state conditions where torque output is independent of iteration number.

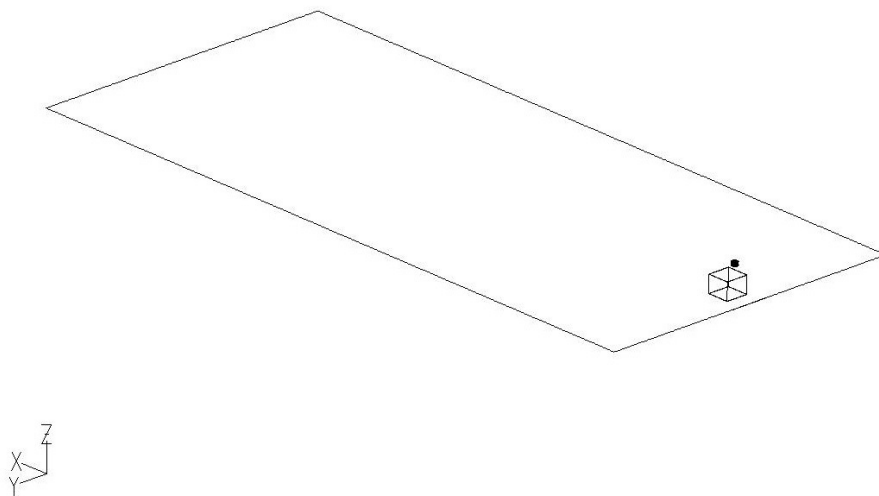


Figure 6-16 Topography CFD model domain showing flat-roof building, wind turbine and ground

6.5.2 Torque Characteristics

The performance of the wind turbine has been studied at two unique locations above the flat roof building namely upstream and downstream as per Figure 6-15. Torque data is presented over a range of wind turbine installation heights relative to the top of the building. This height offset is defined using the non-dimensional relation 'h/D' where 'h' is taken as wind turbine installation height (m) relative to wind turbine outer diameter 'D' (m). To understand the effects of both installation height and wind turbine rotational speed, torque is obtained over an h/D range of 0 - 0.4 in steps of 0.1 which corresponds to the dimensional installation height proposed previously. The range of rotor tip speed ratio used is consistent to that used in previous studies of 0 - 0.4. Here torque data is presented in non-dimensional form (C_T) which uses a free-stream velocity reference again taken from the velocity inlet boundary. Hence this torque data is not comparable to that presented previously due to the increased stream-wise wind turbine location relative to the velocity inlet boundary and the resultant drop in velocity. For comparative purposes a 'free-air' condition has been considered where the building geometry is set to interior boundary conditions to allow for un-disturbed flow passing through the machine. For this condition the wind turbine has been positioned at the same origin as used during solid building simulations where a ground offset equal to the maximum building installation height is used. This 'free-air' condition is investigated over the same dynamic rotor range and is plotted as a dashed red line in all of the following figures. The following figure depicts upstream rotor torque output at a single blade position which corresponds to the design condition used throughout. Here torque output (C_T) is plotted with λ for a range of h/D.

The torque output of this cross-flow rotor is plotted in the following two figures when the wind turbine is positioned at the upstream installation location. The most obvious trend from these plots is the significant increases in rotor torque output when compared to a free-air condition. Increases in torque are noticed at all vertical heights studied indicative of some building induced effects at the leading edge of the building. The magnitude of torque increase is seen to be sensitive to installation height although from this plot no obvious conclusions can be drawn. Maximum torque outputs are consistently generated at $\lambda=0$ which is to be expected given the static torque characteristics reported in previous analysis. The linearity of torque output over the rotor speed range is relatively consistent and comparable to the free-air condition with the exception of h/D = 0.25 which is at closest proximity to the roof and hence wall induced effects are expected to be

more prominent. A maximum torque output of $C_T = 2.2$ is generated at h/D of 1 compared to $C_T = 0.85$ for the free-air condition which is a 61% increase.

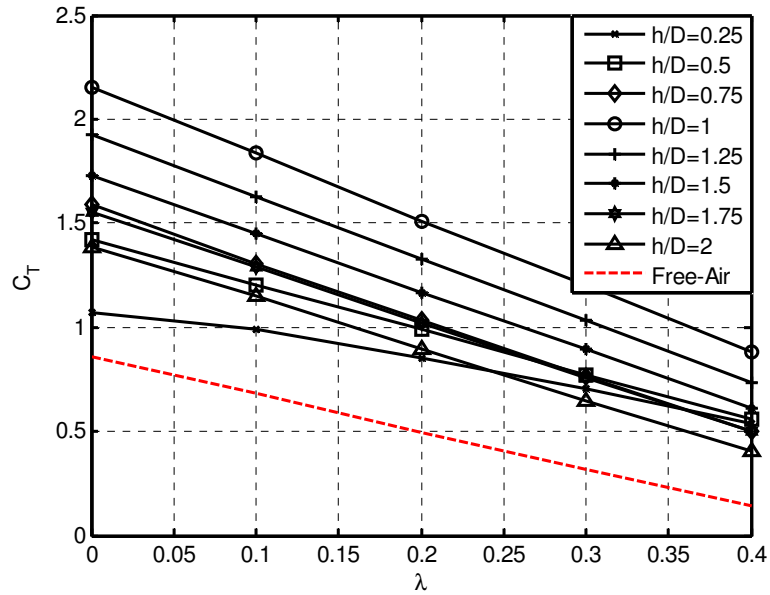


Figure 6-17 Upstream rotor torque output (C_T) plotted with λ for a range of h/D

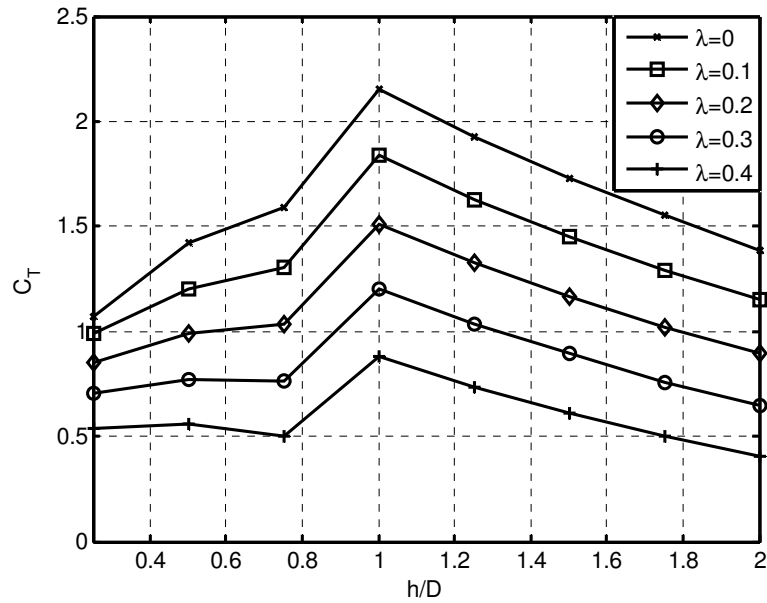


Figure 6-18 Upstream rotor torque output (C_T) plotted with h/D for a range of λ

In order to understand such increases in rotor torque output a cross sectional plane is taken through the central axis of the machine in the stream wise direction. On this plane the contours of velocity magnitude are plotted such that the effect of the building geometry on the flow structures generated across the wind turbine can be identified. This velocity field is plotted in non-dimensional form of V/V_{AVG} and follows the convention defined in the flow field analysis chapter. The velocity data presented is computed at $\lambda=0.3$ which is the peak power generation condition for normal operation at a flow speed of 4m/s. The wind turbine location height conforms to $h/D = 1$ and hence is 2m from the roof of the building.

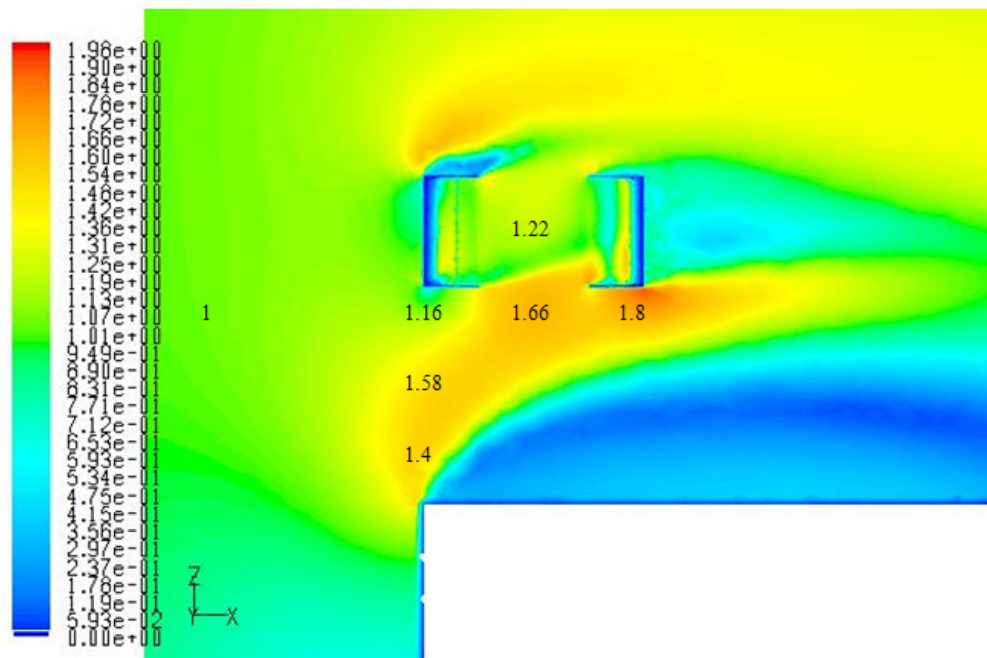


Figure 6-19 Upstream velocity field in ZX plane for h/D of 1 at $\lambda = 0.3$ and $V_{\infty} = 4\text{m/s}$

It can clearly be seen that at the leading edge of the building significant acceleration effects are present which result in increased velocity magnitude on the underside of the wind turbine. When compared to the free-stream flow velocity of 1 the velocity at a midpoint between the top of the building roof and the underside of the turbine is in the order of 1.58 which is a 58% increase. The direction of flow is seen to enter the wind turbine through the core of the rotor and hence energises the leeward blade passages. At the entrance to the rotor core velocity magnitude is in the order of 1.66 which is a further increase of 5.1%. Hence the increases in wind turbine performance are a result of the flow structures generated on the leading edge of the building and sensitive to installation height due to the high velocity flow stream and its direction.

The effects of rooftop topography on the torque generation characteristics are investigated further at the downstream installation location again over the same ranges of λ and h/D . This figure as shown below highlights major differences in the torque curves generated at this particular location. These major differences include a reduction in rotor torque output when compared to the free-air condition for h/D ratios of 0.25, 0.5, 0.75, 1 and 2 which is significantly different to that observed at the upstream installation location. Some similarities are noticed which include the linear torque characteristics at all ratios of h/D along with increases in torque at unique installation heights. These heights correspond to h/D ratios of 1.25, 1.5 and 1.75 which is a similar range to that identified in the upstream torque analysis. Here maximum torque output of 1.75 is generated at $h/D = 1.5$ which is a reduction of 20.5% compared to peak upstream torque. The installation height at which this torque is generated agrees well with the direction of the high velocity flow stream described in Figure 6-19. The velocity field at the downstream location is again evaluated in the following such that a more detailed understanding of the flow conditions the wind turbine is subjected to can be gained. Figure 6-21 depicts rotor torque output when plotted directly with h/D such that the torque profile can be seen over the full range of installation heights.

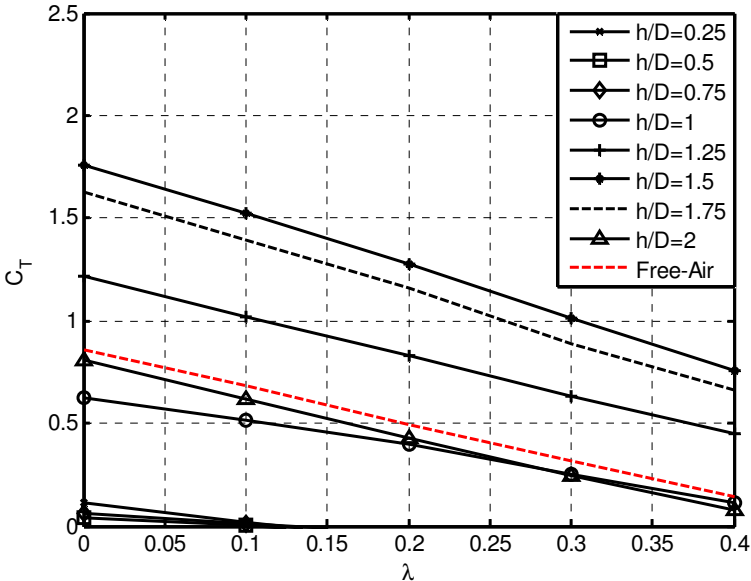


Figure 6-20 Downstream rotor torque output (C_T) plotted with λ for a range of h/D

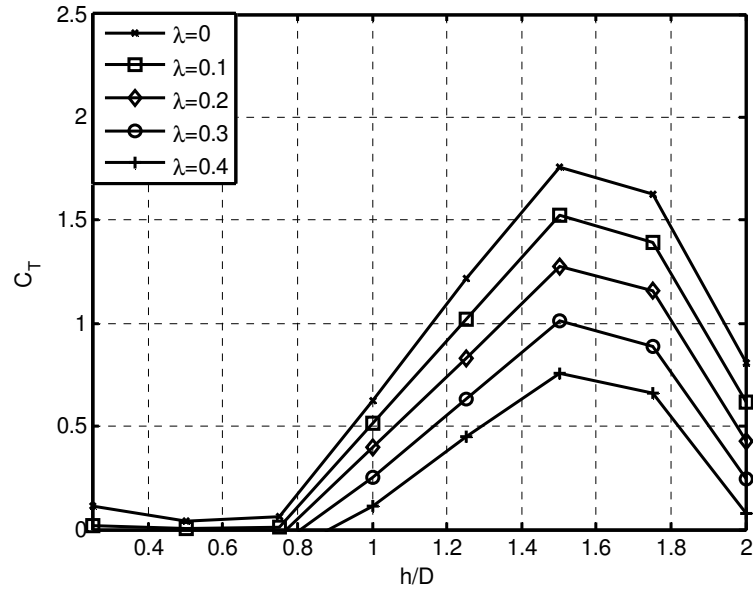


Figure 6-21 Downstream rotor torque output (C_T) plotted with h/D for a range of λ

The velocity field computed over the same cross-sectional plane in the ZX view is provided at $\lambda=0.3$ for $h/D = 1.5$ which highlights some interesting flow features. The high velocity flow stream generated at the leading edge of the building roof is still present and extends across the stream wise length of the building increasing in height. The mid plane point velocity upstream of the wind turbine is 1.16 which is 14% higher than the free-stream velocity hence resulting in increased torque output at this height. The vertical installation heights that yield reduced torque when compared to the free-air condition are expected given the large region of low velocity magnitude which extends over the full length of the roof and with a maximum height of approximately 2m from the roof surface. The velocities at the trailing edge of the rooftop are seen to be 0.13, 0.23 and 0.53 increasing in height. Hence for maximisation of rotor torque output the wind turbine should be located outside of this zone with h/D of at least 1.25.

power curves when plotted directly with h/D are provided in the following figure which highlights the maximum power generating region clearly.

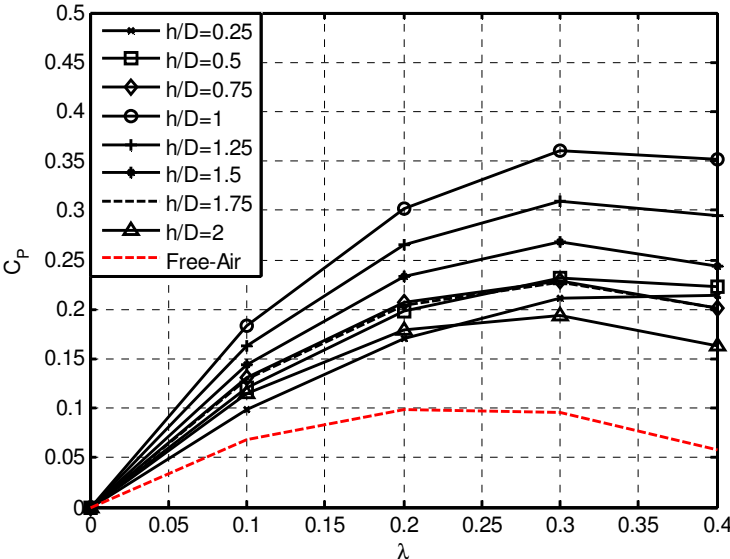


Figure 6-23 Upstream rotor power output (C_p) plotted with λ for a range of h/D

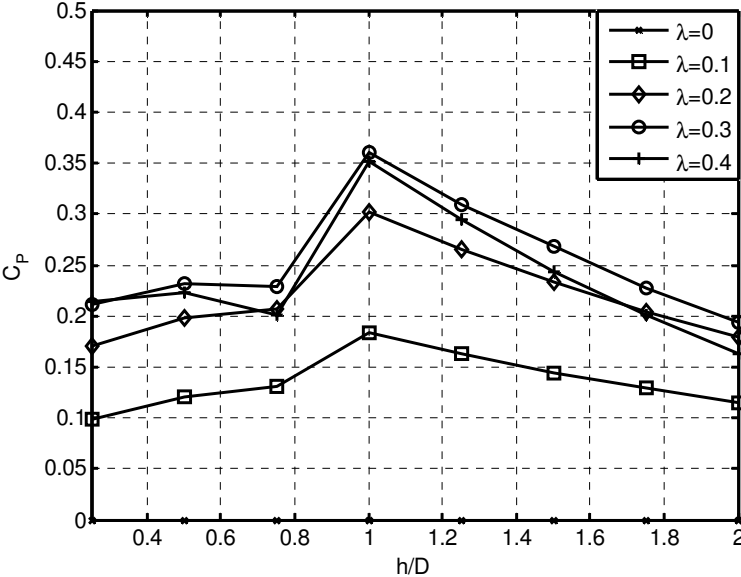


Figure 6-24 Upstream rotor power output (C_p) plotted with h/D for a range of λ

A similar analysis is presented in the following where power characteristics are computed at the downstream installation position using torque and speed data.

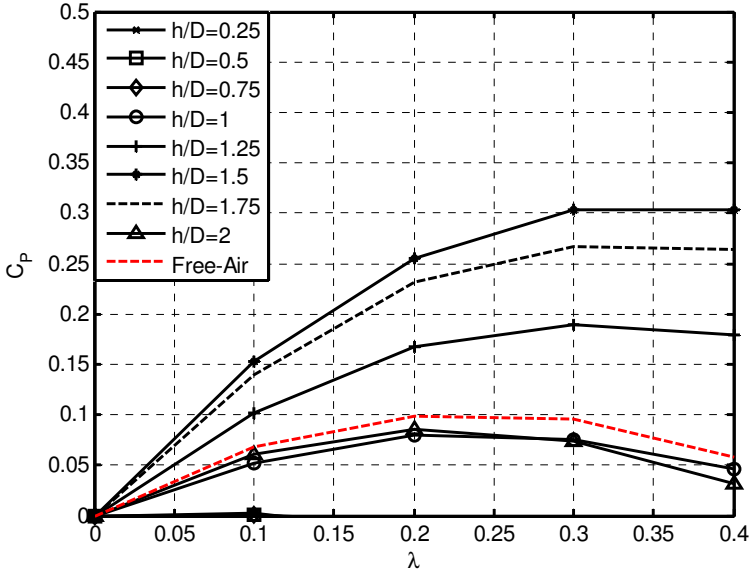


Figure 6-25 Downstream rotor power output (C_p) plotted with λ for a range of γ

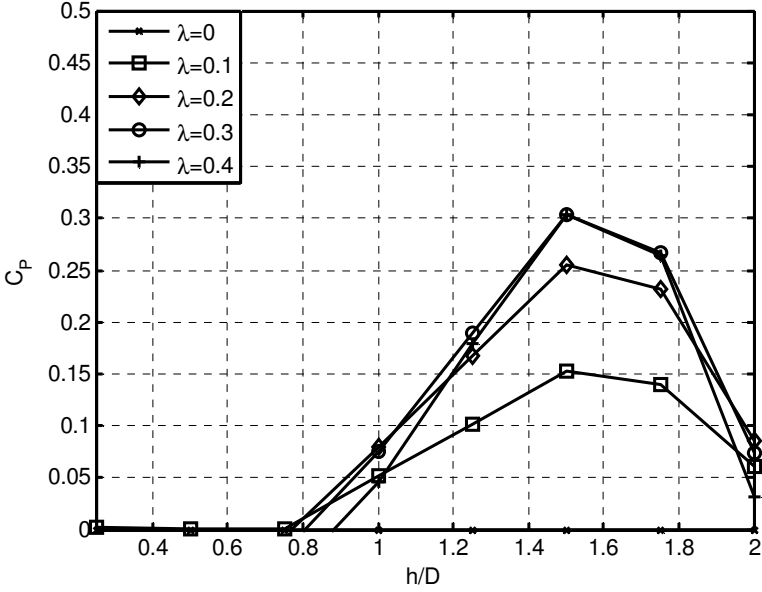


Figure 6-26 Downstream rotor power output (C_p) plotted with h/D for a range of λ

Here rotor power curves show some similarities to the upstream condition in terms of shape and peak power generation points relative to λ . At this location power generation is severely restricted

at close proximity to the building roof which agrees well with the torque data presented from h/D 0.25 – 0.75 and the velocity field provided in Figure 6-22. Such boundary related effects reduce wind turbine power to <0.01 and hence highlights the requirement for a small scale mast to bring the machine into the h/D range of 1.5. Here a maximum C_p of 0.31 is generated at both $\lambda = 0.3$ and 0.4 which is a 13% reduction when compared to the upstream location. This requirement is further highlighted in Figure 6-26 in which the power curves are depicted as a function of turbine installation height.

6.5.4 Summary

The performance characteristics of this cross-flow wind turbine have been examined using the MRF CFD model with the turbine located on the top of a flat roof building. The effects of installation position, height and operating condition have been computed and the major points summarised below:

- Increases in rotor torque output are noticed when installed at the upstream location at all positions studied when compared to the free-air condition. A maximum torque output of $C_T = 2.2$ is generated at h/D of 1 compared to $C_T = 0.85$ for the free-air tests.
- Downstream wind turbine torque output varies considerably depending on installation height in which maximum torque output is generated at h/D range of 1.25 – 1.75. At this location boundary related effects close to the rooftop wall have a strong influence on wind turbine torque generation capabilities.
- Upstream wind turbine power data highlights significant increases in power at all installation heights when compared to free-air data. Maximum powers are generated at $h/D = 1$ and 1.25 respectively for all conditions of λ studied.
- Downstream power data shows some similarities to the torque profiles described in which large reductions in power are observed at installation heights close to the roof. Maximum power generation is produced at $h/D = 1.5$ and 1.75 again for all conditions of λ

- For maximum power generation on flat roof geometry the wind turbine should be located on the upstream side of the building at $h/D = 1$ where a C_p of 0.35 is generated which is a 71% increase over the free-air condition.

CHAPTER 7

OPTIMIZATION & ROTOR DIAGNOSTICS

Scope

The commercial viability of any small-scale wind machine relies on its effectiveness to generate power. The operational characteristics which have been described in previous chapters highlight the machines low speed nature and high torque output. The power output shows similarity to the Savonius rotor which is considerably lower than horizontal equivalents. The following chapter investigates both flow and geometric effects on wind turbine performance with a view to identifying an optimum configuration for maximum power generation.

In addition a novel numerical fault detection model is developed and used to predict rotor blade faults for this cross-flow wind turbine. Using this model predicted torque signatures from the rotor are obtained and cross-examined with full scale experimental data for healthy and faulty modes of operation. The applications of this model are described and scope for future developments identified.

7.1 Parametric Optimization

The aim of this study is to perform a parametric optimization on the wind turbine taking into consideration flow, fluid and geometry. This study uses the three-dimensional MRF CFD model described previously under identical conditions. In order to perform an optimization routine on the machine the initial analysis is aimed at identifying primary performance related parameters that influence wind turbine torque output. These performance related parameters are selected from flow, fluid and geometry such that a unique inter-relation can be determined. The optimization studies are carried out using a fixed wind speed corresponding to 4m/s similar to the expected wind site installation conditions. The turbine blade position is fixed at the design condition described in Chapter 3. The parameters identified for investigation are defined in the following section where a dimensional analysis is performed such that a number of non-dimensional parameters can be obtained that represent the wind turbine operating state.

7.1.1 Dimensional Analysis

The parameters identified for investigation are associated to flow, fluid and geometry and are defined in this section. Although some of these parameters and their resultant effects on the response parameter torque have already been quantified, the parametric inter-relation has not. Additionally, some new parameters are introduced that relate to wind turbine geometry such that combined effects with those previously described can be enumerated. These parameters are presented in the following table and derived from base units.

Dependent Variable	Notation	Units	Base Units
Torque	T	Nm	ML^2T^{-2}
Independent Variables			
Free-Stream Velocity	V_∞	m/s	LT^{-1}
Air Density	ρ	kg/m^3	ML^{-3}
Rotor Angular Velocity	ω	rad/s	LT^{-1}
Baseline Rotor Outer Tip Radius	R	m	L
Stator Blade Number	ϕ	-	$M^0 L^0 T^0$
Rotor Outer Tip Radius	rbr	m	L

Table 13 Dependent and Independent Wind Turbine Variables

From these independent variables their relation with wind turbine torque output (T) can be expressed in the following equation:

$$T = f(V_\infty, \rho, \omega, R, \phi, rbr) \quad (7-1)$$

From these seven variables and three-dimensional units the Buckingham Pi theorem [96] states that four dimensionless Pi terms will be sufficient to represent and predict turbine performance. From this set of variables three repeating terms are noted which have been identified from flow, fluid and geometry. These repeating variables V_∞ , ρ and R are used to define the dimensionless Pi terms.

The derivation of the first Pi terms is as follows where the first non repeating variable T is considered:

$$\pi_1 = TV_\infty^b \rho^c R^d \quad (7-2)$$

Solving for b, c and d yields b = -2, c = -1 and d = -3 and hence the following expression:

$$\pi_1 = TV_\infty^{-2}\rho^{-1}R^{-3} \quad (7-3)$$

In alternative form:

$$\pi_1 = \frac{T}{V_\infty^2 \rho R^3} \quad (7-4)$$

The derivation of the second Pi terms is as follows:

$$\pi_2 = \omega V_\infty^b \rho^c R^d \quad (7-5)$$

Solving for b, c and d yields b = -1, c = 0 and d = 1 and hence the following expression:

$$\pi_2 = \omega V_\infty^{-1} \rho^0 R^1 \quad (7-6)$$

Or alternatively which is also defined as λ or rotor blade tip speed ratio.

$$\pi_2 = \frac{\omega R}{V_\infty} \quad (7-7)$$

The third Pi term is defined using stator blade number which gives:

$$\pi_3 = \varphi \quad (7-8)$$

The stator blade number Pi term is then modified such that it is defined as a ratio between φ and baseline number of stators or φ_{\max} giving:

$$\pi_3 = \frac{\varphi}{\varphi_{MAX}} \quad (7-9)$$

The final Pi term which corresponds to rotor outer tip radius or rbr is as follows:

$$\pi_4 = rbrV_\infty^b \rho^c R^d \quad (7-10)$$

When solving for b, c and d yields b = 0, c = 0 and d = -1:

$$\pi_4 = rbrV_\infty^0 \rho^0 R^{-1} \quad (7-11)$$

Modified relative to baseline design radius R,

$$\pi_4 = \frac{rbr}{R} \quad (7-12)$$

From the Pi terms derived in the above a new relation for wind turbine torque output can be defined:

$$\pi_1 = f(\pi_2, \pi_3, \pi_4) \quad (7-13)$$

Or,

$$\frac{T}{V_\infty^2 \rho R^3} = f\left(\frac{\omega R}{V_\infty}, \frac{\varphi}{\varphi_{MAX}}, \frac{rbr}{R}\right) \quad (7-14)$$

Having successfully obtained dimensional coefficients that represent the wind turbine operating state a Design of Experiments (DOE) approach is taken to determine the factorial configurations used for optimization studies. Here the three factors namely π_2 , π_3 , and π_4 contain multiple levels which correspond to a range of values. These values have been determined from both previous analysis and geometric constraints inherent within the design. Hence the range of π_2 corresponds to the normal operating range of the wind turbine as described in previous chapters. Geometric variable π_3 is constrained by the maximum number of stators permissible from a system cost perspective. Additionally, π_4 is governed by the original design envelope and radius of the outer tip is varied such that stator/rotor ratio effects can be quantified. The variables and their levels are described in the following table.

Pi Term	Minimum Value		Mid Value		Maximum Value
$\pi 1 = \frac{T}{V_{\infty}^2 \rho R^3}$	Dependent Variable	Dependent Variable	Dependent Variable	Dependent Variable	Dependent Variable
$\pi 2 = \frac{\omega R}{V_{\infty}}$	0	0.1	0.2	0.3	0.4
$\pi 3 = \frac{\varphi}{\varphi_{MAX}}$	0.25	n/a	0.5	n/a	1
$\pi 4 = \frac{rb}{R}$	0.86	n/a	1	n/a	1.14

Table 14 Range of Pi Term Values

As per the DOE approach, simulations are carried out such that parametric inter-relations can be determined. The following table provides an overview of the simulation run order along with the various Pi variable values.

Simulation Run Order	$\pi 2$	$\pi 3$	$\pi 4$	Simulation Run Order	$\pi 2$	$\pi 3$	$\pi 4$
1	<i>0</i>	<i>0.25</i>	<i>0.86</i>	24	<i>0.2</i>	<i>0.5</i>	<i>1.14</i>
2	<i>0</i>	<i>0.25</i>	<i>1</i>	25	<i>0.2</i>	<i>1</i>	<i>0.86</i>
3	<i>0</i>	<i>0.25</i>	<i>1.14</i>	26	<i>0.2</i>	<i>1</i>	<i>1</i>
4	<i>0</i>	<i>0.5</i>	<i>0.86</i>	27	<i>0.2</i>	<i>1</i>	<i>1.14</i>
5	<i>0</i>	<i>0.5</i>	<i>1</i>	28	<i>0.3</i>	<i>0.25</i>	<i>0.86</i>
6	<i>0</i>	<i>0.5</i>	<i>1.14</i>	29	<i>0.3</i>	<i>0.25</i>	<i>1</i>
7	<i>0</i>	<i>1</i>	<i>0.86</i>	30	<i>0.3</i>	<i>0.25</i>	<i>1.14</i>
8	<i>0</i>	<i>1</i>	<i>1</i>	31	<i>0.3</i>	<i>0.5</i>	<i>0.86</i>
9	<i>0</i>	<i>1</i>	<i>1.14</i>	32	<i>0.3</i>	<i>0.5</i>	<i>1</i>
10	<i>0.1</i>	<i>0.25</i>	<i>0.86</i>	33	<i>0.3</i>	<i>0.5</i>	<i>1.14</i>
11	<i>0.1</i>	<i>0.25</i>	<i>1</i>	34	<i>0.3</i>	<i>1</i>	<i>0.86</i>
12	<i>0.1</i>	<i>0.25</i>	<i>1.14</i>	35	<i>0.3</i>	<i>1</i>	<i>1</i>
13	<i>0.1</i>	<i>0.5</i>	<i>0.86</i>	36	<i>0.3</i>	<i>1</i>	<i>1.14</i>
14	<i>0.1</i>	<i>0.5</i>	<i>1</i>	37	<i>0.4</i>	<i>0.25</i>	<i>0.86</i>
15	<i>0.1</i>	<i>0.5</i>	<i>1.14</i>	38	<i>0.4</i>	<i>0.25</i>	<i>1</i>
16	<i>0.1</i>	<i>1</i>	<i>0.86</i>	39	<i>0.4</i>	<i>0.25</i>	<i>1.14</i>
17	<i>0.1</i>	<i>1</i>	<i>1</i>	40	<i>0.4</i>	<i>0.5</i>	<i>0.86</i>
18	<i>0.1</i>	<i>1</i>	<i>1.14</i>	41	<i>0.4</i>	<i>0.5</i>	<i>1</i>
19	<i>0.2</i>	<i>0.25</i>	<i>0.86</i>	42	<i>0.4</i>	<i>0.5</i>	<i>1.14</i>
20	<i>0.2</i>	<i>0.25</i>	<i>1</i>	43	<i>0.4</i>	<i>1</i>	<i>0.86</i>
21	<i>0.2</i>	<i>0.25</i>	<i>1.14</i>	44	<i>0.4</i>	<i>1</i>	<i>1</i>
22	<i>0.2</i>	<i>0.5</i>	<i>0.86</i>	45	<i>0.4</i>	<i>1</i>	<i>1.14</i>
23	<i>0.2</i>	<i>0.5</i>	<i>1</i>				

Table 15 Simulation run order and Pi configurations

7.1.2 Geometric Configurations

The geometric variables defined in the above are associated to both stator and rotor blade geometry. The stator blade number or $\varphi/\varphi_{\text{MAX}}$ is defined as the ratio of blade number relative to the baseline blade number of 12. Here stator blade number is varied from 3, 6 and 12 resulting in $\varphi/\varphi_{\text{MAX}}$ of 0.25, 0.5 and 1. The following figures depict the variations in stator geometries:

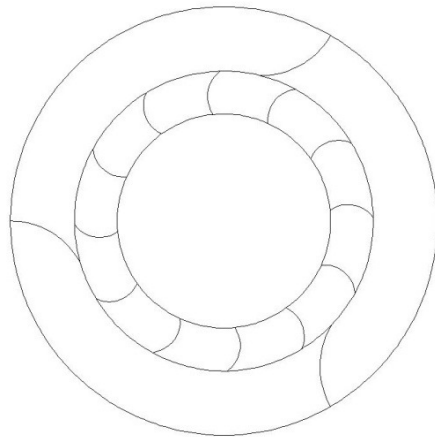


Figure 7-1 Stator blade geometry corresponding to $\varphi/\varphi_{\text{MAX}} = 0.25$

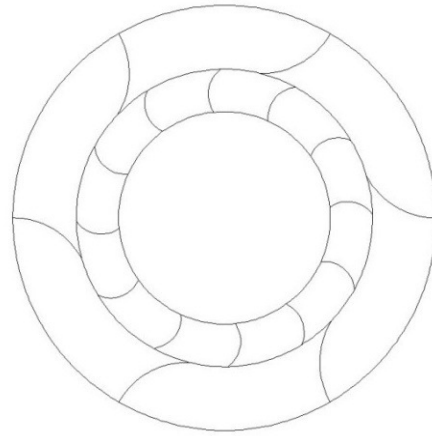


Figure 7-2 Stator blade geometry corresponding to $\varphi/\varphi_{\text{MAX}} = 0.5$

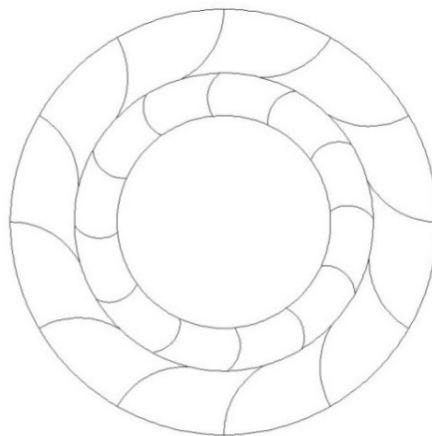


Figure 7-3 Stator blade geometry corresponding to $\varphi/\varphi_{\text{MAX}} = 1$

The rotor blade configurations are associated to blade tip radius and hence the relation r_{br}/R . Here, r_{br} is defined as the rotor blade inlet tip radius and is taken relative to R or the baseline rotor blade tip radius of 0.7m. The values of r_{br}/R correspond to 0.86, 1 and 1.14 respectively and are depicted in the following figures:

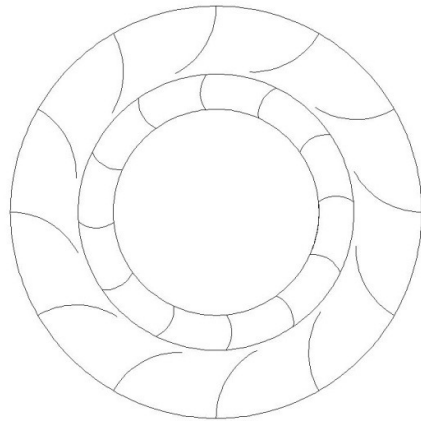


Figure 7-4 Rotor blade geometry corresponding to $r_{br}/R = 0.86$

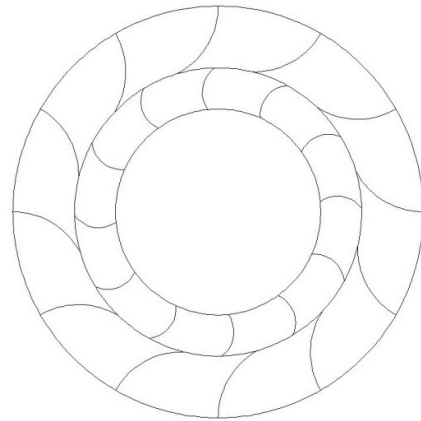


Figure 7-5 Rotor blade geometry corresponding to $r_{br}/R = 1$

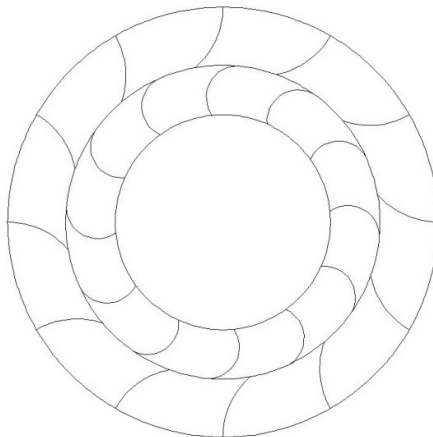


Figure 7-6 Rotor blade geometry corresponding to $r_{br}/R = 1.14$

7.1.3 Torque Characteristics

The following section presents torque data obtained from the wind turbine rotor from each of the simulations defined in Table 15. This torque output is computed from the sum of rotor blade torques and is the effective total rotor torque output. This analysis aims to determine the effects of each of the Pi variables on wind turbine torque relative to the baseline configuration described

'Design, Operation and Diagnostics of a Vertical Axis Wind Turbine'
By Gareth Colley, Department of Engineering & Technology, University of Huddersfield, UK

previously. The torque output (π_1) denoted C_T is plotted with π_2 such that rotational induced effects can be identified. Additionally, the effect of π_3 on C_T is described at each π_4 configuration.

Figure 7-7 depicts the rotor torque characteristics at $\pi_4=0.86$ for a range of π_3 configurations as a function of tip speed ratio (π_2). Hence rotor inlet tip radius is reduced (constant) and stator blade number is varied. It is noticed that when analysing the torque output of the rotor a considerable reduction is observed at each of the configurations tested when compared to the baseline. This trend indicates that a reduction in rotor blade tip radius results in a decrease in wind turbine torque output and is consistent at all stator configurations studied. Additionally, the effect of wind turbine solidity is highlighted in this figure where a reduction in torque is noticed at all rotational speeds when stator number is reduced (π_3). In this plot a maximum reduction of 69% is noticed when the rotor is static when comparing baseline torque to that generated with three stator blades. The stator blade number is also seen to govern the operating range of the machine in which at $\pi_3=0.25$ the range of tip speed ratio is significantly reduced when compared to the baseline. Hence the effect of using stator guide vanes to enhance power generation capabilities as apparent and where possible should be maximised.

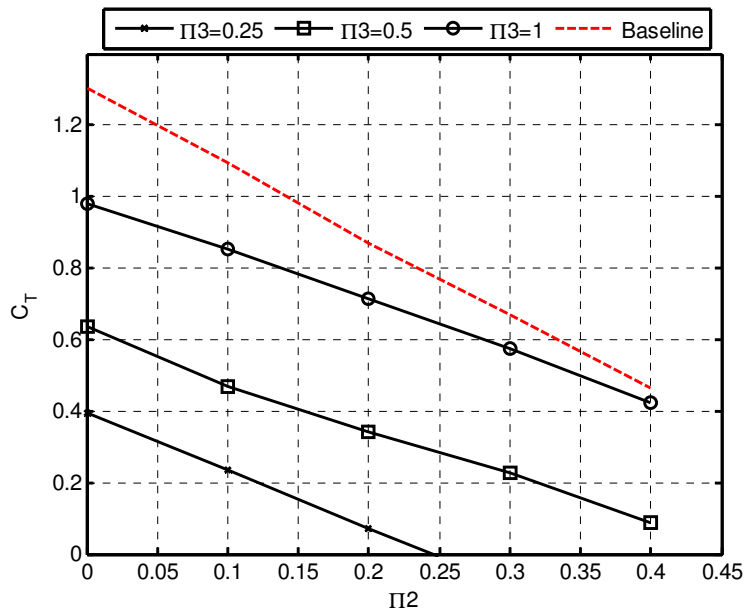


Figure 7-7 Wind turbine torque output (C_T) plotted with π_2 at $\pi_4 = 0.86$ for range of π_3

Wind turbine torque output computed at $\pi_4=1$ which corresponds to the same rotor blade tip radius as the baseline again shows similar trends to those observed previously. Here, rotor torque output decreases again with a reduction in π_3 which further highlights effects of

reducing stator blade number on performance. Additionally, the nature of torque generation shows similarities to the baseline in terms of profile gradient which is to be expected at this rotor blade tip radius. Similar effects are noticed concerning the wind turbine operating range where at $\pi_3=0.25$ torque output tends to zero at $\pi_2=0.33$ which is much lower than that seen for the baseline study described previously in this chapter. When using three stator blades the minimum torque output has increased from $C_T = 0.4$ to 0.64 for a static rotor which equates to an increase of 60% at this blade tip radius.

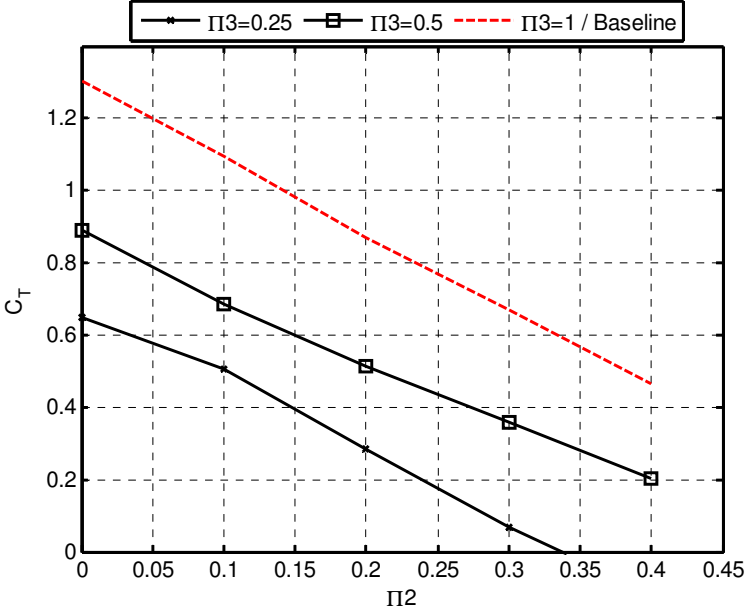


Figure 7-8 Wind turbine torque output (C_T) plotted with π_2 at $\pi_4 = 1$ for range of π_3

Wind turbine torque output computed at $\pi_4=1.14$ is depicted by Figure 7-9 again as a function of both π_2 and π_3 . Rotor blade tip radius is now increased compared to the baseline and results in considerable variations compared to the previous two plots. At $\pi_3=1$ torque output increases by 4% when the rotor is static ($\pi_2=0$) compared to the baseline data. As π_2 increases from 0 - 0.4 this torque output reduces when compared to the baseline configuration. At all other tip speed ratios studied (π_2) torque output is consistently lower than the baseline and also reduces considerably with a reduction of π_3 which agrees well with the previous two plots.

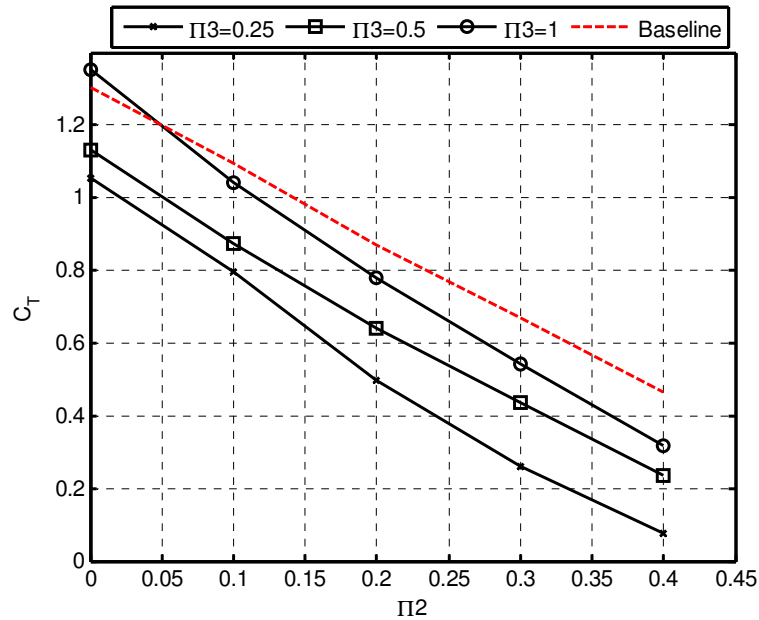


Figure 7-9 Wind turbine torque output (C_T) plotted with π_2 at $\pi_4 = 1.14$ for range of π_3

7.1.4 Power Characteristics

Wind turbine power output as computed from the rotor torque output and instantaneous rotational speed is presented in the following section in which wind turbine power is plotted for each wind turbine configuration. As per previous analysis power is computed using (6-4) and presented in the form of C_p as per (6-5).

The wind turbine power output at $\pi_4=0.86$ is depicted by Figure 7-10 where the effect of reducing rotor blade tip radius is observed. At this configuration power output is reduced at all conditions of π_2 when stator number conforms to the baseline ($\pi_3=1$). This further confirms that a reduction rotor blade tip radius has a negative effect on power generation for this wind turbine. Additionally, effects associated to stator blade number are again identifiable in which considerable reductions in power output are noticed with a reduction in π_3 . The power generation characteristics are seen to vary considerably at $\pi_3=0.5$ and $\pi_3=0.25$ in which the peak power generation point shifts towards a lower value of π_2 . Such effects pose severe limitations on the machines ability to generate electricity given the need to run at relatively high shaft speeds for synchronous power generation when utilizing the peak power point.

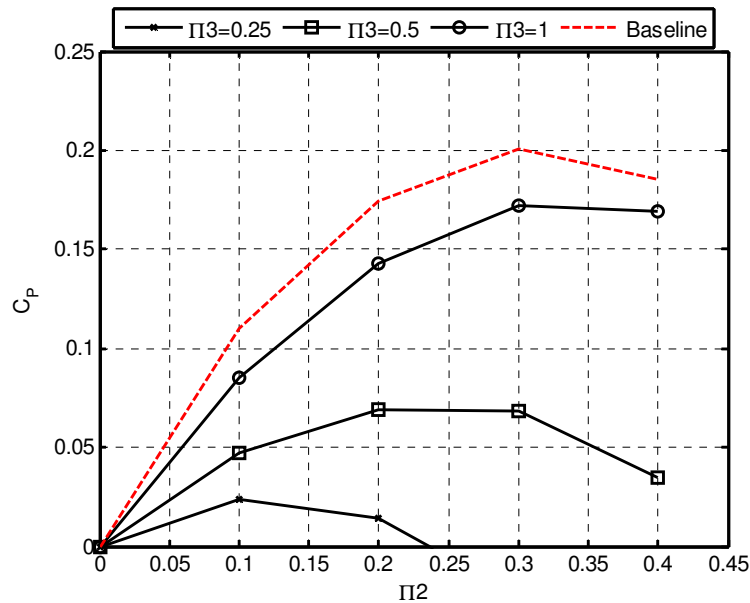


Figure 7-10 Wind turbine torque output (C_p) plotted with π_2 at $\pi_4 = 0.86$ for range of π_3

Wind turbine power output computed at the baseline rotor tip radius of $\pi_4=1$ is shown in Figure 7-11. Here wind turbine solidity follows previous trends observed where power generation is significantly reduced at low stator blade numbers (π_3). Again as per previous analysis the range of wind turbine operating range is seen to be severely reduced at $\pi_3=0.25$ which is indicative of a reduction in energy capture across the machine. The wind turbine power output at $\pi_4=1.14$ as shown in Figure 7-12 highlights the effect of increasing the rotor blade tip radius from the baseline at this particular blade position. It is seen that this geometric change results in a reduction in power output at all configurations of π_3 at all values of π_2 studied. At this rotor blade tip radius effects associated to wind turbine solidity are still prominent and similar trends are again noticed where power output reduces with a reduction in stator blade number.

The power output of this cross-flow wind turbine is therefore extremely sensitive to both changes in stator blade number and rotor blade inlet tip radius. It is seen that power output is reduced at all geometric configurations consistently over the full rotor speed range when deviated from the baseline design configuration.

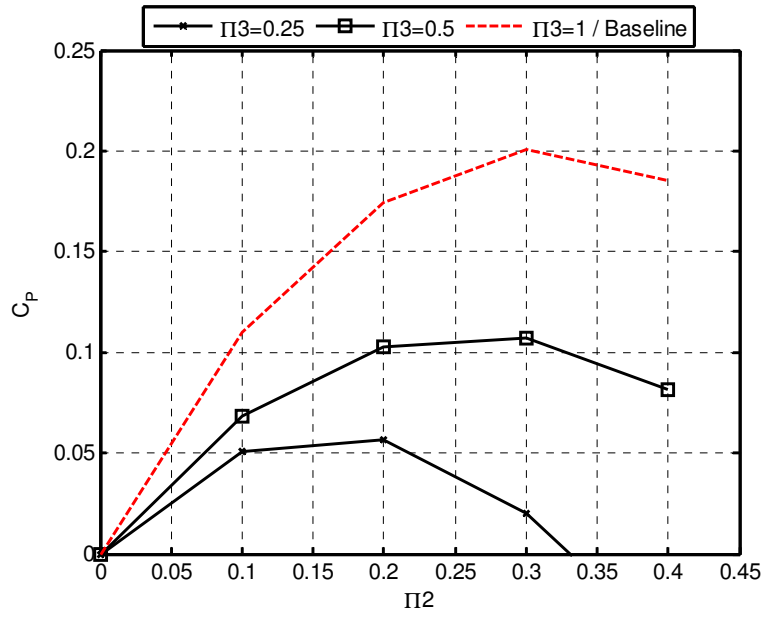


Figure 7-11 Wind turbine torque output (C_p) plotted with π_2 at $\pi_4 = 1$ for range of π_3

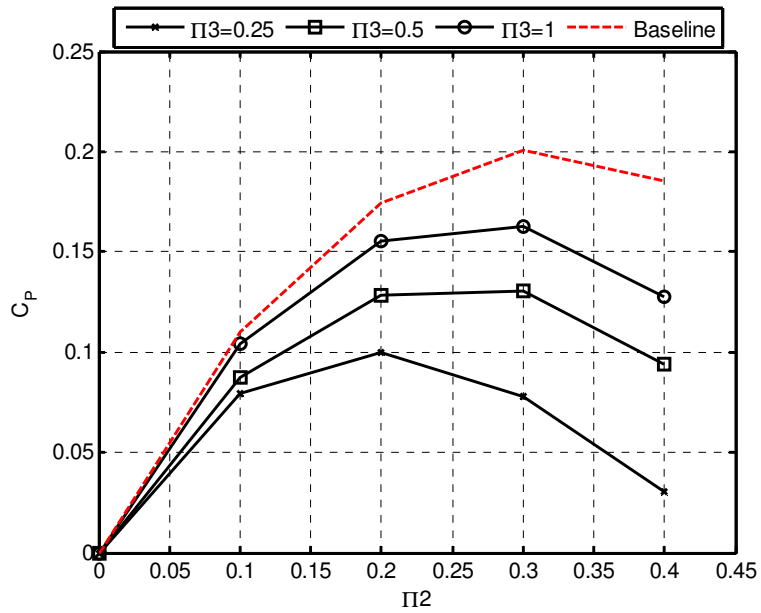


Figure 7-12 Wind turbine torque output (C_T) plotted with π_2 at $\pi_4 = 1.14$ for range of π_3

7.1.5 Regression Analysis

Using data obtained from DOE simulations a regression analysis is performed to determine a functional relationship between the dependent variable ' C_T ' and the independent variables π_2 , π_3 and π_4 . In this case the objective is to determine the regression function of the above independent variables such that predictions of wind turbine torque output can be made. This prediction of rotor torque can be used during the theoretical design stage and can be used to provide initial conditions for structural blade design along with both the support structure and drive train elements. This regression analysis relates the following:

$$y = f(\beta, X) \quad (7-15)$$

Where y is the dependent variable and X is the independent variable. Here β represents a coefficient which may be in the form of a scalar or a vector. For multiple linear regression with n number of independent variables the following relation is defined:

$$y = f(\beta_0 + \beta_1 X_i + \beta_2 X_i^2 + \varepsilon_i) \quad i = 1, \dots, n \quad (7-16)$$

Hence when considering rotor torque output (C_T) and the independent variables of π_2 , π_3 and π_4 the following expression is derived which is used as the primary design equation. Here X_1 , X_2 and X_3 correspond to π_2 , π_3 and π_4 respectively. Hence the regression relation is given by:

$$C_T = \beta_0 + \beta_1 X_1 + \beta_2 X_2 + \beta_3 X_3 + \beta_4 X_1 \cdot X_2 + \beta_5 X_1 \cdot X_3 + \beta_6 X_2 \cdot X_3 + \beta_7 X_1^2 + \beta_8 X_2^2 + \beta_9 X_3^2 \quad (7-17)$$

The following figure (Figure 7-13) depicts the torque output of the rotor which has been obtained from each DOE CFD simulation. Using the regression model described in the above, predicted rotor torque is computed for each DOE configuration which is used as the basis for the design equation given in (7-17). From this figure a strong correlation between CFD data and data generated using the regression model is present and exhibits a good overall fit. In Figure 7-14 the percentage variation between both data sets is computed in absolute terms. This percentage variation is defined as:

$$\% \text{ Variation} = \frac{(CFD - \text{Predicted})}{\text{Predicted}} \times 100$$

(7-18)

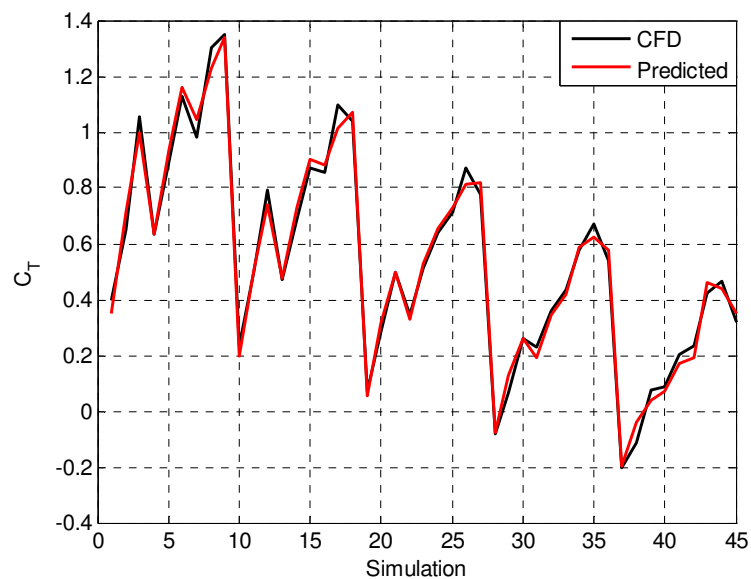


Figure 7-13 Wind turbine torque output (C_T) predicted and CFD

The percentage variation between both data sets is seen to be within +20% and -10% for all DOE configurations with the exception of two spurious points. These points namely from simulations 29 and 38 are a result of the negative torque output generated from the MRF solver at low stator blade numbers which have been omitted from the previous plots. This negative torque is a result of the rotor operating outside of its operational range given rotor speed is set before the solver is initialised. Hence for all practical purposes this erroneous output can be ignored.

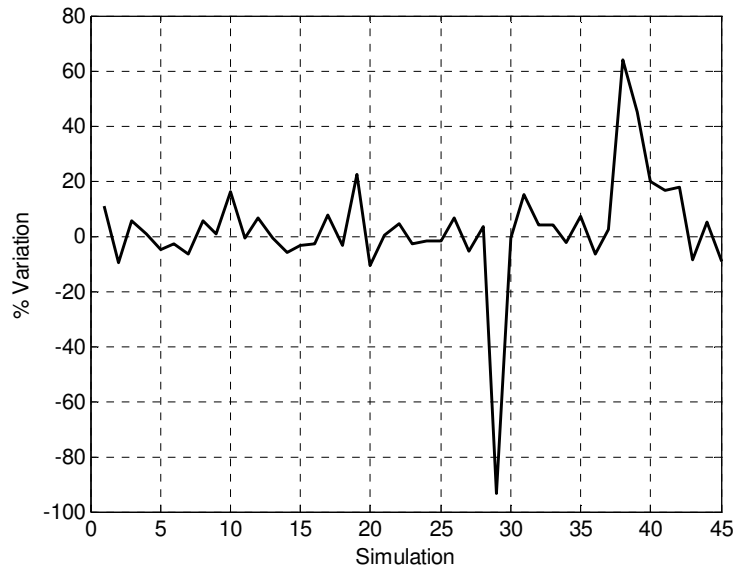


Figure 7-14 Wind turbine torque output (C_T) predicted % variation relative to CFD

Regression coefficients corresponding to (7-17) are given in the table below which can be used to compute cross-flow torque output for unique flow, fluid and geometric conditions:

Regression Coefficient	Value
β_0	-4.2418
β_1	1.5326
β_2	2.8539
β_3	6.6485
β_4	-0.1152
β_5	-3.6167
β_6	-1.6695
β_7	0.5738
β_8	-0.3967
β_9	-1.9647

Table 16 Wind turbine torque output regression coefficients

Using the design equation (7-17) the wind turbine design torque can be calculated. The procedure for calculating this rotor torque output requires a few key input parameters which should be considered during the conceptual design stage. These input parameters are summarised below:

Design Variable	Description
π_2	Rotor Blade Tip Speed Ratio
π_3	Stator Blade Number
π_4	Rotor Blade Inlet Tip Radius

Table 17 Design Variable Descriptions

The primary performance parameter π_2 defines the tip speed ratio of the turbine and hence is a critical parameter. Selecting a reasonable value requires the understanding of the flow conditions at the desired installation location such that a realistic value for π_2 can be computed. The stator blade number or π_3 should also be specified on the basis of local flow conditions and the requirement to increase the energy capture of the machine. When flow conditions are particularly low and self start up is of concern the number as stator blades and hence solidity ratio should be high. This also has leads to structural considerations and the overall cost of the machine. Finally π_4 corresponds to the rotor blade inlet tip radius and hence should be specified based on the specified design envelope and again the required rotor speed given its relation with rotor blade tip speed ratio. Assuming these three parameters have been specified accordingly then the rotor torque output can be computed. This therefore allows for initial torque output of the machine to be computed at unique wind site locations for a range of geometric configurations which is a novelty of this study.

7.1.6 **Summary**

A summary of the key findings of this optimization study are provided below:

- Both torque and power curves show strong dependence on both stator blade number and rotor blade inlet tip radius.

- Torque and power output is seen to be significantly reduced at all geometric configurations with the exception of one rotor speed when compared to the baseline design.
- The performance of the wind turbine is most sensitive to a reduction in stator number which highlights the increased power generation capability when employing high solidity stator arrays.
- Torque response data obtained from CFD simulations has been used to generate a multiple regression model with the purpose of deriving a design equation for cross-flow wind turbine torque output.
- The generated torque data from this model is seen to be within a tolerance band of +20% and -10% for all geometric configurations evaluated. Hence torque output can be computed with reasonable accuracy during the conceptual design phase for a range of operational and geometric configurations.

7.2 Rotor Diagnostics

Renewable energy sources such as wind energy are available without any limitations. In order to extract this energy effectively, the reliability of such technologies is critical if pay back periods and power generation requirements are to be met. Due to recent developments in the field of wind engineering and in particular the expansion of installed capacity around the world, the need for reliable and intelligent diagnostic tools is of greater importance. At present alternative diagnostic techniques are being investigated in which simulation based diagnostics is receiving increased support. Numerical models are now widely used to emulate rotating machinery particularly in the development of wind turbine control systems as presented in [80], [81]. Using a combination of numerical models an approximation of wind turbine performance is obtained with power curves generated using an ideal linear momentum method. From this the torque and speed signatures are computed and used to emulate wind turbine operational behaviour for development of peak power tracking controllers. Although this method allows for approximation of wind turbine performance considerable limitations are present within such models. The use of CFD to predict wind turbine signatures is a new area of research although has recently been used as a diagnostic and control tool as reported in [77–79]. The following section describes the development of a CFD prediction tool that allows for generation of rotor torque signatures for both healthy and faulty modes of operation and hence can be used for diagnostic applications along with general performance prediction.

7.2.1 Numerical Rotor Diagnostics

The following study uses a numerical CFD approach to carry out rotor diagnostics on this cross-flow wind turbine. This approach consists of a two-dimensional Sliding Mesh (SM) CFD model as per that described in Chapter 3. This allows for fully transient data to be obtained from the rotor such that dynamic torque output can be evaluated for both healthy and faulty rotors. The CFD model uses identical geometry to that used for 3D MRF simulations but is of a two-dimensional form to reduce computational demands. The torque output of the rotor is predicted over a base height of 1m which is a default output from the *Fluent 6.3*® solver. The flow condition used for this investigation corresponds to that used experimentally in which measurements taken along the mid-plane of the wind tunnel are used for CFD simulation. The flow profile is imported using a UDF method identical to that described in 4.1. The velocity magnitude computed as an average

velocity over the velocity-inlet boundary is 9.94m/s and is consistent for all CFD simulations presented in this section.

Using this approach two wind turbine geometries are studied which correspond to both healthy and faulty modes of operation. An overview of the geometries used is provided in the following two figures. The first figure presents the healthy condition which is identical to the baseline geometry studied in Chapters 5-7. The second figure depicts the faulty geometry where a single rotor blade has been removed similar to the type of failure expected during normal operation from potential bird strikes or other foreign bodies.

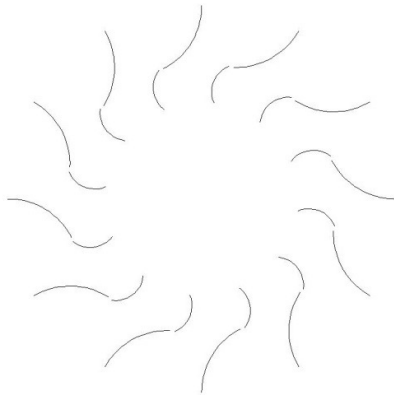


Figure 7-15 Wind turbine healthy geometry featuring 12 rotor blades

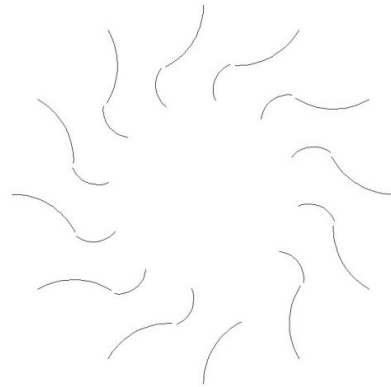


Figure 7-16 Wind turbine faulty geometry featuring 11 rotor blades

Using the above geometry transient simulations are conducted such that the dynamic torque output can be obtained. As per MRF solving technique the rotational speed (ω) of the rotor is specified before the solution is initialized hence acceleration/deceleration events cannot be computed. The data obtained from SM simulations is over four complete rotor revolutions such that the torque output is periodic; the dynamic and mean torque data is computed from the final rotor revolution. In order to obtain high resolution dynamic torque data, a small time-step is used such that the rotor rotates 0.1° at the predefined operating speed. This time step is shown to provide time-independent results when considering rotor torque output. A total number of time-steps are then defined such that the rotor travels four revolutions. Using this dynamic torque output from the final rotor revolution a mean torque is computed from torque output at each blade angular position.

The wind turbine dynamic torque spectrum is depicted in Figure 7-17 where torque output is presented for healthy and faulty rotors. This torque output is plotted in the time domain over one complete rotor revolution and shown for an example operating condition corresponding to $\lambda = 0.34$.

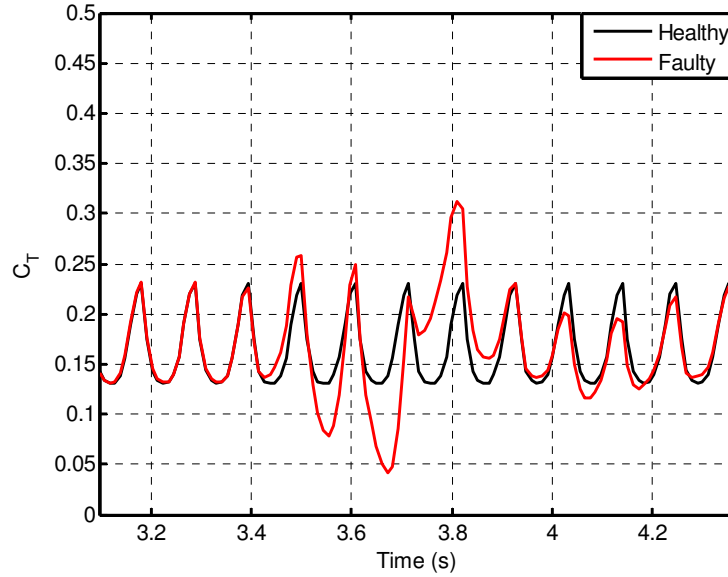


Figure 7-17 Predicted dynamic torque output for healthy and faulty rotor conditions for $\lambda=0.34$ over one revolution

The nature of torque output is seen to be periodic for both healthy and faulty conditions which agrees well with experimental data presented in Chapter 6. From this figure variations in rotor torque for both operating states is clearly visible between $t = 3.5 - 3.9$ seconds. Micro variations in torque are noticed throughout the full rotor revolution which is a result of downstream blade interaction effects as described in Chapters 4 - 6. RMS (6-2) values have been calculated for both healthy and faulty torque signals as shown in the following table:

Condition	RMS
Faulty	0.2243
Healthy	0.2224

Table 18 Rotor torque RMS for faulty and healthy operating conditions

System Component	Frequency (Hz)
Rotor Assembly	0.78
Rotor Blade	9.40

Table 19 CFD Rotor driving frequencies

In order to identify further variations in rotor operation this torque data is analysed in the frequency domain using a Fast Fourier Transform (FFT) [97]. From this data the key driving frequencies within the spectra can be identified such that any variations in amplitude can be used to determine the nature of fault. The torque signal used corresponds to that described for $\lambda=0.34$, at this condition the wind turbine driving frequencies present within the CFD simulation as shown in Table 19. Both healthy and faulty modes of operation are depicted in Figure 7-18 where the decomposed signals show large differences between each condition. The fundamental operating frequency (n) of the rotor assembly is 0.78 Hz along with blade passing frequency of 9.4 Hz ($n \times 12$). When comparing both healthy and faulty plots a large variation at this fundamental operating frequency is noticed. For the rotor under faulty conditions a peak is generated at this frequency along with multiples which are indicative of each blade cycle. Largest torque amplitude is observed at a frequency of 9.4 Hz or blade passing in which magnitudes are seen to be consistent between both rotor states. From this analysis the result of removing a single rotor blade from the 12 blade cross flow rotor is observed which is due to variations in the torque spectra provided previously.

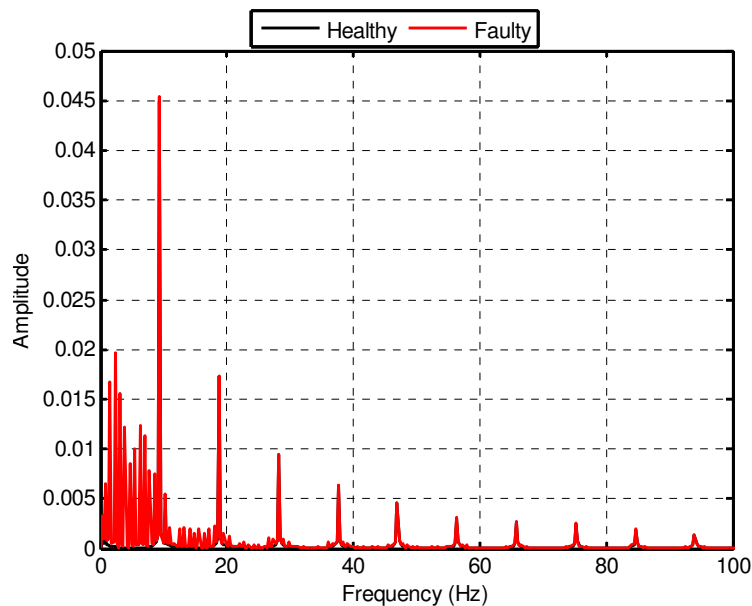


Figure 7-18 Predicted wind turbine FFT torque output (0-100Hz) for healthy and faulty operating conditions at $\lambda=0.34$

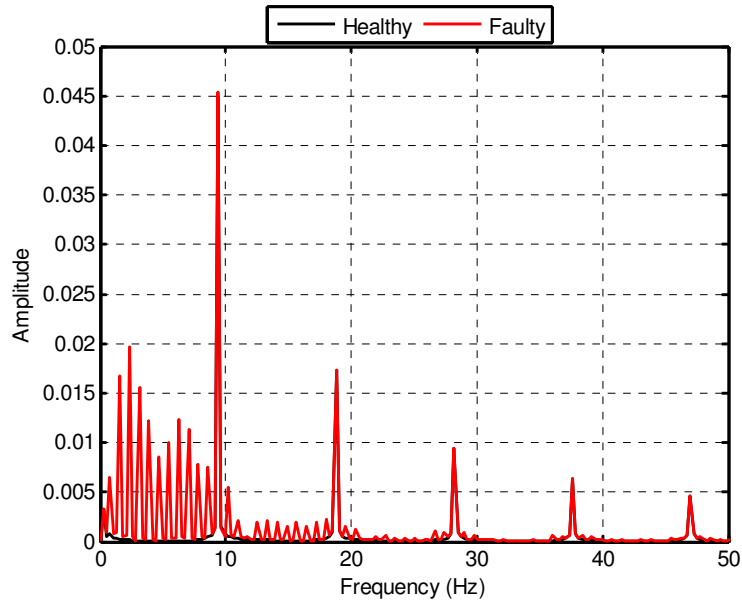


Figure 7-19 Close-Up Predicted wind turbine FFT torque output (0-50Hz) for healthy and faulty operating conditions at $\lambda=0.34$

Further analysis is performed on this torque signal in which Figure 7-20 and Figure 7-21 depict the predicted time-averaged rotor torque (C_T) and power (C_P) outputs over a range of λ . The result of removing a rotor blade during CFD computation appears to have little effect on the overall torque and power curves generated. Justification of this trend is due to the limitations of the CFD solving technique that does not allow for inertial effects within the rotating frame of reference. In practice it is expected that due to a reduction in rotor solidity, variations in torque and speed data will be more pronounced in time-averaged form.

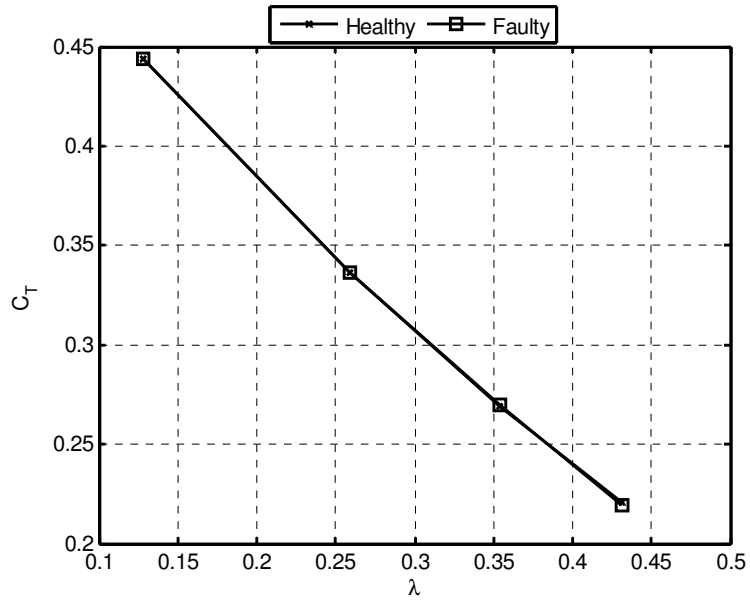


Figure 7-20 Wind turbine predicted time-averaged C_p plotted with λ for healthy and faulty conditions at $\lambda=0.34$

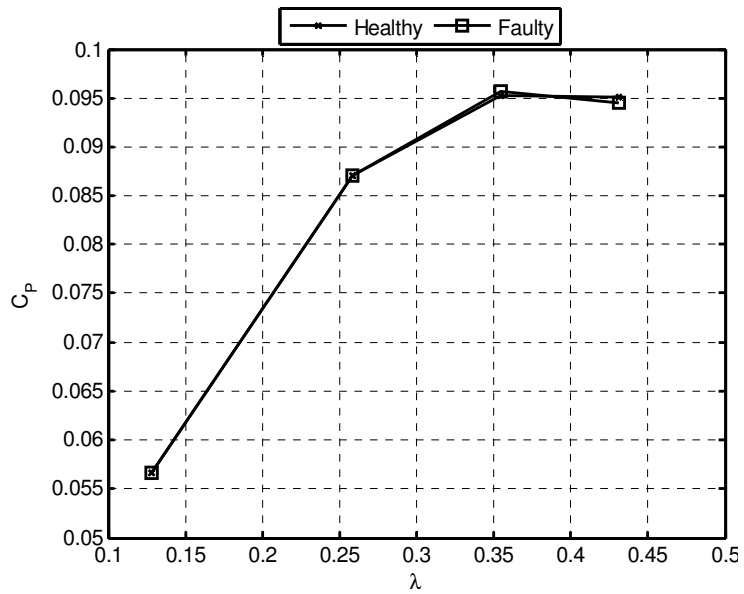


Figure 7-21 Wind turbine predicted time-averaged C_p plotted with λ for healthy and faulty conditions at $\lambda=0.34$

7.2.2 Experimental Rotor Diagnostics

In order to verify the capabilities of the CFD model to predict machine signatures for both healthy and faulty rotor states an experimental study is carried out. This experimental data is obtained from full scale wind turbine testing which conforms to the test setup defined in Chapter 3. For comparative purposes the flow condition used during performance analysis is also held constant such that the rotor operates at $\lambda=0.34$. The data presented is obtained once the rotor has attained steady state operation which is determined using the shaft speed sensor located on the main transmission shaft and an on screen LCD display. To replicate CFD geometrical configurations a rotor blade is removed for testing of the faulty rotor condition. Dynamic torque data from this experiment is provided in the following figure:

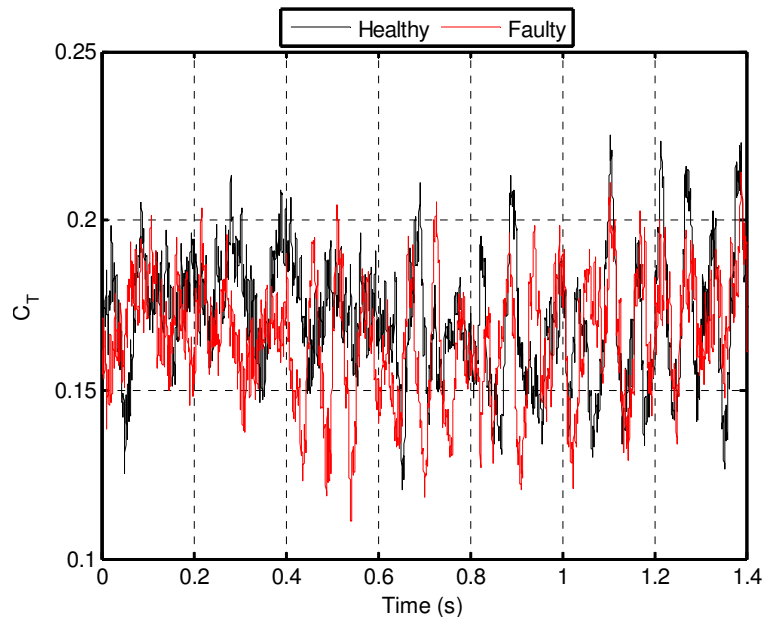


Figure 7-22 Experimental dynamic torque output for healthy and faulty rotor conditions for $\lambda=0.34$ over one revolution

From the above figure the dynamic torque signal can be seen over one rotor revolution. The torque characteristics have some similarities to those predicted using CFD in which a cyclic output is present as a result of the multi-blade format. Variations between both healthy and faulty modes of operation are observed between $t=0.4 - 0.6s$ which are indicative of rotor blade loss from a reduction in torque output. Again RMS values are computed for each torque spectra and compared to numerically predicted data as per the following table.

Condition	RMS
Faulty Numerical	0.2243
Healthy Numerical	0.2224
Faulty Experiment	0.2241
Healthy Experiment	0.2349

Table 20 Rotor torque RMS for faulty and healthy operating conditions

To determine variations in the frequency domain an FFT function is performed on the dynamic signals as depicted below. The driving frequencies present within the machine are calculated and given in the following table. The FFT plots as depicted in Figure 7-23 and Figure 7-24 highlight these driving frequencies for both healthy and faulty rotors. The most dominant frequencies are observed between 0 - 20 Hz which is to be expected given the rotor assembly operating speed and rotor blade passing frequency. As noticed with the analysis of the CFD data notable variations are generated at the fundamental operating frequency its associated multiples. Although the experimental data is not as defined as the ideal data output from CFD this trend is still relatively consistent. Due to this variation in torque output it can be determined that this is due to a reduction in blade number and the resultant micro variations in torque and rotor speed.

System Component	Frequency (Hz)
Rotor Assembly	0.78
Rotor Blade	9.40
Driving Gear	84.24

Table 21 Experimental rotor driving frequencies

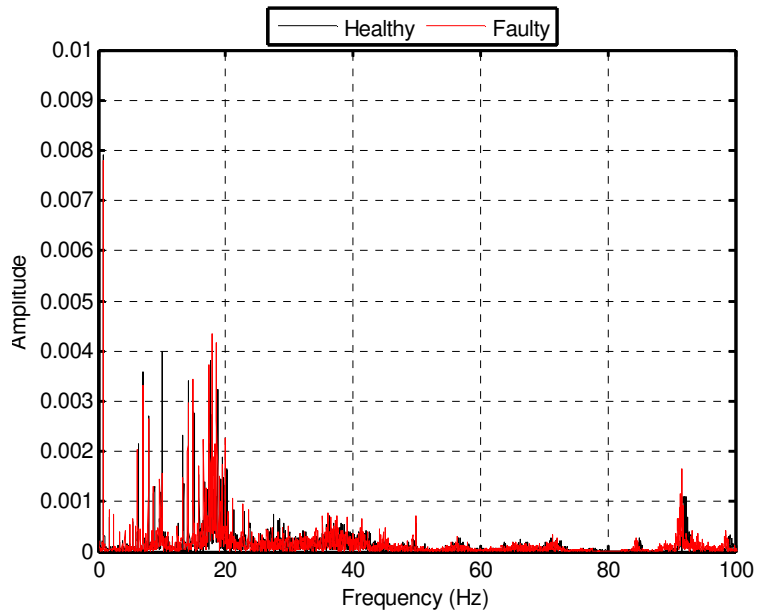


Figure 7-23 Wind turbine FFT torque output (0-100Hz) for healthy and faulty operating conditions at $\lambda=0.34$

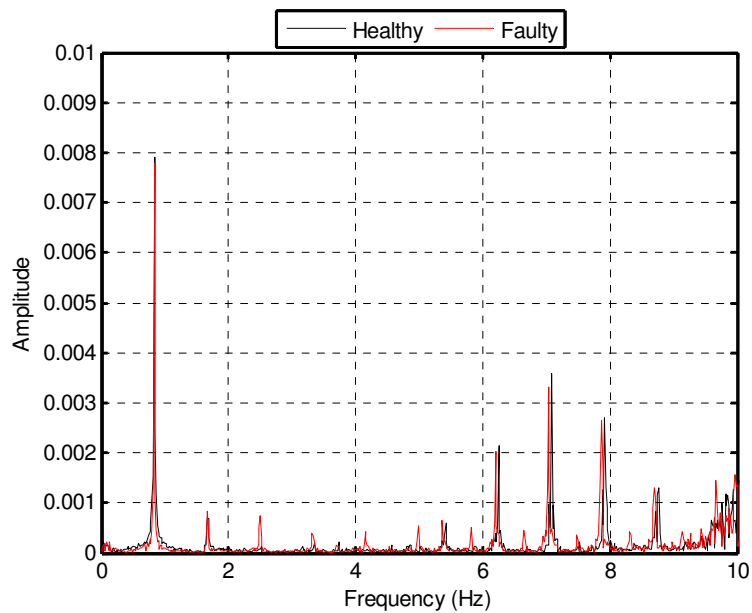


Figure 7-24 Wind turbine FFT torque output (0-10Hz) for healthy and faulty operating conditions at $\lambda=0.34$

In the above figures the operational frequencies of a cross-flow wind turbine are provided which allow for determination of rotor blade loss. These variations between healthy and faulty modes of operation indicate strong changes in the torque output of the rotor which agrees well with the time-averaged data presented in the following. It is seen that the time-averaged torque and power curves highlight large variation between both healthy and faulty conditions. This variation is consistent at

all λ and hence has considerable effects on wind turbine power generation capability. It is noticed that the linearity of torque output is also affected which is due to local acceleration/deceleration events occurring within the rotating frame of reference.

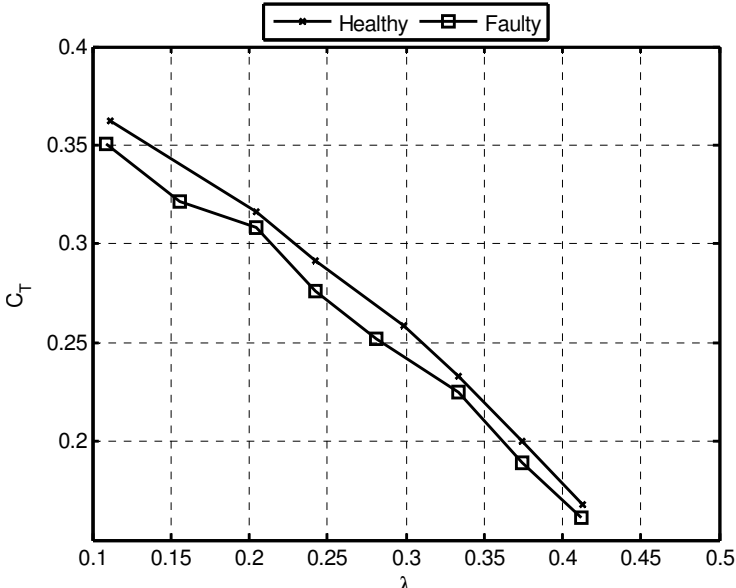


Figure 7-25 Wind turbine time-averaged C_T plotted with λ for healthy and faulty conditions

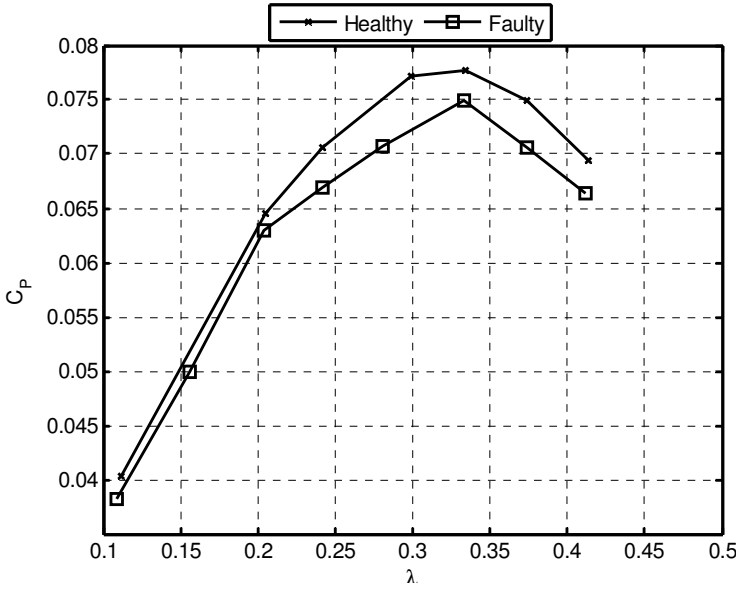


Figure 7-26 Wind turbine time-averaged C_P plotted with λ for healthy and faulty conditions

The effectiveness of the CFD model to predict wind turbine output signatures under fully transient conditions has been demonstrated in the above study. This dynamic torque output data can therefore be computed for a range of flow conditions which are likely to be experienced at the installation site. At present manufacturers are developing wind turbine control systems to improve reliability of systems using fault detection algorithms and also to enhance efficiency from peak power tracking [80], [81]. The use of CFD to replace more approximate performance prediction methods is therefore a more viable and accurate alternative. It also allows for tailoring of specific load profiles relative to the installation site chosen such that power generation capabilities of wind power technologies can be increased. The above model has been demonstrated on a new breed of cross-flow machine in which a relatively simple fault has been studied. This can be extended to multiple technologies and with the advancement in computation hardware the level of fault determined can be significantly reduced in size. Potential applications include crack detection in blades along structural deformations from foreign bodies.

7.3 Summary

The effects of rotor blade loss on the resultant torque output of a cross-flow wind turbine rotor have been examined using both numerical and experimental methods. The main conclusions drawn from this study are summarised in the following:

- Effects associated to rotor blade loss have been predicted using a two-dimensional CFD model in which micro variations in torque output are observed.
- Using a Fast Fourier Transform (FFT) technique dominant frequencies associated to both healthy and faulty modes of operations have been identified from predicted data. Variations between operating states are noticed at the rotor operating frequency in which the faulty rotor generates largest amplitude.
- Predicted time-averaged torque and power outputs show a large degree of similarity between healthy and faulty conditions due to the non-inertial capabilities of the model.
- Experimental torque signal shows considerable variation between healthy and faulty conditions due to reduction in rotor blade number.

- FFT analysis of experimental torque signal shows similar variations to CFD data at the rotor operating frequency which validates the capabilities of CFD fault prediction and overall effect with this rotor.
- Time-averaged torque and power data shows considerable differences between healthy and faulty conditions in which faulty torque and power is significantly reduced at all positions of λ . This is due to inertial effects which allow for variations in torque and speed signatures at the rotor output shaft.

CHAPTER 8

CONCLUSIONS AND FUTURE WORK

Scope

The following chapter provides a brief summary of the research aims defined in Chapter 2 and describes the works carried out in each chapter. The major achievements, conclusions and contributions are summarised and where possible referenced back to the initial aims of the thesis. Finally the works carried out in this study are evaluated and requirements for future work in this area are defined.

8.1 Research Problem Synopsis

Multi-blade cross-flow wind turbines are a new wind power technology receiving increased support due to uni-directionality, high torque output and self starting characteristics. It has been reported in literature that these machines operate within a low range of rotor tip speed ratio similar to that observed for the Savonius rotor [61], [62], [64], [66–68]. The performance capabilities of such machines are seen to vary considerably depending on the type of geometry used and in particular the method of capturing flow via the use of stator guide vanes. Due to a requirement for a new small scale urban wind turbine this cross-flow format has been evaluated in terms of its design features, operational behaviour and existing diagnostic potential.

From a comprehensive review of existing cross-flow wind turbine literature a number of limitations have been identified which are concerned with the above. In order to develop this new type of wind generator a set of objectives have been formulated which define the scope of this thesis. A summary of each is provided in the following along with the major achievements.

8.2 Research Aims and Major Achievements

The major aim of this thesis is to evaluate the performance characteristics of a novel cross-flow wind turbine which utilizes an outer stator guide vane to enhance energy capture. The specific objectives and thesis achievements are as follows:

- **Design & manufacture of a small scale cross-flow multi blade VAWT**

This thesis provides a detailed design methodology for a new cross-flow Vertical Axis Wind Turbine (VAWT) which is currently not available in literature. This design procedure provides design equations such that both rotor and stator blade profiles can be computed independently or for matched operation. The design generated in the present study is of micro VAWT format and is aimed at urban/residential applications where wind speeds are typically low and wind direction is constantly varied. The prototype design features a high solidity ratio such that both rotor and stator rings feature twelve blades. This high solidity is employed on the basis of increased energy capture and high starting torque with a view to providing consistent self start-up. Coupled with the increased energy capture of using multi guide vanes this machine is hoped to generate reasonable power output over a wide range of operational conditions making the design a good alternative to

existing technologies which are proven to underperform in urban applications. Using the generated blade geometry a full-scale prototype machine has been assembled and used during development testing and prototype validation studies. The machine is fabricated using sheet aluminium due to its lightweight characteristics which is cold formed to create the blade profiles. The machine features two distinct zones namely the rotor and stator assemblies which are independent structures located using a cradle type brace which features two bearing housings and locates the central transmission shaft of the machine. This design therefore provides a fixed outer stator blade array which directs the air flow into the rotating rotor assembly which maintains a fixed radial clearance between the stator blades. The prototype design is a relatively low cost lightweight machine which lends itself to residential applications without the need for significant structural framework. Due to the nature of its assembly and composition this machine is also easily serviceable and blades can be replaced in the case of damage or failure. This therefore also has applications in the developing world given the machine can be fabricated with relative ease and without the need for complex tooling. Finally, due to the nature of its high torque output this design also has additional applications other than electrical power generation. Particularly when considering this developing world and remote locations across the world the high torque output would allow for the pumping of water and grinding of produce.

- **Evaluation of wind turbine flow field characteristics**

Due to limitations identified in the literature review a thorough study of both the pressure and velocity fields generated across the wind turbine has been carried out. The variation of these flow field parameters has been evaluated in vertical, angular and radial directions within the turbine which is a major achievement of this study. In addition, the resultant effects of rotor speed have provided both static and rotational operating characteristics which are experienced during normal operation. From this analysis the distribution of pressure and velocity around the wind turbine has been determined along with effects associated to using multi-blade geometry which at present is not well documented. Further, from this analysis machine inefficiencies have been highlighted which can be used for future optimization studies. Secondary studies aimed at evaluating the mass flow distribution across the machine have resulted in further key operational characteristics which have been enumerated at various operating points for a range of expected wind speeds. Hence both 'design' and 'off-design' behaviour has been established which is a further key achievement of this study. Finally, the asymmetric flow fields identified within this design have been quantified in the form of a new performance related parameter namely asymmetry ratio. This ratio has been applied

to quantify energy capture of the wind turbine and also the downstream effects of the machine when considering the use of multiple cross-flow machines.

- **Analysis of wind turbine torque and power generation capabilities**

One of primary studies associated to wind power generation is the capability of the machine to generate torque and power. In the present study an extensive investigation has been carried out at both micro and macro levels to determine the performance characteristics of the machine with a view to benchmarking against existing technologies. These characteristics have been evaluated both experimentally and numerically with the aid of CFD. A key achievement of this study is the determination of individual rotor blade torque contribution computed as a function of rotor angular position which highlights machine inefficiencies which have been correlated with the flow field data obtained. These micro performance characteristics have been further investigated over a range of operating points and expected wind speeds. Combined torque output of these rotor blades has also been studied again over similar operating conditions which has allowed for quantification of expected total torque output of the machine. Using this torque data the rotor power output has been computed again over a full range of rotor and wind speeds in the form of a rotor power coefficient used for benchmarking against existing machines. Secondary performance studies are aimed at understanding topographical effects on performance in which the torque and power output of the turbine have been examined during rooftop installation on flat roof geometry. Further, the effect of rooftop installation location and vertical position have also been studied which is a key achievement of this work.

- **Parametric optimization of wind turbine performance**

In order to understand both 'design' and 'off-design' performance the power generation capabilities of the wind turbine a number of key parameters related to both the flow condition and wind turbine geometry have been identified. Using a Buckingham Pi approach these independent variables have been used to derive a set of non-dimensional Pi terms that sufficiently represent both the flow and geometric configuration of the wind turbine. These parameters namely π_2 , π_3 and π_4 are associated to rotor blade tip speed ratio, stator blade number and rotor tip radius respectively. Using a Design of Experiments (DOE) approach the factorial interaction between these variables and an independent variable torque a unique relation associated to rotor operating speed, turbine geometry and torque output has been determined. This relationship has been derived using a multiple regression method such that a design equation has been formulated which defines torque

output for this type of turbine. This is a major achievement of this thesis and is a novel contribution to the community.

- **Development of CFD based fault prediction model**

Given recent advances condition monitoring the effectiveness of a CFD based fault prediction model has been evaluated. This model has been developed in order to predict wind turbine dynamic torque signatures along with variations between health and faulty rotors. This faulty condition refers to a single rotor blade loss which could occur from a foreign body passing through the machine. The effects of this blade loss on the resultant torque and power outputs of the turbine have been examined. Studies have been conducted using a 2D transient CFD model which is used to predict the dynamic rotor torque signature for both healthy and faulty modes of operation. An operational analysis is performed on the predicted signatures using an FFT function to decompose the signal into the frequency domain. From this analysis the primary driving frequencies of the machine in the CFD solver are determined and variations between healthy and faulty states observed. The prediction capabilities of this model are verified using a follow up experiment in which the prototype wind turbine is subjected to identical faults. Again an operational analysis is performed and correlated with the numerical data. Finally, time-averaged torque and power responses are quantified for respective numerical and experimental approaches in which the potential applications for CFD based fault detection are described.

8.3 Thesis Conclusions

A comprehensive study has been carried out to support existing cross-flow literature and provide novel additions to improve the current understanding of the design process, operational characteristics, geometric related effects and diagnostic approaches for this type of machine. In the following the major conclusions from each facet of research are summarised.

- The wind turbine pressure field generated in the stream wise and normal to stream wise planes through the central axis of the turbine are seen to be highly symmetric about the mid-plane of the machine in the vertical direction. Such trends are consistent for both static and rotational rotor conditions. The pressure field generated at the mid-plane of the machine in the XY view indicates highly asymmetric pressures which are largely dependent on both angular and radial position within the turbine. Such trends are indicative of specific energy transfer zones within the turbine which have been highlighted to be passages S2, S1, S12 and S11 along with corresponding

rotor passages of R2, R1, R12 and R11. Additional trends are noticed on the leeward side of the machine where variations in pressure are observed as a result of interactions between the leeward rotor blades R6 and R7 and the stream wise flow. Such effects are a result of downstream interaction effects which result in counter-rotating torques.

- Secondary studies aimed at evaluating the mass flow distribution across the machine have resulted in the identification of further key characteristics. The overall distribution of mass efflux shows a large degree of symmetry about the centre line of the wind turbine and is consistent for stator and rotor passages at all operating conditions tested. It is noticed that rotor speed has most prominent effects on the leeward side of the turbine due to interactions between the stream-wise flow and downstream rotor blade set. It is shown that both stator and rotor passage mass flow characteristics are consistent over a range of wind and rotor speeds highlighting strong similarities in energy transfer throughout. From this analysis the effect of using both stator guide vanes and a high solidity rotor is seen in which primary inefficiencies of the cross-flow design are highlighted. Maximum mass flow is observed through the centre of machine for both stator and rotor passages where minimum mass flow is present at blade passages close to normal to the stream wise flow direction namely 3, 4, 8 and 9. This characteristic is due to blade angle relative to the flow direction and the resulting blade shielding effects.

- The asymmetric flow fields generated over the wind turbine result in non-uniform energy capture across the machine. This asymmetry has been quantified in the form of asymmetry ratio which relates the windward pressure and velocity fields with those generated on the leeward side. This flow field data is taken within the stator passages and hence signifies overall energy capture. It is seen that pressure asymmetry computed about a plane normal to stream wise is fairly symmetrical about the centre line of the wind turbine. Further, maximum asymmetry is noticed at closest proximity to this centre line at locations s1/s6 and s12/s7 which indicates a large reduction in pressure from the windward side of the machine to the leeward side of the machine. A maximum value of 1.59 is observed at s12/s7 for $\lambda=0.4$. Throughout the effect of rotor speed or λ on this distribution is limited with the exception of s12/s7. The velocity asymmetry ratio is seen to be more sensitive to a change in rotor speed and is of a more complex distribution compared to the pressure data. Here maximum velocity asymmetry is generated at s11/s8 for a static rotor and has a magnitude of 15.9 indicative of significant velocity reduction at this location. Asymmetry ratio has been applied to the downstream velocity field to determine effect of this high solidity machine on the local velocity field when considering multi turbine arrays. It has been reported that when plotting asymmetry as a function of downstream distance significant reductions in performance are expected between $x/D = 0$ and 5. Beyond $x/D = 10$ a maximum variation of 5% between the free-

stream condition is observed and hence is unlikely to have an appreciable effect on overall wind turbine performance.

- It is noticed that rotor blade torque output varies considerably about the central axis of the machine with highest torques generated at blades 1, 11 and 12 agreeing well with flow field data describing the key energy transfer zones. Effect of θ and λ on blade torque have identified 'dead-band' effects on the leeward side of the wind turbine at which counter-rotating torque is generated opposing the direction of motion. The effect of rotor blade position on the resultant torque output is seen to have significant influence on the overall torque output of the machine which agrees well with experimental data. Plot of rotor torque output highlights high torque characteristics of the wind turbine ($C_T = 1.17$) and is generated when the rotor is static. This is considerably higher than reported torque coefficients observed for the Savonius rotor which are in the order of $C_T = 0.3$. Wind turbine power output is seen to have strong similarities to the Savonius rotor in which C_p values of 0.24 have been observed at $\lambda=0.3$ close to mid rotor speed range and is significantly lower than machines reported in literature using similar conditioning devices. The reported values of C_p highlight the limitations of this particular machine in terms of electricity generation given its relatively low power and low operating speed.

- The effect of building topography on cross-flow performance has been evaluated in which a novel analysis has been carried out for a rooftop installation. Here increases in rotor torque output are noticed when installed at an upstream location at all positions studied when compared to a free-air condition. A maximum torque output of $C_T = 2.2$ is generated at h/D of 1 compared to $C_T = 0.85$ for the free-air tests. Downstream wind turbine torque output varies considerably depending on installation height in which maximum torque output is generated at h/D range of 1.25 – 1.75. At this location boundary related effects close to the rooftop wall have a strong influence on wind turbine torque generation capabilities. Upstream wind turbine power data highlights significant increases in power at all installation heights when compared to free-air data. Maximum powers are generated at $h/D = 1$ and 1.25 respectively for all conditions of λ studied. Downstream power data shows some similarities to the torque profiles described in which large reductions in power are observed at installation heights close to the roof. Maximum power generation is produced at $h/D = 1.5$ and 1.75 again for all conditions of λ . For maximum power generation on flat roof geometry the wind turbine should be located on the upstream side of the building at $h/D = 1$ where a C_p of 0.35 is generated which is a 71% increase over the free-air condition and 13% increase when compared to the downstream location.

- Using a Buckingham Pi and DOE approach the effect of varying Pi variables on rotor torque output has been determined. A number of geometric configurations have been derived that consider stator blade number and rotor blade inlet tip radius. The torque response as a function of tip speed ratio has been evaluated and compared to the baseline design configuration. Both torque and power curves show strong dependence on both stator blade number and rotor blade inlet tip radius. Torque and power output is seen to be significantly reduced at all geometric configurations with the exception of one rotor speed (static) when compared to the baseline design. The performance of the wind turbine is most sensitive to a reduction in stator number which highlights the increased energy capture when employing high solidity stator arrays. It is seen that when using three stator blades both torque and power output is reduced along with a reduction in operational speed range of the rotor assembly. This therefore limits power generation capabilities significantly. For optimum torque and power generation the geometric configuration should conform to that proposed in the baseline design under the flow conditions studied. Using the torque response data from the DOE simulations a multiple regression model has been developed in order to derive a relationship between each of the variables. Using this relationship torque outputs have been generated for the same DOE configurations and compared to the CFD torque output. The generated torque data from this model is seen to be within a tolerance band of +20% and -10% for all geometric configurations evaluated. Hence torque output can be computed with reasonable accuracy during the conceptual design phase for a range of operational and geometric configurations.

- Finally, given recent advances in multi-blade VAWTs and the increased probability of rotor failure particularly for urban applications the effect of blade loss on the resultant torque and power outputs of a cross-flow turbine are examined. From this analysis the primary driving frequencies of the machine in the CFD solver are determined and variations between healthy and faulty states observed. Using a spectral analysis rotor blade loss is noticed in a variation at rotor operating frequency or once per revolution. Predicted time-averaged torque and power outputs show a large degree of similarity between healthy and faulty conditions due to non-characterization of variations in inertial properties as a result of blade loss within CFD. The prediction capabilities of this model are verified using a follow up experiment in which the prototype wind turbine is subjected to identical faults. Again using an FFT function on the dynamic torque signal notable variations between healthy and faulty modes of operation are observed again at the rotor operating frequency as predicted using CFD. Verification of the RMS torque signal is also conducted in which CFD predicted data is within acceptable prediction levels. Time-averaged torque and power data shows considerable differences between healthy and faulty conditions in which faulty torque

and power is significantly reduced at all positions of λ . This is due to variations in rotor inertial properties between health conditions which at present commercial CFD solvers are unable to predict. From this analysis it can be concluded that CFD has large potential for use in the machine diagnostic field with a view to predicting specific fault conditions for particular flow and geometric configurations. Using such models torque signatures required for wind turbine emulation can be generated which has use in the development of peak power tracking controllers.

8.4 Thesis Contributions

The major contributions of this thesis are summarised in the following section in which novelties of this research are described:

- A design methodology for a novel multi blade cross-flow has been provided that allows for computation of a matched pair of both stator and rotor blades which can be used during the preliminary design phase. This methodology allows for blade profile computation for a unique operating condition and hence can be used for bespoke turbine design for specific applications.
- The primary operating characteristics of this novel cross-flow machine have been evaluated at both micro and macro levels which is a key contribution of this thesis. The pressure and velocity distribution across the wind turbine has been identified which can be used during structural blade design particularly for component lifecycle analysis. The effects of using a multi-blade rotor as a wind turbine on the flow fields generated have been studied and quantified. This has allowed for the identification of key inefficiencies within this design which are not well documented.
- The mass flow rate distribution around the wind turbine has been computed and highlighted the asymmetric flow profiles within this machine along with regions of the wind turbine that are shielded from the stream wise flow. To quantify the asymmetric energy capture of the machine a new performance related parameter has been proposed which directly quantifies energy capture of specific zone. This has been applied for evaluating downstream effects generated by this machine such that optimum location of multiple wind turbines can be computed.
- The performance characteristics of the machine have also been quantified at design and off-design conditions in which primary in-efficiencies of this technology have been identified. The unique contribution of each rotor blade to overall wind turbine torque output has been reported which is a novelty of this work and further highlights the effect of high solidity cross-flow machines on performance. Further, overall torque and power outputs have been communicated

'Design, Operation and Diagnostics of a Vertical Axis Wind Turbine'
By Gareth Colley, Department of Engineering & Technology, University of Huddersfield, UK

which have been investigated at diverse rotational and wind speeds such that performance capabilities outside of the design point have been established.

- The effect of local topography on micro turbine performance has been studied which is one of the major contributions of this thesis. The resultant effects of mounting the wind turbine on flat roof geometry on the torque and power response have been enumerated which have allowed for quantification of realistic performance levels for a specific urban application. Such characteristics are at present unavailable in literature and hence the power generation capabilities of the machine under urban flow conditions are a critical aspect of power quality. Additionally, effects related to rooftop installation position and height have also been studied which have allowed for recommendations to be made for rooftop mounting with a view to generating maximum power. This provides further contributions to this new area of wind engineering which can be used as a foundation for further studies including more complex topography and flow conditions.

- The effect of varying critical wind turbine geometry on the torque response has been documented over a range of rotational conditions. This has identified the benefits of using stator guide vanes to increase wind turbine performance over a range of operational points. Using this torque data a unique relation has been derived in the form of a design equation which can be used for total rotor torque output calculation for a range of cross-flow geometric configurations over a range of flow conditions. This is a unique contribution to the cross-flow wind turbine area of research and allows for prediction of torque output during preliminary design phase.

- A novel area of research namely CFD based fault detection has been proposed and has been successfully used to predict variations in wind turbine torque output. This novel technique provides a means of predicting a range of machine signatures under health and faulty modes of operation and has specific applications in wind turbine emulation in the development of control algorithms.

8.5 Recommendations for Future Work

The design, operation and diagnostics of a cross-flow VAWT have been determined in the present study such that gaps identified in literature could be satisfied. In light of the concluded remarks provided in the previous section this opens a vast potential for further research on this particular wind power technology. The main areas identified for further work are described in the following and are associated to further performance related analysis, optimization of wind turbine performance and development of numerical fault prediction models.

- This thesis provides a comprehensive flow field analysis and has highlighted the complex nature of flow through the machine. Additional studies should be focussed on obtaining full scale empirical data within both stationary and rotating reference frame under full inlet and transient wind conditions. This dynamic data can be used for further analysis of multi-blade interactions effects and ultimately in minimizing losses through the rotor.
- This thesis provides detailed performance data for the wind turbine geometry used in this study. The quality of power generation has been carefully examined and highlighted a number of concerns related to low power output and low speed nature. Although performance has been studied for a number of geometric configurations significant work is required to improve performance further and make electricity generation capabilities more viable. At present it has been identified that the use of stator guide vanes improves torque output significantly although current power outputs shows large variations to those reported in literature. Hence further work is required to understand why and provide innovative solutions for increasing both energy capture and improving power delivery from both an aerodynamic and transmission design perspective. Finally, from data provided in this report and the small operating range that peak power is generated a bespoke control system is required to maximise power generation in un-steady flow conditions experienced in the field. This particular facet of research requires the development of complex wind measurement equipment and state of the art load control algorithms.
- CFD based fault diagnostics is a new area of research and hence the long term potential and use of this particular tool is not yet well defined. It is however expected that with increases in computational power that CFD models can be used to generate machine signatures when coupled with additional data sources. This method of data fusion can be used in parallel with CFD to reduce the number of sensors used in real-time diagnostics which has the potential to significantly reduce system costs. Although this thesis has highlighted the potential of CFD to predict specific machine faults its scope should be extended to a number of rotating machines in which the level of fault

detail is increased. The use of CFD to predict variations in performance should then be evaluated which may have applications in blade crack detection which is a significant area of research in wind engineering. Additionally, effects associated to local wind conditions should be studied where fully transient wind formations should be investigated in order to determine the robustness of commercially available CFD codes to predict wind turbine healthy and fault signatures over a wide range of conditions.

REFERENCES

- [1] J. Walker, 'Renewable energies: How far can they take us?', 2009.
- [2] EWEC, 'Wind Energy Review', 2009.
- [3] BTM Consultants, 'World market update', 2007.
- [4] WWEA, "'World Wind Energy Report 2008.'", *Wind Energy Association, Charles-de-Gaulle-Str. 5, 53113 Bonn, Germany.*, 2008.
- [5] WWEA, "'New World Record in Wind Power Capacity: 14,9 GW added in 2006 Worldwide Capacity at 73,9 GW.'", *World Wind Energy Association, Charles-de-Gaulle-Str. 5, 53113 Bonn, Germany*, 2007.
- [6] J. . Lemming, 'Future wind energy technology and CO2 perspectives', 2009.
- [7] GWEC, 'Global Wind Energy Council', 2007.
- [8] BWEA, 'England's Regional Renewable Energy Targets: Progress Report', 2009.
- [9] EREC, 'Renewable energy framework directive'.
- [10] 'Storm of protest over planned windfarm | Environment | The Guardian', 06-Jul-2004. [Online]. Available: <http://www.guardian.co.uk/environment/2004/jul/05/windpower.energy>. [Accessed: 09-Aug-2011].
- [11] 'Giant wind turbines face a storm of protest | Environment | The Guardian', 24-Oct-2007. [Online]. Available: <http://www.guardian.co.uk/environment/2007/oct/25/windpower>. [Accessed: 09-Aug-2011].
- [12] 'Latest protest leaves climate strategy twisting in the wind | Environment | The Guardian', 28-Jul-2009. [Online]. Available: <http://www.guardian.co.uk/environment/2009/jul/28/shetland-windfarm-protest-rspb>. [Accessed: 09-Aug-2011].
- [13] E. Dayan, 'Wind energy in buildings: Power generation from wind in the urban environment - where it is needed most', *Refocus*, vol. 7, no. 2, pp. 33–38, March.
- [14] K. Syngellakis, S. Carroll, and P. Robinson, 'Small wind power: Introduction to urban small scale wind in the UK', *Refocus*, vol. 7, no. 2, pp. 40–45, March.
- [15] G. Westerholm, 'The wind energy frontier: Urban retail markets', *Refocus*, vol. 5, no. 4, pp. 42–45, July.
- [16] D. for C. and L. Government, 'Code for Sustainable Homes: A step-change in sustainable home building practice', 13-Dec-2006. [Online]. Available: <http://www.communities.gov.uk/archived/publications/planningandbuilding/codesustainable>. [Accessed: 06-Nov-2011].
- [17] A. D. Peacock, D. Jenkins, M. Ahadzi, A. Berry, and S. Turan, 'Micro wind turbines in the UK domestic sector', *Energy and Buildings*, vol. 40, no. 7, pp. 1324–1333, 2008.
- [18] 'B&Q pulls wind turbines from shelves | Business | guardian.co.uk', 06-Feb-2009. [Online]. Available: <http://www.guardian.co.uk/business/2009/feb/06/windpower>. [Accessed: 23-Jun-2011].
- [19] J. D. Ginger and J. D. Holmes, 'Effect of building length on wind loads on low-rise buildings with a steep roof pitch', *Journal of Wind Engineering and Industrial Aerodynamics*, vol. 91, no. 11, pp. 1377–1400, 2003.
- [20] K. S. Kumar and T. Stathopoulos, 'Wind loads on low building roofs: a stochastic perspective', *Journal of structural engineering New York, N.Y.*, vol. 126, no. 8, pp. 944–956, 2000.
- [21] A. Grant, C. Johnstone, and N. Kelly, 'Urban wind energy conversion: The potential of ducted turbines', *Renewable Energy*, vol. 33, no. 6, pp. 1157–1163, Jun. 2008.
- [22] 'Installer hit by Proven collapse', *BBC*, 14-Oct-2011.
- [23] H. Riegler, 'HAWT Vs VAWT, Re-Focus', 2003.
- [24] R. Romao, 'Integral Analysis of Rotors of a Wind Generator', *Renewable & Sustainable Energy reviews*, 2012.
- [25] B. Sereni, 'Model Simplification and Optimization of a Passive Wind Turbine Generator', *Journal of Renewable Energy*, vol. 34, 2009.
- [26] D. Gorelov, 'Prospects for Development of Wind Turbines with Orthogonal Rotor', *Journal of Thermophysics and Aeromechanics*, 2008
- [27] P. Eccleston and P. Eccleston, 'Urban wind turbines "may be waste of time"', *The Telegraph*.
- [28] V. Akhmatov, 'Influence of Wind Direction on Intense Power Fluctuations in Large Offshore Windfarms in the North Sea', *Wind Engineering*, vol. 31, no. 1, pp. 59–64, Jan. 2007.
- [29] S. Eriksson, H. Bernhoff, and M. Leijon, 'Evaluation of different turbine concepts for wind power', *Renewable and Sustainable Energy Reviews*, vol. 12, no. 5, pp. 1419–1434, Jun. 2008.

- [30] B. Blackwell, 'The Vertical Axis Wind Turbine "How it works"', *Sandia Laboratories*, no. SLA-74-0160, 1974.
- [31] G. Darrieus, 'Turbine Having It's Rotating Shaft Transverse to the Flow of the Current.', *United States Patent No.1*, 1931.
- [32] S. Savonius, 'The S-Rotor and it's application.', *Mechanical Engineering*, vol. Vol. 53, no. No.5, pp. 333-338, 1931.
- [33] V. Modi and M. Fernando, 'On the Performance of the Savonius Wind Turbine', *ournal of Solar Energy Engineering*, vol. Vol.111/71, 1989.
- [34] R. Sheldahl, 'Wind Tunnel performance data for two and three bucket savonius rotors', *J energy*, vol. vol 2, no. no3, pp. pp 160-164, 1978.
- [35] S. Sivasegaram, 'Secondary parameters affecting the performance of resistance-type vertical-axis wind rotors', 1978. [Online]. Available: <http://adsabs.harvard.edu/abs/1978WiEng...2...49S>. [Accessed: 07-Apr-2011].
- [36] B. Clayton, 'Observations of the flow in and around Savonius and Darrieus rotors', *Proc First British Wind Energy association conference, Cranfield*, pp. pp24-31, 1978.
- [37] N. Fujisawa, H. Shirai, and Y. Mizuno, 'Hot wire anemometer measurements of flow fields around savonius rotors in open circuit wind tunnel', *Laser and hot wire/film velocimetries and their applications. (ed by association for the study of flow measurement)*, pp. pp109-122, 1987.
- [38] S. L. Walker, 'Building mounted wind turbines and their suitability for the urban scale--A review of methods of estimating urban wind resource', *Energy and Buildings*, vol. 43, no. 8, pp. 1852-1862, Aug. 2011.
- [39] G. M. Joselin Herbert, S. Iniyar, E. Sreevalsan, and S. Rajapandian, 'A review of wind energy technologies', *Renewable and Sustainable Energy Reviews*, vol. 11, no. 6, pp. 1117-1145, 2007.
- [40] Z. Hameed, Y. S. Hong, Y. M. Cho, S. H. Ahn, and C. K. Song, 'Condition monitoring and fault detection of wind turbines and related algorithms: A review', *Renewable and Sustainable Energy Reviews*, vol. 13, no. 1, pp. 1-39, Jan. 2009.
- [41] Z. Hameed, S. H. Ahn, and Y. M. Cho, 'Practical aspects of a condition monitoring system for a wind turbine with emphasis on its design, system architecture, testing and installation', *Renewable Energy*, vol. 35, no. 5, pp. 879-894, May 2010.
- [42] P. Caselitz and J. Giebhardt, 'Advanced maintenance and repair for offshore wind farms using fault prediction techniques.', *ISET, Division of Energy Conversion and Control Engineering, Germany*.
- [43] European Standards Institution, 2010, EN 13306 Maintenance Terminology.
- [44] Johan Ribrant and Lina Margareta Bertling, 'Survey of Failures in Wind Power Systems With Focus on Swedish Wind Power Plants During 1997-2005', *IEEE Transactions on Energy Conversion*, vol. 22, no. 1, pp. 167-173, Mar. 2007.
- [45] S. Kahrobaee and S. Asgarpoor, "Risk-based Failure Mode and Effect Analysis for wind turbines (RB-FMEA)," *North American Power Symposium (NAPS), 2011*, vol., no., pp.1-7, 4-6
- [46] M. M. Khan, M. T. Iqbal, and F. Khan, 'Reliability and condition monitoring of a wind turbine', in *Canadian Conference on Electrical and Computer Engineering, 2005*, 2005, pp. 1978-1981.
- [47] S. Mertens, 'Wind energy in urban areas: Concentrator effects for wind turbines close to buildings', *Refocus*, vol. 3, no. 2, pp. 22-24, 2002.
- [48] B. Blackwell and R. Sheldahl, 'Wind turbine performance data for the Darrieus wind turbine with NACA 0012 blades', *Sandia Laboratories*, vol. SAND76, 1977.
- [49] R. Sheldahl and B. Blackwell, 'Free-Air Performance Tests of a 5-Metre-Diameter Darrieus Turbine', *Sandia Laboratories*, vol. 77, 1977.
- [50] M. Worstell, 'Aerodynamic Performance of the 17-M Diameter Darrieus Wind Turbine in the Three-Bladed Configuration: An addendum', *Sandia Laboratories*, vol. 79, 1982.
- [51] J. Gavalda, J. Massons, and F. Diaz, 'Experimental study on a self-adapting Darrieus-Savonius wind machine', *Solar and Wind Technology*, vol. 7, no. 4, pp. 457-461, 1990.
- [52] R. Gupta, A. Biswas, and K. K. Sharma, 'Comparative study of a three-bucket Savonius rotor with a combined three-bucket Savonius-three-bladed Darrieus rotor', *Renewable Energy*, vol. 33, no. 9, pp. 1974-1981, Sep. 2008.
- [53] B. Blackwell and R. Sheldahl, 'Wind Tunnel Performance Data for Two and Three-Bucket Savonius Rotors', *Sandia Laboratories*, vol. SAND76, 1977.
- [54] Biswas, A. Biswas, Gupta, R. Gupta, Sharma, and K.K. Sharma, 'Experimental Investigation of Overlap and Blockage Effects on Three-Bucket Savonius Rotors', *Wind Engineering*, vol. 31, no. 5, pp. 363-368, Oct. 2007.
- [55] N. Fujisawa and H. Shirai, 'Experimental Investigation on the Unsteady Flow Field Around A Savonius Rotor at the Maximum Power Performance', *Wind Engineering*, vol. Vol.11, no. No.4, 1987.

- [56] J. Massons, J. Gavaldam, X. Ruiz, and F. Diaz, 'Image Analysis of the Wake Generated by a Savonius Rotor', *Wind Eng*, vol. Vol.12, no. No.6, p. 341, 1988.
- [57] N. Fujisawa, 'On the torque mechanism of Savonius rotors', *Journal of Wind Engineering and Industrial Aerodynamics*, vol. 40, no. 3, pp. 277–292, 1992.
- [58] S. Sivasegaram and S. Sivapalan, 'Augmentation of power in slow-running vertical-axis wind rotors using multiple vanes', 1983. [Online]. Available: <http://adsabs.harvard.edu/abs/1983WiEng...7...12S>. [Accessed: 16-Jun-2011].
- [59] B. D. Altan, M. Atılgan, and A. Özdamar, 'An experimental study on improvement of a Savonius rotor performance with curtaining', *Experimental Thermal and Fluid Science*, vol. 32, no. 8, pp. 1673–1678, Sep. 2008.
- [60] T. Klemm, M. Gabi, and N. Heraud, 'Application of a Cross Flow Fan as Wind Turbine', *Journal of Computational and Applied Mechanics*, vol. 8, no. 2, pp. 123–133, 2007.
- [61] S. Lee, W. Song, J. Park, and Y. Kim, 'Experimental study on control performance of jet wheel turbo wind turbine', *The 9th Asian International Conference on Fluid Machinery, Korea*, 2007.
- [62] J. Park, S. Lee, M. Sabourin, and K. Park, 'A novel Vertical Axis Wind Turbine for Distributed & Utility Deployment', *Ontario Sustainable Energy Association*, 2008.
- [63] A. D. Peacock, D. Jenkins, M. Ahadzi, A. Berry, and S. Turan, 'Micro wind turbines in the UK domestic sector', *Energy and Buildings*, vol. 40, no. 7, pp. 1324–1333, 2008.
- [64] J. Fukutomi, T. Shigemitsu, and H. Daito, 'Study on Performance and Flow Condition of a Cross-Flow Wind Turbine With a Symmetrical Casing', *J. Fluids Eng.*, vol. 133, no. 5, pp. 051101–9, May 2011.
- [65] B. D. Altan and M. Atılgan, 'The use of a curtain design to increase the performance level of a Savonius wind rotors', *Renewable Energy*, vol. 35, no. 4, pp. 821–829, 2010.
- [66] M. Takao, 'A straight bladed vertical axis wind turbine with a directed guide vane row', *Thermal Science*, vol. 18, no. 1, pp. 54–57, 2009.
- [67] K. Pope, V. Rodrigues, R. Doyle, A. Tsopelas, R. Gravelsins, G. F. Naterer, and E. Tsang, 'Effects of stator vanes on power coefficients of a zephyr vertical axis wind turbine', *Renewable Energy*, vol. 35, no. 5, pp. 1043–1051, May 2010.
- [68] K. Pope, G. F. Naterer, I. Dincer, and E. Tsang, 'Power correlation for vertical axis wind turbines with varying geometries', *International Journal of Energy Research*, vol. 35, no. 5, pp. 423–435, Apr. 2011.
- [69] D. Neumann, 'Fault diagnosis on machine-tools by estimation of signal spectra', *Proc. IFAC Symp. SAFEPROCESS'91*, 1991.
- [70] A. Widodo, B.-S. Yang, D.-S. Gu, and B.-K. Choi, 'Intelligent fault diagnosis system of induction motor based on transient current signal', *Mechatronics*, vol. 19, no. 5, pp. 680–689, Aug. 2009.
- [71] C. Kar and A. R. Mohanty, 'Monitoring gear vibrations through motor current signature analysis and wavelet transform', *Mechanical Systems and Signal Processing*, vol. 20, no. 1, pp. 158–187, Jan. 2006.
- [72] C. K. Tan, P. Irving, and D. Mba, 'A comparative experimental study on the diagnostic and prognostic capabilities of acoustics emission, vibration and spectrometric oil analysis for spur gears', *Mechanical Systems and Signal Processing*, vol. 21, no. 1, pp. 208–233, Jan. 2007.
- [73] J. Tretrong, J. K. Sinha, F. Gu, and A. Ball, 'Bispectrum of stator phase current for fault detection of induction motor', *ISA Transactions*, vol. 48, no. 3, pp. 378–382, Jul. 2009.
- [74] R. . Schoen, T. . Habetler, F. Kamran, and R. . Bartfield, 'Motor bearing damage detection using stator current monitoring', *Industry Applications, IEEE Transactions on*, vol. 31, no. 6, pp. 1274–1279, 1995.
- [75] W. Lijun, M. . Lili, and H. Yongliang, 'The application of Lifting Wavelet Transform in the Fault Diagnosis of Reciprocating Air Compressor', *International Conference on Intelligent System Design and Engineering Application*, 2010.
- [76] F. Al-Badour, M. Sunar, and L. Cheded, 'Vibration analysis of rotating machinery using time–frequency analysis and wavelet techniques', *Mechanical Systems and Signal Processing*, vol. 25, no. 6, pp. 2083–2101, Aug. 2011.
- [77] S. Ahmed, R. Leithner, G. Kosyna, and D. Wulff, 'Increasing reliability using FEM-CFD', *World Pumps*, vol. 2009, no. 509, pp. 35–39, Feb. 2009.
- [78] H. Calisto, N. Martins, and N. Afgan, 'Diagnostic system for boilers and furnaces using CFD and neural networks', *Expert Systems with Applications*, vol. 35, no. 4, pp. 1780–1787, Nov. 2008.
- [79] A. G. Gerber, R. Dubay, and A. Healy, 'CFD-based predictive control of melt temperature in plastic injection molding', *Applied Mathematical Modelling*, vol. 30, no. 9, pp. 884–903, Sep. 2006.
- [80] B. Neammanee, 'Development of Wind Turbine Simulator for wind generator testing', *International Energy Journal* 8, pp. 21–28, 2007.
- [81] P. E. Battaiotto, R. J. Mantz, and P. F. Puleston, 'A wind turbine emulator based on a dual DSP processor system', *Control Engineering Practice*, vol. 4, no. 9, pp. 1261–1266, Sep. 1996.
- [82] D. . Wilson and T. Korakianitis, *The design of high efficiency turbo machinery and gas turbines*. .
- [83] Fluent, 'Fluent 6.3 User Guide' . .

- [84] 'Gambit 2.4.3 Modelling Guide'. Fluent Inc.
- [85] J. Aubin, D. F. Fletcher, and C. Xuereb, 'Modeling turbulent flow in stirred tanks with CFD: the influence of the modeling approach, turbulence model and numerical scheme', *Experimental Thermal and Fluid Science*, vol. 28, no. 5, pp. 431–445, Apr. 2004.
- [86] A. Nakayama and G. Fabris, 'Transport equations of conditionally averaged Reynolds stresses for computation of turbulent flows with intermittency', *Journal of Wind Engineering and Industrial Aerodynamics*, vol. 46–47, pp. 155–164, Aug. 1993.
- [87] A. D. Gosman, 'Developments in CFD for industrial and environmental applications in wind engineering', *Journal of Wind Engineering and Industrial Aerodynamics*, vol. 81, no. 1–3, pp. 21–39, May 1999.
- [88] S. Lain and C. Osorio, 'Simulation and evaluation of a straight bladed Darrieus-type cross flow marine turbine', *Journal of Scientific & Industrial Research*, vol. 69, pp. 906–912, 2010.
- [89] D. A. Deglon and C. J. Meyer, 'CFD modelling of stirred tanks: Numerical considerations', *Minerals Engineering*, vol. 19, no. 10, pp. 1059–1068, Aug. 2006.
- [90] B. Launder and D. Spalding, 'The Numerical Computation of Turbulent Flows', *Computer methods in Applied Mechanics and Engineering*, vol. 3, pp. 269–289, 1974.
- [91] W. L. Oberkampf and T. G. Trucano, 'Verification and validation in computational fluid dynamics', *Progress in Aerospace Sciences*, vol. 38, no. 3, pp. 209–272, 2002.
- [92] P. . Roache, 'Verification and Validation in Computational Science and Engineering', *Hermosa Publishers, New Mexico*, 1998.
- [93] K. Pope, G. F. Naterer, I. Dincer, and E. Tsang, 'Power correlation for vertical axis wind turbines with varying geometries', *International Journal of Energy Research*, vol. 35, no. 5, pp. 423–435, Apr. 2011.
- [94] T. Tanino, S. Nakao, and G. Uebayashi, 'Improving Ambient Wind Environments of a Cross-flow Wind Turbine near a Structure by using an Inlet Guide Structure and a Flow Deflector', *J. of Thermal Science*, vol. 114, no. 3, 2005.
- [95] M. Rahman, 'Aerodynamic characteristics of a three bladed Savonius rotor', *MSc Thesis dept of Mech Eng BUET Bangladesh*, 2000.
- [96] W. D. Curtis, J. D. Logan, and W. A. Parker, 'Dimensional analysis and the pi theorem', *Linear Algebra and its Applications*, vol. 47, pp. 117–126, Oct. 1982.
- [97] P. Duhamel and M. Vetterli, 'Fast fourier transforms: A tutorial review and a state of the art', *Signal Processing*, vol. 19, no. 4, pp. 259–299, Apr. 1990.